Doctoral Thesis

Development & Implementation of an Electron Diffraction Approach for Crystal Structure Analysis

Sergi Plana Ruiz

UNIVERSITAT DE BARCELONA

Development & Implementation of an Electron Diffraction Approach for Crystal Structure Analysis

Memòria presentada per optar al grau de doctor
per la Universitat de Barcelona

Programa de doctorat en Nanociències

Autor: Sergi Plana Ruiz

Directora i Tutora: Dra. Sònia Estradé Albiol
Director: Dr. Joaquim Portillo Serra
Directora: Dra. Ute Kolb

UNIVERSITAT DE BARCELONA

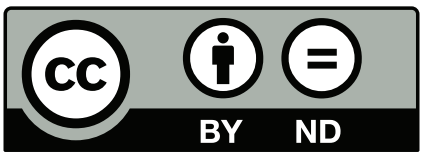

*Dedicated to **my parents**, who have been always here to support me in everything.*

Abstract

The application of electron diffraction to crystallographically characterize all kinds of materials has experienced new developments that have attracted some attention in recent years. A large number of structural analyses from different compounds have been already carried out with the help of 3D electron diffraction data that were not possible with the available X-ray methods. The use of a transmission electron microscope as an electron nano-diffractometer has proved to be advantageous when diffraction data from single nanocrystals are required, for instance in phase mixtures. In this way, the individual phases do not have to be purely synthesized, which always involves the risk of structural changes. The work presented here includes the development and implementation of a novel and universal routine for the accurate and reliable acquisition of electron diffraction data. The potential of this new data collection strategy to solve various crystallographic problems is illustrated using three known materials. In addition, two unknown crystal structures from commercial products are fully determined and refined; an organic dye of low symmetry and an incommensurate modulated structure of a major constituent of cement. In particular, the precise knowledge of the different crystal structures in cement clinkers, such as the α'_H-C_2S, enables the exact phase analysis of these industrial phase mixtures directly from the manufacturing process, and paves the way for its CO_2 emissions reduction.

Zusammenfassung

Neue Entwicklungen zur Methode der Elektronenbeugung für die kristallographische Charakterisierung von nanostrukturierten Materialien haben in den letzten Jahren einige Aufmerksamkeit auf sich gezogen. Mit Hilfe dreidimensionaler Elektronenbeugungsdaten konnte bereits eine Vielzahl an Strukturanalysen von Verbindungen durchgeführt werden, die mit den zur Verfügung stehenden routinemäßig anwendbaren Röntgenmethoden nicht zugänglich waren. Die Verwendung eines Transmissionselektronenmikroskops als Elektron-Nanodiffraktometer hat sich als vorteilhaft erwiesen, wenn individuelle Beugungsdaten von einzelnen Nanokristallen erforderlich sind, beispielsweise in Phasenmischungen. Auf diesem Wege müssen die einzelnen Phasen nicht rein synthetisiert werden, was immer die Gefahr struktureller Veränderungen birgt. Die hier vorgestellte Arbeit beinhaltet die Entwicklung und Implementierung einer neuartigen und universellen Routine zur genauen und zuverlässigen Erfassung von Elektronenbeugungsdaten. Das Potenzial dieser neuen Datensammlungsstrategie zur Lösung verschiedener Kristallographieprobleme wird zunächst anhand von drei bekannten Materialien veranschaulicht. Darüber hinaus werden zwei unbekannte Kristallstrukturen aus kommerziellen Produkten vollständig bestimmt und verfeinert. Zum einen handelt es sich um einen organischen Farbstoff mit niedriger Symmetrie, zu anderen um eine inkommensurabel modulierte Struktur von Klinker einem Hauptbestandteil von Zement. Besonders die genaue Kenntnis der Kristallstrukturen in kommerziellen Phasenmischungen, wie der bisher nur teilweise beschriebenen Klinkerphase α'_H-C_2S, erlaubt die exakte Phasenanalyse von kommerziellen Phasenmischungen direkt aus dem Produktionsprozess und ebnet den Weg zur gezielten Erniedrigung der CO_2-Bilanz von Zement.

Resum

L'aplicació de la difracció d'electrons per caracteritzar cristal·logràficament tot tipus de materials ha experimentat nous desenvolupaments que han cridat certa atenció durant aquests últims anys. Un gran nombre d'anàlisis estructurals en diferents compostos ja s'han dut a terme amb l'ajut de dades tridimensionals de difracció d'electrons que no eren possibles amb els habituals mètodes de raigs X. L'ús d'un microscopi electrònic de transmissió com a nano-difractòmetre d'electrons ha demostrat ser molt més beneficiós quan es requereixen dades de difracció de nanocristalls individuals, per exemple en mescles de fases cristal·logràfiques. D'aquesta manera, les fases individuals no s'han de sintetitzar en estat pur, fet que sempre comporta el risc de canvis estructurals. El treball presentat aquí inclou el desenvolupament i implementació d'una nova rutina universal per l'adquisició precisa i fiable de dades de difracció d'electrons. El potencial d'aquesta nova estratègia de recopilació de dades per resoldre diversos problemes cristal·logràfics s'il·lustra mitjançant tres materials coneguts. A més a més, dues estructures cristal·lines desconegudes de productes comercials han estat determinades i refinades completament; un colorant orgànic de baixa simetria i una estructura modulada incommensurada d'un component principal del ciment. En particular, el coneixement precís de les diferents estructures cristal·lines dels clinkers de ciment, com ara la α'_H-C_2S, permet l'anàlisi exacta de les fases d'aquestes mescles industrials extretes directament del procés de fabricació, i facilita el seu estudi per reduir les emissions de CO_2.

Glossary

3D ED	3D Electron Diffraction
A	Ampere
ADF	Annular Dark Field
ADT	Automated Diffraction Tomography
ARP	Analytical Resolution Pole Piece
BEA	Best Equivalent Amplitude
BF	Bright Field
bfp	back focal plane
CA	Condenser Aperture
CBED	Convergent Beam Electron Diffraction
CCD	Charge-Coupled Device
CFA	Charge-Flipping Algorithm
CL	Condenser Lens
CMOS	Complementary Metal–Oxide–Semiconductor
CM	Condenser Minilens
DC	Deflector Coil
DF	Dark Field
DL	Diffraction Lens
DM	Direct Methods
DME	Digital Micrograph Environment
DP	Displacement Parameter
DQE	Detective Quantum Efficiency
DTA	Differential Thermal Analysis
DVS	Difference Vector Space
EDS	Energy-Dispersive X-ray Spectroscopy
EDT	Electron Diffraction Tomography
EELS	Electron Energy Loss Spectroscopy
Fast-ADT	Fast and Automated Diffraction Tomography
FEG	Field Emission Gun
ffp	front focal plane
FOLZ	First-Order Laue Zone
FWHM	Full-Width at Half-Maximum
FWTM	Full-Width at Tenth-Maximum
GoF	Goodness-of-Fit
GUI	Graphical User Interface
HAADF	High-Angle Annular Dark Field
HRP	High Resolution Pole Piece
IC	Image Coils
IEDT	Integrated Electron Diffraction Tomography
IL	Intermediate Lens
IS	Image Shift
IUCr	International Union of Crystallography
LACBED	Large-Angle Convergent Beam Electron Diffraction

LT	Liquid N_2 Temperature
NBED	Nano-Beam Electron Diffraction
OA	Objective Aperture
ODS	Observable Diffraction Space
OL	Objective Lens
OM	Objective Minilens
PEDT	Precession Electron Diffraction Tomography
PL	Projector Lens
PM	Photomultipliers
post-OL	post-field Objective Lens
pre-OL	pre-field Objective Lens
RED	Rotation Electron Diffraction
ROI	Region of Interest
RT	Room Temperature
$\boldsymbol{s}$	Object distance
$\boldsymbol{s'}$	Image distance
SA	Simulated Annealing
SAA	Selected-Area Aperture
SAED	Selected-Area Electron Diffraction
SEM	Scanning Electron Microscope
STEM	Scanning Transmission Electron Microscope
TEM	Transmission Electron Microscope
TGA	Thermogravimetric Analysis
US1000	UltraScan 1000
US4000	UltraScan 4000
UHRP	Ultra-High Resolution Pole Piece
XRPD	X-Ray Powder Diffraction
ZOLZ	Zero-Order Laue Zone

Contents

Chapter 1

Introduction

From exertion come wisdom and purity;
from sloth ignorance and sensuality.

Walden
Henry David Thoreau

Advances in science and technology require the use of different tools to properly characterize existing and novel materials in order to meet the challenges of the modern world, e.g. higher efficiency of current devices or widely implementation of green solutions. One of the most important steps through this process is the determination of the atomic arrangement of the investigated systems. In other words, which elements are present, and, if there is ordering of the atoms, what are the basic building blocks and the arrangement of atoms within. Tools utilizing the diffraction phenomena successfully retrieve such kind of information and, in this doctoral work, the focus has been aimed to electron diffraction.

After the discovery of electron diffraction in 1927 [1, 2], the acquisition of electron diffraction patterns has been used as a complementary technique for X-ray methods to solve crystallography problems. It was not until the introduction of a tomography-like experiment from the diffraction space in 2007, that sequentially acquired electron diffraction patterns started to be used alone to reliably determine crystal structures [3, 4], the so-called **3D ED** technique. Since then, several developments on acquisition methods [5, 6, 7, 8, 9] and data processing tools [10, 11, 12, 13] have been carried out in order to bring the utilization of the technique on a routine basis [14]. However, the lack of automation still remains as the main disadvantage, which results in several hours of acquisition time for a single dataset that turns the use of the technique for systematic crystallographic investigations very time consuming.

One material that could specially benefit from the 3D ED technique is cement. Cement is a key material in our society as it is a strong building material that can withstand long periods of time. One example of this is the Colosseum of Rome, which was completed in 80 AD and it is still standing against the force of time. This characteristic results in cement being the largest manufactured product on Earth by mass, which combined with water and mineral aggregates form concrete, the second most used substance in the world due to its simple production from widely available materials, its easiness to place it and adjust it to complex geometries, and its high strength and density.

Nevertheless, one of the major concerns is the emission of CO_2. Its production dependence on the burning of fossil fuels contributes up to 5% of the global anthropogenic carbon dioxide emissions [15], thus its proper characterization to foresee alternative components is needed to reduce its impact.

The main component of cement is the clinker, which is an aggregate of different crystallographic phases from which alite (Ca_3SiO_5; 50-70%), belite (Ca_2SiO_4; 15-30%), aluminate ($Ca_3Al_2O_6$; 5-10%) and ferrite (Ca_2AlFeO_5; 5-15%) are the main constituents. The different phase ratios of these chemical components determine the strength development of the resulting cement. Several other chemical components like alkali sulfates or calcium oxides are also present in much lower amounts [16]. Figure 1.0.1 shows scanning electron microscope (SEM) images and chemical maps of a clinker sample. Its micro-structure can be described as follows: big alite and small belite grains crystallized in different polymorphs inside a matrix of ferrites and aluminates that crystallized in the brownmillerite phase of varying Al/Fe ratios [17, 18, 19, 20].

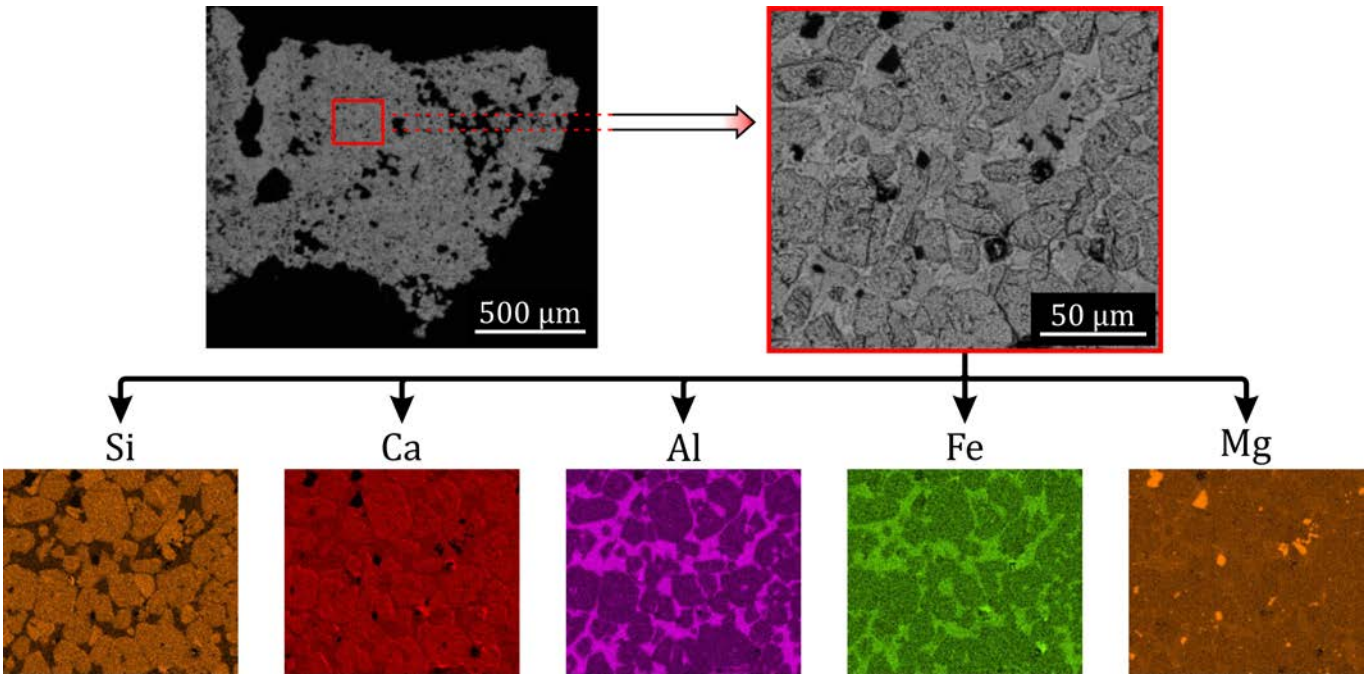

Figure 1.0.1: SEM images and chemical mapping of a clinker sample. Silicon and calcium EDS maps allow to identify alite (Ca_3SiO_5) as the big grains and belite (Ca_2SiO_4) for the small ones, since Si and Ca signals are lower and higher, respectively, for alite. Images are courtesy of Emilia Götz from the Technische Universität Darmstadt.

As shown in Figure 1.0.2, alite and belite constituents can crystallize in different phases, which have closely related cell parameters and space groups according to the temperature and dopants introduced in the manufacturing process. Such amount of crystal structures result in fine crystallographic investigations from X-ray methods unfeasible for real cement samples because of the strong reflections overlap. Therefore, the various crystal phases have to be produced in laboratory conditions to get single crystals or phase pure powder samples for further X-ray diffraction studies, which are not necessarily the same structures present in a sample from a cement plant.

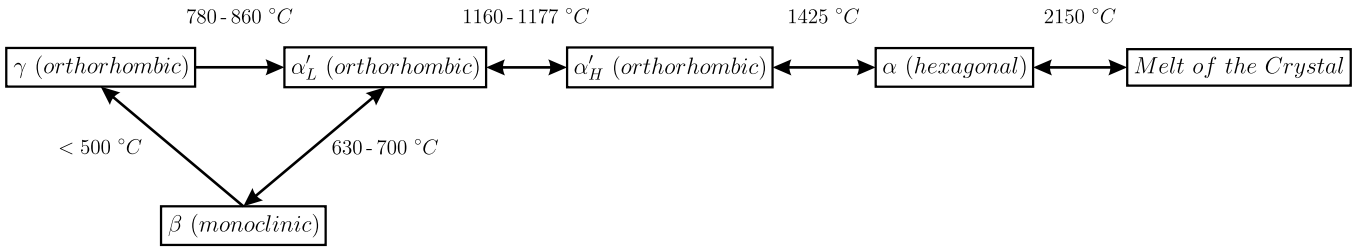

Figure 1.0.2: Schematic of the dicalcium silicate phase transitions between the different polymorphs with respect to temperature [16, 18].

In this context, the 3D ED technique can be very advantageous because an electron beam from a few to hundred nanometres can be set in a **transmission electron microscope** (TEM), and single crystals can be illuminated to acquire individual diffraction data from phase mixtures such as cement samples. Nevertheless, this kind of specimens requires the collection of several datasets from different particles to be able to identify the different crystal phases as well as ascertain the obtained models from more than one crystal. Thus an automated and systematic approach needs to be implemented so that the data acquisition can be routinely and accurately performed. In this doctoral thesis, such necessity has been taken as the main scope by the development and application of the **fast and automated diffraction tomography** (Fast-ADT).

This work is divided in seven chapters that starts from the theoretical background of diffraction, crystallography and TEM, to the crystal structure determination and refinement of a novel modulated structure of a crystalline clinker phase. It covers two distinct parts; a first technical part related to the alignment of a precessed quasi-parallel beam in a TEM and the development of the Fast-ADT technique, and a second one in which the acquisition method is applied to different materials to demonstrate the potential of electron diffraction with an automated approach like the Fast-ADT.

Two different materials have been used to prove the validity of the Fast-ADT and the different experimental setups implemented in this work. First of all, barium sulfate ($BaSO_4$: barite) is used to demonstrate the level of accuracy in the determination and refinement of a crystal structure. Barite is an inorganic salt with an orthorhombic crystal system (*Pnma*) mostly used in oil and gas exploration [21]. It has been chosen as the testing sample because of its particle size of hundred of nanometres as well as its stability under the electron beam. Subsequently, a recently solved new zeolite-like structure ($Si_{42}O_{84}$: RUB-5) is investigated to show the benefits of faster detectors for the characterization of disorder. RUB-5 is a layer silicate that exhibits a new silica polymorph in a monoclinic crystal system ($C2$) [22]. Such kind of structures are important due to their widespread application in catalysis, adsorption and ion exchange, thus its interest to know their crystal structure and fine crystallographic details for further crystalline modifications to best fit the intended purpose [23].

A third material is characterized in this context to show how electron diffraction can be used to reliably identify the absolute structure of non-centrosymmetric crystals. Here, a new silicide phase ($(Fe,Ni,Cr)_{3.92}Si_{1.08}$: π-ferrosilicide) is used, which is a cubic crystal ($P2_13$) formed within an austen-

ite/ferrite matrix of the RR2450 alloy. This alloy is developed by Rolls Royce as a derivative of the Fe-based stainless steel alloy Tristelle 5183 [24] that has been designed as a Co-free alternative for the coating of structural components in nuclear plants, such as pumps and valves, that need to be wear-resistant, strong and corrosion-resistant [25]. Figure 1.0.3 shows the three crystal structures used in this part to demonstrate what can be accomplished with Fast-ADT and the available processing tools.

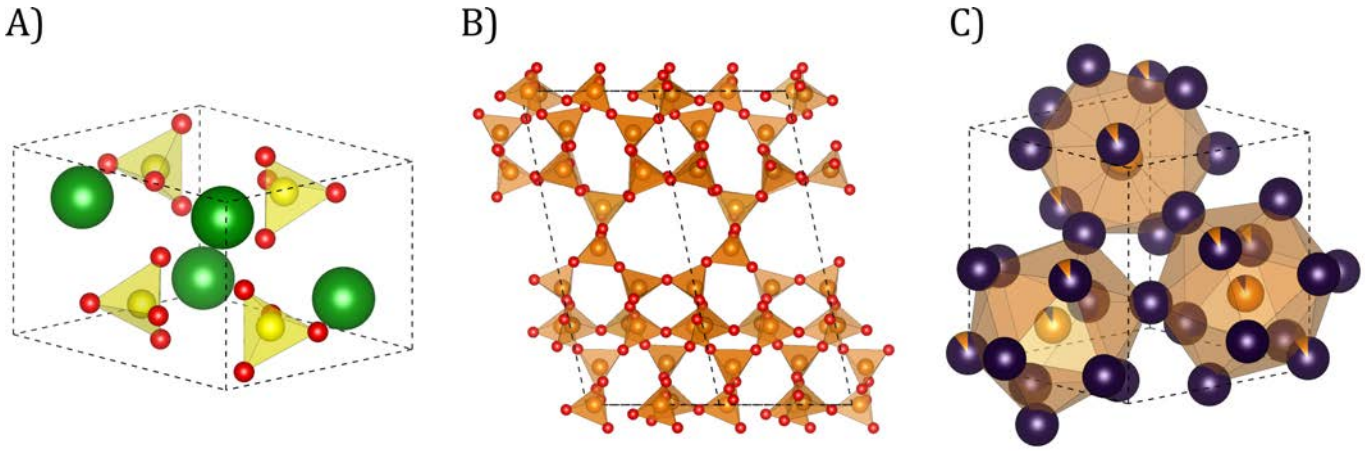

Figure 1.0.3: Structure models for A) barite (orthorhombic), B) RUB-5 (monoclinic) and C) π-ferrosilicide (cubic). Green atoms correspond to barium, red ones to oxygen, yellow ones to sulphur, orange ones to silicon and dark blue ones to iron-nickel-chromium positions.

After the chapter on the applications of Fast-ADT, two more chapters follow in which two unknown crystal structures are fully characterized by electron diffraction. The first one is about the *ab initio* structure determination and refinement of an organic dye called Disperse red 1 ($C_{16}H_{18}N_4O_3$: DRED1). This is a well known dye for its photochromatic properties and, large optical non-linearities and electro-optic properties as dopants or side groups in various polymeric films [26, 27, 28, 29]. However, a few studies have been carried out on the crystal structure of this powder and here a new dehydrated polymorph is discovered and refined.

The last chapter before the final conclusions deals with the crystallographic investigations of cement samples directly from production provided by the Schwenk Zement KG plant in Bernburg. Such study reveals the incommensurate modulation of a polymorph of dicalcium silicate, from which the incommensurate modulated structure is completely determined and refined only by means of electron diffraction data. These results show how Fast-ADT improves the acquisition of several datasets from different samples in an efficient and systematic way for sample screening and successful crystallographic characterizations.

Chapter 2

The Basics of Diffraction, Crystallography & TEM

Qui si convien lasciare ogne sospetto;
ogne viltà convien che qui sia morta.
[Here one must leave behind all hesitation;
here every cowardice must meet its death.]

Divina Commedia: Inferno
Dante Alighieri

X-ray diffraction was first reported in the works of Max von Laue, Paul Knipping and Walter Friedrich in 1912 [30] and Sir Lawrence Bragg in 1913 [31]. They presented photographic plates with a primary intense spot in the middle surrounded by considerable number of less intense spots that were acquired from copper sulphate pentahydrate, potassium chloride, rock salt and fluorspar crystals, thus demonstrating X-ray diffraction. About a decade later, George Paget Thomson and Alexander Reid in 1927, and, independently, Clinton Joseph Davisson and Lester Halbert Germer in the same year, demonstrated electron diffraction by the acquisition of patterns from thin celluloid plates and nickel crystals [1, 2]. Finally, Dane P. Mitchell and Philip N. Powers at the end of 1936, and Hans von Halban and Pierre Preiswerk in the beginning of 1937 acquired diffraction patterns on magnesium oxide and iron crystals from neutron sources [32, 33], thereby confirming the wave behaviour of matter predicted by de Broglie [34].

This doctoral thesis is mainly focused on the use of a TEM for the production of diffraction data of materials with unknown crystal structure, a field of work called **electron crystallography**. Particularly, by using a TEM not as a typical microscope but rather as an electron nano-diffractometer. This introduction chapter is meant to provide the physical foundation of the diffraction phenomena that pave the way to the description of the transmission electron microscope, its illumination and operation modes, the different diffraction patterns that can be acquired from these modes, and the crystallographic information that can be extracted from them.

2.1 The Diffraction Phenomena

Before starting with the theoretical background, it is important to differentiate between scattering and diffraction because "diffracted beams" and "scattered beams" are frequently and indistinctly used in many publications. Scattering is a physical process describing the deviation of radiation caused by the interaction with matter in a particle-like way. Diffraction is a physical process occurring when a wave interferes with an object and produces a pattern as a result. Note that both descriptions are equivalent through the particle-wave duality, thus both of them can be interpreted as two possible explanations of the same result, but diffraction wording is to be used when wave-like behaviour (**diffracted waves**) is discussed and scattering wording for particle-like descriptions (**scattered beams**).

2.1.1 From Huygens Principle to Fraunhofer Diffraction

The original principle of Christiaan Huygens in 1678 pictured light as a wave that propagates through space by means of the generation of secondary spherical waves at each point of the wavefront, which interfere and become the new wavefront [35]. Although it was a big step towards the explanation of light, in contraposition to the corpuscular theory of light [36], it had a main problem, it did not forbid the generation of waves in the opposite direction of propagation. In 1718, Augustin Fresnel introduced the obliquity factor in the Huygens principle to avoid the backward propagation, which states that the wave amplitude is maximum at the source and decreases with distance. This merged contribution plus the waves superposition principle of Fresnel was later referred as Huygens-Fresnel principle and explains several diffraction effects [37]. In 1882, Gustav Kirchhoff provided a mathematical formulation for wave propagation that derives the diffraction formulas used for the different spatial regimes [38]. He found a solution from the homogenous wave equation using the Green's theorem [39, 40, 41]:

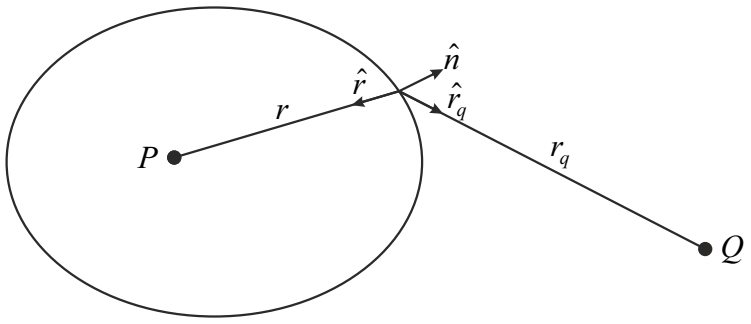

Figure 2.1.1: Parameters considered for the propagation of a wave according to the Kirchhoff formalism.

The disturbance at a point P due to any wave-field $\mathcal{W}$ is given by the integration over any closed surface containing P (see Figure 2.1.1)

$$\mathcal{W}_P = \frac{1}{4\pi} \oint_S \left(\left[\frac{\exp\{-2\pi i k r\}}{r} \right] \cdot \nabla \mathcal{W} - \mathcal{W} \cdot \nabla \left[\frac{\exp\{-2\pi i k r\}}{r} \right] \right) dS \tag{2.1.1}$$

where $k = 1/\lambda$ is the wavevector, λ is the wavelength and r is the distance from P to the surface S to be integrated. In case that the wave-field comes from a point source of unit strength located at

point Q, and all distances are much greater than the wavelength, the equation becomes

$$\mathcal{W}_P = \frac{i}{2\lambda} \oint_S \frac{\exp\{-2\pi i k r_q\}}{r_q} \frac{\exp\{-2\pi i k r\}}{r} \left[\cos\left(\hat{n} \wedge \hat{r}\right) - \cos\left(\hat{n} \wedge \hat{r_q}\right)\right] dS \tag{2.1.2}$$

where r_q is the distance between Q and the point at the surface, r is the distance between P to the point at the surface, $\hat{n}$ is the normal vector to the surface, $\hat{n} \wedge \hat{r}$ is the angle between $\hat{n}$ and $\hat{r}$, and $\hat{n} \wedge \hat{r_q}$ is the angle between $\hat{n}$ and $\hat{r_q}$. It is worth to say that due to the uncertainty principle [42], the origin of radiation cannot be specified with a precision better than about half of its related wavelength, so that *point sources* must be at least this size.

Equation 2.1.2 is particularly interesting because it can be interpreted as the Huygens-Fresnel principle: each secondary spherical wave emitted from each position of the surface, $\exp\{-2\pi i k r\} r^{-1} dS$, has an amplitude proportional to the incident wave from Q, $\exp\{-2\pi i k r_q\} r_q^{-1}$, and an obliquity factor, $\left[\cos\left(\hat{n} \wedge \hat{r}\right) - \cos\left(\hat{n} \wedge \hat{r_q}\right)\right]/2$, that ensures the forward propagation of the wave and adds up to the unity.

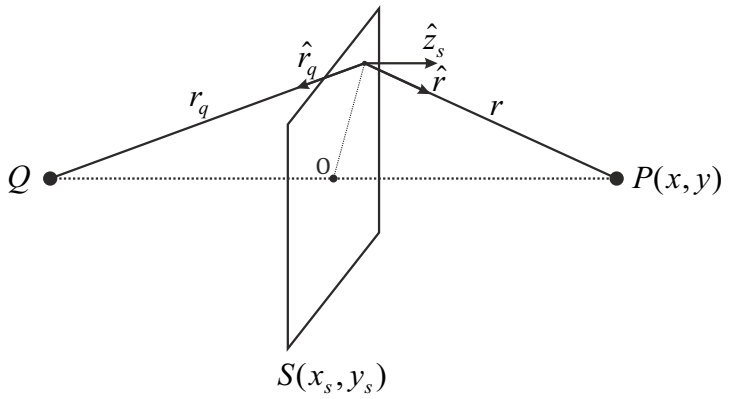

Figure 2.1.2: Parameters considered for the perturbation of a wave due to an object according to the Kirchhoff formalism.

The full potential of equation 2.1.2 is not its use for wave propagation, but rather to describe the case in which the wave-field $\mathcal{W}$ is the wave function of the radiation, $\Psi(x, y)$, modified by the presence of an object. Here the integration surface is conveniently used as the surface of this object. If the simple case of a two-dimensional object between points P and Q is considered, an arbitrary function can be introduced, $S(x_s, y_s)$, that multiplied by the incident wave function, $\exp\{-2\pi i k r_q\} r_q^{-1}$, results in the modification of the amplitude and phase of the wave due to the object. When the dimensions of the object are much bigger than the wavelength, and the emitter of radiation is a point source, the wave function at a given point of observation $P(x, y)$ becomes

$$\Psi(x, y) = \frac{i}{2\lambda} \int\int S(x_s, y_s) \frac{\exp\{-2\pi i k r_q\}}{r_q} \frac{\exp\{-2\pi i k r\}}{r} \left[\cos\left(\hat{z_s} \wedge \hat{r}\right) + \cos\left(\hat{z_s} \wedge \hat{r_q}\right)\right] dx_s dy_s \tag{2.1.3}$$

where the wave propagation is chosen to be along the $\hat{z_s}$ axis for convention, the 2D plane is placed perpendicular to the $\hat{z_s}$ axis, the integration surface is this plane plus another surface closed at infinity

that its corresponding integration tends to 0, and x_s and y_s are the remaining coordinates forming an orthogonal framework with $\hat{z}_s$ (See Figure 2.1.2). This expression can be directly used to describe the interaction of electrons accelerated at voltages higher than 10 keV with matter, since their related wavelength according to the de Broglie principle [34] is much smaller than the actual dimensions of atomic arrangements (See Table 2.1.1). At this point, equation 2.1.3 can be used to derive the most common expressions for Fresnel (near-field) diffraction and Fraunhofer (far-field) diffraction.

V (kV)	λ (Å)
10	0.1220
20	0.0859
50	0.0536
120	0.0335
200	0.0251
300	0.0197

Table 2.1.1: Associated wavelength of electrons (λ) for different acceleration voltages (V). These values are calculated using the de Broglie relation and the relativistic effects; $\lambda = h/\left[2m_0 V q_e(1 + q_e V/2m_0c^2)\right]^{1/2}$, where h is the Planck constant, m_0 is the rest mass of the electron, q_e is the elemental charge of the electron and c is the speed of light.

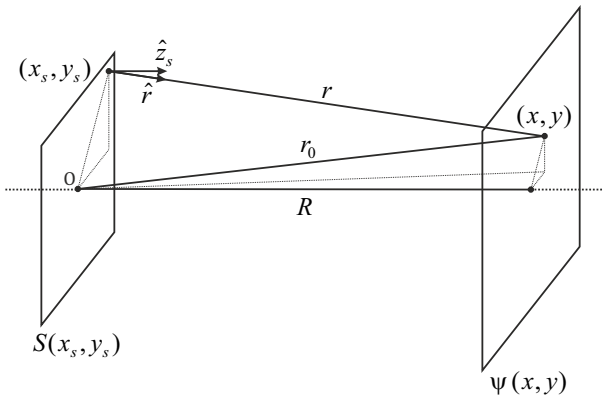

Figure 2.1.3: Parameters considered for the perturbation of a plane wave due to an object, $S(x_s, y_s)$, according to the Kirchhoff formalism. r_0 is defined as the distance between the origin O and the position (x, y) in the plane at a distance R of the object S.

When a plane wave that is propagated parallel to $\hat{z}_s$ is considered, the incident wave of equation 2.1.3, $\exp\{-2\pi i k r_q\}/r_q$, can be replaced with the unit wave, which can be understood as a wave of amplitude 1 and a zero phase at $z_s = 0$. In this way, the modified wave at a distance R beyond the object can be written as

$$\Psi(x, y) = \frac{i}{2\lambda} \int\int S(x_s, y_s) \frac{\exp\{-2\pi i k r\}}{r} \left[1 + \cos\left(\hat{z}_s \wedge \hat{r}\right)\right] dx_s dy_s \tag{2.1.4}$$

where $r^2 = (x - x_s)^2 + (y - y_s)^2 + R^2$ has been used for simplification (See Figure 2.1.3).

Due to the use of the approximation of object dimensions higher than the wavelength, a small angle approximation can be applied. This translates to $\cos(\hat{z_s} \wedge \hat{r}) \approx 1$, $r \approx R$ in the denominator of $\exp\{-2\pi ikr\}/r$ and $r \approx R + ((x - x_s)^2 + (y - y_s)^2)/2R$ in the exponent of $\exp\{-2\pi ikr\}/r$. The diffraction expression turns out as

$$\Psi(x, y) = \frac{i \exp\{-2\pi ikR\}}{R\lambda} \int\int S(x_s, y_s) \exp\left\{\frac{-\pi i\left[(x - x_s)^2 + (y - y_s)^2\right]}{R\lambda}\right\} dx_s dy_s \tag{2.1.5}$$

which is the expression that Fresnel reached after multiple hypothesis in 1718 [37], but here it can be derived without so many approximations. Although it is not frequently used in TEM work, near-field diffraction effects appear in the form of fringes, so-called *Fresnel fringes*, at the edges of the sample in imaging mode, which is quite useful for focusing (see Figure 2.1.4).

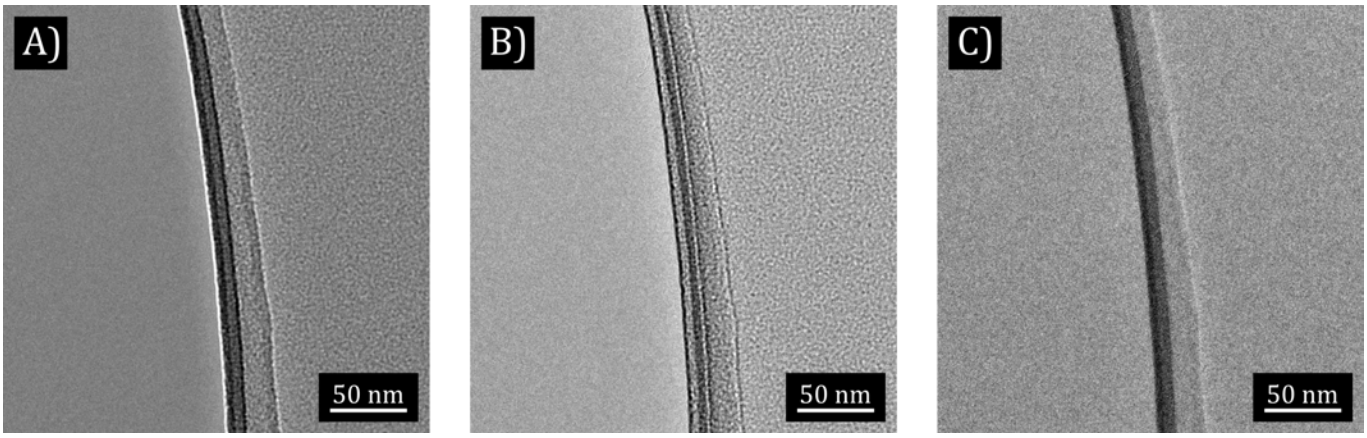

Figure 2.1.4: TEM images of an edge of a carbon film that show Fresnel fringes as A) bright fringes when it is underfocused and B) dark fringes when it is overfocused. C) Once the image is focused, such fringes are not visible.

Now, the case of far-field or Fraunhofer diffraction is considered, in other words, when the distance between the source and the plane of observation is effectively at infinity, which is defined as $S_s/(R\lambda) << 1$ where S_s is the size of the object S. In a TEM, if S_s is the distance between atoms ($\sim$ 1-2 Å) and R is the distance between the sample and the detector ($\sim$ 1 m), such condition is met and Fraunhofer diffraction can be applied to explain the resulting diffraction patterns.

Starting with equation 2.1.3, the obliquity factor can be removed from the integration because the angle differences through the whole $S(x_s, y_s)$ would be almost zero. Therefore, a constant ϕ is assigned to the angle $\hat{z_s} \wedge \hat{r}$ and the obliquity factor is taken out of the integral part. Then, the following approximation can be made

$$\begin{aligned} r &= \sqrt{R^2 + (x - x_s)^2 + (y - y_s)^2} \\ &\approx r_0 - \frac{x}{r_0} x_s - \frac{y}{r_0} y_s \end{aligned}$$

where x/r_0 is $\sin\theta_x$ and y/r_0 is $\sin\theta_y$. θ_x and θ_y are the components of the scattering angle θ. In this way, the expression for a wave diffracted by an object $S(x_s, y_s)$ is

$$\Psi(l,m) = (1+\cos\phi)i\frac{\exp\{-2\pi ikr_0\}}{2r_0\lambda}\int\int S(x_s,y_s)\exp\{2\pi ik(lx_s+my_s)\}dx_s dy_s \tag{2.1.6}$$

where $l = \sin\theta_x$ and $m = \sin\theta_y$. This formula is very interesting because it has the form of a Fourier transform integral. More precisely, it is roughly the Fourier transform of the object $S(x_s, y_s)$, thus providing an important insight on why materials give rise to different kinds of diffraction patterns. It is also worth to note that equation 2.1.6 is derived for two-dimensional objects, which means that only one diffracting event is possible since there is no physical distance for more. This is the basis of what is called kinematical diffraction.

2.1.2 The Fourier Transform and Reciprocal Space

The Fourier transform is a basic and very useful tool in several fields like quantum mechanics or audio signal processing [43]. From a TEM point of view, it helps to align the electron beam with the different optical systems of the microscope and also to process and simulate high resolution imaging data. In crystallography, it is the core analysis tool used in all structure determination and refinement algorithms.

A Fourier series is a mathematical representation by sine and cosine components of periodic functions and functions that are only defined in a delimited interval. It was introduced by Joseph Fourier in 1822 in order to explain heat conduction and diffusion processes [44] and it is defined as

$$f(x) = \frac{a_0}{2} + \sum_{n=1}^{\infty} a_n\cos(nx) + \sum_{n=1}^{\infty} b_n\sin(nx) \tag{2.1.7}$$

where the coefficients a_n and b_n are

$$a_n = \frac{1}{\pi}\int_0^{2\pi} f(x)\cos(nx)dx \quad \forall n = 0,1,2,...$$
$$b_n = \frac{1}{\pi}\int_0^{2\pi} f(x)\sin(nx)dx \quad \forall n = 1,2,...$$

Although equation 2.1.7 is very useful, it has a main limitation, it is not suitable for non-periodic functions. To solve this inconvenience, the series period is extended to infinity and then the sums are converted to integrals. The discrete representation evolves to a continuous one that defines the Fourier transform, $\mathcal{F}$, of a function as

$$\mathcal{F}\left[f(\vec{r})\right] = F(\vec{u}) = \int_{-\infty}^{\infty} f(\vec{r})\exp\{2\pi i\vec{u}\cdot\vec{r}\}d\vec{r} \tag{2.1.8}$$

which is the vectorial form of the transform in three dimensions. $\vec{r}$ is a vector in the direct or real space and $\vec{u}$ is a vector in the Fourier or reciprocal space. (x, y, z) are coordinates of the real space, (u, v, w) are coordinates of the reciprocal space and $\vec{u}\cdot\vec{r} = ux + vy + wz$. In order to retrieve back the function $f(r)$, the inverse Fourier transform is defined as

$$f(\vec{r}) = \mathcal{F}^{-1}\left[\mathcal{F}\{f(\vec{r})\}\right] = \int_{-\infty}^{\infty} F(\vec{u})\exp\{-2\pi i\vec{u}\cdot\vec{r}\}d\vec{u} \tag{2.1.9}$$

Here, the convention to introduce 2π in the exponent instead of the constant $(2\pi)^{-1}$ in front of the transform integral is followed. If the comparison between equation 2.1.6 and equation 2.1.8 is made, the diffracted wave obtained by the Fraunhofer conditions can be understood as a distribution in the reciprocal space, a Fraunhofer diffraction pattern, in which its amplitude is proportional to $F(u)$ and its intensity is $|F(u)|^2$.

The positive exponential in the Fourier transform is also kept following the formalism used by the International Union of Crystallography (IUCr) [45]. Some solid-state physics books exchange the sign of the exponentials and it does not alter anything in the development of the theory [46, 47], but it has to be kept in mind when non-centrosymmetric structures are studied because it determines which is the *right-* or *left-* handed model [48].

	$\boldsymbol{f(x)}$	$\boldsymbol{\mathcal{F}[f(x)] = F(u)}$
Point aperture	$\delta(x)$	1
Translation of an object	$f(x-a) = f(x) \otimes \delta(x-a)$	$F(u)\exp\{2\pi i u a\}$
Slit aperture	$f(x) = \begin{cases} 0 & \text{if} \quad \lvert x\rvert > a/2 \\ 1 & \text{if} \quad \lvert x\rvert < a/2 \end{cases}$	$\sin(\pi a u)\,/\,(\pi u)$
Diffraction grating	$\sum_{n=-(N-1)/2}^{(N-1)/2} \delta\{x-na\} \otimes g(x)$	$G(u)\left[\sum_t \delta\,(u-t/a) \otimes \frac{\sin(\pi N a u)}{\pi u}\right]$

Table 2.1.2: Fourier transform applied to different functions $f(x)$. $\delta(x)$ is the delta function and $\otimes$ stands for the convolution integral. The convolution theorem is used in some of them; $\mathcal{F}[f(x) \otimes g(x)] = F(u)G(u)$.

Some examples of the application of the Fourier transform to different functions are shown in Table 2.1.2. A single delta function in real space translates to a constant in the reciprocal space, thus it does not provide so much information about the object. An interesting characteristic of the reciprocal space is that its square modulus is translational invariant. Since a displacement of an object is equivalent to a phase change in the reciprocal space, its amplitude does not change. A slit aperture is a frequently used object to describe the wave behaviour of matter as its illumination results in a pattern following a $\mathrm{sinc}(u)$ function. Figure 2.1.5 shows a plot of the mathematical function for a 10 Å slit aperture (2.1.5A), its Fourier transform (2.1.5B) and the square modulus of $F(u)$ (2.1.5C), which would approximately be the resulting pattern when the experiment is actually performed. In this case, the reciprocal distance between the maximum and 0 for $F(u)$ will be the inverse of the aperture size a. Finally, the expression for a diffraction grating of a general function $g(x)$ is shown. This is the pattern in reciprocal space of a periodic and finite distribution of an identical object defined by $g(x)$. In this way, the height of each of the maxima is proportional to the value of the Fourier transform of $g(x)$ at that u value. Figure 2.1.5 shows a case example of a diffraction grating with 9 slit aperture of 2 Å in size and separated each other by 10 Å (Figure 2.1.5D). Its Fourier transform (Figure 2.1.5E) results in 9 sinc functions separated each other by 0.1 Å^{-1} and attenuated by $G(u)$, a sinc function coming from the expression of the slit aperture with a reciprocal distance of

0.5 $Å^{-1}$ between its maximum and 0. Figure 2.1.5F shows the resulting intensity pattern, $|F(u)|^2$, where the 9 maxima become sharper than $F(u)$, thus better displayed.

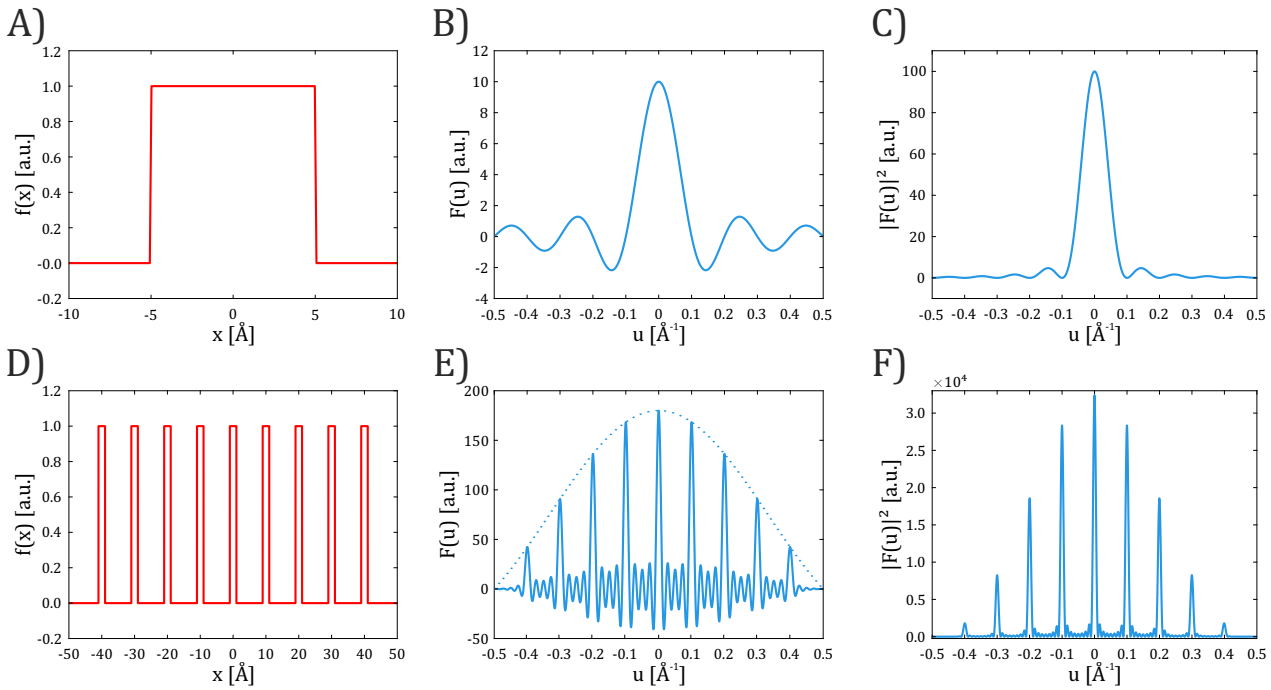

Figure 2.1.5: The application of Fourier transform to two different cases: A) a slit aperture of 10 Å in size and D) a grating of nine 2-Å slit apertures separated 10 Å from each other. B) and E) correspond to their respective Fourier transform, and C) and F) are the square moduli of B) and E) that represent the resulting intensity pattern.

2.1.3 Crystals, Reciprocal Lattices and the Diffraction Space

Up to this point, a mathematical and physical description has been introduced to explain the diffraction phenomena. Now the focus is directed to what happens when a material is used as an object that is in the path of a plane wave.

The classical definition of a crystal is an object that can be described by the repetition of a basic block along the three spatial dimensions. This basic block is called **unit cell** and is formed by the unit cell vectors $\vec{a}$, $\vec{b}$ and $\vec{c}$, which have lengths a, b and c, and angles between the axes α, β and γ. These six values are called **unit cell parameters** and, in general, $\vec{a}$, $\vec{b}$ and $\vec{c}$ are not orthogonal. Then, the electron density with units $e^-/Å^3$ for a conventional crystal is defined as

$$\rho(\vec{r}) = \left[\rho_0(\vec{r}) \otimes \sum_l \sum_m \sum_n \delta\{x - la, y - mb, z - nc\}\right] s(\vec{r})$$

where $\rho_0(\vec{r})$ is the electron density inside the unit cell, l, m and n are integers that create the density along the three dimensions, and x, y and c are coordinates related to the unit vectors $\hat{a}$, $\hat{b}$ and $\hat{c}$. $s(\vec{r})$

is a shape function defined as the three-dimensional form of the slit aperture in Table 2.1.2, which takes into account the finite size of the crystal. In other words, it is a function that chops off the periodic function that defines the crystal in real space.

When a Fourier transform is applied to this distribution, the Fraunhofer diffraction pattern is obtained

$$F(u,v,w) = F_0(u,v,w) \sum_h \sum_k \sum_l \delta(u - ha^*, v - kb^*, w - lc^*) \otimes S(u,v,w) \tag{2.1.10}$$

where u, v and w are coordinates of the reciprocal space, h, k and l are integers of the summations that correspond to the positions of lattice points in the reciprocal space, and a^*, b^* and c^* are the reciprocal distances of the reciprocal vectors $\vec{a^*}$, $\vec{b^*}$ and $\vec{c^*}$ that define a lattice in the reciprocal space, the so-called **reciprocal lattice**. The reciprocal vectors are calculated as follows

$$\vec{a^*} = \frac{\vec{b} \times \vec{c}}{\Omega} \; ; \; \vec{b^*} = \frac{\vec{c} \times \vec{a}}{\Omega} \; ; \; \vec{c^*} = \frac{\vec{a} \times \vec{b}}{\Omega}$$

where $\Omega = \vec{a} \cdot (\vec{b} \times \vec{c})$ is the unit cell volume. The different vectors in real and reciprocal spaces fulfil the orthogonal conditions

$$\vec{a^*}_i \cdot \vec{a}_j = \delta_{ij} \quad ; \quad i,j = 1,2,3$$

For the shape function $s(x,y,z)$, its Fourier transform, $S(u,v,w)$, takes the form of

$$S(u,v,w) = ABC \; \frac{\sin(\pi A u)}{\pi A u} \; \frac{\sin(\pi B v)}{\pi B v} \; \frac{\sin(\pi C w)}{\pi C w}$$

where A, B and C are the dimensions of the crystal along the three axes in real space. This function provides the distribution of the diffraction amplitudes as a sharp peak with strongly decaying oscillations, and the delta function defines these distributions only at each node of the reciprocal lattice. Thereby, the only interesting values of $F_0(u,v,w)$ in equation 2.1.10 are those at the reciprocal lattice points and the earlier expression can be re-written to

$$F(\vec{u}) = \sum_h \sum_k \sum_l \; F_{hkl} \; \delta\{\vec{u} - (ha^* + kb^* + lc^*)\} \otimes S(\vec{u}) \tag{2.1.11}$$

where F_{hkl} is the structure amplitude or **structure factor** of the (h, k, l) reciprocal lattice point given by

$$F_{\vec{g}} \equiv F_{hkl} = \int_0^a \int_0^b \int_0^c \rho(x,y,z) \exp\{2\pi i((hx/a) + (ky/b) + (lz/c))\} dx dy dz$$

where $\vec{g}$ is a vector defined as $\vec{g} = h\vec{a^*} + k\vec{b^*} + l\vec{c^*}$ and the integrals run through the whole unit cell. The structure factor $F_{\vec{g}}$ is the amplitude-weight of the (h, k, l) point in the reciprocal space. Since the electron density inside the unit cell can be calculated by the summation of the contribution of each atom individually, the following expression for the electron density is used

$$\rho(\vec{r}) = \sum_i^N \rho_i(\vec{r}) \otimes \delta(\vec{r} - \vec{r_i})$$

where N is the number of atoms inside the unit cell and $\rho_i(\vec{r})$ is the electron density associated to the i-th atom centred at $\vec{r}-\vec{r_i}$. When this consideration is made, the usual expression for the structure factor using the kinematical approximation is obtained

$$F_{\vec{g}} = \sum_i^N f_i \exp\{2\pi i\,(hX_i + kY_i + lZ_i)\} \tag{2.1.12}$$

where X_i, Y_i and Z_i are the fractional coordinates x/a, y/b and z/c of the atom i inside the unit cell and f_i is the **atomic scattering factor** that depends on the used radiation. This equation can be applied in X-ray, neutron or electron diffraction experiments given that the kinematical approximation is valid. In X-ray diffraction, a X-ray should travel a path length of the order of 1 μm in a single crystal without defects to appreciate the multiple scattering. In neutron diffraction this path is several times greater. In the case of electron diffraction, multiple scattering events become important around a path of the order of one or two hundred Å for light atoms and less for the heavy ones [49]. How to deal with dynamical intensities and use them for crystal structure determinations will be discussed in the fourth chapter.

Equation 2.1.11 is important because it defines what it is called **diffraction space** in this work. It consists on an amplitude-weighted reciprocal lattice created by the crystal periodicity and the diffracting strength of the atoms, plus some diffuse scattering between these nodes caused by the disorder that a crystal may have. A difference shall be made here because the reciprocal space is an abstract space created by the use of the Fourier transform to a given mathematical function. Instead, the diffraction space is created by the physical phenomena of diffraction or scattering, although the already discussed mathematical development needs to be used in order to understand and quantitatively describe what is happening. Furthermore, the detection or measurement of this space does not allow the collection of its whole information, but only its square modulus. This is very inconvenient because it means that only the amplitudes of $F_{\vec{g}}$ can be obtained yet their phases are lost, which carries most of the structural information needed to retrieve the electron density distribution. This diffraction experiment hindrance has been called traditionally as *the phase problem*. However, several algorithms based on the kinematical approximation have been developed during the last century in order to successfully determine crystal structures. The acquired intensities, following this theory, are proportional to $|F(\vec{u})|^2$ as

$$I_{kin} \sim |F(\vec{u})|^2 = \sum_h \sum_k \sum_l |F_{\vec{g}}|^2 \delta\{\vec{u} - (h\vec{a^*} + k\vec{b^*} + l\vec{c^*})\} \otimes |S(\vec{u})^2|$$

$|F(\vec{u})|^2$ is the distribution of scattering power of the crystal and it will be called **observable diffraction space** (ODS) in this work. From this equation, the inverse Fourier transform can be applied to obtain the **generalized Patterson function**

$$\mathcal{F}^{-1}\{|F(\vec{u})|^2\} = P(\vec{r}) = \left[\rho_0(\vec{r}) \otimes \rho_0(-\vec{r}) \otimes \sum_l \sum_m \sum_n \delta\{\vec{r} - (l\vec{a} + m\vec{b} + n\vec{c})\}\right] [s(\vec{r}) \otimes s(-\vec{r})] \tag{2.1.13}$$

This is a periodic function made up by a self-convolution of the contents of the unit cell and a gradual fall-off due to the shape convolution. Although $\rho_0(\vec{r})$ is there and this expression is the basis for some structure determination methods [50, 51], the direct de-convolution to isolate the electrons density

is in general not possible. More details on how to determine the electron density distribution will be given in the fourth chapter.

If the finite size of the radiation source and the detector characteristics are considered, the final acquired intensity could be mathematically expressed as

$$I_{kin} \sim |F(\vec{u})|^2 \otimes R(\vec{u}) \otimes D(\vec{u})$$

where $R(\vec{u})$ is the source function and $D(\vec{u})$ is the function that represents the detector sensitivity and point spread function.

Finally, it is worth to comment on the definition of crystal. The classical definition introduced at the beginning of this section is not the current definition given by the IUCr. The *official* definition is based on the diffraction pattern obtained from the material under study, reproduced here for convenience:

"*A material is a crystal if it has essentially a sharp diffraction pattern. The word essentially means that most of the intensity of the diffraction is concentrated in relatively sharp Bragg peaks, besides the always present diffuse scattering. In all cases, the positions of the diffraction peaks can be expressed by*

$$H = \sum_{i=1}^{n} h_i a_i^* \ (n \geq 3)$$

Here a_i^* and h_i are the basis vectors of the reciprocal lattice and integer coefficients respectively and the number n is the minimum for which the positions of the peaks can be described with integer coefficient h_i.
The conventional crystals are a special class, though very large, for which n = 3."

This definition was introduced in order to classify aperiodic crystals as actually crystals [52]. Aperiodic crystals are materials in which their diffraction patterns contain sharp reflections but cannot be explained with a three-dimensional lattice. Extra dimensions have to be added in the form of modulated vectors to consider the periodicity of the material that is fulfilled outside of the unit cell.

Nevertheless, it can be argued that the use of a diffraction pattern to decide if a material is a crystal is not ideal because it depends on the used radiation. Some materials could not be considered crystals for X-ray diffraction experiments but they could be for electron diffraction. In this way, the classical translational description of a crystal that could include modulated vectors to properly describe aperiodic crystals is preferred because it avoids the experiment dependent factor. Although mathematically more complex, the definition would be more accurate to describe what is the ordering of matter.

2.1.4 Atomic Scattering Factors for Electrons

The potential distribution $\varphi(\vec{r})$ in volts is the physical property that causes the diffraction of the wave or the scattering of the beam. It is related to the electron density by the Poisson's equation

$$\nabla^2 \varphi(\vec{r}) = \frac{|q_e|}{\varepsilon_0} \left[\rho_n(\vec{r}) - \rho_e(\vec{r})\right]$$

where ε_0 is the vacuum permittivity, and ρ_n and ρ_e are the electron densities corresponding to the nuclei and electrons of the atoms, respectively. Then, the atomic scattering factors for electrons are defined as the Fourier transform of $\varphi(\vec{r})$.

$$f_e(\vec{u}) = \int \varphi(\vec{r}) \exp\{2\pi i \vec{u} \cdot \vec{r}\} d\vec{r}$$

It is important to note that in this way these factors are intrinsic properties of the atoms, regardless of the theory used to describe the physical process of diffraction or scattering. $f_e(\vec{u})$ can be related to the well-studied atomic scattering factors of X-rays, $f_X(\vec{u})$ in electron units, following the Mott formula [53]

$$f_e(\vec{u}) = \frac{|q_e|}{4\pi^2 \varepsilon_0} \frac{Z - f_X(\vec{u})}{u^2}$$

where Z is the atomic number of the considered atom and $f_e(\vec{u})$ has volts·Å^3 units. These factors are tabulated in the International Tables for Crystallography vol. C [54], but they are defined according to the first Born approximation of the scattering theory of electrons by atoms; $f_{Born}(\vec{u}) = ((2\pi m_e q_e)/(h^2)) f_e(\vec{u})$ in Å units.

2.1.5 The Geometry of Diffraction

The diffraction space $F(\vec{u})$ depends on the used radiation because the atomic scattering factors are different, but the reciprocal lattice does not change as it only depends on the unit cell of the crystal, i.e. the geometry of the diffraction space is independent of the radiation wavelength. For a given incident wave with wavevector $\vec{k}_0$, the diffracted wave defined by the wavevector $\vec{k}$ has an intensity equal to $|F(\vec{u})|^2$ at the position $\vec{u} = \vec{k}_0 - \vec{k}$ of the ODS. Since the distribution of the scattering power is gathered around the reciprocal lattice nodes, the only positions in which a diffracted wave will have significant intensity are when $\vec{u} = \vec{g}$

$$\vec{u} = \vec{k}_0 - \vec{k} = \vec{g} = h\vec{a^*} + k\vec{b^*} + l\vec{c^*}$$

where λ is the wavelength of the diffracted wave that in this case would be λ_0 because inelastic scattering (absorption) effects are not considered. If this equation is translated to the real space, the **Laue conditions** for diffraction are obtained

$$\vec{g} \cdot \vec{a} = h \quad ; \quad \vec{g} \cdot \vec{b} = k \quad ; \quad \vec{g} \cdot \vec{c} = l \tag{2.1.14}$$

Alternatively to the Laue conditions, another interpretation of diffraction can be used to derive the Bragg's law [31]. The periodicity of a crystal allows the introduction of the atomic planes concept. These are sets of parallel planes that intersect to the centres of atoms and are spaced in regular intervals. The reciprocal vectors $\vec{g}$ are normal to these planes, which are denoted by the *hkl* integers of $\vec{g}$ that are called Miller indices. In a general way, the interplanar distances d_{hkl} between *hkl* planes can be calculated with the following formula regardless of the crystal system

$$\frac{1}{d_{hkl}^2} = \frac{1}{\Omega^2}(s_{11}h^2 + s_{22}k^2 + s_{33}l^2 + 2s_{12}hk + 2s_{23}kl + 2s_{31}lh)$$

where

$$\Omega^2 = a^2b^2c^2(1 - \cos^2\alpha - \cos^2\beta - cos^2\gamma + 2\cos\alpha\cos\beta\cos\gamma)$$
$$s_{11} = b^2c^2\sin^2\alpha$$
$$s_{22} = a^2c^2\sin^2\beta$$
$$s_{33} = a^2b^2\sin^2\gamma$$
$$s_{12} = abc^2(\cos\alpha\cos\beta - \cos\gamma)$$
$$s_{23} = a^2bc(\cos\beta\cos\gamma - \cos\alpha)$$
$$s_{31} = ab^2c(\cos\gamma\cos\alpha - \cos\beta)$$

$1/d_{hkl}$ would be the length of $\vec{g}$ between the origin of the diffraction space to the hkl reciprocal lattice point; thereby, $\vec{g}$ defines the interplanar distance and the orientation of the Miller planes.

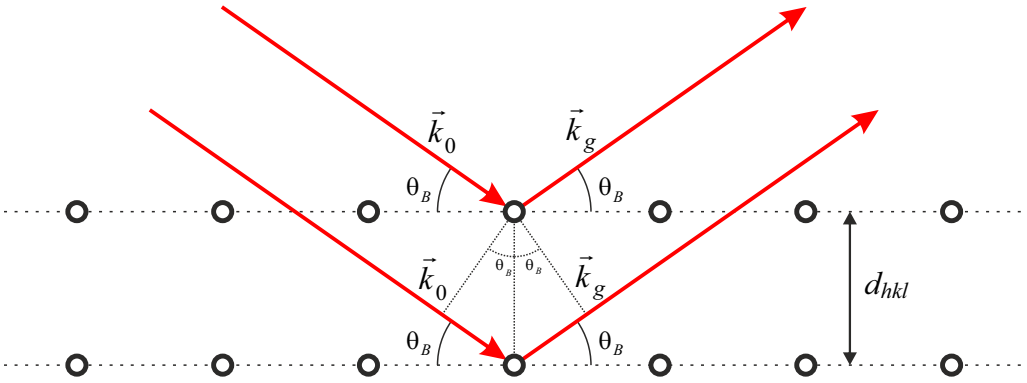

Figure 2.1.6: Bragg interpretation on how a crystal diffracts an incident wave by atomic planes.

According to the model proposed by Bragg, the crystalline planes act as semitransparent mirrors in such a way that different parts of the same wavefront are reflected in different planes, as shown in Figure 2.1.6. These different parts do not travel the same optical path and the only way to have a constructive interference after being reflected is when the path difference is an integer number of the wavelength, so that

$$2d_{hkl}\sin\theta_B = n\lambda \tag{2.1.15}$$

which is the equation known as **Bragg's law**. This optical interpretation of diffraction as a reflection phenomenon is the reason why spots in diffraction patterns are frequently referred as Bragg reflections. In this work, they will be called **reflections** for convenience.

Paul Peter Ewald developed an easy geometric interpretation for the diffraction conditions [55, 56]. First, the ODS is depicted and an arrow with length $|\vec{k}_0| = 1/\lambda_0$ is drawn with the arrowhead at one of the reciprocal lattice nodes, and its direction according to the orientation of the crystal with respect to the incident radiation. Then, a sphere, so-called **Ewald sphere**, is drawn with radius $1/\lambda_0$ and centre at the origin of the vector $\vec{k}_0$. This sphere determines the intensity for the diffracted waves around all possible directions and it will only be significant when the diffraction conditions are fulfilled. In other words, the only spots observed in a diffraction pattern will correspond to the

intensity-weighted reciprocal nodes hit by the Ewald sphere. Interestingly, this geometry can be applied to any radiation by calculating its related wavelength. Figure 2.1.7 shows an example using Cu K_α X-rays (1.5406 Å) and electrons accelerated at 200 kV (0.0251 Å).

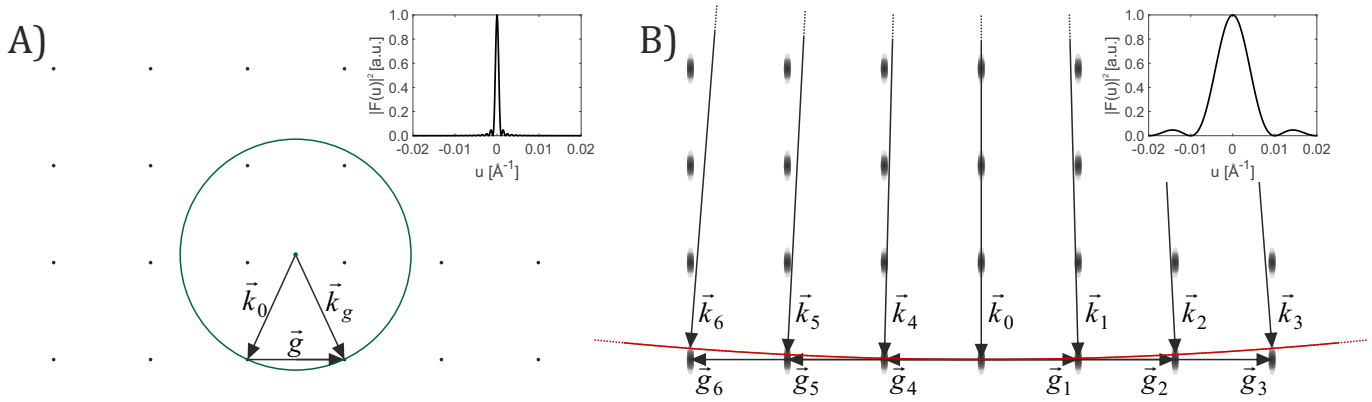

Figure 2.1.7: Geometry of the Ewald sphere construction: A) corresponds to the case of Cu K_α X-rays (green sphere) and B) to electrons accelerated at 200 kV (red arch). The plots inside both figures are the distributions of the scattering power for one of the reflections. The crystal size is 1000 Å and 100 Å for the X-ray and electron cases, respectively, both along the direction of the incident radiation.

X-rays and neutrons have wavelengths that are related to Ewald spheres with radii around the order of the reciprocal unit cell. Diffracted waves can be consequently excited in any direction and goniometric stages need to be used in order to swing the detector through convenient angles. On the other hand, electrons have a much smaller related wavelength and the Ewald sphere is much bigger than the reciprocal unit cell. In this manner, the excitation of diffracted waves mainly come from the first plane of the ODS, the so-called zero-order Laue zone (ZOLZ). A flat detector is usually placed after the specimen and perpendicular to the direction of the incident beam and an almost planar section of the ODS can be acquired.

Another difference between X-rays or neutrons and electrons is the crystal size required to produce the diffraction phenomena. Crystals are in the micrometre regime when X-ray diffraction experiments in individual crystals are performed, i.e. single-crystal X-ray diffraction. In consequence, its ODS will consist of sharp distributions of the scattering power. The situation is different in electron diffraction because crystals have to be thin enough in order to allow the transmission of the electron beam. In this way, the shape function in reciprocal space along the direction of the incident beam will be much broader than in the other directions, which results in an elongated distribution of the scattering power along this direction. The extremely small wavelength and the need of very thin crystals for electron diffraction provide the necessary conditions to simultaneously excite several diffracted waves and produce diffraction patterns populated by a high number of spots, yet the quantification of the reflection intensities become problematic.

Laue conditions and Bragg's law are strict rules because they do not account for how the intensity is distributed around each node of the reciprocal lattice, but they rather focus on the position of these points. Equation 2.1.5 can be modified to add another vector, the **excitation error** $\vec{s_g}$, to take

into account the deviation from the Bragg condition when the Ewald sphere still hits the scattering power of the reflection and some intensity can be recorded. As it is sketched in Figure 2.1.8, the excitation error depends on the intensity distribution as well as the length of the reciprocal vector $\vec{g}$, since the Ewald sphere is further away from the ZOLZ according to the distance from the origin of the diffraction space. This vector relation is mathematically described as

$$\vec{k}_g - \vec{k}_0 = \vec{g} + \vec{s}_g$$

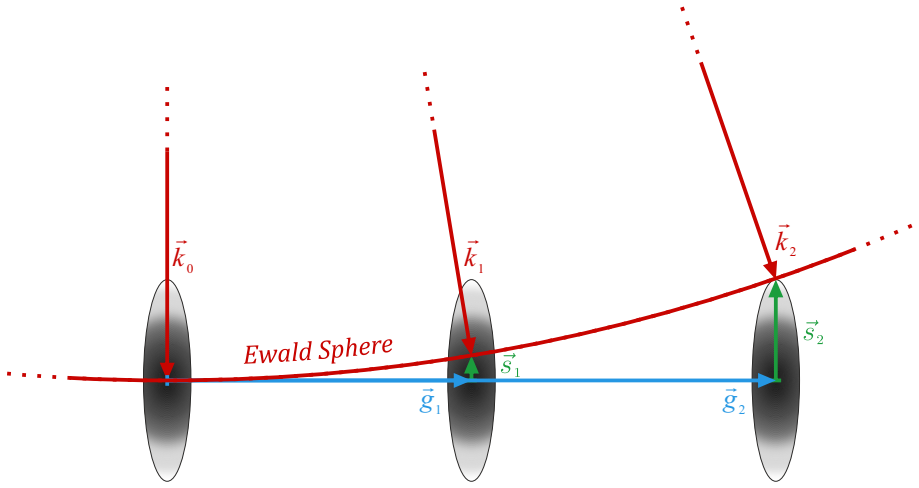

Figure 2.1.8: Sketch of the Ewald sphere intersection with two reflections of the diffraction space. Red arrows correspond to the direction of diffracted waves, blue ones to reciprocal vectors and green ones to excitation error vectors.

The shape function provides the broadening of the scattering power at the reciprocal lattice nodes but also the beam conditions play a role on how reflections are acquired. They determine the volume from the diffraction space that will be sampled. Two of the most influential parameters that cause the widening of the Ewald sphere are the convergence angle and the wavelength spread, which are sketched in Figure 2.1.9.

A crystal cannot be illuminated with a cylindrical flow of radiation due to the finite size of sources and other optical limitations. Instead, beams always have an inverted cone-like shape that translates into a distribution of the $\vec{k}_0$ directions. Intuitively, the Ewald sphere changes to a spherical shell in which its thickness varies with the distance from the origin of the diffraction space as shown in Figure 2.1.9A. In this way, a disk-shaped section is defined for each $\vec{k}_i$ direction that samples and integrate the diffraction space at that specific direction to result in its diffracted intensity.

The wavelength spread appears because no ideal monochromatic source can be designed, thus a distribution of wavelengths is always present. In this case, the resulting shape of the Ewald shell consists of Ewald spheres of different radii according to the spread of wavelengths as shown in Figure 2.1.9B. In this case, the integrating section is a line that varies in length and orientation according to the scattered beam direction.

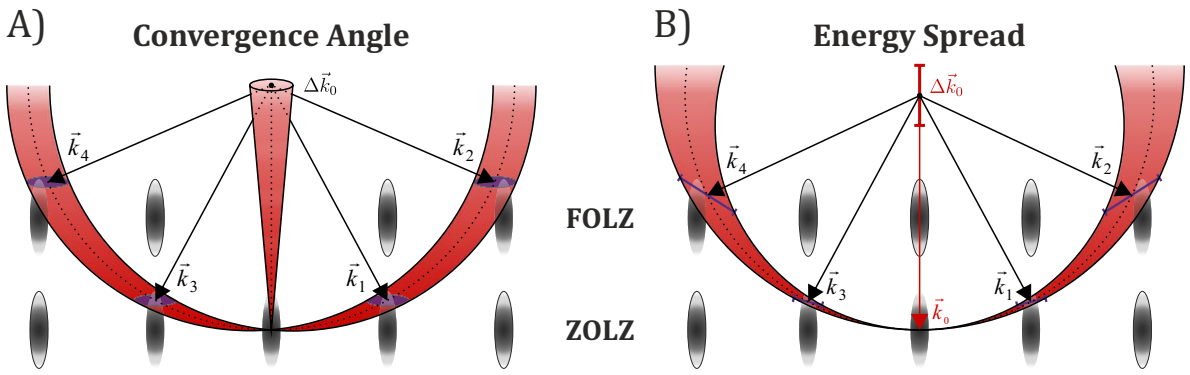

Figure 2.1.9: Two different effects that modify the initial and basic Ewald sphere concept: A) the convergence angle and B) the energy spread. The purple sections on the spherical shells pointed by the different wavevectors $\vec{k}_i$ correspond to the sections of the diffraction space that will be integrated to give the intensity for that $\vec{k}_i$ direction. ZOLZ and FOLZ stand for zero-order and first-order Laue zones, respectively.

The combination of both experimental deviations mentioned above produces an integration shape for the different directions of the diffracted waves that mostly varies with the scattering angle θ. In consequence, reflections in a diffraction pattern will decrease their related intensity according to the well-studied dependence on the atomic scattering factors to θ and the experimental conditions used to acquire them [54]. In electron diffraction, the energy spread of electron sources is around 1 eV, which is equivalent to a wavelength width of 10^{-6} times the electron wavelength, thus its effect on the integration shape is much smaller than the convergence of the beam as it will be shown in following sections of this chapter.

A way to avoid these device limitations is to carefully study the diffractometer and implement a respective function, called Lorentz factor, which is multiplied to the acquired reflection intensities and usually depends on the scattering angle and the diffraction geometry [57, 58]. When working in X-rays, the radiation polarization and the Lorentz factor are calculated together and applied as a single factor, the LP factor. For a common case in which the emitted, monochromatic and scattered beams are coplanar, the LP factor is written as

$$\mathrm{LP} = \frac{1 + A\cos^2(2\theta_B)}{(1+A)\sin(2\theta_B)} \; ; \; A = \cos^2 2\theta_M$$

where θ_B is the Bragg scattering angle from the targeted crystal and θ_M is the Bragg scattering angle from the monochromator. Then, the reflection intensity is approximated as

$$I_{kin} \sim \mathrm{LP} \cdot |F_{hkl}|^2$$

2.1.6 Electron Diffraction Patterns and the Real Space

Electron diffraction patterns can be considered planar sections of the ODS to some extent, as shown in Figure 2.1.7. At this point, it is appropriate to see which is the relationship between sections in the diffraction space and the real space. The projection of $\rho(\vec{r})$ along the direction of the electron beam, say the z-axis, can be mathematically described as

$$\rho(x,y) = \int_{-\infty}^{\infty} \rho(\vec{r})dz = \int\int\int\int F(\vec{u}) \exp\{-2\pi i(ux + vy + wz)\}dudvdwdz$$

The integral that runs over z results in the delta function, $\delta(w)$, as the integral of $\exp\{-2\pi iwz\}dz$ can be considered the Fourier transform of the unit. Thus

$$\rho(x,y) = \int\int\int F(\vec{u}) \exp\{-2\pi i(ux + vy)\}\delta(w)dudvdw = \int\int F(u,v,0) \exp\{-2\pi i(ux + vy)\}dudv$$

which can be understood as $\rho(x,y)$ being the inverse Fourier of $F(u,v,0)$. So that the inverse Fourier transform of the intensity distribution of a diffraction pattern will result in the projection of the generalized Patterson function along the beam direction. In this way, crystals can be considered as two-dimensional phase and amplitude perturbations, which justifies the use of Fraunhofer diffraction theory to describe the acquired diffraction patterns.

2.2 The Transmission Electron Microscope as an Optical System

The diffraction phenomena have been explained in the context of crystallography through the last section. Now, the instrumentation required to produce and acquire electron diffraction data is going to be described: the transmission electron microscope.

2.2.1 The Abbe Theory of Image Formation

During the beginning and middle of the XIX century, the scientific field of optics was mostly working on the understanding and development of devices capable of resolving features that were far away from the observer, in other words, telescopes. It was not until the work of Ernst Abbe in 1873 [59] and Hermann von Helmholtz in 1874 [60] that a theory of image formation by the diffraction phenomena in a microscope started [61, 62]. The different idea that Abbe introduced was to treat matter as a grating illuminated by plane waves, not as a luminous point like a star in a dark sky. He also realised that the amount of rays taken from a diffraction pattern generated after a lens will determine the final image.

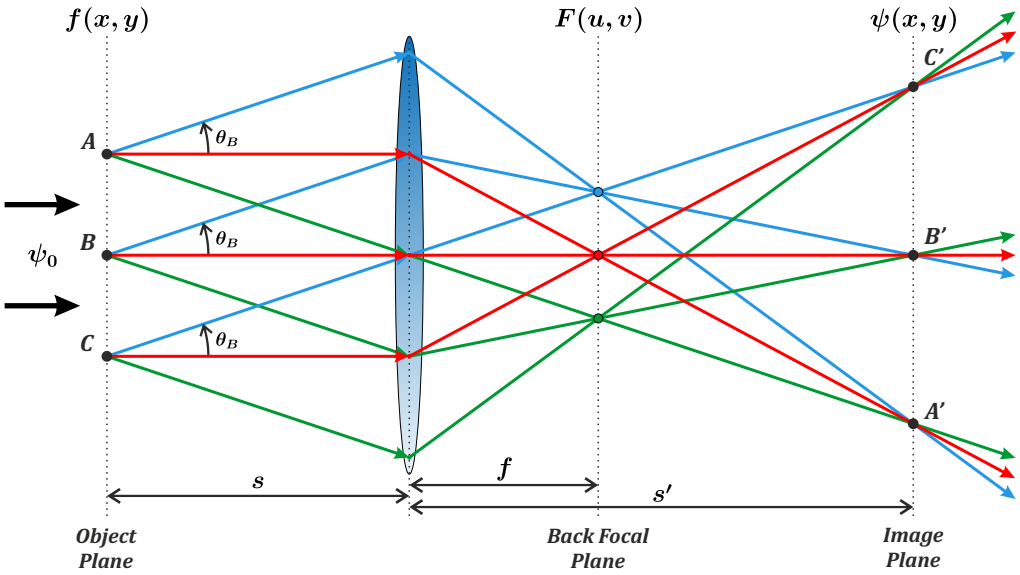

Figure 2.2.1: Ray diagram for a simple optical system of one lens. ψ_0 is the incident plane wave, $f(x, y)$ is the object at the object plane that disrupts ψ_0 , $F(u, v)$ is the Fourier transform of $f(x, y)$ at the bfp, $\psi(x, y)$ is the magnified image of $f(x, y)$ at the image plane, s is the object distance, f is the focal distance and s' is the image distance. (x, y) corresponds to coordinates from the real space and (u, v) are from the reciprocal space.

Figure 2.2.1 shows a geometric-optics diagram that summarizes the ideas of Abbe on the image formation. Plane waves are disturbed by an object $f(x, y)$ and waves are diffracted as a consequence at different angles θ according to the Bragg's law.

At a distance s from the object, a thin lens is positioned in order to form an image at a distance s' from the lens, following the **thin lens equation**

$$\frac{1}{s'} + \frac{1}{s} = \frac{1}{f} \tag{2.2.1}$$

where f is the focal distance of the lens. Values for distances s and s' are positive because the origin is taken at the centre of the lens. f can be calculated by the lens maker's equation

$$\frac{1}{f} = (n-1)\left[\frac{1}{R_1} - \frac{1}{R_2} + \frac{(n-1)d}{nR_1R_2}\right] \tag{2.2.2}$$

where n is the refractive index of the lens material, R_1 and R_2 are the curvature radii from the two surfaces of the lens, and d is the thickness of the lens measured from the vertices of the surfaces. R_1 and R_2 are positive values if the light has not gone through the centre of curvatures before reaching the surface and negative otherwise. For instance, $R_1 > 0$ and $R_2 < 0$ represents a convergent lens. In the approximation of a thin lens, R_1 and R_2 are quite large, thus

$$\frac{1}{f} \sim (n-1)\left[\frac{1}{R_1} - \frac{1}{R_2}\right]$$

It is important to notice from Figure 2.2.1 that all rays scattered at an angle θ_B converge in the same position at the **back focal plane** (bfp). This is equivalent to interference of waves at a point from the infinity, thus the amplitude distribution at the bfp corresponds to the Fourier transform of $f(x, y)$. A Fraunhofer diffraction pattern can be acquired from this plane. In turn, the image formed at a distance s', called **image plane**, can be understood as an interference pattern from emission sources at the bfp, hence the Fourier transform of the amplitude distribution at that plane. This is a very interesting characteristic of the experimental setting because it allows the navigation through the different planes of an optical system using the Fourier transform.

Mathematically, the optical geometry from Figure 2.2.1 can be explained as follows when small angle or paraxial approximation is taken into account. All objects in an optical system can be described as planar distributions that have a transmission function $f(x, y)$. The propagation of waves in a medium of refractive index n is described through the convolution with a propagation function defined as $(i/\lambda s)\exp\{-\pi i(x^2+y^2)/\lambda s\}$. If a thin lens is considered, its transmission function can be approximated to $\exp\{\pi i(x^2+y^2)/\lambda f\}$. In this manner, a plane wave that is diffracted by an object with transmission function $f(x, y)$ and goes through a thin lens will produce an interference pattern at a distance s' from the lens given by

$$\psi(x,y) = \underbrace{\Bigg[\underbrace{\Bigg[\underbrace{\Bigg[f(x,y) \otimes \exp\left\{\frac{-\pi i(x^2+y^2)}{\lambda s}\right\}\Bigg]}_{\text{Propagation along } s} \exp\left\{\frac{\pi i(x^2+y^2)}{\lambda f}\right\}\Bigg]}_{\text{Transmission through a thin lens}} \otimes \exp\left\{\frac{-\pi i(x^2+y^2)}{\lambda s'}\right\}\Bigg]}_{\text{Propagation along } s'}$$

where multiplier constants have been omitted for clarification and the three brackets correspond to the three different events occurring in the physical process. If convolutions are written as integrals, it

can be demonstrated that $\psi(x,y)$ is $F(u,v)$ when $s' = f$, which is equivalent to the Fraunhofer diffraction pattern with $u \sim x/\lambda f$ and $v \sim y/\lambda f$. It can be seen as well that $\psi(x,y) = f(-sx/s', -sy/s')$ when equation 2.2.1 is used, hence the image is inverted and magnified by a factor s'/s, as expected from geometrical optics.

This mathematical treatment also describes the image formed at an observation plane that is not at the back focal neither the image plane, i.e. an out-of-focus image, and it can be understood from two different points of view. The first one would be to consider that the in-focus image at the image plane is propagated by a distance $\Delta s'$ from this plane to create the out-of focus image. In this way, the acquired image would be

$$\psi_{out\text{-}of\text{-}focus}(x,y) = \psi_{in\text{-}focus}(x,y) \otimes \exp\{-\pi i(x^2+y^2)/\lambda\Delta s'\}$$

The second one is to consider that the image is in-focus but it is imaging a plane that is Δs away from the object plane. Therefore, an object is imaged with transmission function

$$f_{shfited\text{-}plane}(x,y) = f(x,y) \otimes \exp\{-\pi i(x^2+y^2)/\lambda\Delta s\}$$

and the amplitude distribution at the bfp will be

$$F_{shifted\text{-}plane}(u,v) = F(u,v)\exp\{-\pi i\lambda\Delta s(u^2+v^2)\} \tag{2.2.3}$$

In this way, the defocusing of an object can be understood as an addition of a second order phase term to the diffraction space that is sampled at the bfp. Higher order terms can be added when lens aberrations are taken into account, which are later presented in this section.

Another interesting feature of this formalism is that it can be easily implemented in multi-component optical systems. Particularly, modern TEMs, since they consist of several and comparable optical components and deal with small scattering angles. The generalization is stated as follows:

A source radiation emits an amplitude distribution $q_0(x,y)$ and it goes through different planar objects defined by transmission functions $q_i(x,y)$, where $i = 1, ..., N$. Being R_i the distance between the i-th object and the $(i+1)$-th object, a propagation function $p_i(x,y)$ is defined following the small angle approximation used in Fresnel diffraction as

$$p_i(x,y) = \frac{i}{R\lambda}\exp\left\{\frac{-2\pi i R_i}{\lambda}\right\}\exp\left\{\frac{-\pi i(x^2+y^2)}{R\lambda}\right\}$$

Then, the amplitude distribution for N objects at a given plane of observation can be written as

$$\psi_{N+1}(x,y) = q_N(x,y)\,[\,...\,[q_1(x,y)\,[q_0(x,y) \otimes\ p_0(x,y)] \otimes\ p_1(x,y)]\ ...\,] \otimes\ p_N(x,y)$$

The Fraunhofer diffraction pattern from these N objects is obtained by using the convolution and multiplication theorems of the Fourier transform on ψ_{N+1}. The final equation is written as

$$\Psi_{N+1}(u,v) = Q_N(u,v) \otimes ...\ [Q_1(u,v) \otimes Q_0(u,v)P_0(u,v)]\,P_1(u,v)...P_N(u,v)$$

where the multiplications inside the brackets take place before the convolution.

2.2.2 How to Focus Electrons

When trajectories of light rays have to be modified for a specific purpose, optical lenses that are transparent to light are used. These lenses follow the lens maker's equation (Equation 2.2.2) and converge the rays coming from the infinite at the focal distance, i.e. rays parallel to the optic axis of the system are focused in a specific point defined by the geometry and material of the lens. These optical components cannot be used in a TEM because electrons cannot be deviated in the same way as photons. Their optical path has to be modified with electromagnetic fields.

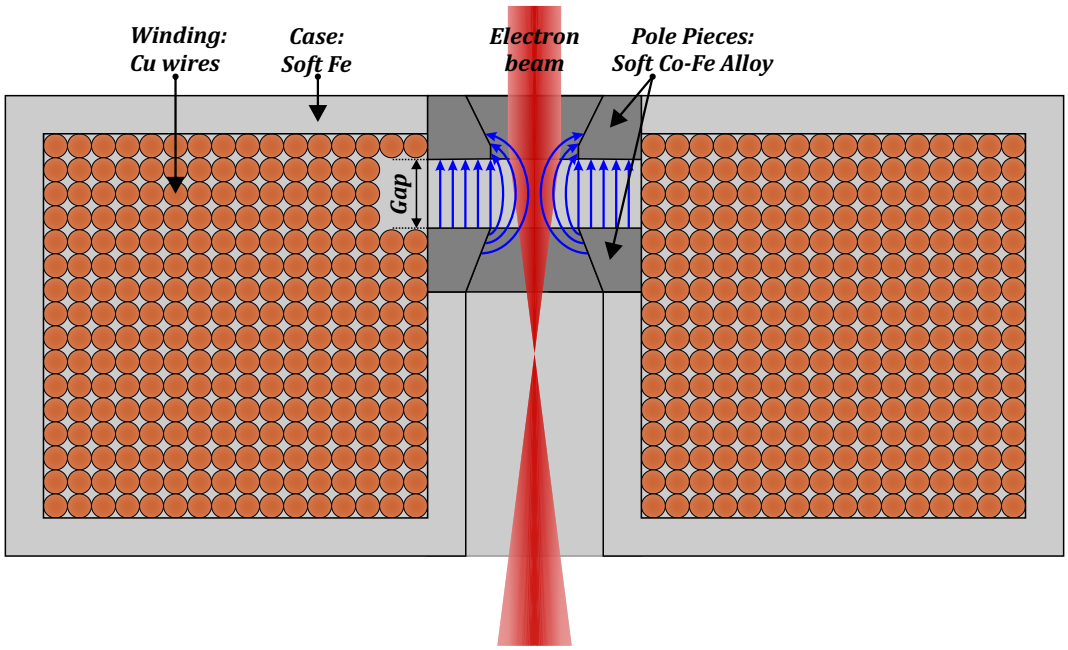

Figure 2.2.2: Depiction of a cross-section from a magnetic lens. The blue arrows represent the magnetic field generated by the current flowing through the copper wires in the direction out of (in) this sheet for the left (right) part of the lens.

Electron movement is controlled by forces exerted by electromagnetic fields according to the Lorentz force, $\vec{F}_{em} = (q\vec{E}) + (q \cdot v \times \vec{B})$ [63]. While the electric field increases the energy of electrons because it accelerates them, the magnetic field only modifies the velocity direction because the vectorial product implies a force perpendicular to the velocity vector. For this reason, TEMs mainly contain magnetic lenses which aim to set an electron beam suitable for the desired experiment. Although electrostatic lenses could be used as well, they have higher spherical aberrations than the magnetic ones under similar conditions, which hinder the achievement of high resolution [64]. In this context, electrostatic fields in an electron microscope are only used in the electron sources in order to give the required energy to the electrons and specific electron-optical components for energy filtering.

Hans Busch was the pioneer on the development of magnetic lenses. He theorised the focus of electrons by a cylindrical magnetic lens in the paraxial approximation [65] and he proved it one year later [66]. That was a big step towards electron microscopy because it triggered the work of Max Knoll and Ernst Ruska on the early developments of the TEM some years later [67, 68]. Several lens

designs have been studied and tested since then [69], but only the basic design used in TEM and their mathematical modelling will be briefly described here.

Magnetic lenses in TEMs are designed to concentrate a strong magnetic field (up to 2-3 T, [70]) with azimuthal symmetry in a very narrow space. This ensures a short focal distance required for atomic-resolution imaging. As shown in Figure 2.2.2, they are composed of Cu windings covered by a shell of an unalloyed soft Fe (like Hyperm 0) and pole pieces made by a soft alloy of Co-Fe (like Permendur or Vacoflux 48) in the middle of the lens. The gap between the pole pieces is very important because it determines how the magnetic field will be distributed in the hole where the electron beam will go through. According to Ampère's law [71], the magnetic field of such design will be proportional to the current flow through the Cu wires multiplied by the number of turns in the coil. In this way, the magnetic field can be controlled externally with a potentiometer, i.e. a knob in the TEM control panel.

When the differential equations from Newton's law in cylindrical coordinates are used, an azimuthal symmetry field with $B_\varphi = 0$ is considered and the paraxial approximation is applied, the following equation for the trajectory of electrons immersed in a magnetic field is obtained

$$\frac{d^2r}{dz^2} = -\frac{q_e}{8m_0V^*} r B_z^2(z) \tag{2.2.4}$$

where $V^* = V(1 + (q_eV)/(m_0c^2))$. The component r of $\vec{B}$ was approximated to $(-r/2)(\partial B_z/\partial z)$ because of the paraxial approximation. This equation is known as the **paraxial ray equation** and it describes the trajectory $r(z)$ of electrons accelerated at a voltage V and rotating in a meridional plane at the Larmor frequency $\dot{\varphi} = (q_e/2m)B_z(z)$.

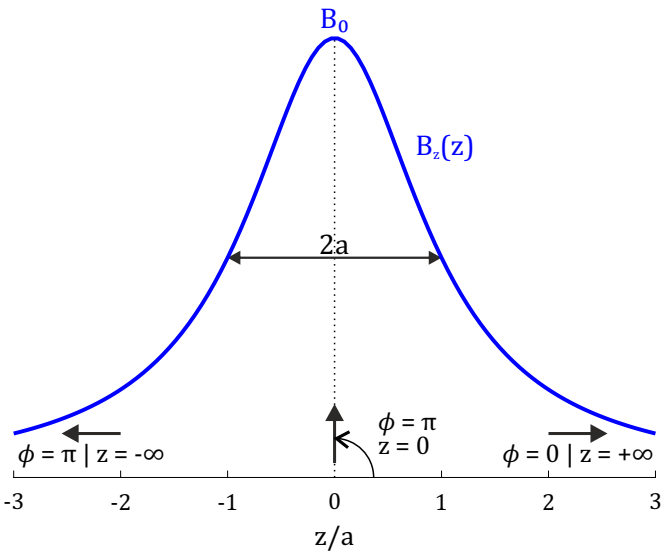

Figure 2.2.3: Glaser's bell-shaped magnetic field distribution along the optic axis. Cylindrical coordinates ϕ and z are displayed for reference. $2a$ is the FWHM of the field curve.

The magnetic field in these lenses can be approximated by the Glaser's bell-shaped field [72], showed in Figure 2.2.3, which states that the magnetic field along the optic axis can be described as

$$B_z(z) = \frac{B_0}{1 + (z/a)^2}$$

where B_0 is the maximum value of $|\vec{B}|$ at the centre of the lens ($z = 0$) and $2a$ is the full-width at half-maximum (FWHM) of this distribution. When this expression is substituted into equation 2.2.4, the resulting differential equation can be solved for an object in front of the lens and the following solutions are obtained

$$\begin{aligned} z_0 &= a\cot(\phi_0) \\ z_{Ii} &= a\cot(\phi_{Ii}) \quad \forall i = 1, 2, ... \end{aligned}$$

where

$$\phi_{Ii} = \phi_0 - i\frac{\pi}{w} \quad ; \quad w = \sqrt{1 + \frac{q_e B_0^2 a^2}{8 m_0 V^*}}$$

here ϕ is the polar coordinate that is 0° when $z = +\infty$ and π when $z = -\infty$. z_0 is the object distance, ϕ_0 is the polar angle for the object in front of the lens ($\pi > \phi_0 > \pi/2$), and z_{Ii} are the image distances given by ϕ_{Ii} and the strength parameter w. The consequence of the expression for z_{Ii} is that several image planes are possible.

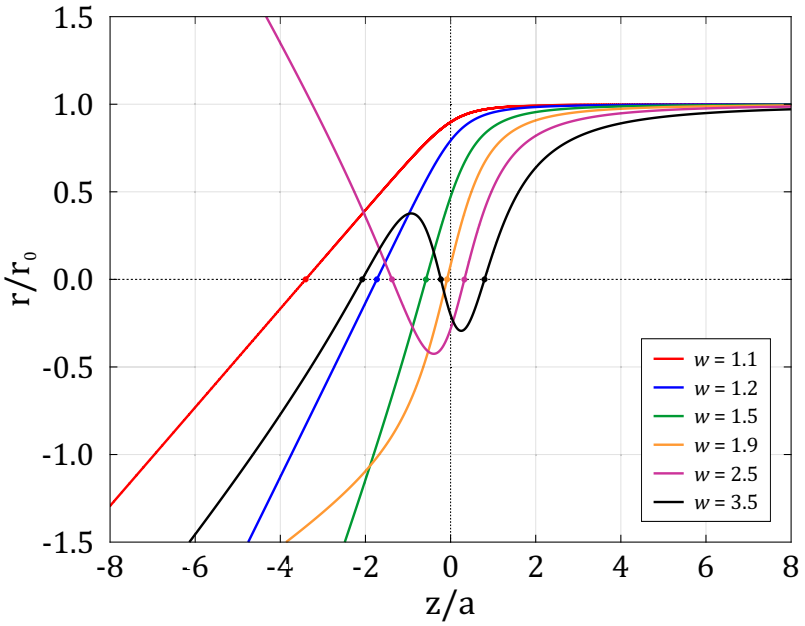

Figure 2.2.4: Trajectories of electrons through a bell-shaped magnetic field distribution towards negative z-axis values. Rays are initially travelling parallel to the z-axis at a distance r_0. Different strength parameters w are considered. a corresponds to half of the FWHM of the Glaser's bell-shaped function.

Figure 2.2.4 shows the special case of electron rays initially moving parallel to the z-axis towards negative z values and at a distance r_0 that go through a Glaser's magnetic field distribution for different strength parameters [73]. Here the equations of the trajectories are

$$\frac{r}{r_0} = \frac{1}{w}\frac{\sin(w\phi)}{\sin(\phi)} \quad ; \quad \frac{z}{a} = \cot(\phi)$$

For w between 1 and 2, electrons are focused on one single position after crossing the lens centre. Therefore, there will be only one image plane when the strength parameter lies between these values, which are common for these lenses [69]. In fact, $w = 2$ would be the optimum value in the sense that it gives the shortest focal length [74]. When higher strengths are considered, such as 2.5 or 3.5 in Figure 2.2.4, electrons are focused one or more times before and after the lens centre.

The substitution of the ϕ_{Ii} expression in the solution of z_{Ii} gives the following equation

$$\left[z_0 - a\cot\left(i\frac{\pi}{w}\right)\right]\left[z_{Ii} + \cot\left(i\frac{\pi}{w}\right)\right] = -a^2\csc^2\left(i\frac{\pi}{w}\right) \tag{2.2.5}$$

which is equivalent to the Newton form of the thin-lens equation

$$(z_0 - z(F_0))(z_1 - z(F_1)) = f_0 f_1$$

where F_0 and F_1 are the foci, and f_0 and f_1 are the focal distances before and after the lens. Although both expressions are equivalent, magnetic lenses cannot be strictly treated as thin lenses because the focal distances are different to the distances from the centre of the lens ($z = 0$) to the foci, $z(F_0)$ and $z(F_1)$. Nevertheless, the equivalence means that real image formation is possible when the object is not at the infinity, and it is characterized by the focal distance of the magnetic lens

$$f_0 = -f_1 = a\csc\left(i\frac{\pi}{w}\right)$$

In practical terms, the behaviour of a magnetic lens can be treated as an optical lens. The focal distance is decreased when the current through the lens is increased and, in consequence, the image distance is decreased as well. The magnification of such image is defined as $M = f_0/(z_0 - z(F_0)) = (z_1 - z(F_1))/f_1$.

Finally, the rotation angle between the object and the image is obtained by substituting the ϕ_{Ii} expression inside equation 2.2.4 and solving the integral. In this way, the final form of the angle is given by

$$\varphi = k\frac{\pi}{\sqrt{1+k^2}}$$

thus describing the helicoidal movement of the electrons through the optic axis of the microscope depending on the strength of the lens.

Apart from the single or double pole piece lenses that follow the description from above, quadrupoles, hexapoles and octupoles with four, six and eight coils, respectively, are also present in TEMs. The main difference is that the magnetic field is perpendicular to the beam direction and the applied Lorentz force is stronger. While quadrupoles and octupoles are present in all TEMs to shift, tilt and correct astigmatisms on the electron beam, the other designs are only found in aberration-corrected TEMs, which are microscopes with minimized lens aberrations.

2.2.3 Aberrations: Deviations from the Ideal System

Real life is never an ideal system. Although the description of a physical phenomena by means of a set of approximations helps to explain it in most current situations, fine details always become important when experiments are performed to get the most of them. This exactly happens when the resolution of a TEM is pushed to view smaller and smaller portions of a sample. The deviations that the real TEM measurements have with respect to the results from the electron-optical model are called *aberrations*, which they can be differentiated as chromatic, geometric and parasitic aberrations according to their origin.

Chromatic aberration appears when electrons do not have a unique wavelength but a spread of wavelengths. Since the focusing power of a magnetic lens varies according to the strength parameter w, electrons are focused at different distances from the lens, hence an ideal object point becomes a disc in the image plane. Although this non-ideal situation is a limiting factor for both atomic-resolution imaging and spectroscopic measurements, it gives an interval of focus values, so-called focus depth, where the image is theoretically focused. Technically, the energy spread is given by the electron source, e.g., around 1-1.5 eV for thermionic sources (single-crystals of LaB_6 oriented along the [110] direction) and down to 0.3 eV for field-emission guns (thin needles of single-crystal W oriented along the [310] direction) in the case of TEMs working at 100 keV [75]. However, the interaction of the electron beam with the sample also produces a spread in the electrons energy that depends on the thickness and the elements in the specimen. The thicker the sample, the higher the energy dispersion of the electron beam. Typical values are between 15 eV and 25 eV for most of the electrons going through a foil of 50-100 nm [76].

The correction of chromatic aberration needs the use of several electromagnetic components. Electrostatic and magnetic fields have to be used in order to disperse the electrons trajectory according to their energy, and then a mechanical slit is positioned to select a portion of these electrons [77, 78]. If such electron-optical elements are placed before or after the acceleration tube of the electron source, they are called *monochromators*. They can provide electrons with energy spreads between 25-100 meV, yet the disadvantage is that the electron beam has a much smaller probe current (q/s) because the slit is filtering out much of the electron beam. When they are placed after the specimen plane, they are called *energy filters* and they are the bases for energy filtered imaging and electron energy loss spectroscopy (EELS) acquisitions.

Geometric aberrations are consequence of perfectly cylindrical symmetry lenses. The way to obtain the different contributions is to introduce a perturbation function on the paraxial ray equation (Equation 2.2.4). These contributions are the spherical aberration, off-axial coma, off-axial astigmatism, curvature of image field and distortion, here ordered from the higher to the lower dependence on axial angle [79]. Axial means that the aberration solely depends on the angle between the optic axis and the ray direction with the origin at the object plane, i.e. its angular position with respect to the lens. On the other hand, off-axial means that the aberration depends on the position at the object plane outside of the optic axis but it can also depend on the axial angle. Since the objective lens in a TEM is imaging a very small area of the sample, the spherical aberration is the main contributor to its deviation from the ideal Gaussian wave. In fact, Otto Scherzer demonstrated in 1936 that this aberration cannot be avoided at all [80]. However, Scherzer also noted that it can be partially

compensated by a specific defocus value [81]. When the magnifying system of the microscope is considered in the final image formation, the off-axial aberrations have to be taken into account for accurate modelling.

Parasitic aberrations appear due to the deviation from the ideal symmetric system: non-perfect cylindrical symmetry of the lenses bore, microstructural inhomogeneities of the lenses iron, mechanical misalignment of the sequence of lenses, contamination on the apertures that generate charging effects or misalignment of mechanical apertures. These aberrations are axial astigmatism and axial coma. The most common one is the two-fold astigmatism and it is routinely corrected by the use of octupoles called stigmators. In terms of stronger effect, axial-coma and three-fold astigmatism follow two-fold astigmatism but they can be minimized by a proper alignment of the electron beam tilt with respect to the optic axis [82].

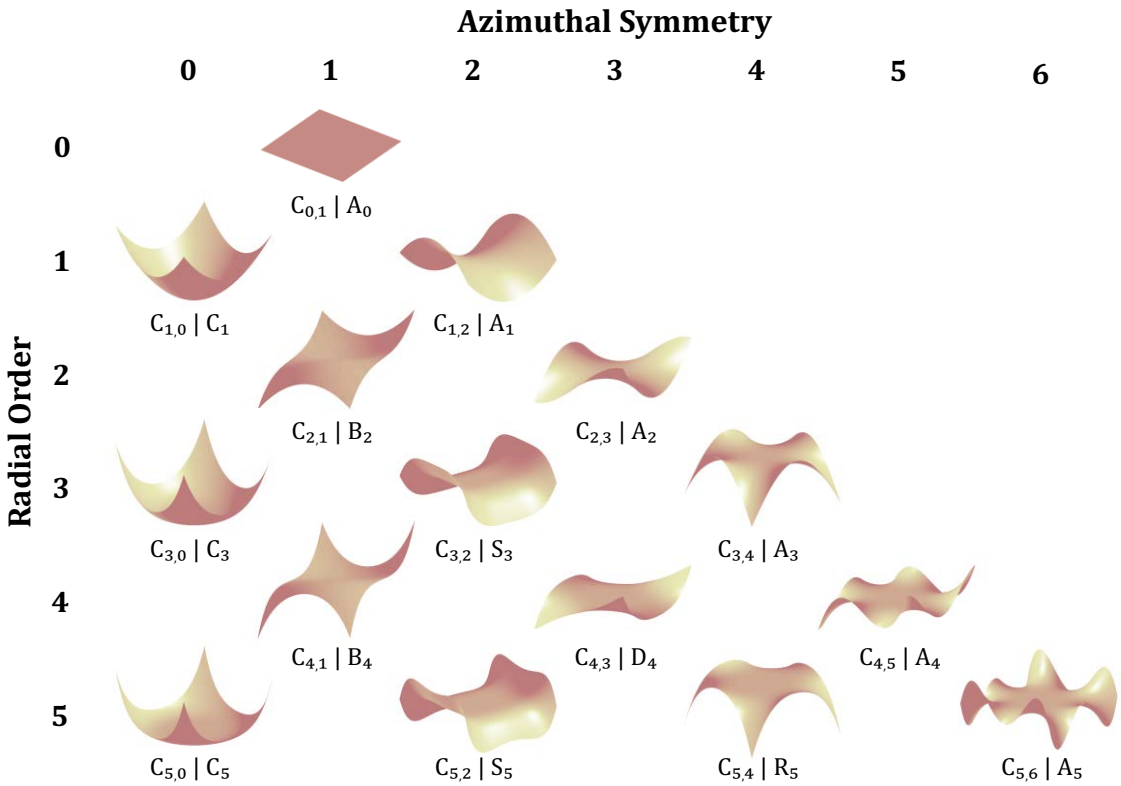

Figure 2.2.5: 3D rendering of the different distortions introduced to the wavefront up to the fifth order according to the aberration function $\chi(\omega)$. Each aberration includes the notation given by Krivanek et al. [83] and Uhlemann et al. [84], respectively. $C_{0,1}$ or A_0 correspond to image shift, thus it does not introduce any distortion to the wave because it is only a constant.

Mathematically, axial aberrations can be grouped in an aberration function that is expanded in a double power series of axial angles $\alpha_x^n \alpha_y^m$. Physically speaking, this function represents the deviation of the wavefront from an ideal spherical wave. A compact mathematical notation using a complex angle $\omega = \alpha_x + i\alpha_y$ that has a specific azimuthal dependence can generate a sequence of terms

separated by azimuthal orders. In this way, the aberration function $\chi(\omega)$

$$\chi(\omega) = \frac{2\pi}{\lambda}\text{Real}\left[\sum_{n=1}\sum_{s=0}^{n+1}\frac{1}{n+1}C_{nm}\ \omega^{s}(\omega^{*})^{n+1-s}\right]$$

where $m = 2s - n - 1$ is the azimuthal order of each term and coefficients C_{nm} are complex. Several terms can be repeated in this summation but only one of each form is kept. Expanding this series to the fifth order yields

$$\begin{aligned}\chi(\omega) = \frac{2\pi}{\lambda}\text{Real}\Big[&\frac{1}{2}C_{1,0}\ \omega^{*}\omega + \frac{1}{2}C_{1,2}\ \omega^{*2} + \frac{1}{3}C_{2,1}\ \omega^{*2}\omega + \frac{1}{3}C_{2,3}\ \omega^{*3}\\ &+ \frac{1}{4}C_{3,0}\ \omega^{*2}\omega^{2} + \frac{1}{4}C_{3,2}\ \omega^{*3}\omega + \frac{1}{4}C_{3,4}\ \omega^{*4}\\ &+ \frac{1}{5}C_{4,1}\ \omega^{*3}\omega^{2} + \frac{1}{5}C_{4,3}\ \omega^{*4}\omega + \frac{1}{5}C_{4,5}\ \omega^{*5}\\ &+ \frac{1}{6}C_{5,0}\ \omega^{*3}\omega^{3} + \frac{1}{6}C_{5,2}\ \omega^{*4}\omega^{2} + \frac{1}{6}C_{5,4}\ \omega^{*5}\omega + \frac{1}{6}C_{5,6}\ \omega^{*6} + ...\ \Big]\end{aligned}$$

where $C_{1,0}$ is defocus, $C_{1,2}$ is two-fold astigmatism, $C_{2,1}$ is coma, $C_{2,3}$ is three-fold astigmatism, $C_{3,0}$ is spherical aberration, $C_{3,2}$ is two-fold astigmatism of $C_{3,0}$, $C_{3,4}$ is four-fold astigmatism of $C_{3,0}$, $C_{4,1}$ is fourth order coma, $C_{4,3}$ is fourth order of three-fold astigmatism, $C_{4,5}$ is five-fold astigmatism, $C_{5,0}$ is fifth order spherical aberration, $C_{5,2}$ is two-fold astigmatism of $C_{5,0}$, $C_{5,4}$ is four-fold astigmatism of $C_{5,0}$ and $C_{5,6}$ is six-fold astigmatism of $C_{5,0}$. This is the notation employed by Krivanek et al. [83] to define the different coefficients, but another notation established by Uhlemann et al. is also used in other works [84]. A translation table between different notations is found elsewhere [85]. Figure 2.2.5 shows the graphical representation of the angular deviation of a beam for each of the aforementioned distortions classified according to its radial and azimuthal order.

The use of $\chi(\omega)$ allows introducing the effect of aberration to the image formation of the objective lens. In diffraction space, this is the modulation of the different frequencies (or scattering angles) by a complex function

$$H(u,v) = \exp\{-i\chi(u,v)\}$$

and following equation 2.2.3, the resulting interference pattern in the bfp of the objective lens is

$$F_{aberrated}(u,v) = F(u,v)H(u,v) = F(u,v)\exp\{-i\chi(u,v)\}$$

The different coefficients can be independently characterized for each microscope and electron-optical devices are commercially available to correct them [85, 86]. These are ensembles of lenses with quadru-, sex-, octu-, dodeca- and/or even twelve-poles coils that are especially designed to correct the aberrations by introducing negative coefficient values in such a way that the related distortions are highly minimized or suppressed. In fact, most modern correctors are able to correct chromatic and spherical aberrations at the same time [87].

2.2.4 The Optical Configuration of a TEM

Modern TEMs are designed with multiple electromagnetic components and detectors in such a way that they are engineered for a desired purpose, mostly analytical or atomic-resolution imaging experiments. The most advanced and unique TEMs are designed for multi-purpose experiments at the

atomic scale [88, 89]. Figure 2.2.6 shows the schematics of the most important electron-optical and mechanical components of modern multi-purpose TEMs. Nevertheless, the initial design used by Ernst Ruska at the end of 1933 that stated the bases for the subsequent technical development of the TEM is used here as the starting point [90].

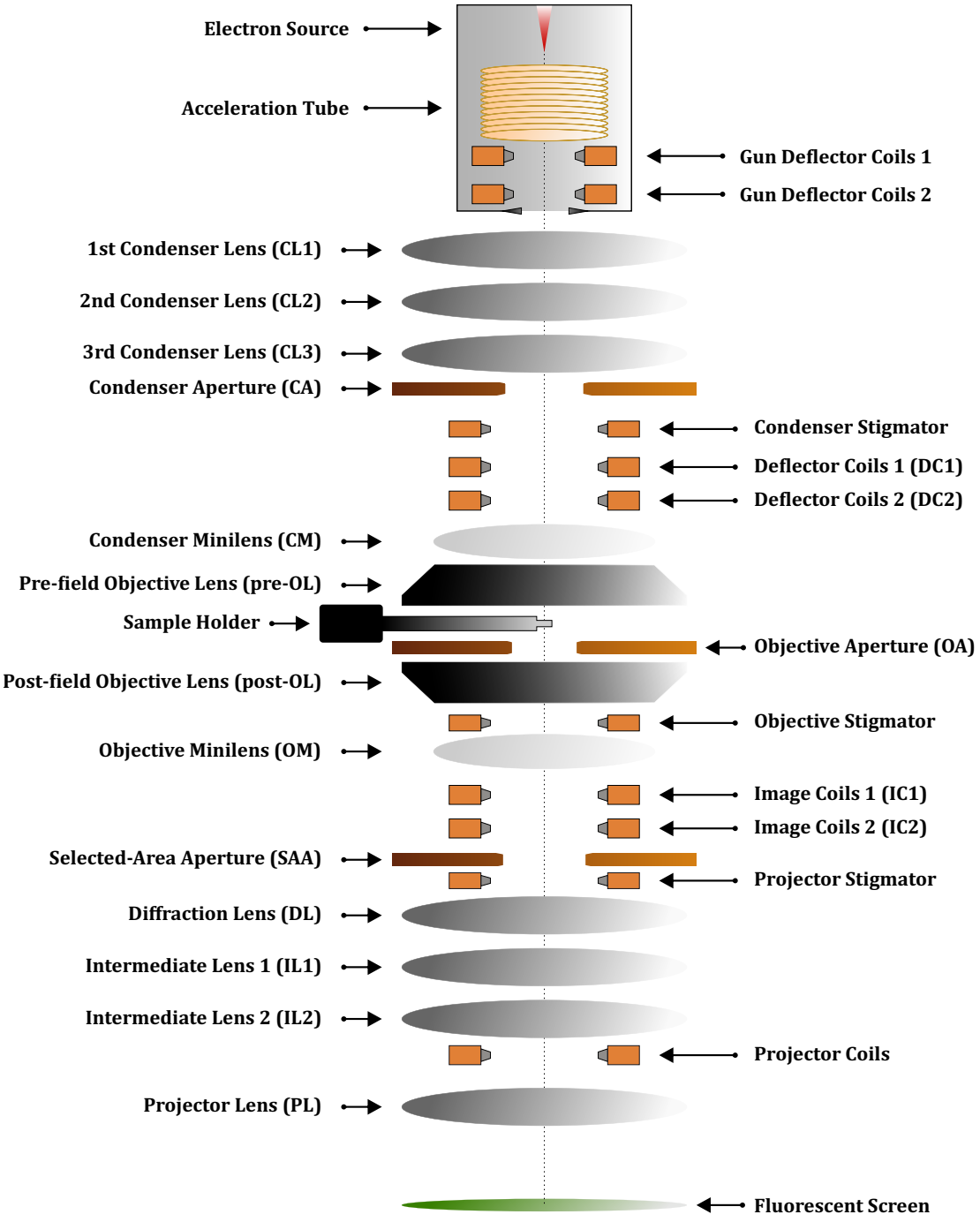

Figure 2.2.6: Schematics of the most important electron-optical and mechanical components of a modern TEM.

A TEM is based on three optical parts with their different functions; the condenser, the objective and the projector systems, which are arranged in this order when the TEM column is viewed from top to bottom. The aim of the condenser system, also called illumination system, is to collect the electron beam from the source and bring it to the object. The objective system is responsible for the creation of an image or diffraction pattern of the illuminated object. Subsequently, the projector system controls which plane to see from the objective lens (back focal or image plane) and the magnification of such projected plane. Initially, each system consisted of one magnetic lens of small focal length that allowed a maximum magnification of 12000 [90, 91]. Nowadays, it is far more complex as they consist of several lenses, minilenses, apertures and different coils. Here the single or double pole-piece lenses and the quadrupole, hexapole or octupole lenses are distinguished by simply referring to the former as **lenses** and the latter as **coils**. A minilens is a smaller lens that behaves as a normal one but it has to be energized by higher currents and it needs a better water-cooling system. The use of such lenses is advantageous to reduce the height of the TEMs. Apertures are literally holes in thin plates that can be inserted in the TEM column in order to limit the beam that goes through the optic axis. They are commercially available with dimensions as small as 5 μm in diameter.

Modern condenser systems are made up of three or four lenses, several coils, one or two apertures and sometimes a minilens. The aim of the **first condenser lens** (CL1) is to magnify or de-magnify the image of the electron source created by the electromagnetic system that provides the accelerated electrons, thus it controls the beam size. The higher the lens current, the smaller the focal distance and the electron beam will be focused closer to the lens centre. In most commercial TEMs, this is controlled by the parameter called *Spot Size*. The higher its number, the higher the lens current, the smaller the beam size and current. The beam current decreases with the Spot Size number because the beam deflection is increased and the electrons with higher tilt with respect to the optic axis will hit the TEM column, which is electrically connected to the ground. The functions of the next CLs depend on the configuration of the condenser system.

- **Condenser System with 2 CLs**. The **second condenser lens** (CL2) is used to adjust the illuminated area on the specimen by bringing the electron beam to the pre-field of the objective lens (pre-OL). The variation of the CL2 strength changes the image position of the CL1 crossover (that is the object for CL2) and it is brought near to the **front focal plane** (ffp) of the pre-OL, which usually has a fixed current. CL2 is controlled by a knob in the control panel called *Intensity* or *Brightness*. A set of apertures is introduced after the CL2 (in Thermo Fisher TEMs, former FEI, it is usually called CL2 apertures) in order to limit the beam current and the convergence angle of the beam when this is focused. After the **condenser aperture** (CA), two sets of coils are placed, so-called **deflector coils** (DC), in order to allow the shift and tilt of the beam at the specimen plane. Previous to properly use them, they have to be adjusted with the help of voltage wobblers to enable a tilt without shift and a shift without tilt. Another coil is also introduced in the same area of the deflector coils to correct the astigmatism of the beam caused by the condenser lenses, which is frequently called **condenser stigmator**.

  Such configuration is limited because the convergence angle cannot be tuned as desired since it is defined by the excitation of CL2 and the size of CA, i.e. the illuminated area. This lack of flexibility is disadvantageous for the idea of a multi-purpose TEM, yet it is enough for standard image and diffraction experiments.

- **Condenser System with 2 CLs and 1 CM**. Basically, this system is similar to the previous one but a **condenser minilens** (CM) is introduced closer to the objective lens of the objective system. The use of three lenses results with one more possible crossover of the electron beam before it reaches the sample. This allows the control of the convergence angle because the CM is responsible to bring the beam to the pre-OL. For a given strength of the OL, the more CM current, the less CL2 strength to focus the beam on the specimen; therefore, less convergence angle. Another important point of this configuration is that the CA plane is conjugate to the bfp of the post-field OL. This means that the CA is seen when the TEM is switched to view the diffraction plane. To sum it up, the combination of the CA size and the CM strength determines the convergence angle of the beam.

  Here the CL2 is controlled by the *Brightness* or *Intensity* knob and it is tuned to select the sample area to be illuminated as well. The CM current cannot be changed continuously by a knob because it requires the adjustment of time-consuming alignments and it can only be modified in this way by means of a free lens control module. Nevertheless, default illumination modes are available with different stored CM excitations and coils alignments. In JEOL microscopes like the JEOL 2100, the parameter that controls the CM excitation is called *Alpha* and it can vary from 1 (most parallel beam) to 9 (high-convergent beam). In the old ARM200 series from JEOL, only two options for the convergence setting are available, which are called S for a small convergence angle beam and L for large convergence angle beam. In case of the Tecnai series from Thermo Fisher, only two illumination modes can be selected: *Microprobe* for a parallel beam and *Nanoprobe* for a convergent beam.

  Although the CM provides the necessary conditions to set different beams, the beam size cannot be changed without the variation of the convergence angle, i.e. the convergence angle is not independent of the spot size.

- **Condenser System with 3 CLs**. This configuration is based on the use of three condenser lenses in which the CM is substituted by a **third condenser lens** (CL3), but it is placed closer to CL2 than the OL. Such optical arrangement allows the realization of Köhler illumination in a TEM [92], which was initially thought for light microscopy [93]. The main idea of this parallel illumination is to keep the image of the electron source to the ffp of the pre-OL by the CL3 and the imaging of the CA into the specimen plane by the pre-OL. In this way, the illuminated area of the sample is defined by the CA, which is located at the CL3 plane in this case, and the pre-OL strength. On the other hand, the convergence angle is determined by the (de-)magnified source image produced by the CL1 and CL2. The only disadvantage is that the illuminated area is limited by the mechanical size of the CA and this may not be desired for some experiments [94]. Such non-CM configuration was developed and commercialized by Zeiss Microscopy company but its TEM unit was discontinued some years ago.

When convergent beams are required, the three CLs are tuned to (de)magnify the electron source as much as needed and place it on the image plane of the pre-OL. Here the convergence angle and beam size are dependent on the CL2 and the CA once again. All TEMs achieve the most convergent beams by using this optical approach with the CM off of their condenser systems.

- **Condenser System with 3 CLs and 1 CM**. This is the condenser system used by all modern TEMs and enables the possibility to independently control the beam size and the convergence angle. The first two CLs are responsible to control the spot size and the beam current at a fixed image plane of the CL2. CL3 and CM control the convergence angle and the illuminated area of the specimen. Illumination based on focused beams is obtained by placing the CL3 image at the ffp of the CM, which brings the image to the infinity for the pre-OL and this acts as an ocular for the sample. In case of parallel beams, the CM brings the crossover to the ffp of the pre-OL [95].

The objective system is the core of a TEM because it contains the goniometric stage that allows the introduction of samples in the microscope, and the double pole piece lens (**objective lens**, OL) from which images and diffraction patterns of these specimens can be obtained. It also contains an **objective minilens** (OM) that is used to obtain images at very low magnification values when the OL is switched off, a stigmator to correct the OL astigmatism (**objective stigmator**), and an aperture located at the bfp of the post-field OL (**objective aperture**, OA).

- **Goniometric Stage**. It is a mechanical system located in-between the pole pieces of the objective lens that is used to insert and retract different sample holders by means of an airlock, and move the sample along x, y and z directions and tilt it (alpha). The α-tilt is available in all goniometric stages and it corresponds to the axial direction of the holder axis. The tilt through the perpendicular direction of α is only possible when the holder has a plate designed for this tilting capability. The most sensitive stages include piezoelectric sensors for almost mandatory fine movement of the specimen (down to 20 pm per step) in atomically resolved experiments.

- **Objective Lens**. It was initially designed as a magnetic lens positioned below the specimen in such a way that the OL magnetic field was very weak at the sample plane [68]. Due to its higher spherical aberrations, low probe current and limited tilting capabilities because of the interference with the upper pole piece, the design was switched to the one proposed by Walter Glaser [72]. This magnetic lens is designed with two lenses; one is positioned above the sample (pre-OL) and the other one below (post-OL). The unalloyed soft iron case covers both of them. The specimen is immersed in the magnetic field where the axial component is strongest, following the magnetic field model of Glaser [64]. The pre-OL works as a condenser lens for the in-coming electron beam while the post-OL acts as the objective lens of a typical optical system, which is the reason why this type of OL is frequently called *single-field condenser objective* and the TEM column is sometimes divided between the probe-forming system and the image-forming system.

  This OL type is still kept by TEM manufacturers but the geometrical design of the pole pieces and the gap between them changes with the main purpose of the microscope. An analytical

TEM needs an OL with a large gap in order to be able to tilt the holder at higher angles before it touches the pole pieces (an undesired event) and to measure emitted X-rays, secondary electrons or elastic backscattered electrons with different detectors. An atomic-resolution TEM requires a shorter gap pole piece because it needs a uniform and isotropic magnetic field over the illuminated area to have the maximum wave coherence for atomically resolved images. Recently, two OLs have been used to create a magnetic field free environment at the specimen plane to measure magnetic materials with atomic resolution [70].

In comparison to the high strength variations that are applied to the condenser lenses, the OL current is kept most of the time around a fixed and stored value that can be recalled anytime by means of a button in the TEM control pads, called *Std Focus* in JEOL microscopes and *Eucentric Focus* in Thermo Fisher microscopes. TEM manufacturers set this value because it ensures minimum spherical aberrations of the lens and it also determines the position of the objective, condenser and selected area apertures since they have to be placed in the bfp of the post-OL, a conjugated plane of the post-OL bfp in the condenser system and the image plane of the post-OL, respectively.

- **Objective Aperture**. This aperture is quite important for the imaging process. Since it is placed at the bfp where the diffraction pattern is formed, it can be used to limit the diffracted waves from the sample that are going to interfere to create the image. If a small aperture is used and placed at the centre of the diffraction pattern, a *diffraction contrast* image will result. When it is placed in such a way that only one of several scattered beams are selected, an image will be formed that contains brighter areas from where this selected diffracted wave come while the rest would be darker, i.e. with reverse contrast. The former case is referred as *bright field imaging* and the latter one is referred as *dark field imaging*. They are the basic imaging operations in a TEM. If a bigger aperture is used that takes the primary beam and several scattered ones, a *phase contrast* image will be obtained that depends on the sample orientation, thickness and crystallinity.

The projector system, or imaging system, is the last optical part of a TEM column and its aim is to transfer the image or diffraction pattern created by the post-OL to the different detectors. Initially, the projector system consisted of one lens that highly limited the magnification [91]. Later on, another lens was added to have an independent control of the optical plane that is going to be visualized, i.e. the bfp or the image plane of the OL, and its projection to the fluorescent screen or photosensitive film [64]. Nowadays, modern TEMs have a projector system with two sets of coils to shift the image created by the OL, so-called **image coils** (IC), a stigmator (**projector stigmator**), four lenses in order to have a flexible image formation system, and another set of coils (**projector coils**) before the last lens to shift the final projected plane without affecting the magnifying part. It also contains an aperture, called **selected-area aperture** (SAA), that is placed at the image plane of the post-OL.

The first lens is called **diffraction lens** (DL) and it is responsible to switch between image and diffraction mode. Its current is highly changed in image mode according to the selected magnification, while in diffraction it is slightly tuned from a reference value to finely focus the diffraction patterns. The OL current is gently tuned as well but only when the exact focus of the image has

to be found. The DL works in a similar way as an objective lens but in the diffraction plane. Two lenses called **intermediate lens 1** (IL1) and **intermediate lens 2** (IL2) are subsequent to the DL. Their current is changed according to the projection mode and the magnification (image) or camera length (diffraction pattern). The last lens is called **projector lens** (PL) and its function is to bring the projected plane from IL2 to the detection plane.

When the projector system is in image mode, there are generally three main optical regimes. The first one is usually called *low mag* and the principal difference is that the OL is switched off and the objective minilens is on. The rest of the lenses below the OL are low excited. This approach enables the projector system to obtain images at magnifications as low as 50, which is quite useful to find the **region of interest** (ROI) at the beginning of a TEM session. Another optical regime called *Mag* or *SA* is available for middle to high magnifications. The OL is switched on again and the objective minilens is off. In this case, DL and IL1 currents are increased while IL2 current is decreased in order to gain magnification. The reduction of the IL2 strength makes the ffp of the IL2 to match the image plane of the IL1; hence, it creates an image that comes from the infinity for PL. Finally, higher magnifications are achieved in the *High Mag* optical regime. Here DL and IL1 are strongly excited and IL2 is switched off. In the diffraction mode case, the projector system works in the same optical regime most of the time since the physical size of the diffraction pattern in a detector does not change as much as an image. The DL current is kept around a reference value, as mentioned above, and IL1 and IL2 currents are tuned to increase or decrease the camera length. Generally, IL1 strength is increased and IL2 is decreased to create a magnified diffraction pattern in front of the PL.

It is worth to note that the TEM optical system described here is the simple and averaged one of contemporary microscopes. Extra pair of coils, different apertures and energy filters can be added to the TEM column for specific measurements. The most frequent add-ons are the lens aberration correctors. They are differentiated according to their physical location: before the pre-OL and after the post-OL. Pre-OL correctors or probe-correctors are placed between the CL3 and the deflector coils to produce highly convergent and angstrom-sized electron beams. Post-OL correctors or image-correctors are placed between the objective minilens and the image coils to produce images in TEM mode with atomic resolution. Further details and key references on the development of such complex systems can be found in the excellent review by Peter W. Hawkes [96].

2.3 Scanning Transmission Electron Microscopy - how does it work?

A transmission electron microscope has two main operation modes. The first and obvious one is the TEM mode, which is based on the illumination of the area of interest of a sample by a spread electron beam. The second one is the **scanning transmission electron microscopy** (STEM) mode. The fundamental idea is the same as the scanning electron microscope (SEM) but transmitted electrons are used instead of secondary electrons. STEM mode consists in focusing the electron beam on the specimen plane by means of the condenser system and the pre-field OL to maximize the demagnification of the emitter source. In this condition, sawtooth signals of selectable amplitude (for magnification control) are sent to the deflector coils to scan or raster the focused beam over the ROI. The DCs are used to send the beam to the ffp of the pre-OL, which ensures that the electron beam emerging from this pivot point scans the specimen parallel to the optic axis. The projector system is kept in diffraction mode during the scanning and the image is formed by electronic processing of the primary beam intensity (bright field, STEM-BF) or the overall intensity from the scattered beams (dark field, STEM-DF). In this way, each scanned beam position corresponds to a pixel location on a digital frame.

The first STEM was built in 1939 by Manfred von Ardenne working for Siemens in Berlin, but the resolution obtained using this microscope setup was lower than in TEM mode due to the filament sizes used as electron sources [97]. Therefore, there was no real benefit to switch to STEM. Around 30 years later, Albert Crewe and coworkers developed the **field emission gun** (FEG), which improved the achievable beam diameters with respect to thermionic emission sources [98]. They coupled the FEG in a simple STEM-dedicated microscope that was operated at 30 kV and they were able to obtain images with higher resolution than the static TEM mode at that time [99, 100]. The use of a FEG was doubly beneficial. First, it allowed a convergent electron beam much smaller than the attainable with a thermionic source, therefore lateral resolution was highly increased in STEM and proved to be comparable to TEM mode. Second, the brightness of a FEG, which is defined as the current density per unit solid angle of the source, is 10 times higher than that of a LaB_6 thermionic source. This boosted immediately analytical applications such as energy-dispersive X-ray spectroscopy (EDS) and EELS measurements. Nowadays, TEMs are designed in such a way that they can be operated in both operation modes, usually referred as (S)TEMs, and the achievable resolutions in both modes are similar if no mode-specific electron-optical component is added.

Different detectors are used to integrate the intensity from transmitted beams in STEM mode. The two most common ones are the *semiconductor detectors* and the *scintillator-photomultiplier (PM) detectors*. Semiconductor detectors are formed by single-crystal sheets of doped silicon designed as a p-n junction. A signal is generated by the creation of electron-hole pairs when a high-energy electron hits these sheets. It takes a few nanoseconds to remove the created carriers from the detection area but a large capacitance of the electronics makes it not very responsive to rapid changes in signal intensity. On the other hand, scintillator-PM detectors are composed by a fast decay time scintillator material, like a yttrium-aluminium garnet or a perovskite, and a photomultiplier that is connected to the scintillator via a light pipe. This detector has lower noise level and it is faster than the semiconductor detector. These conditions ensures scanning speeds down to µs per pixel, thus 1 Hz frame

refreshing is feasible. Although the energy-conversion efficiency is lower, it is preferred for STEM imaging.

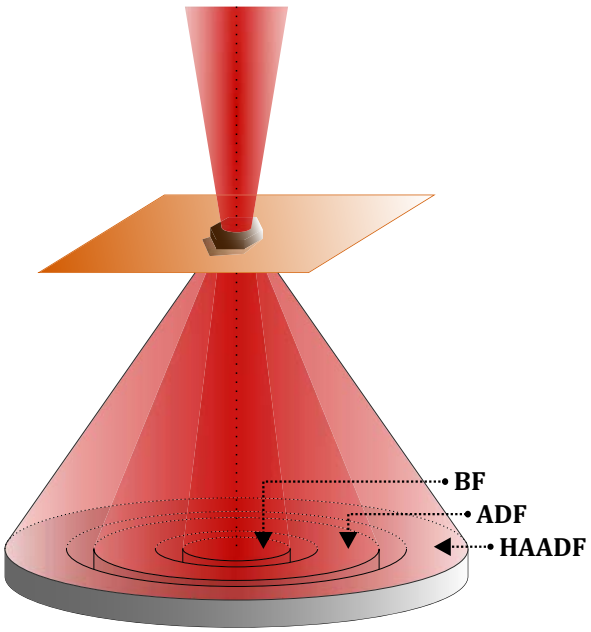

Figure 2.3.1: Schematics of the three different available STEM detectors according to the collection angle: bright field (BF), annular dark-field (ADF) and high-angle annular dark field (HAADF).

Both detector types can be designed in different shapes to acquire different forward scattered beams, schematically shown in Figure 2.3.1. A detector that is designed to detect the primary beam and the close-by intensity is usually referred as STEM-BF detector. Then, annular detectors that are circular but with a hole in the centre from where the primary beam will go through are frequently called STEM annular dark field (ADF) detectors. In general, the usual angular interval for STEM-ADF is between 1° and 3°. When the diameter of the inner ring of the detector is even bigger (geometric angles bigger than 3°), then they are called STEM high-angle annular dark field (HAADF) detectors. Although the geometric angular range for the active area of these detectors is fixed, the amount of radiation that reach them can be modified by changing the camera length, i.e. the diffraction "magnification". Moreover, these three different designs can be azimuthally segmented in 2, 4 or even 16 parts and differential phase contrast imaging of magnetic and electric fields can be mapped [101, 102, 103].

2.4 Convergent and Quasi-Parallel Beam Illuminations

The beam illumination in TEM mode and STEM mode can be differentiated by the use of a spread or focused beam for imaging, as it is sketched in Figures 2.4.1A and 2.4.1B. Using STEM mode, the electron beam is usually referred as **electron probe** due to the similarity to other scanning techniques. In this context, one important parameter for diffraction pattern acquisitions needs to be introduced that describes the illumination setting of the electron beam, the **convergence angle**.

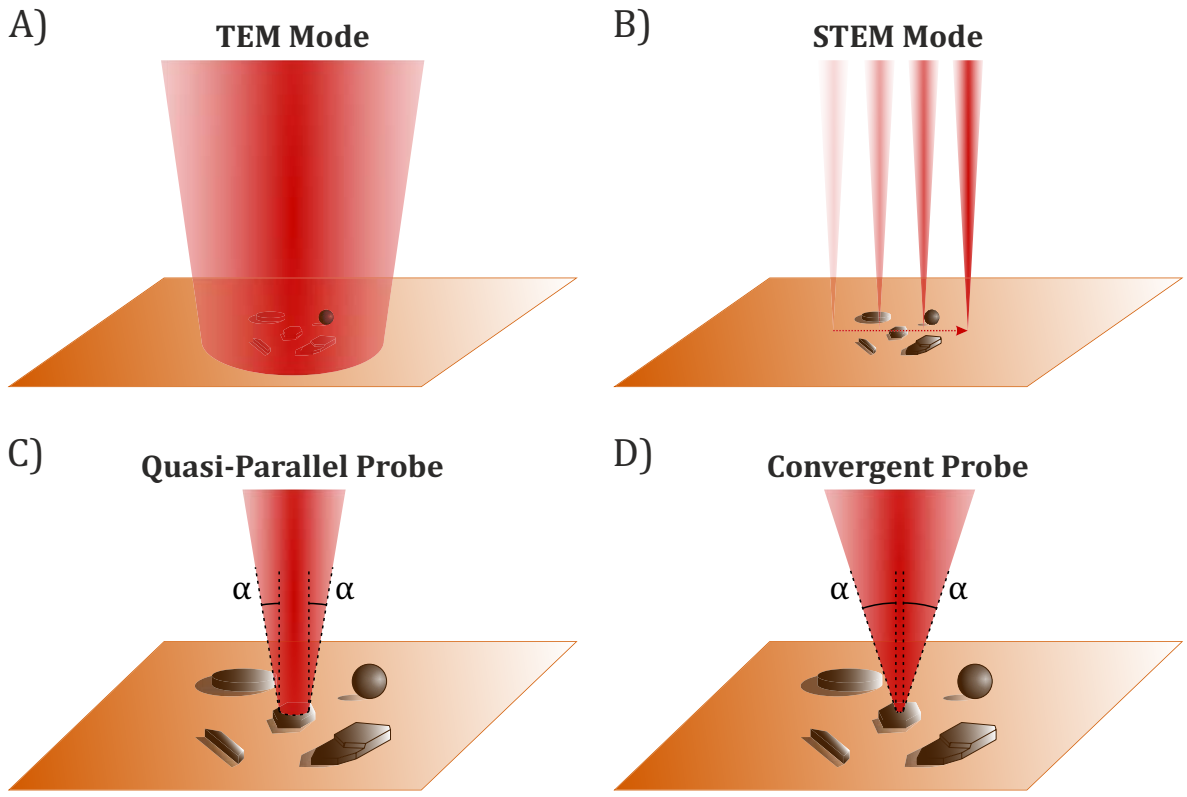

Figure 2.4.1: Sketch of the two possible operation modes in a TEM; A) the TEM mode and B) the STEM mode. C) and D) correspond to the two different illumination modes that the electron beam can adopt. α is the convergence angle of the electron probes. Note that the beam diameter changes with the convergence angle.

The convergence angle, α, is the maximum tilt that electrons from the electron beam have at the specimen plane with respect to the optic axis. In this work, a beam with low convergent angle ($<$ 2 mrad) will be called **quasi-parallel beam** and a higher convergence angle beam will be called **convergent beam**. An example of such two beams while illuminating a particle is sketched in Figures 2.4.1C and 2.4.1D. The measurement of this angle is practically impossible when the projector system is in image mode, but it is possible if it is switched to diffraction mode. Since the bfp of the post-OL can be considered an angular plane in the sense that distances from the primary beam are equivalent to scattering angles, the measurement of the FWHM of non-saturated reflections from very crystalline materials can be used to calculate the convergence angle.

By using Bragg's law and the paraxial approximation

$$\begin{gathered} 2\ d_{hkl} \sin\theta_B = \lambda \\ 2\ d\ \theta \approx \lambda \\ d\ 2\theta \approx \lambda \\ \alpha = 2\theta \approx \frac{1}{d}\lambda \end{gathered}$$

where $1/d$ is half of the FWHM of a non-saturated reflection and λ is the electron wavelength. This method is a rough calculation because mosaicity (spread of crystalline orientations in a single-crystal) and the point spread function of the detector (spread of intensity to more than one pixel cell) is not taken into account, yet it still provides a good approximation for characterizing the beam illumination. Some literature define the convergence angle as two times the convergence angle defined here, thus it points out the inverted cone shape of the beam on the sample. That is the reason why in these publications *our* convergence *angle* corresponds to the convergence *semi-angle* [76, 104]. However, the electron beam has not exactly an inverted cone shape because the tip is not infinitely sharp, it has a finite size that is the probe diameter, and that is the reason why the definition given here is preferred.

The convergence angle is tuned with the lenses from the condenser system and it is limited by the CA. As the post-OL bfp is conjugated to the plane of the CA, the effect of the aperture size on the convergence angle can be directly observed by changing it while being in diffraction mode. However, the aperture sizes are limited to 5 µm due to mechanical difficulties but also because beam currents are highly decreased and very low amount of electrons could reach and image the sample. It is worth to note that neither the OA nor the SAA will modify the convergence angle as they are placed below the specimen. The angle of the electron beam with respect to the optic axis below the sample plane is called **collection angle** and it can be changed by the OA.

Microscope aberrations depend on how much the electron beam is tilted with respect to the optic axis. The more the electrons are tilted, the higher the convergence angle, the higher the aberrations contribution. While working with high resolution imaging in TEM mode, a balance between beam current and convergence angle has to be achieved in order to have enough intensity and small contribution of the aberrations. A CA of 50 or 100 µm is usually inserted and the TEM is operated at a medium-high spot size. An OA may be inserted as well to block the highly scattered beams that contribute to the blurring of the image. If the convergence angle is still too big for a desired experiment or resolution, the electron beam can be spread even more than the imaged area to simulate a reduction of α, that is because the highly tilted electrons will be deviated to the TEM column.

High resolution imaging in STEM mode is approached in a different way. STEM mode works with an electron probe. Therefore, the attainable resolution of high resolution STEM imaging is directly linked to the size of the probe. The smaller the probe size, the smaller the scanning step without illuminating specimen area of the previous position. However, physical and technical constrains limit the minimum beam diameter. If the de-magnifying capability of the condenser system is higher than the following limitations, which is a totally valid assumption for modern TEMs, the minimum beam diameter can be determined according to three different contributions that depend on the convergence angle:

- **Source diameter**. This is the Gaussian diameter determined by the brightness B of the source and the probe current I_p on the sample [105]

$$d_G = \left(\frac{2}{\pi}\sqrt{\frac{I_p}{B}}\right)\frac{1}{\alpha}$$

- **Aberration-limited diameter**. Spherical aberrations produces a disk in the image plane of an object point. The minimum diameter of this disk is formed at a plane before the image plane called plane of least confusion [106]. The FWHM of this disk is given by

$$d_S = 0.3\ C_{30}\ \alpha^3$$

- **Diffraction-limited diameter**. This is the limit imposed by the diffraction phenomena. When a circular aperture is illuminated by a uniform illumination, the results is a pattern of concentric rings called *Airy pattern* [107]. The expression for the FWHM of the bright central disk of this pattern is

$$d_D = 0.517\ \lambda\ \frac{1}{\alpha}$$

The final probe size can be calculated by adding these three contributions in quadrature [108]

$$d_T = \sqrt{d_G^2 + d_S^2 + d_D^2}$$

Despite its simplicity, this expression gives an idea on which parameters need to be taken into account when working at different convergence angle regimes. Figure 2.4.2 shows a plot of the three different contributions. A single plot for the source contribution is misleading because it presupposes that the convergence angle can be highly tuned without modifying the aperture, thus the probe current. For this reason, an interval is displayed that has a lower limit defined by the usual settings of a FEI Tecnai F30 for diffraction pattern acquisition ($I_p = 1.5$ x 10^{-13} A), and an upper limit determined by small probes used in elemental mapping ($I_p < 1$ x 10^{-9} A [104]).

When working with quasi-parallel probes in STEM mode, the probe current is low and the beam diameter is limited by the diffraction of the beam through the CA. On the other hand, a convergent probe for spectroscopy or atomic-resolution imaging easily exceeds 5 mrads [88, 104] and the lens aberrations strongly limit the minimum achievable diameter of the beam. Since the diffraction limit for low α is completely unavoidable, the efforts for atomic-sized probes were logically directed to higher convergence angles with the enhancement of the pole pieces from the objective lenses and the development of correctors, hence the preference to work with a convergent probe in STEM mode.

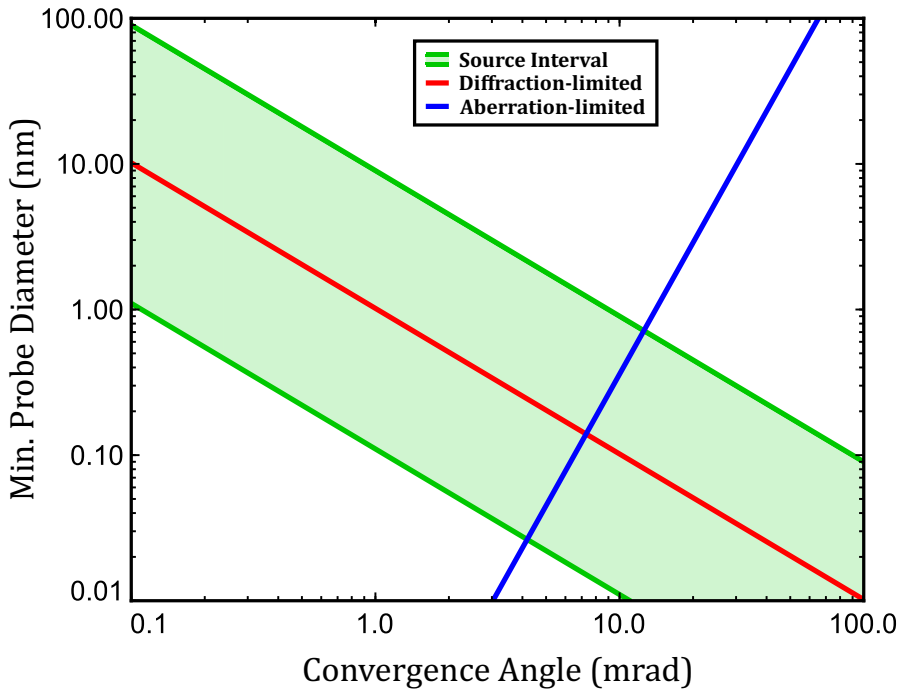

Figure 2.4.2: Log-log plot of the minimum probe diameters at FWHM against the convergence angles of the different possible contributions. The source contribution is split into an interval to take into account different probe currents, lower limit at $I_p = 1.5$ x 10^{-13} A and upper limit at $I_p = 1$ x 10^{-9} A. The values $B = 5$ x 10^8 A/cm^{2}sr, $\lambda = 0.0197$ Å and $C_{30} = 1.2$ mm were used to simulate a FEI Tecnai F30 S-Twin operated at 300 kV.

2.5 SAED against NBED

There are two methods to acquire diffraction patterns with a TEM; the **selected area electron diffraction** (SAED) and the **nano-beam electron diffraction** (NBED). Both techniques result in the formation of a diffraction pattern from a desired area of the TEM sample, but the main difference is how to select this area. An important alignment that has to be followed for diffraction, as well as for imaging, just after the holder is inserted, is the adjustment of the z-axis to the **eucentric plane** or **eucentricity**. This is the z-position of the stage in which the image is focused with the OL at the reference current value and the lateral displacement of particles is minimized when the stage is tilted around the primary tilt axis of the holder (the α-tilt). This procedure ensures that the specimen plane is located at the object plane of the post-OL and, in consequence, the image plane is conjugated to the specimen plane.

SAED relies on the SAA to choose the ROI. Since this aperture is placed in the image plane, all electrons going through it form the diffraction pattern on the detector. The SAA acts as an aperture (virtual aperture) in the specimen plane. Another way of interpretation is that the diffraction pattern has already formed from the whole illuminated area defined by the condenser system and the SAA only accepts the diffracted waves related to the selected part of the image. While the projector system is in image mode to select the diffracting area, the DL should be tuned if possible in order to have a sharp image of the aperture to ensure that the image plane of the OL is correctly projected. The SAA and the focused beam should be placed at the middle of the fluorescent screen in order to have the most azimuthal symmetry of the beam intensity, which avoids undesired distortions of the diffraction patterns caused by highly tilted rays. The optical regime for the projector system during imaging has to be the *SA* because it makes sure that the selected part of the projected image plane is the responsible of the final diffraction pattern in the detector. Once all these considerations are taken into account, the electron beam is spread to simulate a quasi-parallel beam and the projector system is switched to diffraction mode. At this point, the DL should be finely tuned to have the sharpest reflections and a proper SAED pattern can be acquired.

NBED does not use the SAA, instead the beam is focused on the area interested to diffract at. This means that the reflections diameter in the diffraction patterns will be mainly determined by the convergence angle of the electron beam. In this way, two kinds of patterns can be distinguished; one with disk-like reflections, also known as convergent beam electron diffraction (CBED) patterns, and the other one with sharp spotty reflections similar to SAED patterns, named NBED patterns. CBED patterns are very interesting because the features inside the disk-like reflections are purely based on dynamical diffraction, i.e. multiple-scattering events occurring when electrons are going through the crystal. Therefore, the determination of all point groups is possible by the identification of symmetries inside the CBED reflections [109]. Nevertheless, space groups can also be determined by means of spotty-like reflections, which is going to be shown in chapters five, six and seven of this work. An important step while acquiring NBED patterns is to tune the DL excitation to project the bfp of the post-OL, because the sharpness of the reflections cannot be used as in SAED due to the convergence angle. In this situation, the OA is inserted and the DL strength is changed until the aperture is in focus. The DL value in diffraction mode is usually around a fixed value and it is equivalent to the OL standard value in image mode.

The comparison between both methods shows that they are complementary. SAED does not require a special illumination setting and an intense beam can be used at all times as it will be highly spread during the diffraction pattern acquisition. Special care has to be taken for the intensity of the primary beam to avoid burns on the detector used for the acquisition. On the other hand, the minimum illuminated area is restricted to about 400 nm using a 10-µm SAA [76] and the mechanical position of the aperture limits its movement precision. NBED gets rid of these limitations because it is working with a beam whose size is limited by the diffraction of the CA and it can be precisely and flexibly positioned through the deflector coils. For a convergence angle of around 0.1 mrad that can be obtained in SAED, the achievable minimum beam diameter for a 300 kV TEM in NBED decreases down to $\sim$ 100 nm. However, a special alignment for a quasi-parallel beam has to be carried out and the smallest CA is usually necessary, which turns into a low intensity beam that may be inconvenient in some measurements. The procedure and workflow to set and characterize such electron beam for its use in any diffraction pattern-related experiment are explained in the third chapter.

2.6 Precession Electron Diffraction

Precession electron diffraction (PED) stands for TEM applications which use an electron beam that precesses at the specimen plane. It is similar to the Buerger precession method in X-ray crystallography where the stage is precessed instead of the X-ray beam [110]. Although technically different, the core idea is the same: the wobbling of the Ewald sphere in the diffraction space that results in the reflections integration at the detector.

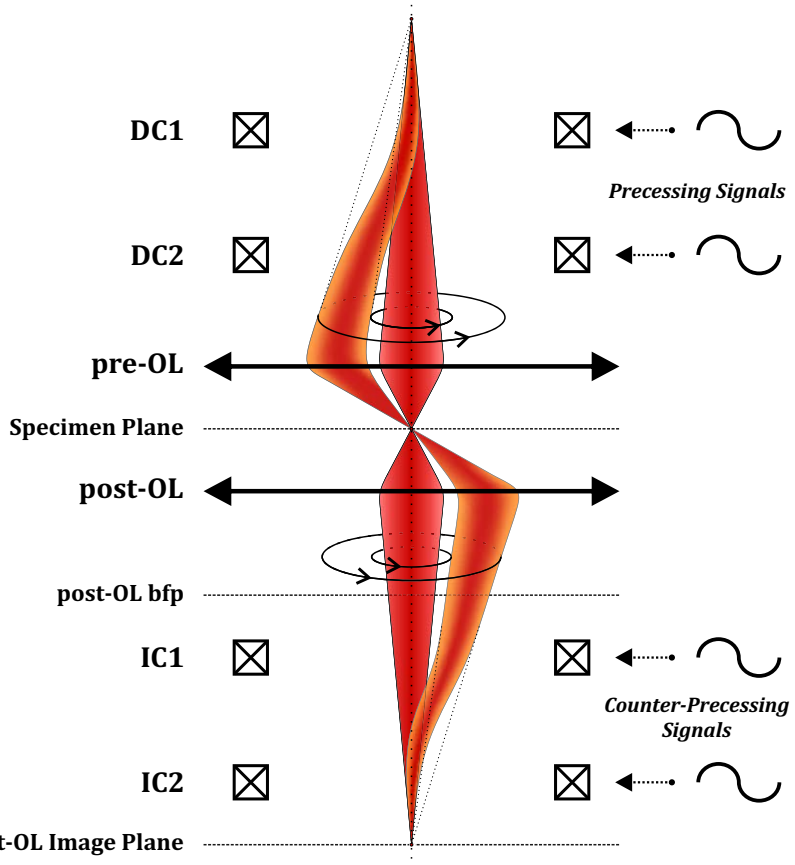

Figure 2.6.1: The trajectory of the electron beam in a TEM with (orange contour beam) and without precession (full red beam). The optical diagram has been simplified without minilenses, apertures and stigmators for better understanding of the beam behaviour while precessing. DC stands for deflector coils and IC for image coils.

The precession movement of the electron beam is achieved by sending sinusoidal signals to the deflector coils in order to produce an inverted illumination cone, also called rocking illumination in some publications, that moves at the frequency set by these signals (up to 400 Hz depending on the coil driver filters of the TEM electronic boards) and pivots with the tip of the cone at the specimen plane. To recover a pseudo-stationary diffraction pattern at the bfp of the post-OL, as well as a pseudo-stationary image in the image plane at the same time, additional sinusoidal signals are sent to the image coils below the specimen to bring back the beam to the optic axis. In this way, the beam subsequently excites different sections of the diffraction space at high frequency, and the precessed

diffraction pattern will retain the intensity of all excited reflections averaged over the number of precession turns used in the pattern acquisition.

Figure 2.6.1 shows a sketch on how the electron beam is deflected by the different coils. If only the precessing signals are sent to deflector coils and the beam is pivoting at the specimen plane, the beam will be focused in the image plane. Yet the diffraction pattern in the bfp of the post-OL will consist of rings with a radius proportional to the precessing angle, which is used for calibration. Thus counter-precessing signals are needed to recover the focus at the post-OL bfp. If only precessed diffraction patterns are needed, a counter-precessing signal to one set of image coils is enough because it allows tilting the beam in such a way that the electron beam direction viewed from below the image plane seems like it is coming from the focused spot of the post-OL bfp. However, the standard procedure is to keep a focused and precessed beam in both planes, which requires both sets of image coils. Alignment details will be extensively discussed in chapter three.

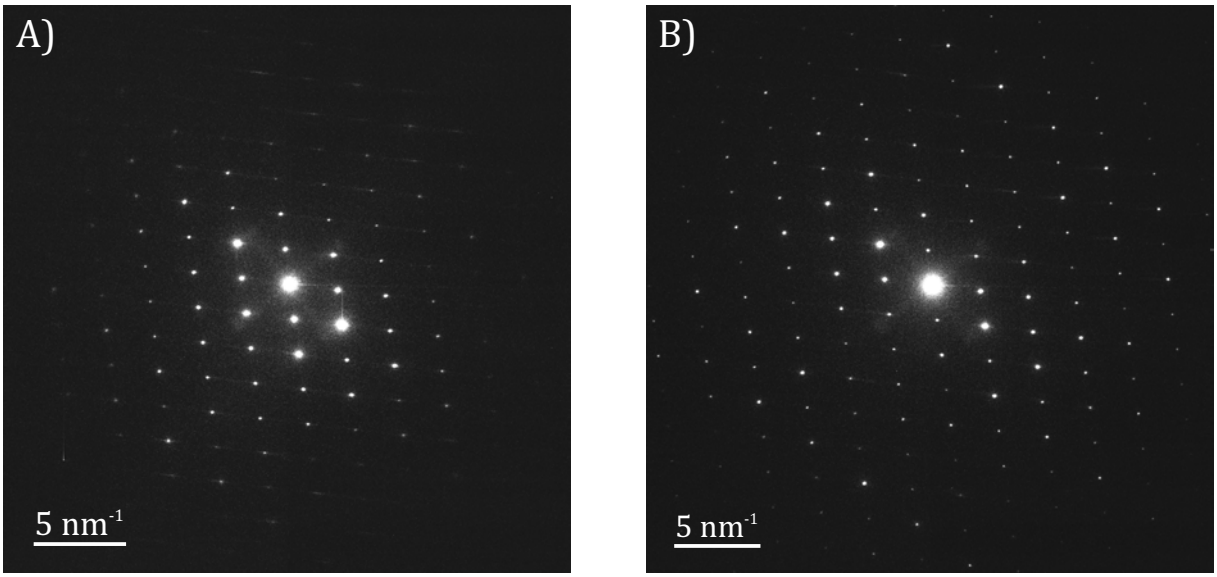

Figure 2.6.2: [131] zone-axis diffraction patterns from a $Ca_2(Al,Fe)_2O_5$ crystal A) with and B) without 1° of beam precession.

PED was developed to collect integrated intensities that are more suitable for structure determination by electron diffraction [111]. It helps to diminish the non-systematic dynamical effects, such as double-diffraction and Kikuchi lines, and makes the crystallographic analysis easier [112, 113, 114]. PED data is sometimes referred as *pseudo-kinematic* data in the sense that dynamical effects are strongly reduced and the kinematical theory can be used for crystal structure determination. Nevertheless, it has to be noted that PED patterns are still intrinsically dynamical by nature and therefore they have to be treated as such for precise and accurate structure refinement [115, 116]. Figure 2.6.2 shows diffraction patterns with and without precession for the same orientation of a brownmillerite crystal. The use of 1° of precession allows the statistical meaningful acquisition of intensities from many more reflections at the same crystal orientation, the intensity re-distribution that minimizes the possibility of saturated reflections, and the diminishing of disorder effects, i.e. diffuse scattering.

Some diffuse streaks can be seen at the top of Figure 2.6.2A, while they are highly reduced in Figure 2.6.2B and reflection intensities emerge in this diffraction space area.

The key application in which beam precession is routinely used is the electron diffraction tomography (EDT) technique or, recently conventionally called, **3D electron diffraction** (3D ED) [14]. Briefly, the main procedure of the technique is the following: acquisition of non-oriented diffraction patterns from a single crystal at subsequent and different usually equidistant tilts of the sample holder, reconstruction of the ODS from the diffraction data and reflection intensity extraction to retrieve the electron density or electrostatic potential of the crystal structure [12]. Since the publication of Mugnaioli et al. that introduced the coupling of PED with 3D ED [117], this acquisition tool has been essential to understand the atomic ordering of hundreds of different crystals. Acquisition methods, data processing algorithms and different examples will be extensively explained in chapter four.

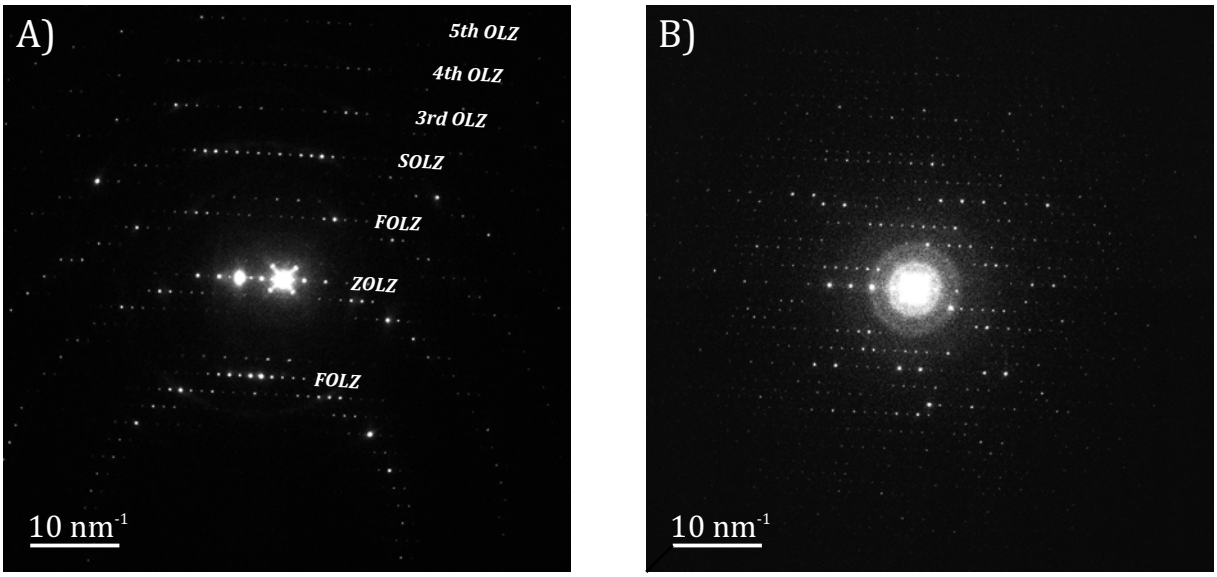

Figure 2.6.3: Non-oriented diffraction patterns A) without and B) with 1° of precession from a lutetium aluminium garnet ($Al_5Lu_3O_{12}$) crystal. Reflections from up to the 5th order Laue zone can be visualized without precession due to the high crystalline quality of the material. Contrast, brightness and gamma has been modified in both images for better display.

Another effect of the precession movement is the increase of visible reflections in the diffraction pattern, as already shown in Figure 2.6.2. This effect is mainly interesting for 4D-STEM applications. Here, a quasi-parallel probe is scanned through a ROI and a diffraction pattern is stored for each beam position; 2D for the x-y coordinates (beam positions) of the STEM image and 2D more for the x-y coordinates of the diffraction pattern in each (x, y) position of the STEM image. Sawtooth signals mixed with sinusoidal signals are sent to the coils for simultaneous scanning and precessing of the electron beam. Phase and orientation maps are beneficial of this illumination setting because they rely on template-matching algorithms that are based on the cross-correlation between simulated and acquired patterns [118, 119], but also strain maps are enhanced because more spots are available to correlate their distance between strained and non-strained regions [120, 121]. Apart from the

increased number of reflections, PED also enables an accurate localization of the reflections due to the induced uniform distribution of the reflection intensity inside each spot. Common precession angles are between 0.6° and 1.5°, yet it has to be kept in mind that the beam will be broadened at high angles because of the lens aberrations, thus it reduces the lateral resolution of 4D-STEM maps.

The maximum precession angle is only limited by the overlapping of different Laue zones [122]. Figure 2.6.3 shows two diffraction patterns acquired with and without precession. Since the crystallinity of the material is high, i.e. its atomic ordering is largely extended along the three spatial dimensions, reflections that belong up to the 5th order Laue zone can be acquired. When precession is applied to the acquisition of such patterns, the integrated Laue zones are expanded and reflections from different zones come closer. In this case, the precession angle was not big enough to overlap them but the zones cannot be distinguished anymore. The danger of overlap becomes higher when working with large unit cells and low indexed zones.

Apart from experiments based on the acquisition of diffraction patterns, electron beam precession has also been used in imaging and spectroscopy. Rebled et al. [123] showed that the use of precession in TEM image mode reduces contrast artefacts, like bend contours, due to Fresnel diffraction and curvature of thin foils. Precession-assisted image tomographies of such samples result in clearer identification and reconstruction of the features of interest. On the spectroscopic side, EELS and EDS spectra are also benefit from the precession movement. Estradé et al. [124] demonstrated that the use of precession when acquiring EELS spectra in zone-axis conditions enhances the edge signals by the reduction of the channelling effect. One year later, Liao et al. [125] showed that the same enhancement is visible for EDS measurements. Interestingly, precession-assisted EELS acquisitions in two-dimensional materials where the channelling effect is not present also provides an increase on the signal [126]. The smearing of the Bethe ridge allows the use of a bigger OA that increases the overall acquired signal without reducing the signal-to-background ratio [104]. In this way, the precession movement of the electron beam is shown to be advantageous in a big range of applications in the TEM.

2.7 Experimental Electron Diffraction Patterns

Previous sections have shown how different an electron diffraction pattern can look like according to beam precession as well as the convergence angle of the electron beam: while the use of quasi-parallel beams on crystalline materials result in spotty-like patterns, convergent beams produce disk-like patterns. However, the distribution of the scattering power depends on the object from which the scattering process occurs, in this case, the periodicity or crystallinity of the material under the beam. In this context, crystalline diffraction patterns acquired in a TEM are generally differentiated between three types, which are shown in Figure 2.7.1.

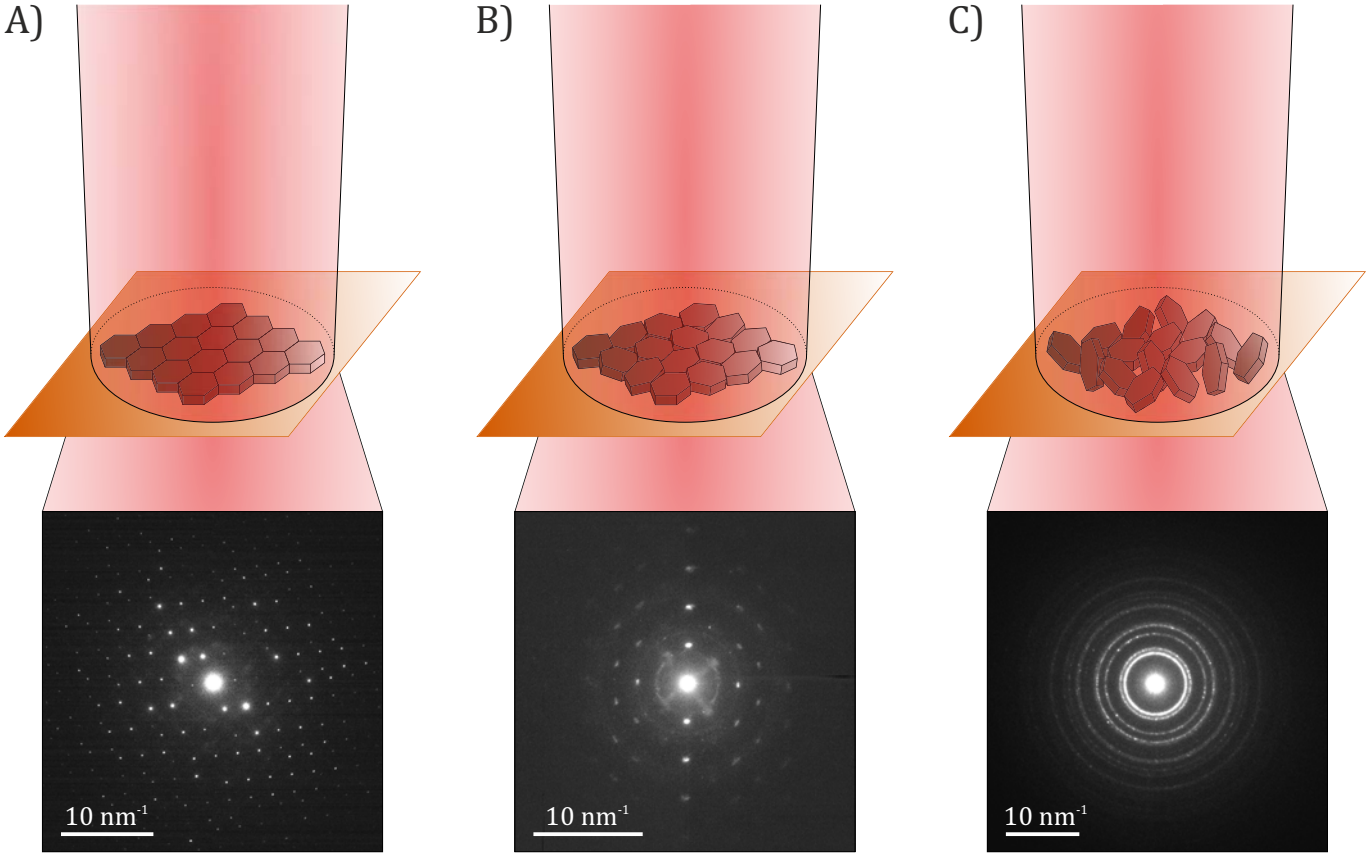

Figure 2.7.1: Sketches of electron beam illuminations of particles formed by hexagonal-shaped crystalline domains. A) is the case of a single-crystal diffraction pattern from a ferrosilicide [25], B) corresponds to a slightly textured pattern from a reduced phase of $La_2NiO_3F_{2-x}$ [127] and C) refers to a poly-crystalline pattern from a standard Au grating replica.

Figure 2.7.1A portraits the case in which a particle is formed by several hexagonal-shaped crystalline domains that are crystallographically oriented in the same way, i.e. all unit cells of all domains are aligned in the same direction. The resulting diffraction patterns of such particles show clear and sharp reflections like the ferrosilicide example in Figure 2.7.1A [25]. These kind of patterns are usually referred as to **single-crystal diffraction patterns**. When the different domains are slightly disoriented with respect to each other, the ODS contains a set of reciprocal lattices that are oriented

in a slightly different way as well, and the subsequent diffraction pattern consists of arch-like reflections. These patterns are generally called **textured diffraction patterns** and Figure 2.7.1B shows an instance from a reduced phase of $La_2NiO_3F_{2-x}$ [127]. The final type is related to particles that are formed by crystalline domains that are randomly oriented along all directions. The illumination of these particles generates diffraction patterns with rings around the primary beam, which correspond to the beam scattered by all possible Miller planes according to the space group, while the former patterns exhibit only those planes that are approximately parallel to the electron beam direction. Such patterns are called **poly-crystalline diffraction patterns** and Figure 2.7.1C displays one from a standard Au grating replica.

It has to be noted that the resulting patterns according to this classification depend on the area illuminated by the electron beam. For example, if a smaller beam diameter is used to illuminate only one single crystalline domain in Figure 2.7.1B or 2.7.1C, a single-crystal diffraction pattern with sharp reflections similar to 2.7.1A will be obtained in all cases. That is the reason why the use of single-, textured or poly- adjectives to describe the atomic ordering of matter is misleading, since it all depends on how small the crystalline domains are and whether the used radiation can individually illuminate such domains. At this point, the advantage of electrons compared to X-rays is that electrons can be focused at atomic-scale areas without the need of very large facilities. Even the most advanced beam lines in unique X-ray sources, like the European Synchrotron Radiation Facility, cannot illuminate such small areas [128]. On the other hand, a TEM provides a ready-to-use nano-diffractometer without that huge infrastructure and it allows the identification of the possible atomic ordering down to the atomic scale.

Real space defect	$\longleftrightarrow$	**Diffuse scattering**
Point (0D); Vacancies	.....	3D undefined and anisotropic
Line (1D); Dislocations	.....	2D planes $\perp$ to line defect direction
Planar (2D); Stacking Faults	.....	1D stripes $\perp$ to planar defect directions
Bulk (3D); Intergrowth	.....	0D additional intensities

Table 2.7.1: Relations between the dimensionality of the defects present in a solid with an instance of each one and the related diffuse scattering in the ODS.

Apart from the distribution of the scattering power related to the 3D periodicity of a crystal, diffuse scattering may appear in the ODS. This occurs when the periodicity of the crystal is not fully maintained, thereby non-periodic atomic defects emerge due to, for example, growth or working conditions of the material. Such description of solids is generally referred as **disorder**. Table 2.7.1 shows the different relationships between the dimensionality of the disorder with an example of each and its related diffuse scattering in the ODS [12]. An excellent review from a historical perspective for disorder characterization using different radiations is available by Thomas R. Welberry and Thomas Weber [129], and a useful review paper has been recently published by Enrico Mugnaioli and Tatiana Gorelik for further details on how to interpret and deal with 3D ED data for such analyses [130].

Defects of the crystal periodicity are always encountered in crystals, although most of the times are not significantly strong or the illumination by the electron beam can be adjusted to avoid their effect

on the acquired patterns. However, the characterization of them is necessary to fully understand the atomic structure of the material under study. The most encountered type of defects are 2D planar defects. These kinds of defects mostly appear in layered structures during their growth and a difference needs to be made between intergrowth of similar crystal phases and stacking disorder [131]. Generally, building-blocks are considered and their stacking is what produces the diffuse streaking in the ODS. These blocks can be different crystal structures (intergrowth) or the same crystal phase but shifted along the crystallographic directions perpendicular to the stacking direction [132]. In electron diffraction, the diffuse scattering can be modelled according to these building-blocks that are identified from averaged structure determinations from 3D ED data or HRTEM images, and simulated, for example, through the *DISCUS* program [133]. Then, the proposed models can be evaluated by the comparison of the simulated patterns with the corresponding sections obtained from the reconstructed ODS of a 3D ED dataset [134, 135]. An example of this characterization approach is the disorder analysis on the RUB-5 layer silicate carried out by Krysiak et al. [22].

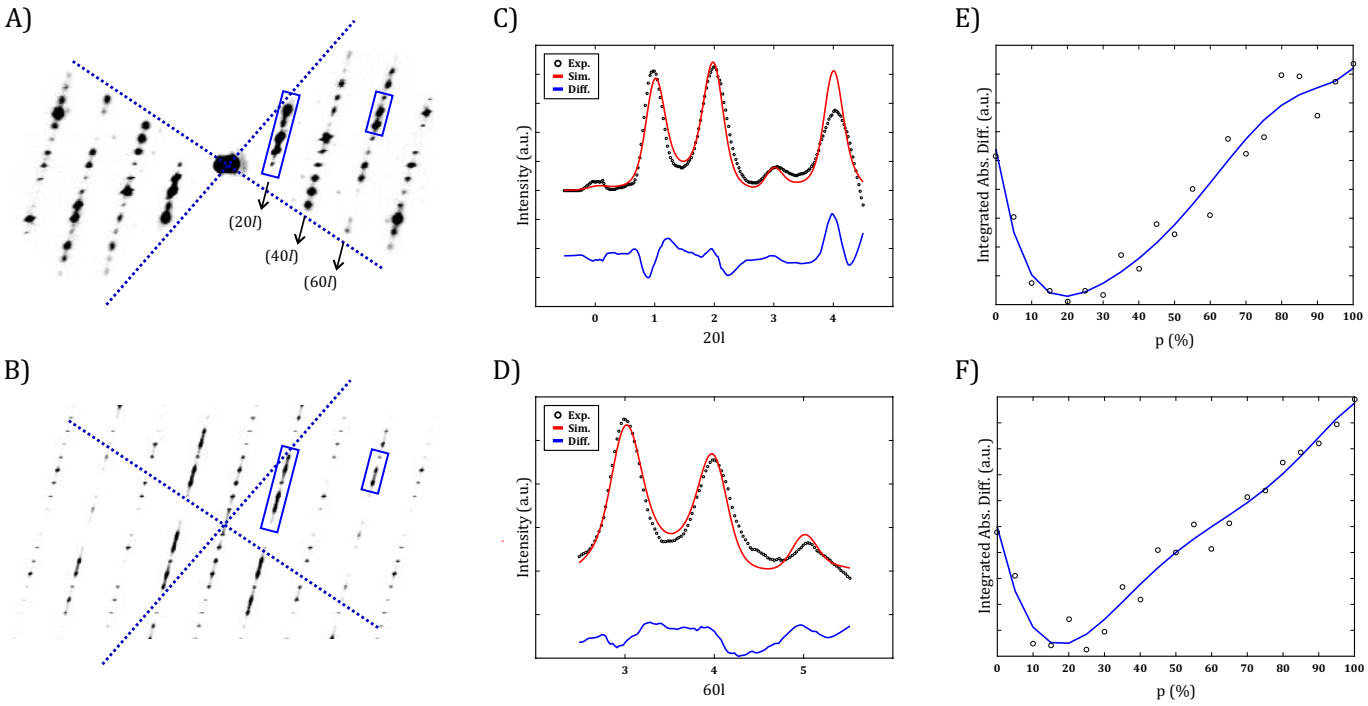

Figure 2.7.2: A) $h0l$ section of the reconstructed ODS of a RUB-5 particle and B) simulated diffraction pattern of the disordered model. C) and D) are intensity profiles of the two blue rectangles marked in A) and B) that correspond to the $20l$ and $60l$ rows. The black profile belongs to the experimental data, the red one to the simulated and the blue one is the difference. E) and F) are plots of the integrated absolute difference between the simulated and experimental profiles with respect to the probability of the layer stacking, which belong to the $20l$ and $60l$ rows, respectively. Figure courtesy of Dr. rer. nat. Yaşar Krysiak from the Czech Academy of Sciences in Prague.

Due to the layered nature of RUB-5, the growth of these crystals tends to have stacking disorder, which means that, for instance, one structural layer could crystallized three or four times along the stacking direction but the next one turns out to be a different layer. Such crystalline growth is probabilistic and, since electron diffraction is acquired with beam sizes between 50 nm to 400 nm, the

resulting patterns are related to an average of a large number of unit cells, which is a perfect scenario to analyse disorder effects. In this case, three different layers (called α, β and γ) were identified and two probabilities were evaluated.

First of all, the disorder modelling was carried out only as a function of the stacking probability of α and γ layers, p_y. This resulted in a probability of around 0.05 for the stacking of γ layer on top of α layers and facilitated the modelling only focusing on α and β layers. Figure 2.7.2 shows the intensity profile analysis for the $20l$ and $60l$ rows of the [010] zone-axis pattern based on the stacking probability of the β layer on top of the γ layer. Here, simulated diffraction patterns are obtained by modelling a particle in which the probability of the presence of layer α is $(1 - p_x)(1 - p_y)$, layer β is $p_x(1 - p_y)$ and layer γ is p_y. In this case, p_y was fixed to 0.05 and p_x was modified in 0.05 steps in order to find the simulated intensity profile that fits best to the experimental ones. Both analysis on these diffuse lines resulted in a p_x of 0.20(5) and 0.25(5) for $20l$ and $60l$, respectively, and demonstrated the possibility of quantitative disorder analysis of the disorder with such routines. Further modelling details, structure analysis and crystallographic description can be found in the paper of Krysiak et al. [22].

Nevertheless, when the layer stacking has a real random behaviour, the result is illustrated in Figure 2.7.3. In this case the projection of the reconstructed ODS along the stacking direction (Figure 2.7.3A) shows a 2D lattice related to the periodicity of the layer itself. When projections are obtained through the in-plane axes of the layer (Figures 2.7.3B and 2.7.3C), intensity rows without sharp reflections are visualized, which only come from the strong diffuse scattering. In other words, the material is composed by unit cells that are periodically distributed as a plane that forms the layer, but the periodic arrangement in the third spatial dimension is non-existent. Effectively, this is considered a stack of 2D crystals.

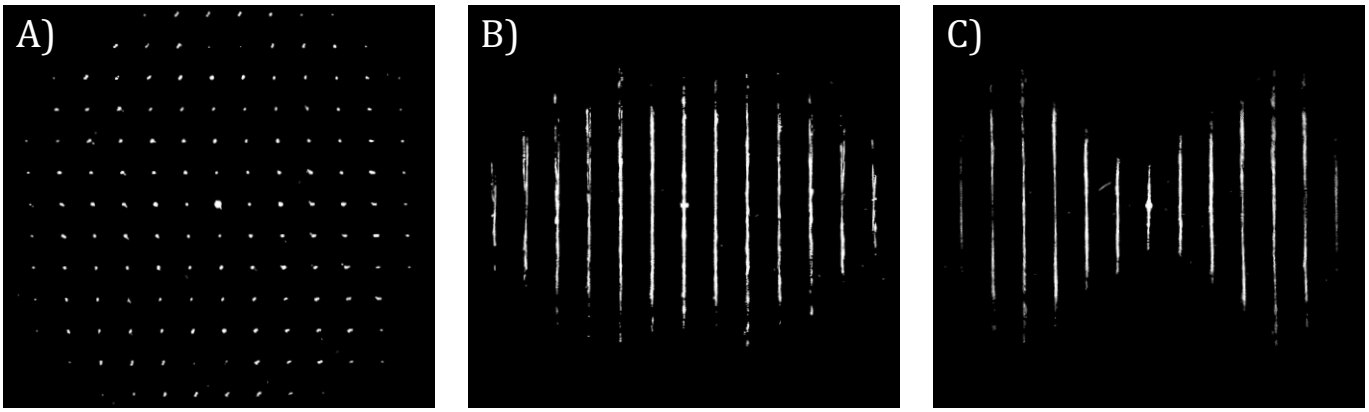

Figure 2.7.3: Projections of the reconstructed ODS of the layer silicate Na^+-magadiite along A) the stacking direction, B) one of the in-plane layer axes and C) the other in-plane layer axes.

Diffraction patterns can also be acquired from materials that are not crystalline. These materials do not have long-range order that characterize crystalline solids, but still retain basic building components without translational symmetry. They are called **amorphous materials**, and their electron diffraction patterns result in wide and diffuse rings that belong to repetitive inter-atomic

pairs through the specimen. An example of an amorphous diffraction pattern from calcium carbonate/calcium hydrogen phosphate is shown in Figure 2.7.4 [136].

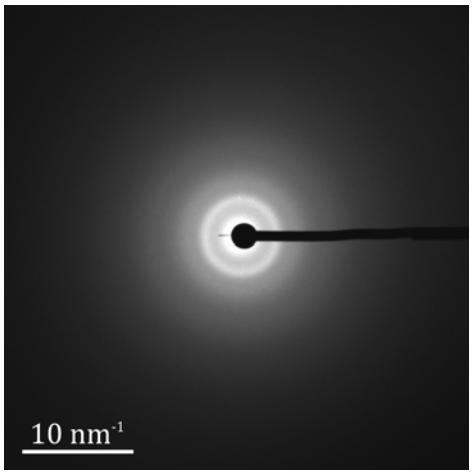

Figure 2.7.4: Amorphous diffraction pattern of calcium carbonate/calcium hydrogen phosphate [136].

2.8 Brief Review of Aperiodic Crystals

After Jean-Baptiste Romé de l'Isle proposed in 1772 that crystals are formed by microscopic building blocks [137], René-Just Haüy shortly afterwards enunciated that each crystal face is uniquely characterized by three rational integers, which he called as *the law of rational indices* [138] and it is currently referred as Miller's indices (equation 2.1.14). Electron diffraction patterns are usually properly indexed by the use of these three *hkl* integer values that result from the periodic arrangement of the atoms along the three dimensions. However, some crystals are not formed following this general rule and their 3D translational symmetry is lost. Disorder is one example of these exceptions where diffuse scattering appears in between Bragg reflections, which is consequence of small or large modifications of the atomic structure inside the unit cell through the whole crystal, as briefly described in the previous section. Another exception to this rule is the case of **aperiodic crystals**.

Aperiodic crystals are solids in which the translational symmetry is lost but their diffraction patterns still consist of sharp and discrete reflections, i.e. problems appear when indexing the reflections with only three integer indices. The first reported questioning about the general validity of Haüy's statement dated back to 1903 by Herbert Smith [139], which was followed by other studies during the XXth century [140, 141, 142, 143, 144, 145, 146, 147, 148]. Three different types of aperiodic crystals can be identified according to their building principles: quasicrystals, incommensurate composite crystals and incommensurately modulated structures [149].

2.8.1 The Different Types of Aperiodic Crystals

Quasicrytals are solids in which its description requires the use of non-crystallographic point symmetries, e.g., five-fold, eight-fold, ten-fold or twelve-fold symmetries, thus a space of higher than three dimensions has to be used in order to properly describe the position of the scattered reflections. The discovery of this kind of materials by Dan Shechtman and collaborators in 1984 [148] led to the Nobel Prize of Chemistry in 2011. The reviews of Walter Steurer or Akiji Yamamoto are acknowledged for further information [150, 151].

Incommensurate composite crystals encompass crystalline solids that are formed by the intergrowth of two periodic structures. An example of such ordering is the case of layered composite crystals in which two chemically different layers are alternately stacked. These sub-systems share a common periodicity along the stacking direction but one of the directions parallel to the layer is incommensurate with respect to the other layer, i.e. an irrational number of unit cells is needed to retrieve the periodicity along this direction. The atomic arrangement of these crystals result in diffraction patterns that contain strong reflections surrounded by weaker reflections that cannot be indexed by the three Miller indices of the two sub-systems. These reflections are called **satellites** [141]. This is different to the disorder case of RUB-5 shown in the previous section because the building blocks maintain the unit cell periodicities along the directions within the layer planes, hence satellites do not appear.

The third kind of aperiodic crystals are the incommensurately modulated structures. These are characterized by a translational periodic average structure that can be determined by ignoring the satellites, yet the true atomic positions in the crystal are defined by **modulation functions**. In this

way, the averaged structure and the atomic positions modulated by special functions recover a perfect long-range order but without 3D translational symmetry. It is worth to note that displacement parameters and atomic modulations are different physical effects of the atoms inside the crystal structure, since the former are considered time-dependent shifts caused mostly by temperature inside one unit cell, and the latter represent periodic displacements across the material with a period of an incommensurate number of cells.

2.8.2 How to Understand Incommensurate Modulated Structures

Diffraction patterns that exhibit satellite reflections need to use the concept of superspace, a (3+d)D space, in order to properly fit all observed reflections and recover the translational symmetry [147, 152]. In this context, new reciprocal base vectors called **modulation wavevectors**, $\vec{q}$, have to be introduced that are defined from the 3D unit cell reciprocal basis vectors. Generally,

$$\vec{q} = \alpha\vec{a^*} + \beta\vec{b^*} + \gamma\vec{c^*}$$

where α, β and γ are coefficients that define the modulation wavevector and at least one of them has to be irrational to fulfil the property of incommensurability, otherwise a supercell can be selected to index all reflections. Because the intrinsic nature of an experiment cannot distinguish between rational and irrational numbers, a structure is considered to be incommensurate if the denominator of the rational approximation of at least one of the coefficients of the modulation wavevector is large enough [153]. In this way, satellites are located at $\pm m\vec{q}$ distance from the main reflections and, in principle, there is no limit to the number of modulated wavevectors required to index all reflections that, at the same time, determine the number of extra dimensions in the superspace. m is an integer number that defines the order of the satellites for a given $\vec{q}$ and its maximum, m_{max}, is set according to the observable satellite intensities in the diffraction dataset. Satellites up to the 9th order have been found, but these are extremely exceptional cases [154].

Once the modulation vectors have been defined, any reciprocal lattice vector in the constructed superspace is described as

$$\vec{g}_s = \sum_{k=1}^{3+d} h_{s,k}\vec{a^*}_{s,k}$$

where d is the additional number of dimensions added to index all reflections and $\vec{a^*}_{s,k}$ are the reciprocal basis vectors of the reciprocal superspace Σ^* that are mathematically defined as

$$\Sigma^* = \begin{cases} \vec{a^*}_{s,i} \equiv (\vec{a^*}_i, 0) & i = 1,2,3 \\ \vec{a^*}_{s,3+j} \equiv (\vec{q}_j, \vec{b^*}_j) & j = 1,...,d \end{cases}$$

where $\vec{a^*}_{s,i}$ describe the reciprocal lattice basis in the 3D space and $\vec{a^*}_{s,3+j}$ the additional basis defined from the 3D space and the extra components $\vec{b^*}_j$ of the reciprocal superspace, which are perpendicular to the 3D space. Figure 2.8.1 shows a sketch of Σ^* for a 1D incommensurately modulated structure. Since it is not possible to physically draw a 4D space in a 2D plane or 3D volume, the 3D space that belongs to the ODS is folded in a line while the extra dimension is shown perpendicular to this line. In this way, when a diffraction experiment is carried out, it can be interpreted that the position of each reflection is projected into the 3D space along the directions defined by $\vec{b^*}_j$ in the reciprocal

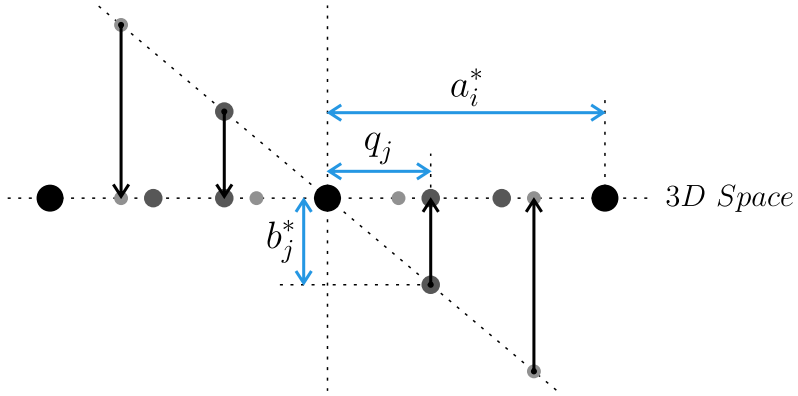

Figure 2.8.1: Sketch of the reciprocal superspace interpretation of a (3+1)D incommensurately modulated structure. The dashed line labelled as "3D Space" represents the projection of the 3D ODS into a line. The vertical line represents the extra dimension that defines the reciprocal superspace. The ODS of such structures is interpreted as the projection of the reciprocal superspace into the 3D reciprocal space along $\vec{b^*}_j$. q_j is the modulus of the modulation vector along $\vec{a^*}_i$ in the 3D reciprocal space. Dark grey spots represent first order satellites and light grey ones to the second order satellites.

superspace. Then, the definition of a reciprocal lattice vector in the ODS introduced in this chapter can be extended to include the possible modulation of a crystal structure as

$$\vec{g} = \sum_{k=1}^{3+d} h_k \vec{a^*}_k$$

where $\vec{a^*}_k$ are $\vec{a^*}$, $\vec{b^*}$, $\vec{c^*}$, $\vec{q}_1$, ..., $\vec{q}_d$.

At this point, the superspace in the "real" space can be obtained by bringing the reflection intensities and positions from the 3D reciprocal space to the reciprocal superspace, and applying the inverse Fourier transform to retrieve the electrostatic potential or electron density in the "real" superspace.

$$\rho_s(\vec{r}_s) = \frac{1}{\Omega} \sum_{\vec{g}_s} F(\vec{g}_s) \exp(-2\pi i \vec{g}_s \vec{r}_s)$$

where Ω is the volume of the unit cell in the real 3D space. To visualize the obtained potential, a similar approach to Figure 2.8.1 has to be followed, which is shown in Figure 2.8.2. The positions of the basis vectors $\vec{a}_1$, $\vec{a}_2$ and $\vec{a}_3$ from the real 3D space have to be identified in real superspace with respect to the extra-dimension vectors. If the example of Figure 2.8.1 is followed in such a way that the modulation wavevector $\vec{q}$ is only along $\vec{a^*}_{s,1}$, $\vec{a}_{s,4}$ is perpendicular to $\vec{a}_1$, and the superspace axis $\vec{a}_{s,1}$ is rotated with respect to $\vec{a}_1$ according to the component α of the modulation wavevector as $\tan(\vec{a}_{s,1}, \vec{a}_1) = \alpha/|\vec{a}_1|$. In other words, the modulation wavevector defines the orientation of the real 3D space inside the real superspace. This construction scheme can be followed for a general case of a modulation vector with components α, β and γ as the related extra dimension is defined perpendicular to the whole 3D reciprocal space [155].

One important consequence of the superspace concept is that atomic positions are not defined by a fixed location in space, instead they are understood as domains that are expanded along the introduced extra dimensions, the so-called **atomic domains** [155]. Each one is described as

$$
\begin{aligned}
x_i &= \bar{x}_i + \sum_{w=1}^{d^2-1} u_{w,i}(\bar{x}_{s,4}, ..., \bar{x}_{s,(d+3)}) \\
\bar{x}_i &= x_i^0 + l_i \\
\bar{x}_{s,j} &= t + \vec{q}_k \vec{r} \quad ; \quad j = 4, ..., (d+3) \\
\vec{q}_k \vec{r} &= \alpha_k \bar{x}_1 + \beta_k \bar{x}_2 + \gamma_k \bar{x}_3 \quad ; k = 1, ..., d
\end{aligned}
$$

where x_i^0 are the fractional atomic coordinates in the first unit cell, l_i are integers defining the lattice vectors in the real 3D space, $u_w(\bar{x}_{s,j}, ..., \bar{x}_{s,d})$ are modulation functions with period 1 that fit to the shape of the electrostatic potential along the extra dimensions, t is the initial phase of these functions and $\vec{r}$ is a vector with coordinates $\bar{x}_i$. The above expression includes $d^2 - 1$ modulation functions to consider the possibility of inter-modulations between different modulation waves.

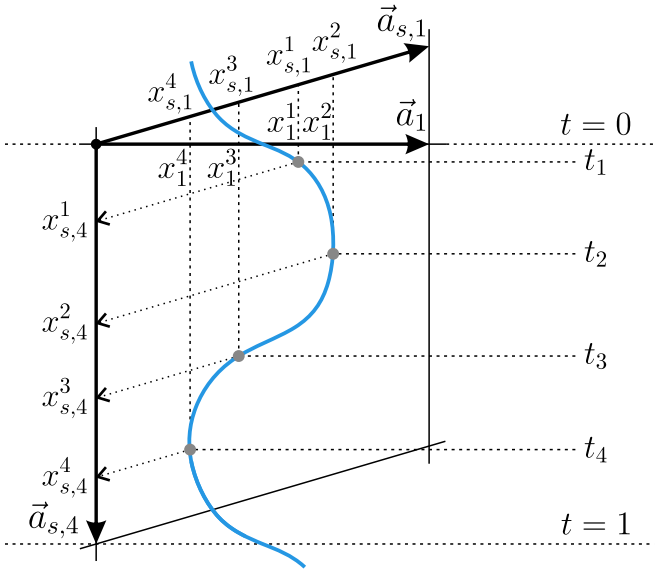

Figure 2.8.2: Sketch of a ($x_{s,1}$,$x_{s,4}$) de Wolff section of the superspace representation for a given atomic domain. $\vec{a}_1$ is the basis vector $\vec{a}$ of the 3D unit cell. $\vec{a}_{s,1}$ and $\vec{a}_{s,4}$ correspond to two basis vectors of the superspace unit cell. The blue curved line represents the domain of a given atom in the superspace from which four positions with their related superspace coordinates ($x^i_{s,1}$, $x^i_{s,4}$) are shown. The horizontal dashed lines labelled as t_i correspond to the different 3D sections of the superspace that retrieve the aperiodic 3D representation of the given atom with its related different x^i_1 positions.

The most common modulation applies to the position of the atoms, which is generally referred to as **displacive modulation**. Nevertheless, in some cases atomic occupancies and even atomic displacement parameters can be modulated, the so-called **occupational** and **thermal modulation**, respectively. Since most structural modulations are continuous and the number of parameters is finite,

truncated Fourier series are frequently used in order to properly describe the satellite intensities. Such series for a 1D modulation would be

$$\vec{u}(\bar{x}_{s,4}) = \sum_{i=1}^{n} \vec{A}^i \sin(\bar{x}_{s,4}) + \sum_{i=1}^{n} \vec{B}^i \cos(\bar{x}_{s,4})$$

where $\vec{A}^i = (A_1^i, A_2^i, A_3^i)$ and $\vec{B}^i = (B_1^i, B_2^i, B_3^i)$. At first approximation, the satellite intensities of order m can be determined by the Fourier components up to the same order [156]. Stronger modulated structures may need discontinuous functions to correctly fit the electrostatic potential, and in these cases functions such as crenel and sawtooth functions are used that exist in an interval of $x_{s,4}$ defined as $(x_{s,4}^0 - \Delta/2,\, x_{s,4}^0 + \Delta/2)$ where $\Delta < 1$ [157].

Figure 2.8.2 shows an example of an atomic domain following a harmonic function along the extra dimension $\vec{a}_{s,4}$ in a $(x_{s,1},\, x_{s,4})$ section of the superspace, also known as de Wolff section, from which each 3D section of the superspace at the different modulation phase t between 0 and 1 corresponds to a possible aperiodic 3D unit cell. As seen in this figure, the translational symmetry is recovered in the superspace, thus the resulting potential is periodic as well and a superspace symmetry can be derived. In this context, the symmetry is investigated by the observation of possible systematic extinctions in the diffraction patterns including the satellite reflections, and superspace groups can be identified following the guidelines described by Sander van Smaalen in his book "Incommensurate Crystallography" [149] or through the tables available in the "Incommensurate and Commensurate Modulated Structures" section of the International Tables for Crystallography vol. C [54]. De Wolff sections are also used in order to check that the selected symmetry together with the modulated functions properly follow the retrieved potential in the 2D section of the superspace.

As it has been shown above, the 3D translational symmetry has been lost due to the introduction of a modulation wavevector that contains at least one irrational coefficient. Although the translational symmetry is lost along the direction parallel to $\vec{q}$, it is worth to comment that the perpendicular directions to the modulated wavevectors may still retain the 2D translational symmetry. For instance, if only one modulation vector is present and it is only directed along $\vec{a}_2^*$, the plane composed by $\vec{a}_1$ and $\vec{a}_3$ in real 3D space will have 2D translational symmetry. This is an important point to take into account when modulated crystal structures are physically described.

Chapter 3

Quasi-Parallel PED-STEM

Untersuchung und Beobachtung,
Philosophie und Erfahrung dürfen
nie einander verachten noch ausschließen.
[Investigation and observation, philosophy and experience, must neither despise nor exclude one another.]

Vom Kriege *[On War]*
Carl von Clausewitz

The previous chapter has introduced the basics of the diffraction phenomena in a general way, how a transmission electron microscope works, the available methods to acquire electron diffraction patterns, and the different kind of patterns that can be obtained according to the illumination and the material under study. Here, the focus is directed to the alignment of the TEM for the best illumination settings to acquire electron diffraction data from small ROIs. The chapter provides a set of manufacturer-independent procedures to align a quasi-parallel beam while the TEM is operated in scanning mode, the so-called **quasi-parallel STEM**. Furthermore, a novel alignment of a precessed electron probe in STEM is proposed, from which the coupling of quasi-parallel STEM with precession is shown to get the TEM ready for optimum acquisitions of electron diffraction patterns, a preferred electron illumination referred to **quasi-parallel PED-STEM**. These new alignment methods have been tested on different microscopes and the resulting electron beams have been characterized to show their effectiveness and feasibility.

3.1 TEM vs STEM

The two main operation modes of modern (S)TEM microscopes are mainly distinguished by the way the images are formed. While TEM mode is based on a spread beam that illuminates the whole area of interest, and an image is formed at the detector plane when the projector system is in image mode, STEM mode uses a focused beam to scan the selected area of the sample, and the image is formed by the intensity integration of the primary beam and/or scattered beams from the resulting diffraction pattern at each scanned position.

Both available modes are used for high-resolution imaging. FEG electron sources and optimized pole piece geometry enable scientists to acquire high-resolution images in a routine basis. STEM-HAADF may be beneficial in some specimens when elemental contrast is needed to properly distinguish, for instance, different layers of multi-layer systems or different shells in nanoparticles. In other samples, TEM may be better to visualize stacking faults and grain boundaries by means of dark field imaging or under two-beams condition.

The traditional application difference between TEM and STEM is when spectroscopic or diffraction-based experiments are carried out. The usual STEM illumination setting is based on highly convergent probes that result in high beam currents. This condition facilitates the acquisition of EDS and EELS single-spectra as well as spectrum maps with highly resolved features. The most impressive works include 3D reconstructions of atomic distribution in nanostructures [158, 159], compositional maps at the atomic scale [160], EELS spectroscopic tomography [161] or 3D reconstructions of oxidation states in nanoparticles [162]. On the other hand, diffraction-based experiments are performed most of the time with the microscope in TEM mode. Using the conventional SAA for SAED or, if available, the low-convergent illumination options for NBED, allows an easy and routine check of specimen crystallinity as well as fine crystallography analyses, such as *ab initio* structure determination of a huge variety of materials [163, 164, 165, 166], disorder analyses [131] and even the localization of hydrogen atoms [167] or the determination of absolute structures [168]. When high-convergent beams are considered, CBED or large convergence angle CBED (LACBED) patterns are also frequently acquired. In this case, the analysis of Kossel-Möllenstedt (non-overlapped diffraction disks) and Kossel (overlapped diffraction disks) patterns enable the determination of the crystal symmetry and, in some instances, the thickness and the direct lattice-strain of the illuminated area [76]. Furthermore, the use of defocused Kossel patterns acquired in LACBED conditions proved to be very valuable to the identification of line and planar defects such as dislocations and grain boundaries [169]. Although all the aforementioned works are based on the acquisition of diffraction data in TEM mode, it does not mean that they could not be done in STEM mode. In fact, the same results can be obtained in STEM mode because they rely on the quality of the acquired diffraction patterns.

A diffraction-based application in which STEM is implicitly used is 4D-STEM. Briefly, the low-convergent probe is scanned over a ROI and a diffraction pattern is stored for each beam position instead of its integrated intensity in STEM detectors. Different processing tools applied to the available patterns can result in phase, orientation and/or strain maps. Since this application needs the availability of quasi-parallel options, the microscope is usually kept in TEM mode. In this way, the projector system is switched to diffraction mode, an external optical camera placed at the binocular position is used for pattern acquisition and an external scanning generator is connected to the

deflector and image coils to raster the beam [170, 171]. Therefore, the microscope is explicitly operated in TEM mode but the data acquisition is implicitly performed in STEM mode. During this last decade, technological advances have been made towards the development of fast and sensitive cameras using complementary metal–oxide–semiconductor (CMOS) technology for direct electron detection, or intermediated by a scintillator and an optical fibre plate, which triggered the increased commercialization of hardware setups focused on 4D-STEM acquisitions [172]. As a consequence, TEM manufacturers are pushed to provide default quasi-parallel illumination options with the microscope in STEM mode.

It is not only the technological push that brings quasi-parallel STEM to the stage, but also its intrinsic advantages for diffraction-based experiments with respect to TEM mode. It permits a fast and clear visualization of tiny or layered crystals using low electron doses, reduces the beam damage for crystal imaging, provides an easy pin-point to check the crystallinity of different parts of the sample, and avoids lens hysteresis effects because the projector system does not need to switch between imaging and diffraction mode. Furthermore, the scanned image does not suffer from the aberrations of the projector system and the positioning of the electron beam on the specimen plane is highly accurate, a feature technically called *beam registration* [173]. STEM mode is also of benefit for external equipment solutions because it activates and de-activates some of the electronic filters at the coil driver boards and it allows the transmission of external high-frequency signals without much interference. For single diffraction pattern acquisitions, NBED is used instead of SAED, which avoids the mechanical insertion of the selected area aperture and enables the full software control of the measurements for enhanced speed and ease of use.

3.2 Quasi-Parallel STEM: Available Options

The aim of using a quasi-parallel beam in STEM mode is to have an illumination setting ready to acquire scanned images and diffraction patterns without strongly changing the lens strengths. Since the minimum size of a low convergent angle beam is limited by the diffraction of the CA, the lateral resolution of the scanned image is intrinsically worse than using a high-convergent beam. This can be seen in Figure 2.4.2 of the previous chapter where the minimum probe diameter below 10 mrad is diffraction-limited; thereby, the higher the convergence angle in this regime, the higher the attainable lateral resolution before the spherical aberration becomes stronger. Thus, a compromise has to be reached between lateral (beam size) and angular resolution (two times the convergence angle) that allows to clearly identify the desired feature in the scanned area in order to position the beam for diffraction and avoids reflections overlap.

Mode	**Spot Size**	**Alpha**	**CL1 (A)**	**CL2 (A)**	**CM (A)**	ϕ_{beam} **(nm)**	α **(mrad)**
CBD[a)]	5 nm	1	2.39	2.76	5.41	3.58 ± 0.05	0.82 ± 0.01
CBD[a)]	5 nm	2	2.31	2.68	4.74	3.40 ± 0.05	0.85 ± 0.01
CBD[a)]	5 nm	3	2.23	2.58	4.06	3.31 ± 0.05	0.94 ± 0.03
CBD[a)]	5 nm	4	2.16	2.50	3.39	3.39 ± 0.13	1.09 ± 0.01
CBD[a),b)]	5 nm	5	2.08	2.42	2.63	3.50 ± 0.20	1.27 ± 0.03
CBD[b)]	5 nm	6	2.01	2.33	2.03	3.60 ± 0.26	1.41 ± 0.10
CBD[b)]	5 nm	7	1.94	2.23	1.35	3.92 ± 0.33	1.57 ± 0.02
CBD[b)]	5 nm	8	1.86	2.14	0.68	4.57 ± 0.36	1.67 ± 0.01
CBD[b)]	5 nm	9	1.79	2.04	0.00	5.43 ± 0.52	1.69 ± 0.01
CBD[b)]	3 nm	9	1.95	2.23	0.00	3.71 ± 0.22	1.70 ± 0.01
CBD[b)]	2 nm	9	2.12	2.41	0.00	2.69 ± 0.18	1.68 ± 0.02
CBD[b)]	1 nm	9	2.44	2.69	0.00	1.71 ± 0.04	1.62 ± 0.02
CBD[b)]	0.5 nm	9	3.11	2.88	0.00	1.28 ± 0.12	1.64 ± 0.01
TEM	5	1	1.87	2.02	4.50	8.81 ± 0.57	0.94 ± 0.01
TEM	5	2	1.87	2.02	3.16	6.84 ± 0.11	1.17 ± 0.01
TEM	5	3	1.87	2.02	2.63	6.35 ± 0.25	1.33 ± 0.01

Table 3.2.1: The minimum beam diameter ϕ_{beam} and convergence angle for different condenser system settings in the JEOL 2100 LaB_6 with a 10-µm CA. *Mode*, *Spot Size* and *Alpha* are the settings available in the user interface of the microscope in the TEM operation mode. The measurement error for CL1, CL2 and CM currents is ± 0.01 A in all cases.
[a)] condenser setting available as well in *NBD* mode. [b)] condenser setting available as well in *EDS* mode.

A condenser system with three lenses is the foremost requisite in order to set a small and low convergent probe. That system can consist of two CLs and one CM or three CLs. Microscopes designed during the decades of 1990 and 2000 started to have the 2 CLs + 1 CM configuration and TEM manufacturers provide several illumination settings. In the case of JEOL, some of these microscopes are the 2100, 2010 or the ARM200F. For the former two, a variety of default beam illuminations is available in TEM mode, which are called by the following acronyms: *TEM*, *CBD*, *EDS* and *NBD*. TEM is the basic operation mode of the microscope with three different alphas or convergent angle

settings and five spot sizes that allows an easy and extended illumination of the sample ROI. CBD is the Convergent Beam Diffraction mode that allows to select nine different alphas and five spot sizes. This mode was proposed by Michiyoshi Tanaka and co-workers for JEOL microscopes in order to have an illumination system that easily allows the change of the convergence angle while keeping the same probe size on the specimen [174]. NBD and EDS modes consists of illumination settings already implemented in the CBD mode. EDS contains the last five alphas of the CBD mode, while NBD has the first five alphas. In both cases, the same five selectable spot sizes are available. JEOL designed it in this way so that the user would select the EDS mode for more convergent beams for the acquisition of EDS signals, i.e. higher electron dose, and the NBD mode for the acquisition of diffraction patterns with low convergent angles but small spot sizes. The high number of settings available in the CBD mode was thought to confuse the non-experienced user and they decided to implement the easier accessibility to these sub-modes to facilitate the use of the microscope for the different kind of measurements. Table 3.2.1 shows the different beam settings of the JEOL 2100 LaB_6 according to the selected mode, spot size and alpha. In the case of the ARM200 series, the available options while working in TEM are equivalent but with different naming. The main difference is that the *TEM* mode consists of two sub-modes called *S* and *L* that are designed to illuminate small or large areas and have a lower and higher convergence angle, respectively. Five spot sizes are selectable for both sub-modes. *NBD* and *CBD* are also available under the *Probe* mode with six different spot sizes but only one convergence angle option in each case. Unfortunately, when these microscopes are switched to STEM mode there are different selectable probe sizes only with the most convergent probe option (CBD Alpha 9 - CM deactivated).

In the case of FEI, the most known and sold microscopes are the Tecnai series. These ones provide two convergence angle options with 11 different spot sizes each one, called *Microprobe* and *Nanoprobe* for low (CM deactivated) and high (CM activated) convergence angles, respectively. STEM mode comes with the exact Nanoprobe mode by default but the Microprobe has to be purchased apart.

Modern TEMs, such as the JEOL Grand ARM and NeoARM or the Thermo Fisher Themis and Spectra, are built with 4-lens condenser systems that include three CLs and one CM. This flexible probe-forming system allows an independent control over the probe size and the convergence angle from which a variety of default illumination settings is provided in both TEM and STEM modes. A quasi-parallel beam in these TEMs is obtained by high excitation of the CM. This is not a problem for most samples but it could be for magnetic samples because of the magnetic field generated by the CM, even when the OL is off. In this way, a quasi-parallel probe set only by the 3 CLs would be of particular interest for diffraction measurements on magnetic materials. However, most laboratories do not have cutting-edge TEMs and the STEM mode is limited to the convergent setting or the available quasi-parallel option, which may not be optimized for diffraction experiments. For these reasons, a microscope-independent alignment method is needed in order to set a quasi-parallel illumination in STEM mode that fits best the desired diffraction experiment with the available scientific tools.

3.3 Quasi-Parallel STEM: the Universal Alignment

The quasi-parallel STEM mode has been described and reported previously under different acronyms such as NBD-STEM [175] or D-STEM [176], but always focusing on specific TEM columns and not aiming at generalizing the method to other microscopes. Voyles et al. [177] studied medium range order in amorphous silicon by developing the quasi-parallel STEM in a JEOL 2010F FEG with an analytical resolution pole piece (ARP). They reported probe sizes from 0.9 to 5.2 nm at 0.5 mrad of convergence obtained by strong excitation of both CL1 and CM. Alloyeau et al. [175] controlled the STEM illumination on a JEOL 2100F FEG with a high-resolution pole piece (HRP) to produce probes of 1 to 2 nm at less than 1 mrad of convergence in order to study CoPt nanoparticles. Their method modified CL2 and CM to place the beam above the ffp of the pre-OL for levelled minimization of both probe size and convergence angle. Ganesh et al. [176] set their D-STEM on a JEOL 2010F FEG with an ultra-high resolution pole piece (UHRP) and achieved similar lateral and angular resolutions to those of Alloyeau et al. Furthermore, they provided a workflow for implementation of the method, but with no reference to general tests on other microscopes. Yi et al.[178] used a FEI Titan probe-corrected and operated at 200 kV, which includes 3 CLs, the CEOS aberration corrector and a CM, to obtain a probe of 1.5 nm at 1 mrad of convergence with the corrector in neutral state. Unfortunately, capabilities of this illumination system for CM variation were not explored. Panova et al. [179] reported the use of 4D-STEM to localize crystalline regions in polymer blends using the Microprobe setting in STEM mode on a FEI Titan probe-corrected at 300 kV with the corrector deactivated, which yielded a 7 nm probe at 0.5 mrad. Unfortunately, they did not describe any special alignment method to control the illumination.

In the context of this doctoral work, a universal alignment method is proposed to obtain a quasi-parallel electron probe, given that the microscope has the following minimum requisites:

1. Condenser system with either 2 CLs and 1 CM or 3 CLs (or CM not active if present).
2. A 10 to 30 μm CA.
3. A software or hardware module that allows free user control of the microscope lens currents (condenser, objective and projector lenses).
4. Computer storage and loading capabilities of tuned lens and coil values.

Smaller CA sizes than 10 μm, although not tested in this work, are considered not suitable for quasi-parallel diffraction work due to the extreme low probe current, which would yield noisy diffraction patterns for non-direct detection cameras and would not even be advantageous in terms of lateral resolution.

The lateral resolution during the alignments is retrieved from an image of the electron probe obtained by switching the projector system to image mode at a high magnification. A 2D Gaussian is fitted to the image of the beam and its variance in x and y (σ_x^2 and σ_y^2) are used to calculate the full-width at half-maxim (FWHM $= 2\sigma\sqrt{2\ \ln 2}$, being σ the average of σ_x and σ_y), which is considered the beam probe diameter, hence approximately the lateral resolution in STEM. Other definitions of image resolution are available in transmission electron microscopy to define the minimum resolvable distance,

for instance, by the use of Rayleigh's criterion or the point resolution or information limit of the phase contrast transfer function of the OL. Since here the interest is to resolve different nanometre-sized areas but also to diffract these parts without reflection overlapping, it is more appropriate to use the beam probe diameter as the indicator of the resolution, i.e. a **spatial diffracting resolution**. On the diffraction space, the angular resolution is obtained by a Gaussian fitting on an intensity line profile from a non-saturated reflection of a diffraction pattern. Such pattern is acquired from a highly crystalline material to minimize any other effect that could modify the shape of the reflections.

For generalization of the alignment procedure, two cases have been considered depending on the availability or absence of the CM in the condenser system of the TEM. These two different approaches have been tested on a JEOL 2100 LaB_6 operated at 200 kV with a 4-lens condenser system (3 CLs and 1 CM) and a HRP. The first setup was a condenser system with CL1, CL3 and CM (CL2 deactivated) and the second one with all CLs activated and CM switched off, realized by using the available free lens control module of the microscope user interface.

3.3.1 Condenser Systems with CM

First of all, the electron beam has to be aligned in the high-convergent STEM mode with the scanning stopped and the CM at zero excitation, otherwise the beam could move away from the fluorescent screen during the rest of the quasi-parallel STEM alignment. Considering that the eucentric height is found based on the standard OL value in TEM mode, the conventional alignment to have a concentric and centred movement of the beam is performed in STEM mode. This ensures that the beam is following as much as possible the optic axis. For OL current values that give rise to beam focus above and below the specimen plane, the spot and bright coils are used to shift the focused beam and the caustic image to the same position, respectively, so-called *bright tilt/shift method*. The caustic image in a TEM is a bright spot that corresponds to the projection of the electron probe surrounded by a bright envelope, which is generated by the interference of electron rays deviated from the ideal conditions due to the aberrations of the lenses.

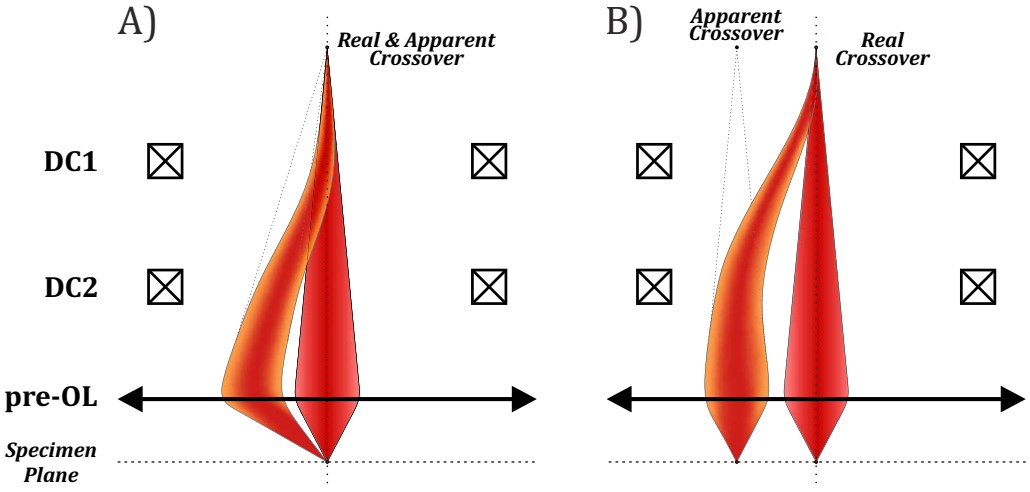

Figure 3.3.1: Sketch showing the A) tilt and B) shift of the electron beam by means of the deflector coils. Orange-contoured beam represents the beam when the function of the coils is applied with respect to the red beam. The CM is omitted for simplification.

Figure 3.3.1 shows the difference between tilt and shift of an electron probe in a TEM. The beam tilt is achieved by deflecting the beam in such a way that the apparent crossover and the real crossover come from the same point, while the beam shift brings the apparent crossover shifted the desired amount with respect to the specimen plane. The bright tilt/shift procedure is iterated until probe and caustic image are formed at the same place of the fluorescent screen and then the OL current is changed back to the standard one. This adjustment is done with the projector system in image mode at 20K of magnification and the projector and deflector coils are initially neutralized.

The alignment for non-zero values of CM follows by activation through the free lens control module. Initially, the largest spot size is chosen (low excitation of CL1) and CA is removed for enhanced illumination on the fluorescent screen. Then, the convergence-controlling CM current is increased by up to 1 Ampere (A), and the bright tilt/shift method is performed once again for correct beam centring. The process is iterated while increasing the CM excitation in order to reduce beam convergence and maintain an aligned beam.

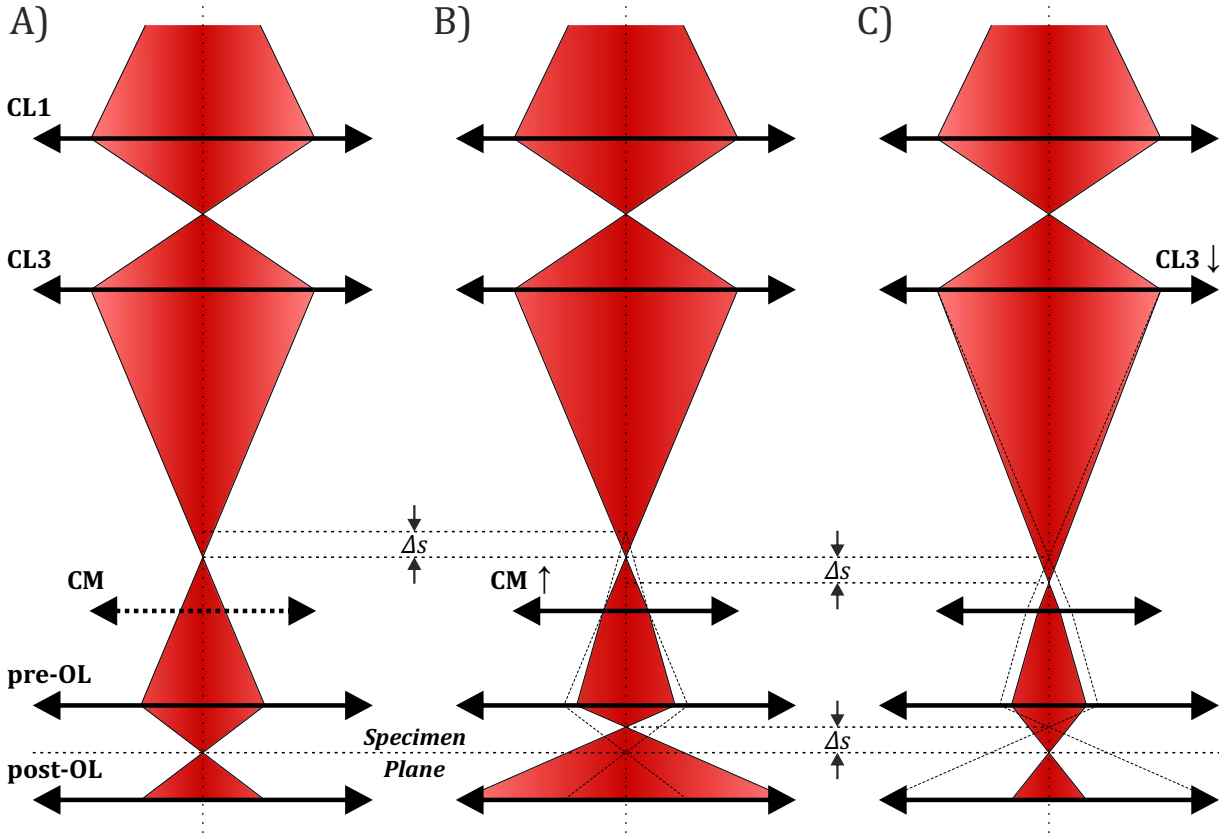

Figure 3.3.2: Ray diagrams for a condenser system with 2 CLs and 1 CM during the alignment of a quasi-parallel probe. A) corresponds to the default ray trajectories in high-convergent STEM with CM deactivated, B) is the ray diagram during the alignment of the quasi-parallel beam in which the CM is switched on and its current increased, and C) is the setting for quasi-parallel STEM. Dashed lines in B) represent the ray trajectories without CM activated, and the ones in C) show the ray trajectories of B).

The bright tilt/shift method will become less effective beyond a range of CM values and the beam centring must be performed with the *HT modulation* or the *condenser/objective alignment* traditionally used in TEM mode. This consists in the activation of the HT wobbler (Rotation centre in Thermo Fisher microscopes), the adjustment of the tilt capability of the DCs to get a concentric movement of the focused beam and the positioning of the probe close to the screen centre using the shift capability of the DCs. The emphasis should be on the concentric beam oscillation rather than on its exact screen centring. Once the alignment convergence is reached, the projector system is switched to diffraction mode and the transmitted beam is placed at the centre using the projector coils (Diffraction shifts in Thermo Fisher microscopes). Then, the projector system is switched back to image mode and the condenser/objective modulation is checked again. If the lens modulation does not produce a concentric beam movement, the spot coils are used to readjust it. This is because an offset may be introduced by the software that was not previously there. The spot coils are an extra set of coils available in JEOL microscopes to have a coarse control of the beam shift. Thermo Fisher microscopes have a different design and their DCs can perform the same function as the spot and shift coils in JEOL microscopes.

Once the electron beam is well aligned, the lateral and angular resolutions are checked. After insertion and alignment of the smallest available CA, the beam is focused at the specimen plane through the knob controlling the CL3 (CL2 for 3-lens condenser systems) in image mode, the projector system is switched to diffraction mode and the electron beam scan is enabled. The obtained scanned image should be as sharp as possible, which will demand some degree of OL change, as well as condenser stigmator tuning for best results. Figure 3.3.2 shows the ray diagrams for each step that change the ray path according to the variations of the lens currents. The increase of the CM brings the focused probe above the specimen plane because the object distance for the pre-OL is increased, thus a higher area is illuminated by the beam (Figure 3.3.2B). Then the decrease of the CL3 compensates this z-displacement and brings the probe back to the sample (Figure 3.3.2C). The CA has been omitted in this figure for clarity.

The use of the smallest CA and the beam set in the quasi-parallel condition results in the disappearance of the typical Ronchigram in high-convergent STEM, hence it cannot be used for focus optimization. Instead, optimum focus is found through the scanned image sharpness, which becomes maximum for the OL value at which the spot is exactly focused on the specimen plane. If the sample under study offers an extended amorphous region, one may proceed to find the optimum OL focus as in high-convergent STEM, which means removing CA, adjusting the OL focus to visualize the Ronchigram and correcting the two-fold astigmatism when the iso-radial condition of the converging fringes is attained; the smallest CA is inserted as the final step of the alignment procedure using the centre of the transmitted beam as the reference to position and align the aperture. Finally, the focus of the diffraction patterns is adjusted through the diffraction focus knob, which controls the DL of the projector system (Diff lens for Thermo Fisher microscopes). If the obtained lateral and/or angular resolutions are not enough for the desired experiments, the CM value and/or spot size have to be increased, respectively, and the alignment steps have to be performed again. In case that the spot size is changed, the present values for the condenser lenses, except CL1, and coils have to be used as a starting point for the subsequent alignment. Finally, when the best conditions are reached, the lens and coil values are saved as an alignment file to be recalled any other time, after lens relaxation routine is applied to avoid hysteresis. The highest resolution in both direct and diffraction spaces

will be achieved when the image of the electron probe from the CM is placed near the ffp of the pre-OL, but not at the exact distance. It is worth noting that the high excitation of the CL1 and the use of the smallest CA result in low electron doses on the specimen under study.

Figure 3.3.3 shows a sequence of STEM-HAADF images and diffraction patterns during the implementation of the alignment in the JEOL 2100 LaB_6 using a 10-μm CA and a deactivated CL2.

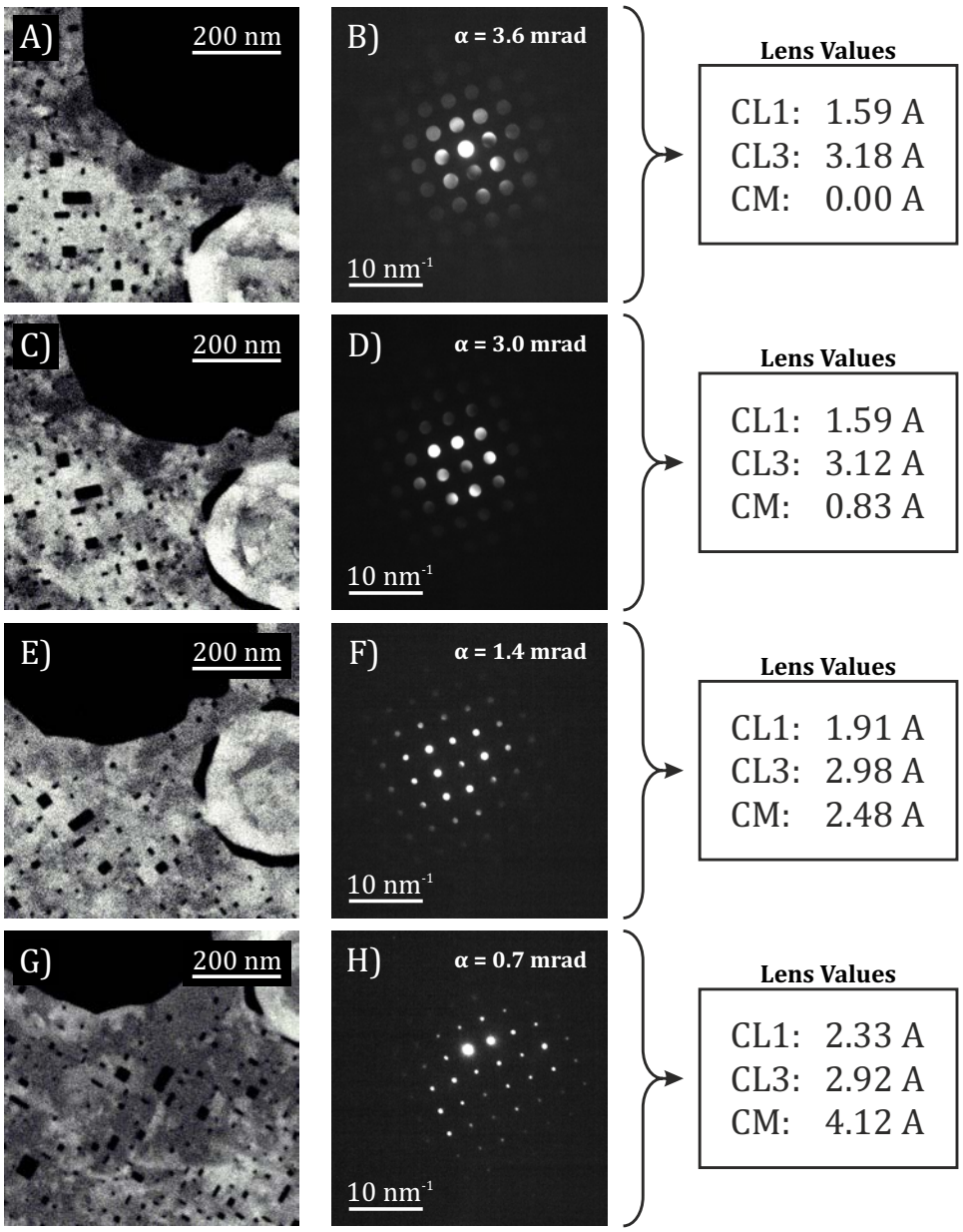

Figure 3.3.3: STEM-HAADF images (left column) and diffraction patterns (middle column) of a standard Au oriented sample obtained with the JEOL 2100 LaB_6 using a 3-lens condenser system (CL2 deactivated) during the quasi-parallel STEM alignment. The right column shows the lens values of the condenser system. A) and B) correspond to the high-convergent STEM, C), D), E) and F) correspond to an intermediate STEM, and G) and H) correspond to the quasi-parallel STEM.

Figures 3.3.3A and 3.3.3B correspond to the high-convergent STEM setting, Figures 3.3.3C to 3.3.3F are intermediate steps between the two illumination modes and Figures 3.3.3G and 3.3.3H are the final result for the quasi-parallel STEM, using in all cases the 10-μm CA. The excitation of the CM decreases the convergence angle but causes a slight beam size increase. Therefore, the CL1 has to be increased and the CL3 has to be decreased in order to recover the probe size at the specimen plane. Interestingly, as the probe becomes more parallel, the same amplitude of the sawtooth signals sent to the scanning coils will deflect further the beam position than if it were convergent, causing a greater area in the sample to be scanned and a smaller magnification (larger field of view) to be seen on the display. A stronger magnetic field would be necessary to deflect a convergent beam compared to a parallel one because of the higher angular change of the electron trajectories. For this reason, the displayed magnification value while working in quasi-parallel STEM mode will be smaller than in the high-convergent STEM and thus it needs to be recalibrated. On the other side, the camera length will be the same because the OL and DL are kept around the same value.

3.3.2 Condenser Systems without CM

The quasi-parallel STEM alignment for those microscopes without or deactivated CM is only different in the initial step compared to the previous routine. The CL2 current value is decreased about 0.2 A and the CL3 current value is increased in order to focus the spot on the specimen plane. The subsequent adjustment steps are the same as the ones from CM-activated machines (CM-used TEMs).

Figure 3.3.4 shows the ray diagrams for the quasi-parallel STEM alignment from the high-convergent setting to better understand the probe-forming mechanism. The beam crossover displacement, Δs, due to the decrease of the CL2 strength is projected to the CL3 image distance as well as the pre-field OL image distance, which brings the probe below the specimen plane. CL3 current has to be increased in order to recover the Δs and place back the beam on the sample. Alternatively to the strength increase of the CL3, the z-height or the current value of the OL could be modified. However, one of the final purposes of this configuration would be to perform tomography-like experiments and large deviations of the z-height with respect to the eucentric height will result in large sample displacements when the holder is slightly tilted. On the other hand, the strong decrease of the OL will take the electron beam out of the optimal conditions and enhance the lens aberrations on the probe. This is more evident when the microscope has an ARP (BioTWIN or TWIN pole pieces for Thermo Fisher microscopes) because the axial homogeneity of the magnetic field between the pole pieces is fulfilled at smaller regions compared with HRP or UHRP (S-TWIN or U-TWIN pole piece for Thermo Fisher microscopes). Nevertheless, fine tuning of the OL is performed at the end of the alignment to get the more precise positioning of the electron beam on the specimen, similar to atomic-resolution procedures in aberration-corrected microscopy.

The resulting lateral resolution is better in this case than the 2 CLs + 1 CM case because the modification of the current values for two of the CLs preserve the magnification power of the emission source. If one considers a reversal role of CL2 and CL3 that is, increasing CL2 current while decreasing CL3 current, it will result in a similar demagnification power, but the convergence angle will not be reduced due to the CA. The CA limits the electron beam cone travelling down the column and a CL2 increase produces a high angle cone above CL3, which results in an unchanged angular resolution.

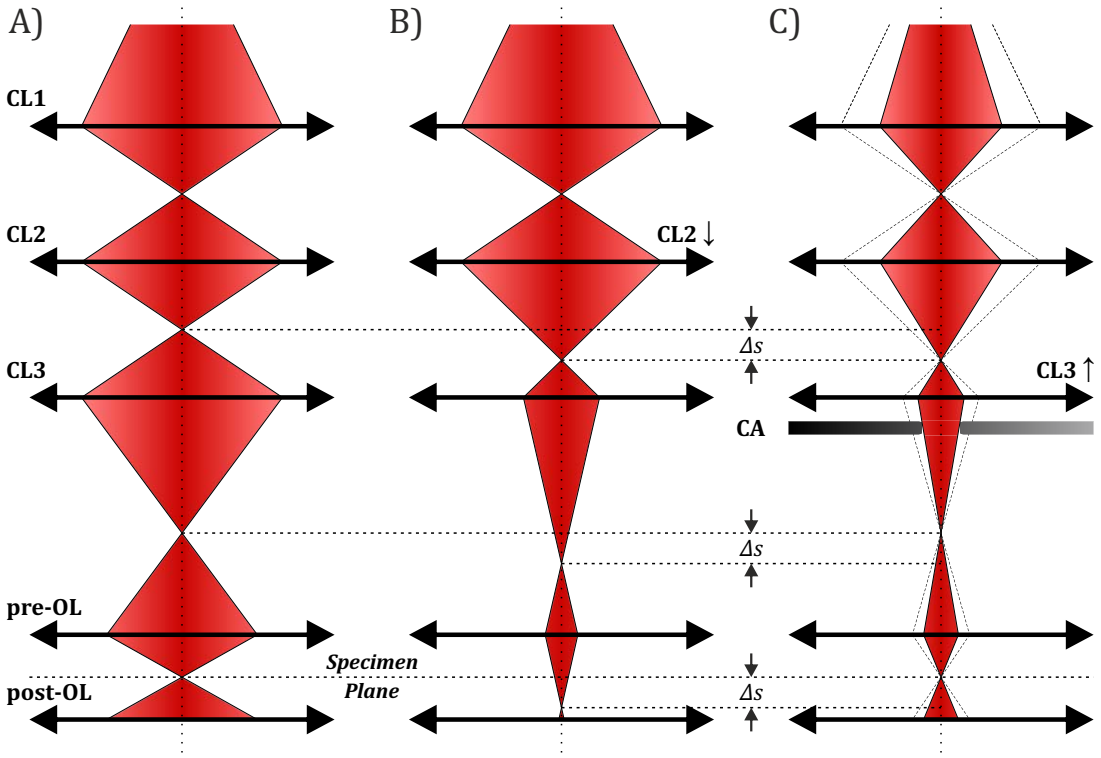

Figure 3.3.4: Ray diagrams for a 3-lens condenser system without a CM during the alignment of a quasi-parallel probe. A) corresponds to the default ray trajectories in high-convergent STEM, B) is the ray diagram during the alignment of the quasi-parallel beam in which the CL2 current is decreased, and C) is the setting for quasi-parallel STEM. Dashed lines in C) represent the ray trajectories if the CA is not used.

Figure 3.3.5A shows the balance of CL2 and the CL3 current values for the aligned system on the JEOL 2100 LaB6 at three different values of CL1 (spot size). While decreasing CL2, CL3 has to be increased in order to recover the probe z-displacement at the specimen plane until the minimum angular resolution is reached (see Figure 3.3.5B). Then, the parallel condition is fulfilled (image distance of the crossover for CL2 coincides with the CL3 ffp) and the convergence angle starts to increase again. At this point, the object for CL3 becomes virtual and its strength has to be strongly decreased to recover a focused beam on the specimen plane, which is seen in the sudden drop of the CL3 current value in Figure 3.3.5A that fits to the situation after the minimum angular resolution is achieved in Figure 3.3.5B.

Another interesting conclusion from the plots of Figure 3.3.5 is that a higher spot size results in a lower angular resolution. Figure 3.3.6 shows the ray diagram that compares two different spot sizes (different CL1 excitations). The difference may not seem significant but the convergence angle can change from 0.5 mrad to 0.25 mrad. Since CL2 current is lower and CL3 current is higher for the higher spot size (higher CL1), the parallel condition for CL3 is reached at a smaller focal distance. In these conditions, the inverted cone of electrons converging at the object distance of the pre-OL is formed by electrons with lower tilting trajectories compared to the lower spot size case, thus the final convergence angle at the specimen plane is lower as well.

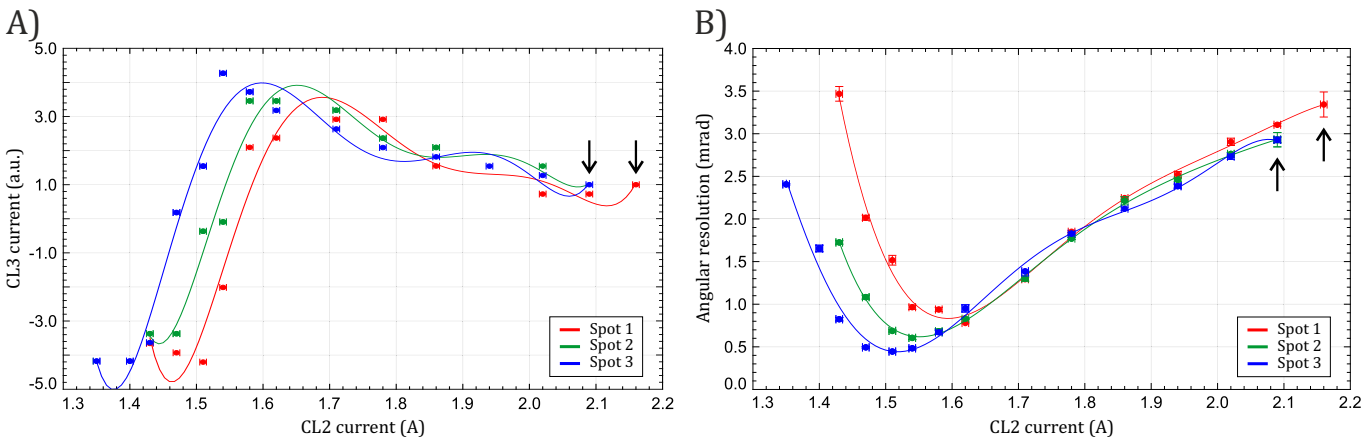

Figure 3.3.5: A) CL3 current and B) angular resolution (2α) against the CL2 current obtained with a JEOL 2100 LaB_6 using a 3-lens condenser system (CM deactivated). Interpolated curves are obtained by six-order polynomial fittings. The black arrows indicate the initial default values for the different spot sizes.

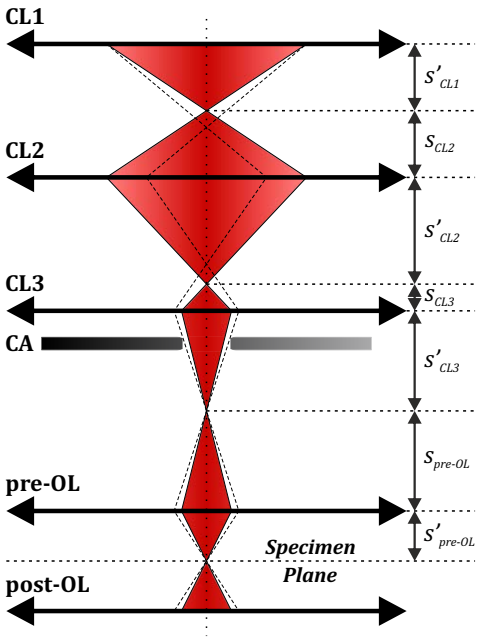

Figure 3.3.6: Ray diagram with two different excitations of CL1 (spot size). The dashed ray trajectories correspond to a beam with lower CL1 and CL3 strengths and higher CL2 strength (lower spot size case) compared to the red-coloured beam. s and s' stand for object and image distance, respectively, for the corresponding lens.

Finally, it is worth to mention that although this 3 CLs system allows the realization of the Köhler illumination with electrons [92], the CA limits the achievable beam size, thus the explained electron-optical mechanism is required to shape quasi-parallel and nanometre-sized beams.

Figure 3.3.7 sums up the necessary steps to set the quasi-parallel STEM mode depending on the configuration of the condenser system as well as the comparison with the alignment for the high-convergent STEM. Once the desired spot size and convergence angle is set, the main difference between illumination alignments is how to finely find the STEM image focus and correct the condenser astigmatism. While the Ronchigram is used for high-convergent beams, the quality of the scanned image is checked for quasi-parallel settings.

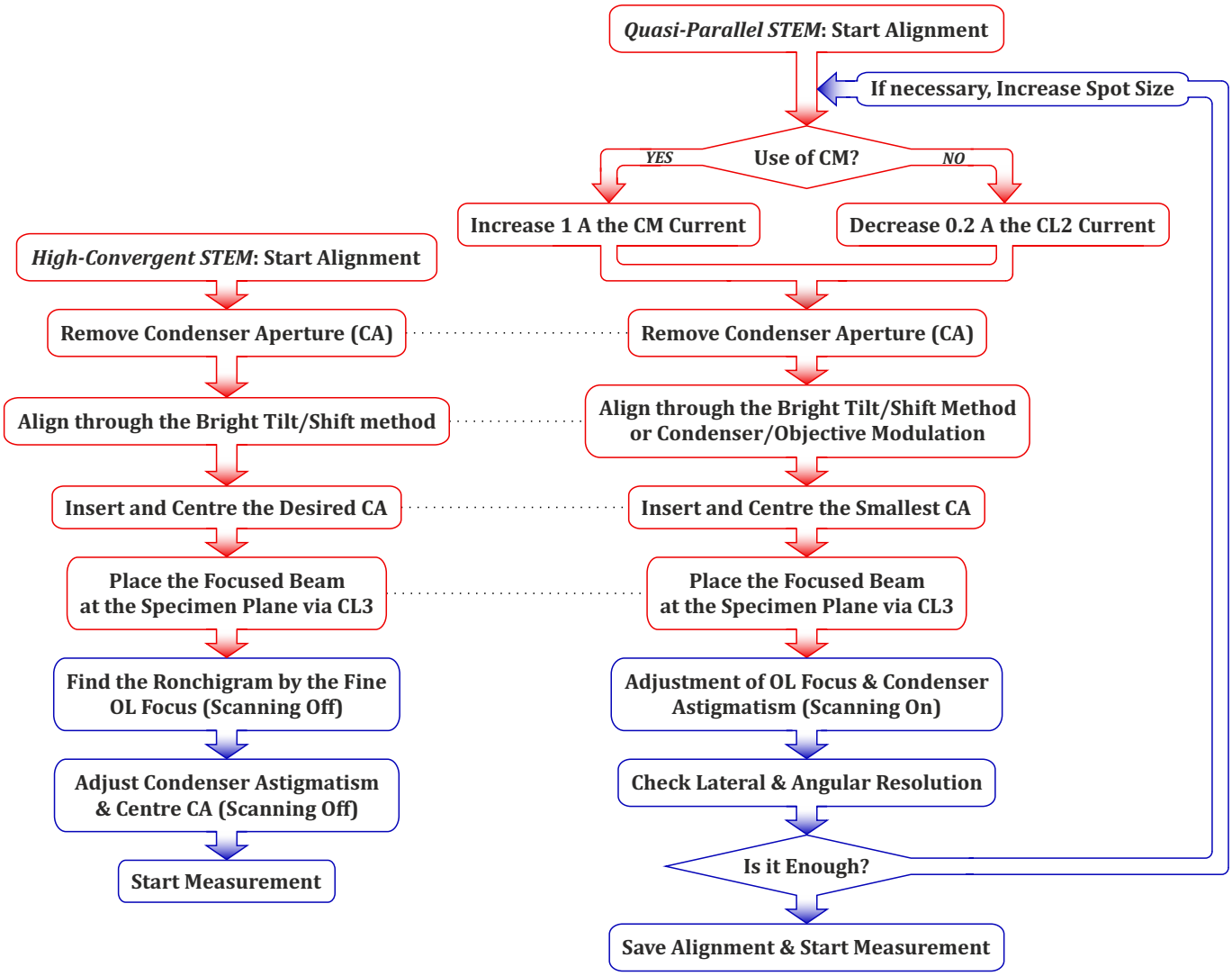

Figure 3.3.7: Flowcharts for the alignment procedures of the high-convergent and quasi-parallel illuminations in STEM mode. Boxes in red and blue correspond to adjustment steps carried out with the projector system in image or diffraction mode, respectively. Dashed lines between flowcharts indicate steps similarly followed by both of them. It is assumed that the eucentric height has been previously found in TEM mode with a comparable strength of the OL.

3.4 Precession Alignment in STEM mode

The usual and static PED alignment performed in TEM mode can be extrapolated to STEM mode. In TEM mode, the alignment is carried out as follows: the beam pivot point is adjusted with the projector system in image mode while the counter-precession is off. Then, the projector system is switched to diffraction mode and the de-scan is adjusted to obtain focused patterns. Although this alignment is easy to follow and fast to implement, the image obtained by the projector system is not exactly the specimen plane because of the lens aberrations of the projector system [180], which means that the z-adjustment and OL current modification to focus the TEM image do not result in the precise projection of the specimen plane. This is the reason why the OL or the CL3 strength has to be modified in order to get a focused STEM image after the probe was perfectly focused with the projector system in image mode. In other words, the TEM alignment results in a non-accurate probe pivoting on the specimen plane suitable to make a so-called coarse alignment for STEM mode, but the following precession alignment in STEM mode is required to correctly find the optimal beam pivot point position.

First of all, the STEM mode is selected and the illumination alignment is checked. Figure 3.4.1A shows an initial image from the aligned quasi-parallel STEM mode. Then, the precession signal is enabled with the following initial parameters: 30% of maximum amplitude for X and Y signals, and 0° and 90° for the respective phases on both DCs. This will probably result in a fringed scanned image like Figure 3.4.1B, which is caused by a pivot point shift of the precessed probe with respect to the exact position of the specimen plane. To correct this probe shift along the optic axis of the microscope, the signal sent to DC2 (the so-called *beam pivot point*) is adjusted using the precession control system, thus changing the amplitude and phase of the sinusoidal signals until the fringes are minimized. Some white lines in-between the fringes may appear due to the non-focused reflections of the pattern, even when the counter-precession signal is on (Figures 3.4.1C and 3.4.1D). At this point, the beam scanning is stopped and the diffraction focus is recovered modifying the counter-precession signal of IS1 (the so-called *de-scan*). These two last steps may be iteratively performed until both scanned image and diffraction pattern are focused (Figures 3.4.1E and 3.4.1F). Once the alignment is finished, some contrast fringes may remain due to the non-completion of the last precession cycle for each pixel, i.e. the precession frequency is not an integer number of the scanning frequency. In this situation, the beam pivot point alignment has to be carefully performed using the edges of a reference (preferably in orthogonal directions) instead of the contrast on the sample surface. This will ensure that the probe is pivoting at the specimen plane.

As STEM mode works with the projector system in diffraction mode, the 6-coils method explained above can be followed because the recovered focus is only needed at the bfp of the post-OL. However, the 6-coil method may result insufficient to counter-precess the beam in some microscopes, since it has been noticed that the addition of a signal to the second pair of IS coils increases the strength of the first pair. This is because of the cross-talk between IS coils and the DL, which means that any current change on a coil or lens may produce a magnetic interference to the closest coils and/or lenses. This cross-talk effect is microscope dependent and it is also present in the beam DCs, limiting the maximum precession angle without the use of non-linear signals for compensation [180]. It is noted as well that these non-linear effects strongly depend on the connection points of precession in the controlling boards of the coils, thus the different electronic filters alter and distort the ap-

plied sinusoidal signals. For this reason, it is advised to solder the cables of the precession signals as close to the last electronic controlling stage of the boards as possible to avoid these undesired behaviours. This reduces the possibility of interference by electronic noise yet cross-talk effects may still be present. In this case, a constant signal may be sent to IS2 to help IS1 to recover a focused diffraction pattern during the PED alignment.

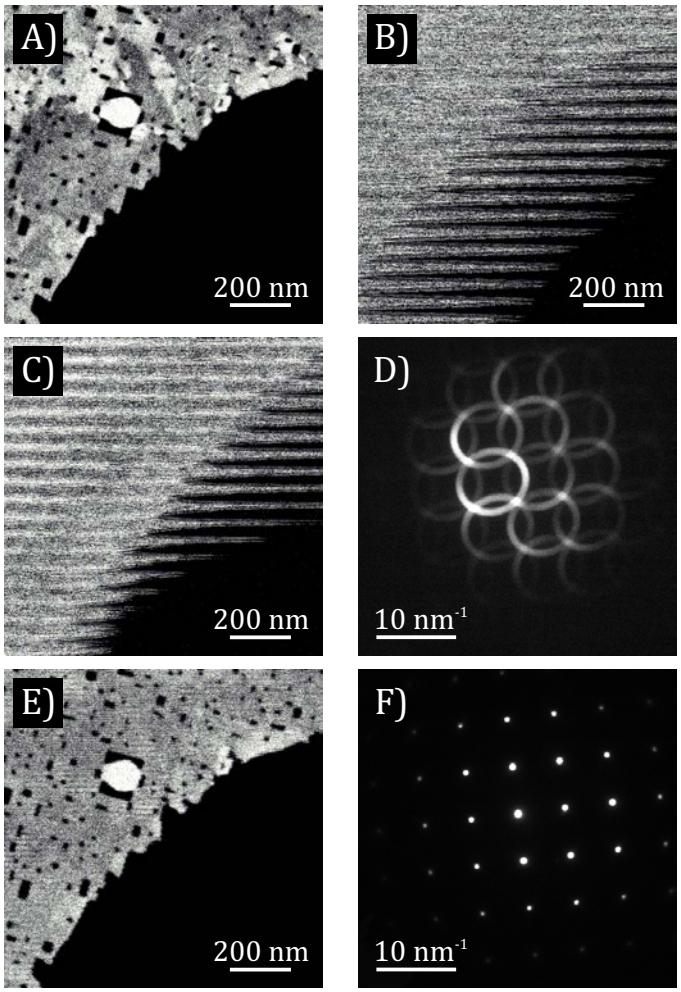

Figure 3.4.1: STEM-HAADF images and diffraction patterns from a standard Au oriented sample obtained with a JEOL 2100 LaB_6 during the PED-STEM alignment. A) Quasi-parallel STEM image, B) quasi-parallel PED-STEM image with precession misaligned, C) quasi-parallel PED-STEM image with precession signal aligned but misaligned counter-precession, D) precessed diffraction pattern with misaligned counter-precession, E) and F) correspond to a quasi-parallel PED-STEM image and its related precessed diffraction pattern at 0.7° of precession angle.

The whole alignment in STEM mode is performed without changing the projector system to image mode, thus the precessed electron beam has not been aligned on the image plane of the OL. In some cases it could be interesting to have an aligned precessed probe in the image plane, e.g., for reduced contrast artefacts in TEM imaging [123]. If this application is desired, the projector system is switched to image mode and the counter-precessing signal sent to the IS2 (so-called *image pivot*

point) is adjusted until a focused beam is obtained. Then, the projector system is switched back to diffraction mode and the de-scan may need to be re-adjusted to focus back the reflections. These last two steps may be iteratively performed until the precessed beam is focused on both planes. Once this alignment is finished, the switch between diffraction and image mode with precession activated will result in focused diffraction patterns and focused TEM images, while the microscope is in STEM mode and the probe is accurately pivoting at the specimen plane. This method is referred to as the 8-coils based alignment. Figure 3.4.2 shows the summarized steps to align PED in STEM mode according to the coils based method once the initial values of amplitudes and phases are already applied.

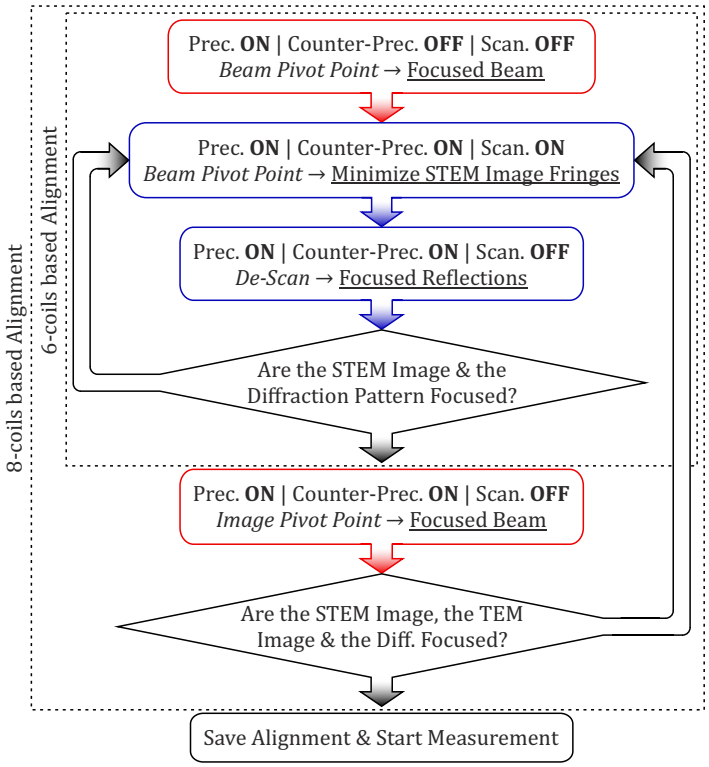

Figure 3.4.2: Flowchart of the precession alignment in STEM mode. Prec., Counter-prec. and Scan stand for precession, counter-precession and scanning of the beam, respectively. Red boxes mean that the adjustment is performed with the projector system in image mode and the blues ones in diffraction mode.

All steps of the PED alignment procedure should ideally only require phase modifications in order to preserve the uniformity of the applied signals and the circularity of the precessed beam. However, this is never the case because it depends on the previous alignment of the beam, the TEM lenses mechanical positions, the pole piece geometry and the z-position of the holder for eucentricity condition. Therefore, the signal amplitudes have to be modified as well. Interestingly, this PED alignment can be performed in high-convergent STEM and the signal parameters can be stored to be used as a starting point for the alignment in quasi-parallel STEM. In this case, the amplitudes have to be modified by a factor on both directions to retrieve the same precession angle, and slight changes on amplitudes and phases are enough to recover the diffraction focus and the precessed probe at the specimen plane.

3.5 Electron Dose

An important parameter to characterize from the different settings of the illumination system is the electron dose (e-dose) rate, which is defined as the number of electrons over area and time ($e^-/Å^2s$). In this work, the e-dose rate is estimated following the method already applied by Kolb et al. [3]; the integrated intensity on the charge-coupled device (CCD) detector is calibrated against the e-dose rate from the fluorescent screen for high dose measurements and extrapolated as a straight line for the low-dose range where the screen is not sensitive enough. By using this procedure, the mean e-dose rate for the quasi-parallel STEM in the JEOL 2100 LaB_6 with the 10-µm CA and spot size 3 using the tested CM and the non-CM settings turn out to be around 250 $e^-/Å^2s$ and 650 $e^-/Å^2s$, respectively, if the FWHM circular area of the probe is used, while it decreases down to $\sim$ 170 $e^-/Å^2s$ and 450 $e^-/Å^2s$, if the full-width at tenth-maximum (FWTM) is considered. The e-dose rate for the high-convergent STEM in the same microscope with the 10-µm CA and spot size 3 is $\sim$ 800 $e^-/Å^2s$ and 400 $e^-/Å^2s$ (FWHM and FWTM respectively).

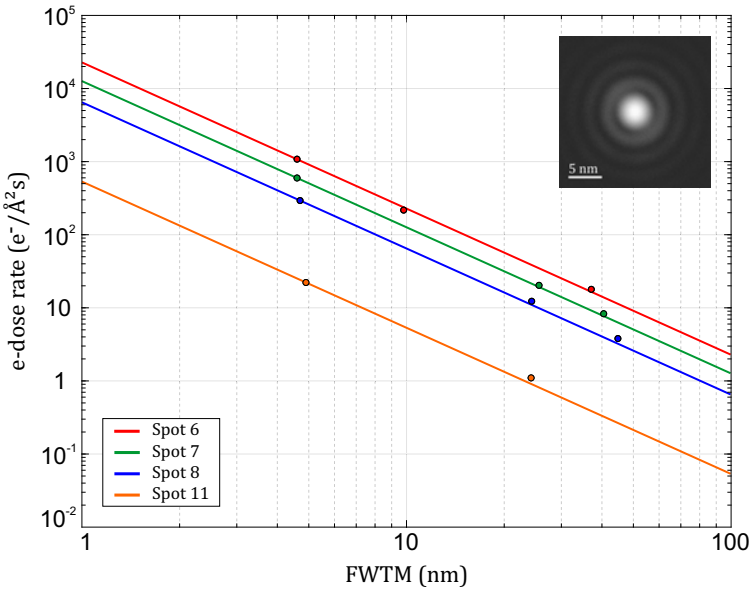

Figure 3.5.1: Electron dose rate ($e^-/Å^2s$) against the FWTM of the electron probe (nm) in log-log scale for different spot sizes of a FEI Tecnai F30 operated in Microprobe mode, 10-µm CA and gun lens 8. The interpolated lines have been obtained by a power function according to e-dose rate = a/FWTM^2, where a is the parameter to determine by the fitting. The inset image corresponds to the probe image at spot size 8 showing the different rings that are visible by the high coherence of the electron beam in a FEG.

Another intensively used microscope in this work providing a brighter source is a FEI Tecnai F30 FEG (2 CLs + 1 CM system) operated at 300 kV with a S-Twin OL in which the available Microprobe mode is enough to carry out diffraction experiments. The standard illumination setting is spot size 6, gun lens 8 and 10-µm CA, which produces a diffraction-limited probe of 2.7 $\pm$ 0.1 nm at FWHM or 4.8 $\pm$ 0.1 nm at FWTM with a convergence angle of $\sim$ 0.4 mrad. The e-dose rate is around 1850 $e^-/Å^2s$ (FWHM) and 1100 $e^-/Å^2s$ (FWTM). Figure 3.5.1 shows a plot of the e-dose

rates according to the FWTM of the electron probe at different spot sizes of this microscope. If the spot size is increased up to 11, the e-dose rate decreases down to ~ 2 e$^-$/Å^{2}s at FWHM of the beam diameter and ~ 1 e$^-$/Å^{2}s at FWTM without further reducing the minimum beam diameter because of the diffraction limit.

When working in STEM mode, the accumulated e-dose on the scanned area has to take into account the probe diameter and the pixel size or beam shift for each pixel during the scanning (nm/pixel). Each shift step of the probe that corresponds to a defined pixel does not imply that the beam is not interacting on previous or following probe positions, as this depends on the beam size in comparison to the pixel size. This overlapping possibility is more likely the bigger the probe diameter is, such as the case of quasi-parallel STEM. Consequently, the accumulated e-dose (D) on the scanned image is the e-dose rate (D_{rate}) multiplied by the dwell time (t_{pixel}) and the factor between the probe area and the beam step:

$$D = \frac{\pi(d_{beam}/2)^2}{(\text{Beam Step})^2} \cdot t_{pixel} \cdot D_{rate} \left(\text{in } \frac{e^-}{\text{Å}^2}\right) \tag{3.5.1}$$

where D_{rate} has to be calculated or measured using a circular area of d_{beam} diameter in order to be consistent. An interesting case is the accumulated e-dose difference between Figure 3.3.3A (high-convergent beam) and 3.3.3G (quasi-parallel beam) for the JEOL 2100 LaB_6. Here, the beam step and the dwell time were set to 1.8 nm and 3.1 ms in both images and the only difference was the beam diameter and its related e-dose rate. The probes had a size of 8.5 nm and 14.6 nm (FWHM), which lead to a strong overlap when such small beam steps are applied. While the high-convergent beam illuminates the pixel area 17 times the dwell time, the quasi-parallel beam is shinning 50 times the pixel area. Following equation 3.5.1 and the correlation error formulae, the accumulated e-dose turns out to be 4 ± 2 e$^-$/Å^2 and 4 ± 1 e$^-$/Å^2 for the high-convergent and quasi-parallel STEM image, respectively. Although the beam is illuminating more area when a quasi-parallel beam is used, the e-dose rate is higher for a convergent beam, and, therefore, the accumulated e-dose of both images is similar at the end. In this way, these low values are in the range considered as *low-dose* [181] and it demonstrates that the STEM mode can be used as an alternative way to obtain images of beam sensitive materials without the use of a direct detection detector.

3.6 Results and Discussion

The quasi-parallel STEM mode has been tested in a JEOL 2100 LaB_6 TEM following both alignment procedures (with and without CM). Figure 3.6.1 displays the TEM images of the resulting electron probes for the different studied illumination conditions. The assessment of lateral resolution by measuring the beam diameter in TEM imaging does not yield a reliably accurate value by itself, due to lens aberrations in the projector system that become significant at high magnifications [180, 182]. Nevertheless, it provides a good estimate to compare between the different electron beam settings.

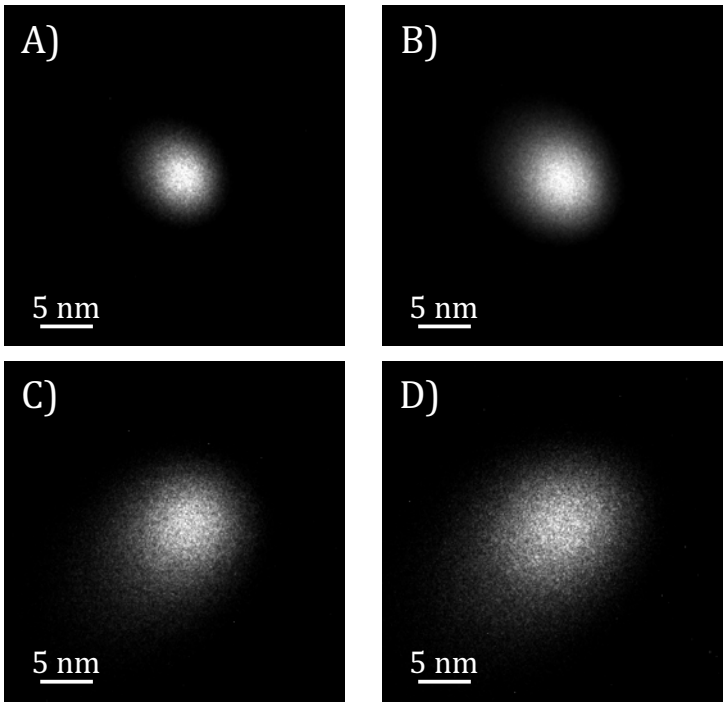

Figure 3.6.1: Electron probe images for A) high-convergent STEM with FWHM of 8.5 ± 0.2 nm, B) quasi-parallel STEM using 3 CLs with FWHM of 11.3 ± 0.4 nm, C) quasi-parallel STEM using 2 CLs and the CM with FWHM of 14.6 ± 0.6 nm, and D) quasi-parallel PED-STEM using 2 CLs and the CM at 0.7° of precession angle but counter-precession deactivated with FWHM of 16 ± 1 nm. All images were acquired with a JEOL 2100 LaB_6 at spot size 3 (CL1 at 2.92 A). C) and D) were obtained with the same probe-forming current settings. Images are displayed on a linear scale with the same intensity range.

The CM-used alignment with CL2 deactivated reported a lateral resolution of 14.6 ± 0.6 nm and 0.50 ± 0.03 mrad of convergence angle. On the other hand, the alignment with CM deactivated resulted in a better lateral resolution (11.3 ± 0.4 nm) and lower convergence angle (0.25 ± 0.03 mrad). Such difference comes from the bigger distance from the last active lens to the specimen for the non-used CM case, thus an increased demagnification of the electron source that is also reported in the work of Yi et al. for a FEI Titan probe-corrected [178]. Another important point from these values is that they are far from the theoretical limits given by the diffraction of the CA (5.3 nm and 2.6 nm for 0.25 mrad and 0.5 mrad, respectively). That is because the CL1 is not excited to its maximum strength during this characterization due to the high decrease of the probe current that result in too

noisy STEM images for proper and step-wise analysis. In consequence, the final probe size on the specimen is mainly determined by the demagnifying power of the condenser system. If spot size 5 is tested, the beam diameter is reduced to around 8 nm for the 3 CLs case and 11 nm for the 2 CLs and one CM case. While the diffraction-limit situation is approached in the former, the later is still far from this condition. In this context, it is clear that a LaB_6 TEM needs an extra CL in the condenser system in order to gain enough de-magnification power to generate the smallest quasi-parallel beam possible, as it is designed in the JEOL 2100 LaB_6. The small tail observed on these beam images that come from the wear of the LaB_6 tip as well as the non-correctable tilted emission of the source also avoids to reach the desired optimum minimum probe.

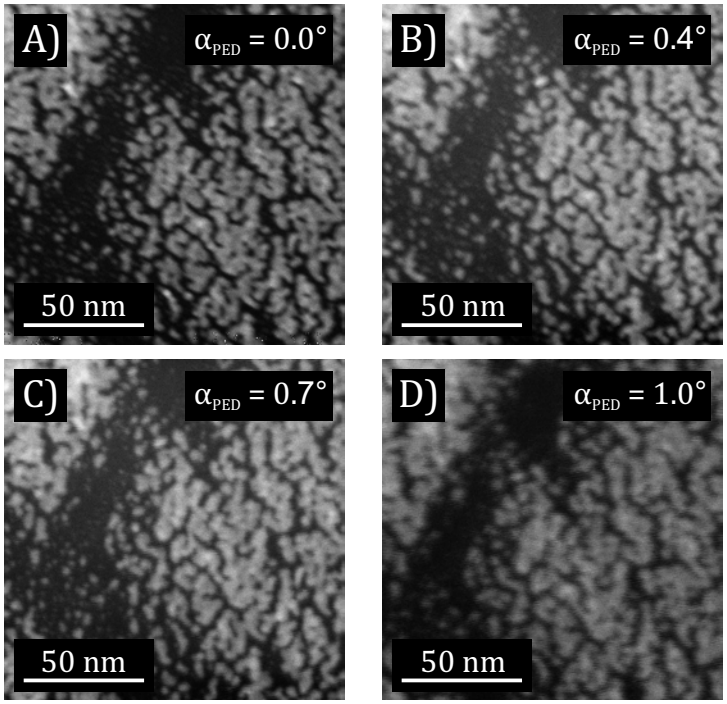

Figure 3.6.2: High-convergent STEM-HAADF images A) without and B) 0.4°, C) 0.7° and D) 1.0° of precession with a JEOL ARM200F probe-corrected. These images of 1024 x 1024 pixels were acquired with a HAADF detector at 40 µs of dwell time.

Figures 3.6.1C and 3.6.1D show that the probe diameter is increased about 1.8 nm when precession is applied while keeping a constant OL strength. The initial expression introduced by Vincent and Midgley [111] ($d_{prec} = 4C_{30}\alpha_{PED}^2\alpha$) defines the disk of least confusion when precession is applied by taking into account the spherical aberration of the OL. It provides the theoretical guideline for the behaviour of the probe under precession, but in this case it underestimates the enlargement as it predicts an increase of only ~ 0.3 nm ($C_{30} = 1$ mm, $\alpha = 0.0005$ rad and $\alpha_{PED} = 0.012$ rad). Recent work showed that this expression is followed at higher precession angles (more than 1.5°) in which the probe size is limited by the tilt-induced two-fold astigmatism caused by the off-axis condition of the precessed beam [173]. Although precession angles higher than 1.5° have not been explored in this work, the precession alignment was tested in a JEOL ARM200F with a UHRP and equipped with a CESCOR probe corrector using the high-convergent STEM mode. Since the initial alignment

was optimized for a non-precessed beam, the OL current and the stigmator had to be finely retuned to achieve the maximum STEM image sharpness after precession was activated and the precessing pivot point was correctly adjusted on the specimen plane. This amounts to compensate minor beam offsets along the optic axis and retrieve an aberration-corrected precessed probe nearly equivalent to the non-precessed one [183]. Figure 3.6.2 shows the accurate precession alignment that can be obtained using the described alignment method with a probe size of about 2.5 Å and 6.8 mrad of convergence angle. Under these considerations, the only source for beam broadening shown in the comparison of Figures 3.6.1C and 3.6.1D at 0.7° of precession angles is the electronic noise from the controlling boards of the DCs, which is also suggested in the work of Barnard et al. [173]. It has been observed that this noise can be highly suppressed when specifically-designed alternate current driving boards for the DCs are used to send the precessing signal instead of direct current boards.

An alternative precession alignment procedure based on the adjustment of the sharpness of the shadow image inside the primary beam disk was proposed by Barnard et al. [173], which reported very good results comparable to the ones obtained in this work. However, this alignment can only be performed when TEM observations are carried out with FEG-equipped machines, but not if using a thermionic electron source due to its low coherence. Another notable inconvenience is the use of different CAs during the alignment procedure, which may lead to additional aberrations or beam shifts. It is true that the STEM image sharpness adjustment proposed in this work contains some uncertainty, but not much more than that of the usual focusing of a STEM image, and accurate precessed pivot point positioning on the specimen plane can be obtained without being dependent on the emitting source and the mechanical change of apertures. A more favourable case scenario for the Barnard et al. method is when high precession angles are used and compensation curves need to be applied. Here, if the 6-coils based method is used, this last adjustment may be difficult because the changes on the probe are not highly significant, thus the rapid scanned image does not show enough accuracy to detect it and subsequently correct it. Therefore, the first step of the 6-coils based method has to be re-done to carefully obtain a focused probe in the image plane, following the compensation method shown by Viladot et al. [119]. Alternatively, the projector system can be kept in diffraction mode and the compensation could be checked on the shadow image easier than in the scanned image, given that the beam coherence is good enough.

When diffraction experiments are considered, the accumulated e-dose on the sample is an important parameter to ascertain whether the electron beam can damage the sample in some way. The material sensitivity needs to be taken into account at this point, but also the detector sensitivity, since it determines the exposure time needed to acquire reflection intensities of good signal-to-noise ratio. 1 and 2 seconds are usual values used in CCDs, which raises the e-dose at FWHM up to $\sim$ 1300 $e^-/Å^2$ and 1600 $e^-/Å^2$ per pattern for the JEOL 2100 LaB_6 (quasi-parallel and high-convergent STEM, respectively, with spot size 3 and 10-µm CA), and $\sim$ 3700 $e^-/Å^2$ for the FEI Tecnai F30 with spot size 6, gun lens 8 and 10-µm CA. These e-doses are quite high and they are not appropriate for diffraction applications on beam sensitive materials. Moreover, the results from the JEOL 2100 microscope show that a highly-convergent beam could easily induce more carbon contamination formed by electron beam induced polymerization of surface hydrocarbons in comparison to a low-convergent beam, as the probe diameter is smaller while keeping similar probe currents. In order to overcome these limitations, two beam sizes have to be used; one for scanned imaging and one for pattern acquisitions with a higher probe diameter, as it is standard for 3D ED experiments. This

will greatly decrease the e-dose, as shown in the plot of Figure 3.5.1, and increase the number of acquired patterns before the full crystalline degradation of the material. Furthermore, the increase of the beam size also reduces the convergence angle and allows to obtain more focused reflections in the diffraction patterns. Although this is a feasible solution for single pattern acquisitions, it cannot be applied to 4D-STEM applications because the lateral resolution will get worse. One way to minimize the beam damage with the current hardware setting would be to align and set the illumination conditions on a close-by area of the interesting region, and shift to the desired area only when the diffraction data is acquired. Nevertheless, the best solution would be to use faster and more sensitive detectors as explained in the previous chapter. It is worth to point out that the STEM images shown here were not optimized for low-dose experiments as the sample areas are oversampled (the beam step is smaller than the beam diameter), but they quantitatively demonstrate the validity of STEM imaging for beam-sensitive applications.

3.7 Conclusions

An alignment method that takes into account the different optical elements of the condenser system has been explained in order to align a quasi-parallel beam while the microscope is in STEM mode. The use of the CM in the four condenser lens system of the JEOL 2100 LaB_6 has been studied by considering two different minimum settings: 2 CLs plus 1 CM and 3 CLs. The achieved probe diameters in both systems demonstrate that electron diffraction studies at spatial resolutions up to 15 nm and convergence angles limited below 0.5 mrad can be performed with both settings. The electron dose measurements show that such illuminations are feasible for investigations on beam sensitive materials. However, when high excitations of CL1 (high values of spot size) are applied, more sensitive detectors need to be used in order to enhance the signal-to-noise ratio of the measurement. It has also been shown that these three condenser lens systems together with the conditions of a LaB_6 filament hinder the possibility to reach the diffraction-limited probe, and the beam diameter is mainly determined by the de-magnifying power of the optical system. These results justify the design of the 4 CLs system in the JEOL 2100 LaB_6 in order to obtain the smallest possible beam in quasi-parallel conditions as it is seen in the reported values of Table 3.2.1. The use of a 4 CLs system in FEG TEMs is only necessary when flexible illumination settings are desired, as the smallest physical probe can be obtained as shown in the example of the FEI Tecnai F30.

A novel precession alignment method has also been described while working entirely in STEM mode and without switching the projector system to image mode. Such procedure allows to accurately position the precessing pivot point at the specimen plane down to the angstrom spatial resolution, thereby ensuring that the precession movement during the acquisition of STEM images and diffraction patterns is exactly applied at the sample, and it is not shifted along the optic axis. The explained methodology has been compared to a recently reported method and it has been demonstrated that the alignment of this work has a wider range of applicability while yielding similar results. Since it does not depend on the illumination settings of the condenser system, the alignment workflow can be followed as well when a high-convergent probe is used.

In this way, the presented alignments allow to set the quasi-parallel PED-STEM mode and get the TEM ready for the required electron diffraction experiments. In the context of this doctoral thesis, these alignment methodologies are used as the pre-condition to develop a new technique for the acquisition of 3D ED datasets and its application to the crystallographic characterization of several different materials.

Chapter 4

Fast-ADT: The Technique

Нельзя все понять сразу, мы не можем
начать с совершенства сразу!
[One can't understand everything at once,
we can't begin with perfection all at once!]

Идиот *[The Idiot]*
Fyodor Dostoevsky

The last chapter has shown how an electron beam is aligned in a TEM to work with a precessed and quasi-parallel illumination in STEM mode for experiments based on the acquisition of diffraction patterns. This chapter is focused on the summary and description of the acquisition and processing tools of 3D ED data for crystal structure determination and refinement, and the development of an automated and reliable routine to systematically acquire such diffraction data in TEM or STEM mode. The novel acquisition method has been called **fast and automated diffraction tomography** (Fast-ADT) and it is based on two subsequent tilt scans of the goniometric stage; the first one to generate a crystal tracking file from the imaging of the targeted crystal, and a second one for the automatic acquisition of the diffraction patterns while the beam is following the crystal according to the previously created file. Such technique has been separately implemented in *Digital Micrograph* and *Matlab* environments to be accessible to as much types of microscopes and detectors as possible.

4.1 3D Electron Diffraction

The concept of 3D ED has been recently established and conventionalized in order to refer to the electron diffraction patterns collection and its 3D data evaluation for crystal structure characterization, independently of the used acquisition method and data processing tools [14]. In the past, the EDT acronym was more widely used to address this specific methodology, but the word *tomography* in this context could be misleading. Tomography is a combination of the Greek-originated words *tomo-* and *-graph*. Tomo- stands for cut or section while -graph means draw or meaning, although here it would be more appropriate to translate it as description. Thereby, tomography is a section descriptor. The origin of this wording goes back to 1914, when the polish radiologist Karol Mayer was the first to attempt to describe how to produce tomographic images of humans, i.e. sections of the inner body [184]. In this way, tomography sounds correct for an electron diffraction pattern since it is an ODS section, hence a single diffraction pattern is a tomogram of the ODS. However, to refer as tomography to the 3D reconstruction of the ODS by means of several diffraction patterns is not strictly correct, if its original meaning based on the real space is taken into account. Image tomography consists on the acquisition of different projections from a physical object, and their processing through filtered back projection or iterative algorithms to obtain a 3D reconstruction from which sections can be extracted. An electron diffraction pattern is not a projection but a section of the sampled space, as shown through the Ewald geometry in the second chapter, and the 3D reconstruction procedure is different because the object projection has not to be considered. For this reason, the 3D ED acronym fits better to define the acquisition and reconstruction of the ODS, since it avoids the confusion of what tomography means in this case and graphically explains what you obtain before and after data processing.

4.1.1 The Reasons and Core Idea of 3D ED

The core aim of 3D ED is to obtain significant and quantitative information from the electron diffraction space to carry out reliable crystal structure determinations. The structural characterization by means of TEM techniques is not a novel method despite some claims during the last years [185, 186, 187]. It is true that the development of fast and sensitive detectors triggered the easier and more reliable acquisition of electron diffraction data from beam sensitive materials, like organic or protein crystals, yet several crystallographic studies were carried out in the past. In fact, one of the first quantitative electron crystallography analyses was done on a thin layer of paraffin by R. Rigamonti back in 1936 [188].

The usual method in earlier days of electron diffraction dealt with the acquisition of SAED single-crystal or textured patterns oriented in zone-axis. Zone-axis means that the measured crystal is oriented with Miller planes related to low *hkl* indexes parallel to the incident radiation, which allows to identify the possible symmetry relationships and systematic extinctions related to the crystal space group in an easier way than in a randomly oriented pattern. The intensity integration of the reflections from such 2D sections of the ODS allowed to obtain the projected atomic potential along the zone-axis direction. In some cases, a few of these analyses enabled the determination of crystal structures in organic [189, 190, 191, 192] and inorganic [193, 194, 195] materials. Less frequently, poly-crystalline diffraction patterns were also used in a similar way as X-ray powder diffraction (XRPD), even discussing the possibility of hydrogen positions determination [196, 197]. More infor-

mation about the historical perspective and initial works of electron crystallography can be found in the books and reviews of Boris K. Vainshtein and Douglas L. Dorset [198, 199, 200, 201].

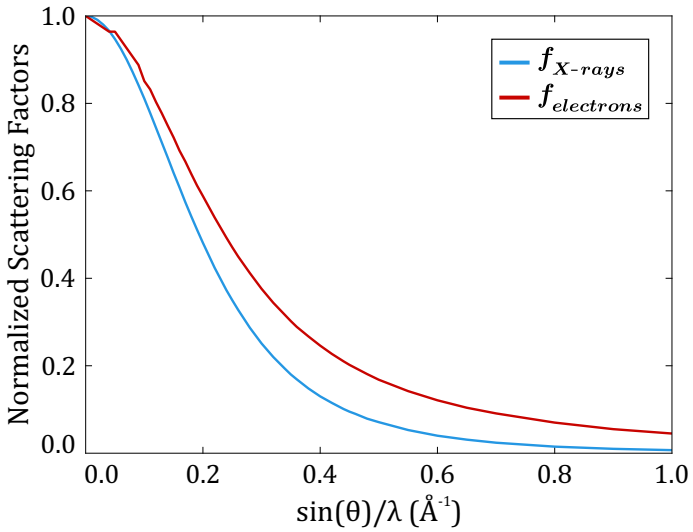

Figure 4.1.1: Normalized scattering factors for the hydrogen atom using X-rays (blue) and electrons (red) against $\sin(\theta)/\lambda$. Values are obtained from the International Tables for Crystallography, Vol. C [54].

The initial electron crystallography works reported reasonable results for light-atom structures. From a kinematical point of view, datasets from electron diffraction should provide an "easier" detection of hydrogen positions compared to X-ray diffraction due to the higher scattering factors (see Figure 4.1.1). Furthermore, the values of the scattering factors decrease between Li and Ne for electron diffraction, while they increase according to the atomic number in X-ray diffraction. This characteristic provides an alternative way to locate such light atoms and confirm results from X-ray diffraction. The problem arises when the same methods are applied to heavier-atom structures.

The second chapter of this work has shown that the interactions of electrons with matter is much stronger than X-rays or neutrons. Crystals with thicknesses of around 50 Å are enough to produce several diffracting events for a given incident electron wave [49]. Crystals are usually thicker than a hundred Å and, if they are composed of heavy atoms, the possibility of multiple scattering events becomes almost certain. That is the reason why some lack of confidence was present in the crystallography community between 1950 and 1970 regarding the structural characterization of materials by electron diffraction [202, 203, 204]. Nevertheless, it has to be said that during that time the structure determination algorithms were also developed and optimized only for X-rays, hence the poor convergence on the crystallographic solutions for electrons.

After 1970, TEM resolution started to reach the point in which atomic-resolution imaging was possible. Initially, crystallographers used HRTEM images and its related spectrum image (the Fourier transform of the image) to extract amplitudes and phases of crystals and subsequently solve different structures [205, 206, 207], yet the combination of HRTEM imaging and SAED single-crystal diffraction patterns was even better. While the former was used to identify the heavy atom positions, the latter could determine the lighter ones and refine the crystal structure [208, 209]. Although this

approach yielded good results, it was not generally followed because it was not always possible to acquire atomically-resolved images due to beam damage or crystal thickness.

Single-crystal patterns started to be used more frequently to solve *ab initio* inorganic crystals during the 90s in spite of dynamical effects, mainly because of the higher accessibility to programs for structure solutions based on electrons [210, 163]. However, it was still tricky to retrieve the crystal phase with confidence and it was not until the development of PED that reliable structure determination started to become possible [111]. The acquisition of precession-assisted diffraction patterns in zone-axis showed that dynamical scattering was reduced on the reflection intensities and several inorganic structures could be solved considering them *pseudo-kinematic* [211, 212, 165]. Some corrections were proposed to apply on the integrated reflection intensities to take into account the Ewald sphere wobbling in the diffraction space and the remaining multiple scattering, yet intensities were still intrinsically dynamical [213, 214]. In this context, 3D ED emerged as the definitive solution for structure determination via electrons.

The main idea of 3D ED is the acquisition of electron diffraction patterns from a single crystal at subsequent or continuous tilt angles of the sample holder around an arbitrary crystallographic axis. This new idea was initially developed and implemented by Ute Kolb and coworkers during 2007-2008 [3, 4], and it has several advantages compared to previous methods, all of them focused on an increased possibility of reliable crystal structure characterization.

1. The crystal does not need to be oriented around a specific crystallographic axis, hence previous information on the crystal is not needed, and the electron bombardment on the crystal, that is susceptible of damage, is reduced.

2. Since zone-axis patterns are less likely to be acquired, the integrated intensities are closer to the ones predicted by the kinematical theory. The inclination of the electron beam from the zone axis reduces systematic dynamical effects arising from the interaction of systematic reflection classes (such as 00l) [12].

3. The diffraction space is finely sampled over the used angular range of the specimen holder. This increments the number of available independent reflections according to the crystal system, the so-called **completeness** (%) of the dataset.

4. For unknown materials, it avoids to intensively investigate zone-axis patterns in order to determine the crystal system. The ODS reconstruction allows an easy identification of possible unit cells and reflection indexing.

5. 3D ED data enables an easier accessibility to the study of crystal disorders, twinning or polycrystallinity because of the 3D visualization of the diffraction space.

Two years after this approach was published, Mugnaioli et al. presented its coupling with PED to optimize the minimization of dynamical effects for successful structure determination based on the kinematical theory [117]. For all these reasons, 3D ED was established as the main technique for electron crystallography. Figure 4.1.2 shows a sketch of the main steps followed by electron diffraction to determine crystal structures.

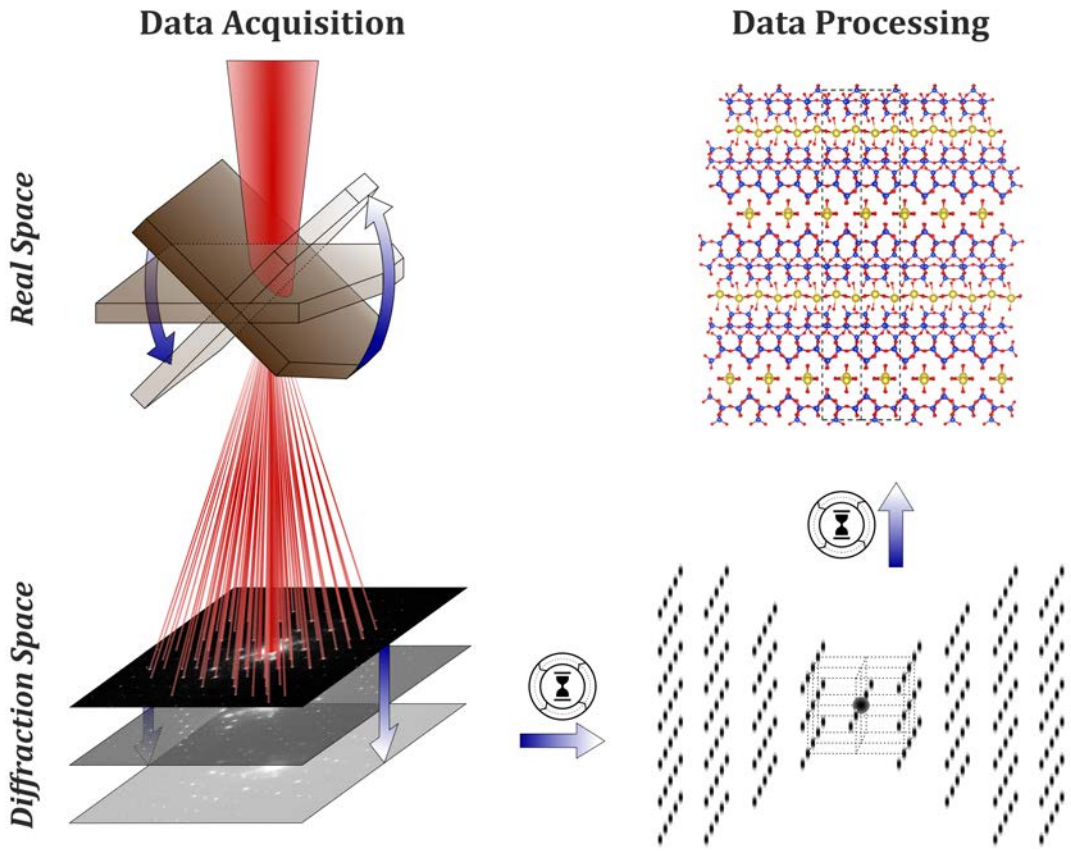

Figure 4.1.2: Main steps followed by electron diffraction; from diffraction data acquisition to crystal structure determination. The symbol of the hourglass indicates that data processing tools are being used.

4.1.2 The Processing of 3D ED Data

Several programs have been developed for the data processing of stacks of electron diffraction patterns. Most of the electron crystallography community uses one of the following programs in order to index and extract the reflection intensities from the ODS: *eADT* [12], *PETS2* [13], *EDT-Process* [10], *RED data processing* [11], *XDS* [215, 216] or *DIALS* [217]. The basic procedure on all of these software packages is quite similar because the same algorithms from single-crystal X-ray diffraction were adapted to the case of electron diffraction. Apart from the appearance of the graphical user interface, the main significant difference among them is how the intensity of the reflections is integrated and extracted. Figure 4.1.3 shows the basic workflow with the different steps from the acquired diffraction data to the extraction of the intensities of reflections based on the *eADT* program developed by U. Kolb and coworkers.

Initial steps on the diffraction data processing are focused on the unit cell determination, i.e. the reciprocal lattice that fits most of the reflections positions in the best way. At this point, the intensities of the different reflections do not play a leading role and algorithms related to their change can be applied for enhanced performance of peak search procedures and better visualization of the reconstructed ODS. This preparation process is frequently called *data pre-processing*.

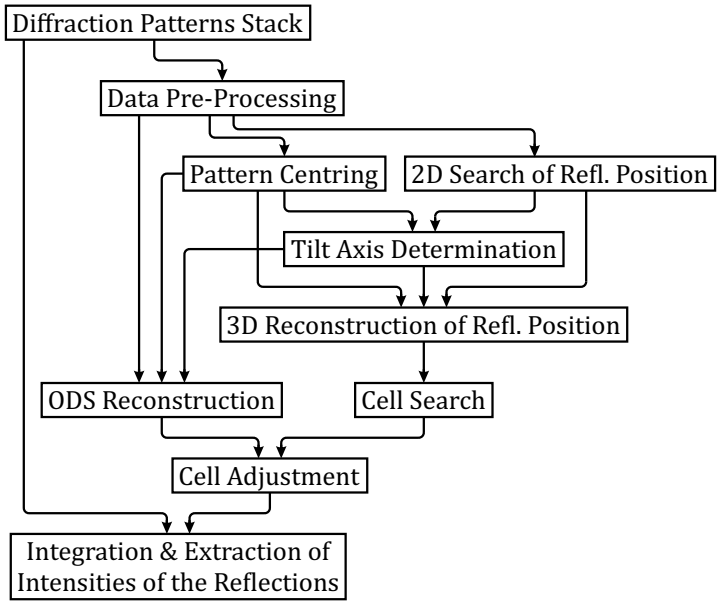

Figure 4.1.3: Basic workflow of 3D ED data processing from the raw diffraction data to the integration and extraction of the intensities of the reflections based on the *eADT* program. "Refl." stands for reflections.

eADT has three different algorithms to modify the intensities of the diffraction patterns. The first two are directed to background subtraction of the pattern. One is based on the fitting of 2D Gaussian functions with a given reflection size in pixels, and the other one is a rolling-ball algorithm [218] with an input of minimum and maximum intensities from background peaks. The third algorithm blurs the patterns by the convolution of a given-size 2D Gaussian function to each position of the whole diffraction pattern. These three routines facilitate the different processing steps mentioned in Figure 4.1.3, which are briefly explained below.

- **Pattern centring**. There are two ways to find the centre for each diffraction pattern. If a beam stopper is necessary due to beam damage, a set of symmetric reflection pairs that fulfils the Friedel relation ($|F(hkl)|^2 = |F(\bar{h}\bar{k}\bar{l})|^2$) can be identified [219], and the intersection of lines drawn between them is considered the centre. When the primary beam is available, the search for the pattern centre is more straightforward as it is assumed that it corresponds to the highest intensity with the largest extent. Here the rolling-ball blurring algorithm helps to smear out possible heterogeneities of the intensity shape of the strongest beam and helps to accurately find its centre. In case that scattered beams have higher intensity than the primary beam, a maximum displacement value according to the previously found centre can be set to avoid the algorithm to pick highly different centre positions for subsequent patterns. If necessary, the pattern centres can be manually corrected as well.

- **2D search of reflections position**. High intensities of individual pixels are searched above a certain threshold value. Once these pixels are identified, a clustering routine is performed with minimum and maximum number of pixels in the cluster as the input parameters. In this way, the obtained clusters formed by groups of a defined number of pixels are assigned as reflection positions for each diffraction pattern.

- **Tilt axis determination**. The tilt axis position in the diffraction patterns must be precisely known to enable a non-distorted 3D reconstruction of the diffraction data. Although it may slightly change during the 3D ED acquisition because of defocus on the particle due to the z position variation, it is assumed that it is constant during the measurement. Since periodicity is the primarily characteristic of a crystal, it can be used to determine the tilt axis position. In *eADT* this position is defined as the angle ϑ with respect to the y-axis of the frame that has its origin at the centre of the pattern and it is considered positive when moving clockwise (see Figure 4.1.4A). Then, difference vectors from the reflection vectors that have their origin at the centre of the patterns are calculated and several ϑ for a given range are used to reconstruct their related difference vector spaces (DVS). In order to precisely determine ϑ, a stereographic projection is calculated for each reconstructed DVS (analogous to the Wulff net [220]). Figure 4.1.4 shows three of these projections for the same diffraction dataset at different values of ϑ. The tilt axis position is correctly selected from the projection that contains sharper lines and points, for instance, Figure 4.1.4C in the example below.

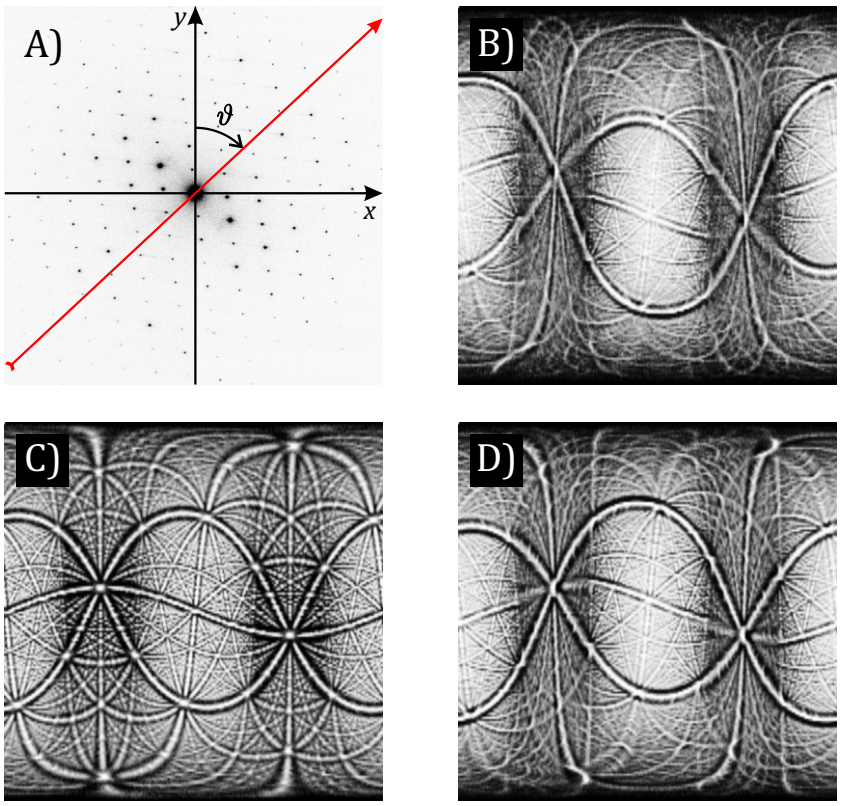

Figure 4.1.4: A) Diffraction pattern overlapped with the framework and the tilt axis (red arrow) considered by *eADT*. B), C) and D) are stereographic projections of a ferrosilicide [25] diffraction dataset. B) corresponds to a deviation of -10° from the correct ϑ, C) is the best fitting ϑ and D) is deviated +5° from the correct one.

- **3D reconstruction of reflections position**. The 3D coordinates of the identified reflections are calculated by means of the determined tilt axis position, the pattern centres and the tilt step assigned to each diffraction pattern. As each individual frame does not strictly correspond

to a plane section of the ODS, but is slightly curved as shown from the Ewald sphere geometry, the positions must be calculated according to a curved surface whose radius depends on the electron wavelength.

- **Cell search**. The unit cell determination can be carried out directly from the 3D reconstruction of the reflections position. However, since a translation grid is looked for, the calculation of its DVS is advantageous because the periodic distances between reflection positions will result in groups of points. The more points a group has in the DVS, the more times that periodic distance is present in the 3D reconstructed data. These groups need to be clustered in order to reduce uncertainty from the clouds of points and enhance the positioning of the unit cell vectors. Since the number of clusters and its exact shape changes with different measured crystals, a density-based algorithm called "density based spatial clustering of applications with noise" is used [221]. The main idea of the algorithm is to recognise high-density regions (reflections) from low-density regions (background). In this way, the minimum number of points needed to form a cluster, the maximum distance between points within a cluster, and the cluster density for a given box size are the parameters used to make the clustering of the DVS. In other words, an initial set of clusters determined from the 3D reconstruction of the reflection position is used for a second clustering based on their density. This procedure is implemented in *eADT* and it allows an automatic determination of the primitive unit cell that should describe all significant cluster points by an integer multiple of the basis vectors [222]. Nevertheless, the automatic result has to be checked and, if necessary, manually corrected in the DVS.

- **ODS reconstruction**. Apart from the 3D reconstruction of the reflection positions, the sampled ODS during the 3D ED experiment can also be reconstructed. This does not require algorithms that take into account projected objects, like in image tomography, because diffraction patterns are sections of the diffraction space. Therefore, its 3D reconstruction is a basic geometric routine that positions the acquired intensities according to the centre, the position of the tilt-axis and the assigned tilt angle of the pattern. The visualization of the sampled ODS allows to inspect the diffraction space and look for diffracting effects that may be overlooked by the previous routines based on localizing intensity peaks, such as reflection texture, diffuse scattering or weak reflections that violate systematic extinctions of an initial selected space group.

- **Cell adjustment**. The unit cell found from the DVS could match perfectly the clustered positions but the fitting of its related reciprocal lattice to the reconstructed ODS may not be as good as it could. For this reason, the reciprocal lattice is overlapped to the reconstructed ODS to check by visual aids if all observed reflections are indexed and, if necessary, correct and modify the six unit cell parameters to obtain the best match. Here the centring and extinction conditions can be examined in different ODS sections and rows of reflections in order to retrieve the possible space groups of the investigated crystal.

Once the unit cell is accurately adjusted, the orientation matrix, UB, is obtained. The UB relates the a, b and c axes of the found unit cell with the x, y and z axes of the tomographic acquisition framework. Mathematically, a vector $\vec{g}$ in the unit cell framework is described in the framework of the experiment by

$$\vec{g}_{tomo} = UB \cdot \vec{g}$$

$$UB = \begin{pmatrix} a_x^* & b_x^* & c_x^* \\ a_y^* & b_y^* & c_y^* \\ a_z^* & b_z^* & c_z^* \end{pmatrix}$$

In this way, the program has the coordinates from where the reflections are and the integration of their intensity in each diffraction pattern can be carried out.

- **Integration and extraction of the intensities of reflections**. The assignment of an intensity to a given reflection is called intensity extraction in the crystallography community and it is usually saved in a standard file with *hkl* extension. The *hkl* file contains for each reflection its h, k and l indices, the related extracted intensity and its standard deviation (σ). The determination of this intensity is done with the raw diffraction data, which should be modified as little as possible to preserve the intensity ratios between reflections. In this sense, only the subtraction of the background close to the reflection that may come from the amorphous diffraction pattern of the carbon film supporting the material under study, and/or electronic noise of the detector, is performed. In *eADT*, the intensities from the pixels that form the edge of the box that constitutes the area of the reflection in the diffraction pattern are summed. Then, this value is divided by the number of edge pixels to obtain an averaged background intensity that is subsequently subtracted to the intensity of all pixels inside the reflection box. Such procedure is applied to all available reflections in each diffraction pattern.

The second chapter has shown that the scattering power for a reflection is distributed according to the spatial periodicities and size of the crystal. Since crystals or illuminated areas are much smaller in electron diffraction compared to X-ray, the corresponding intensity distribution is much wider, thus the excitation error is higher. This means that intensities from the same reflection are recorded more than one time in subsequent frames of a 3D ED dataset. A plot that shows the integrated intensity with respect to the excitation error for a given reflection is called **rocking curve**. From the experimental point of view, the smaller the tilt difference between frames and the closer reflections are to the primary beam, the higher the sampling of reflections.

The second chapter showed as well that in principle the ODS is composed of reflections following sinc functions. Experimentally, crystals have certain mosaicity, deformation and/or thickness variations that hinder the fast oscillation of reflection intensities, which results in a smooth curve that, in some cases, can be fitted to a Lorentzian profile [13]. Nevertheless, the intensity for a given reflection is usually assigned to the maximum of its obtained rocking curve or via the integration of the curve. When electron beam precession is applied for the acquisition of a 3D ED dataset, the rocking curves exhibit a different profile. This can be best explained using a CBED pattern in two-beam condition, where the crystal is oriented to significantly excite only the primary and one scattered beam, and the scattered beam is formed by interference fringes produced by the dynamical interaction of electrons with matter. Although similar to the kinematical case, the distance between fringes is different and it depends on the crystal structure. Figure 4.1.5 shows the (004) reflection of a CBED pattern in two-beam condition from a silicon sample of 80 nm in thickness. The plot in the middle corresponds to the resulting non-precessed rocking curve if the crystal is tilted by small tilt steps along the direction of the reflection, and a spotty diffraction pattern is acquired at each tilt step to obtain its intensity.

The mechanical tilt of the crystal induces the displacement of the fringes, hence the corresponding different intensities for a given spotty-like reflection. The blue line in the CBED disk marks such a hypothetical scanned region. When precession is activated, the resulting rocking curve changes to the red curve in the right side. Here it has to be considered that the beam is also moving on the specimen, which results in an integrating circle in the diffraction space for each tilt step that is defined by the precession angle and $\vec{g}$. Three different tilt positions are shown as red circles in the CBED disk of Figure 4.1.5. The maximum of this intensity profile does not appear when the crystal is tilted to fulfil the Bragg condition, but when the precession cycle integrates most of the intensity from the strongest fringe of the reflection. Since this condition is fulfilled two times (when approaching and leaving the Bragg condition), the result is a double-peaked curve with oscillations related to the weaker fringes. When diffraction patterns are acquired from less perfect crystals and they are out of the two-beam condition, which is the general case in 3D ED datasets, reflections do not have such interference patterns and rocking curves appear as double-peaked profiles without the ripples associated to the shown fringes.

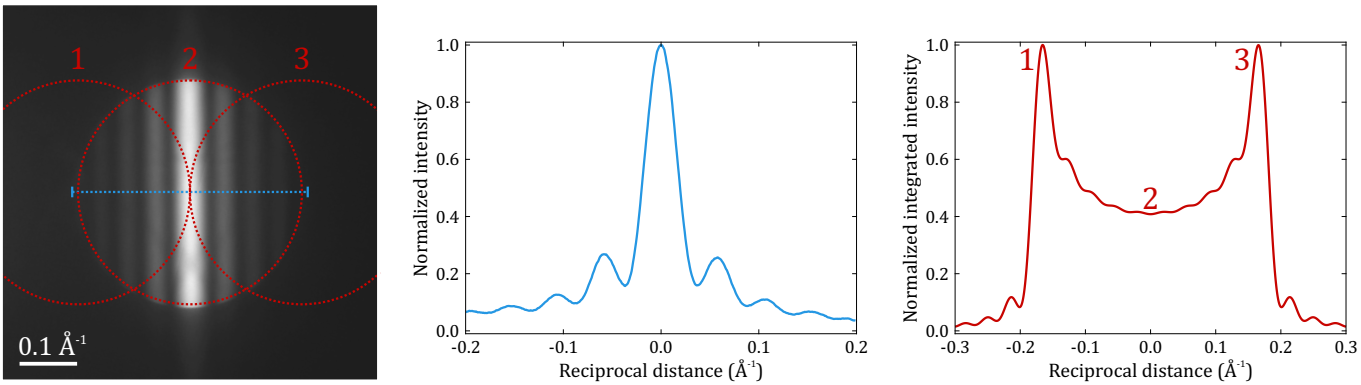

Figure 4.1.5: CBED disk of the (004) reflection of silicon acquired in two-beam condition. The plot in the middle corresponds to the intensity profile of the region marked with a blue dashed line in the CBED disk. Right side plot is the resulting rocking curve when precession is applied at different tilts along the reflection direction. The three dashed red circles in the CBED disk correspond to the integrated intensities by precession for the two peaks and the local minimum of the rocking curve. x axes are in reciprocal distance units with their origin at the centre of the reflection. The CBED pattern is courtesy of Dr. rer. nat. Lukáš Palatinus and Dr. Mariana Klementová from the Czech Academy of Sciences in Prague.

PETS2 takes into account the shape of the precessed rocking curves for a fitting based on a double-peaked function convoluted to a pseudo-Voigt function that mimics the broadening of the curve due to crystal mosaicity. The parameters of this function are calculated by means of the least-squares method on the strongest reflections of the 3D ED dataset classified in diffraction data resolution intervals. **Diffraction data resolution** is defined in this work as the largest inverse $\vec{g}$ moduli available or selected in the dataset; the higher the resolution, the higher the reciprocal distance from the primary beam, and the higher the number of available reflections. In this way, the scale factors between the experimental curves and the normalized and calculated rocking curves are used as the assigned intensities to the reflections. Furthermore, the use of the least-squares method between simulated patterns based on these

extracted intensities and the experimental ones enables an accurate refinement of the orientation angles (α, β and ϑ angles) for each frame with respect to the UB, down to 0.05° in accuracy [13]. *eADT* works with precession datasets as well but it assigns the maximum of these curves as the intensity for the reflections. Although the fitting of a double-peaked function avoids the problem of poor sampling of reflections at high diffraction data resolutions, the maximum-intensity methodology used by *eADT* has reported excellent results since its invention [223, 224, 225, 226, 227] .

Once the unit cell, its possible space groups and a *hkl* file have been retrieved from the 3D ED data processing, the only missing information for crystal structure determination is the chemical composition. This can be obtained by means of the chemical routes used for the synthesis of the material, but also EDS and EELS measurements can be used to identify the elements present in the crystal and the approximated ratios between them. When molecular crystals are investigated, Hofmann tables [228] can be used to calculate the molecule volume and determine the number of molecules inside the found unit cell.

4.1.3 Structure Solution Algorithms

The crystal structure determination is a procedure that can be done with several approaches and programs. The use of the Patterson function, already introduced in the second chapter, was one of the first implemented methodologies for such purpose, but, for brevity, only the three algorithms used through this work will be revisited here. Since the aim is to solve the phase problem, this process has been traditionally referred to find the structure solution.

4.1.3.1 Direct Methods

The second chapter showed that reflection intensities are proportional to the square modulus of their structure factors according to the kinematical theory of diffraction.

$$I(\vec{g}) = |F(\vec{g})|^2 = \sum_{j=1}^{N} f_j^2 + \sum_{j>k\geq 1}^{N} f_j f_k \cos(2\pi\vec{g}(\vec{r}_j - \vec{r}_k))$$

This equation implies that intensities are acquired on an absolute scale, which is not correct because intensity values are not direct counts of the diffracted radiation. For this reason, observed intensities are described as

$$I_{obs}(\vec{g}) = |F_{obs}(\vec{g})|^2 = K|F(\vec{g})|^2 \exp(-2Bs^2) \tag{4.1.1}$$

where K is a scale factor, the scattering factors $f(\vec{g})$ are calculated from the IUCr tables [54], s is $\sin\theta/\lambda$ and B is the overall isotropic atomic **displacement parameter** (DP). B is sometimes referred to as "temperature factor" yet it is a misnomer because in some cases it may have nothing to do with temperature [229]. Arthur Wilson proposed a straightforward method to determine both K and the overall B [230].

For a given set of reflections that fall in a range of s in which the difference of the scattering factors can be neglected, the average values of equation 4.1.1 result in

$$\langle|F_{obs}|^2\rangle_s = K\langle|F|^2\rangle_s \exp(-2B\langle s^2\rangle) = K\sum_{j=1}^{N} f_j^2 \exp(-2B\langle s^2\rangle)$$

If the natural logarithm is applied to both sides of the previous equation, the expression becomes

$$\ln\left(\frac{\langle|F_{obs}|^2\rangle_s}{\sum_{j=1}^{N} f_j^2}\right) = \ln K - 2B\,\langle s^2\rangle$$

so that the fitting of a straight line in the plot of the mean obtained intensities normalized by the sum of scattering factors against the s range will result in the values of K and B. Experimental data will never give a straight line because this equation is based on the equiprobability of atomic positions, i.e. all points in the unit cell have the same probability of hosting an atom, yet structural regularities are the rules for crystals and some positions are likely preferred than others. Nevertheless, it gives a scale factor for the reflection intensities and an overall B that should be positive and conventionally around 1-2 Å^2 for reliable structure solutions in electron diffraction. This overall DP can be understood as a quality factor for the proposed structure model, while the assignment of a DP for each atom at the asymmetric unit allows to smear the sharp electrostatic potential obtained from the scattering factors, fit better the experimental potential, and independently assess the validity of each atomic position. Such atomic DPs are usually called Debye-Waller factors [57, 231].

The term **direct methods** (DM) describes those methods that try to derive phases directly from the observed amplitudes of the structure factors through mathematical relationships. These were established from the two most important properties of the electron density; it is positive everywhere and it is composed of discrete atoms. In 1953, Herbert A. Hauptman and Jerome Karle laid the concepts and probabilistic foundations of DM [232] and, around the same time, David Sayre presented the equation that revealed the triplet relation. The Sayre equation is defined as

$$F(\vec{g}) = \frac{(f_g/h_g)}{\Omega}\sum_{\vec{k}} F(\vec{k})F(\vec{g}-\vec{k})$$

where h_g is the scattering factor derived from the square of the electron density and Ω is the unit cell volume. If both sides of the equation are multiplied by $F(-\vec{g})$,

$$|F(\vec{g})|^2 = \frac{(f_g/h_g)}{\Omega}\sum_{\vec{k}} |F(-\vec{g})F(\vec{k})F(\vec{g}-\vec{k})|\exp\left[i\left(\varphi_{-g}+\varphi_k+\varphi_{g-k}\right)\right]$$

When $|F(\vec{g})|$ is large and real, it is likely that the large values from the right side of the equation will be positive and real as well. For this reason, if $|F(\vec{k})|$ and $|F(\vec{g}-\vec{k})|$ have large values, then

$$\Phi_{gk} \equiv \varphi_{-g} + \varphi_k + \varphi_{g-k} \simeq 0 \tag{4.1.2}$$

which is usually referred to as the triplet relation. Since this expression is given in a probabilistic form, probability techniques are needed to identify its reliability. Another important relation is derived from structure factors that are structure invariants, i.e. they are independent of the choice of origin. They are generally represented by the product

$$F(\vec{g}_1)F(\vec{g}_2)...F(\vec{g}_m) \approx |F(\vec{g}_1)F(\vec{g}_2)...F(\vec{g}_m)|\exp\left[\varphi_{g_1}+\varphi_{g_m}+...+\varphi_{g_m}\right]$$

when

$$\vec{g}_1+\vec{g}_2+...+\vec{g}_m = 0$$

The sets of $F(-\vec{g})F(\vec{k})F(\vec{g}-\vec{k})$ that fulfil the above condition are called **triplet invariants** and play the primary role in DM. Finally, normalized structure factors, $E(\vec{g})$, are introduced to have amplitudes that do not decrease with $\sin(\theta)/\lambda$ and, in this way, the triplet relations do not depend on the scattering angle.

$$|E(\vec{g})| = \frac{|F(\vec{g})|}{\sqrt{\langle |F(\vec{g})|^2 \rangle_{\vec{g}}}}$$

The probability formula for triplet invariants with a distribution associated to equation 4.1.2 was derived by William Cochran [233] as

$$P(\Phi_{gk}) = (1/L)\exp(G_{gk}\cos\Phi_{gk}) \tag{4.1.3}$$

where $G_{gk} = (2/\sqrt{N})|E_{\vec{g}}E_{\vec{k}}E_{\vec{g}-\vec{k}}|$ for materials with only one element inside the unit cell and $G_{gk} = 2(\sigma_3/\sigma_2^{1.5})|E_{\vec{g}}E_{\vec{g}}E_{\vec{g}-\vec{k}}|$ with $\sigma_n = \sum_{j=1}^{N} Z_j^n$, being Z_j the atomic number for the j-th atom, for different elements inside the unit cell. L is a normalization term. $P(\Phi_{gk})$ is a so-called von Mises distribution [234] with a maximum at $\Phi_{gk} = 0$ and it has a trend similar to a Gaussian function.

If there are r pairs ($\varphi_{\vec{k}}$,$\varphi_{\vec{g}-\vec{k}}$) that define the same $\varphi_{\vec{g}}$ by equation 4.1.2, the probability distribution of $\varphi_{\vec{g}}$ becomes the product of distributions following equation 4.1.3

$$P(\varphi_{\vec{g}}) = \prod_{j=1}^{r} P_j(\varphi_{\vec{g}}) = L'\exp\left[\sum_{j=1}^{r} G_{gk_j}\cos(\varphi_{\vec{g}} - \varphi_{\vec{k}_j} - \varphi_{\vec{g}-\vec{k}_j})\right] \tag{4.1.4}$$

where L' is another normalization factor. The exponent can be developed in such a way that equation 4.1.4 becomes

$$P(\varphi_{\vec{g}}) = L'\exp\left[\alpha_{\vec{g}}\cos(\varphi_{\vec{g}} - \beta_{\vec{g}})\right]$$

where

$$\alpha_{\vec{g}} = \left[\left(\sum_{j=1}^{r} G_j\cos(w_j)\right)^2 + \left(\sum_{j=1}^{r} G_j\sin(w_j)\right)^2\right]^{1/2}$$

$$\tan\beta_{\vec{g}} = \frac{\sum_{j=1}^{r} G_j\sin w_j}{\sum_{j=1}^{r} G_j\cos w_j} \tag{4.1.5}$$

with $G_j \equiv G_{gk_j}$ and $w_j \equiv \varphi_{\vec{g}-\vec{k}_j}$. Equation 4.1.5 is known as the **tangent formula** and it gives the most probable value for $\varphi_{\vec{g}}$.

Other relations have been derived for reliable estimation of phases, which are all based on the selection of "appropriate" sets of normalized structure factors moduli, the so-called **phase magnitudes**. All these relations are focused on identifying them, ranking them according to their effectiveness in estimating structure invariants or semi-invariants and deriving their related probability distributions. Semi-invariants are single phases or linear combinations of phases that do not change with an origin shift but are restricted to the positions of the unit cell with the same point symmetry.

The representation theory given by Carmelo Giacovazzo [235, 236] gives precise rules for the identification of the phase magnitudes by means of a general use of the space-group symmetry. The

program *Sir2014* used in this work is based on this theory [237]. Initially, triplet invariants are evaluated by means of the P10 formula defined by C. Giacovazzo [238] and an early figure of merit is used as an indicator for the more promising crystal phases [239]. The number of initial trials generated by the tangent formula depends on the size of the structure given by the user. Then, these candidate phases are refined via a direct-space procedure based on the iterative modification of the electron density distribution obtained from the initial phases in the diffraction space, and diagonal least-squares refinements [239]. A final figure of merit and a residual value are used to evaluate the found structure model with respect to the acquired reflection intensities. The bigger and the smaller these values are, respectively, the better the match between the model and the experimental data. The **residual** R is defined in *Sir2014* as

$$R = \frac{\sum_{\vec{g}\in M} ||F_{obs}(\vec{g})| - K'|F_{calc}(\vec{g})||}{\sum_{\vec{g}\in M} |F_{obs}(\vec{g})|} \tag{4.1.6}$$

where M is the set of reciprocal vectors available by the experimental data and K' is a factor that brings the calculated structure factor moduli to the same scale as the observed ones. Another evaluator factor is given, called **internal residual** R_{int}, that shows how good the observed reflections are with respect to the symmetries from the space group introduced as an input.

$$R_{int} = \frac{\sum_{\vec{g}\in M} |F_{obs}(\vec{g}) - \langle F_{obs}(\vec{g})\rangle|}{\sum_{\vec{g}\in M} |F_{obs}(\vec{g})|} \quad ; \quad \langle F_{obs}(\vec{g})\rangle = \frac{\sum_{\vec{h}\in M_{eq}(\vec{g})} (1/\sigma(\vec{h})^2)|F_{obs}(\vec{h})|}{\sum_{\vec{h}\in M_{eq}(\vec{g})} (1/\sigma(\vec{h})^2)}$$

where the sums of $\langle F_{obs}(\vec{g})\rangle$ run over the set of symmetry equivalent reflections $M_{eq}(\vec{g})$ related to $\vec{g}$ and $\sigma(\vec{g})$ is the standard deviation for the given reflection intensity.

Electron diffraction data are affected by dynamical intensity distribution and symmetry equivalent reflections may have different intensities. As a consequence, the question regarding which intensity reflection should be used as the equivalent one arises. In *Sir2014*, an algorithm called "best equivalent amplitude" (BEA) is used to improve the given structure solutions [240]. After an initial structure model is retrieved using the averaged amplitude of the equivalent symmetry reflections, only the equivalent amplitude that agrees best with the current structure model is selected to iteratively run the modifications of the electron density distribution and diagonal least-squares refinements.

4.1.3.2 Charge-Flipping Algorithm

The **charge-flipping algorithm** (CFA) belongs to a group of methods classified as heuristic dual-space iterative algorithms that try to find the atomic positions in the crystal structure through alternating modifications both in direct and reciprocal space [241, 242]. In contrast with DM, the applied modifications in both spaces are equally important to reach the algorithm convergence.

The CFA includes the following steps schematically displayed in Figure 4.1.6:

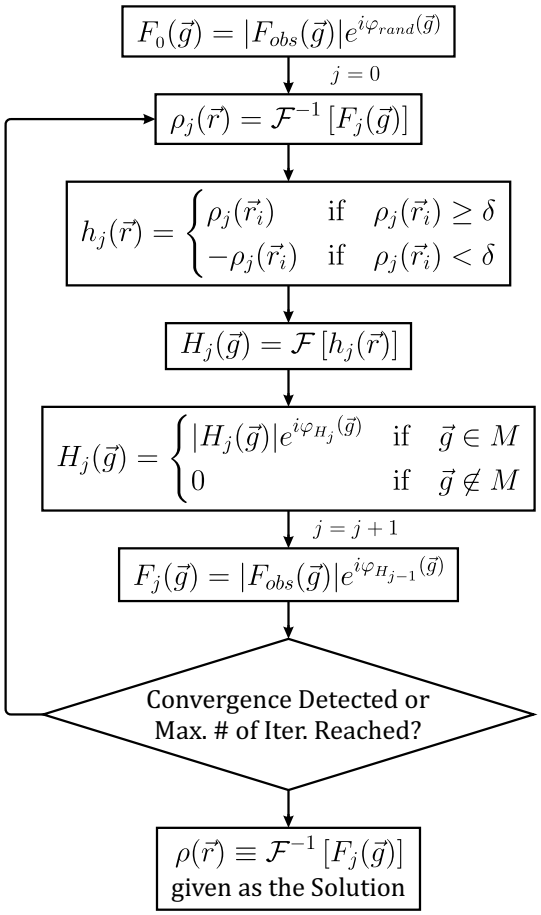

Figure 4.1.6: Workflow of the charge-flipping algorithm. φ_{rand} are the initial random phases that satisfy Friedel's law and δ is the flipping parameter.

1. An initial structure factor $F(\vec{g})$ is built by using the amplitudes from the experimental data $|F_{obs}(\vec{g})|$ and a set of random phases φ_{rand} that fulfil Friedel's law $\varphi(-\vec{g}) = -\varphi(\vec{g})$.

2. An inverse Fourier transform is applied to $F(\vec{g})$ to retrieve the electron density $\rho(\vec{r})$.

3. The flipping operation is applied, which consists on multiplying by -1 the values of $\rho(\vec{r})$ that are below a non-zero positive threshold parameter, δ. This can be thought of as an inversion of charge, hence the name "charge-flipping". Mathematically, $h(\vec{r})$ is obtained by

$$h(\vec{r}) = \begin{cases} \rho(\vec{r}_i) & \text{if} \quad \rho(\vec{r}_i) \geq \delta \\ -\rho(\vec{r}_i) & \text{if} \quad \rho(\vec{r}_i) < \delta \end{cases}$$

4. A Fourier transform is applied to $h(\vec{r})$ to obtain the distribution in the reciprocal space $H(\vec{g})$. This distribution is constrained to the positions $\vec{g}$ that are available from the experiment (a set M) and the rest are set to 0.

5. A new structure factor $F(\vec{g})$ is created by replacing the amplitudes of $H(\vec{g})$ with the observed amplitudes $|F_{obs}(\vec{g})|$. At this point, the algorithm convergence is evaluated by means of the residual value R_{cf} defined as

$$R_{cf} = \frac{\sum_{g \in M} ||H(\vec{g})| - |F_{obs}(\vec{g})||}{\sum_{g \in M} |F_{obs}(\vec{g})|} \tag{4.1.7}$$

   It is worth to note that R_{cf} is not used as a measure of the quality of the crystallographic solution but as an indicator of convergence.

6. Steps 2 to 5 are repeated until the algorithm convergence or the maximum number of iterations is reached.

The flipping parameter δ depends in a complicated way on the diffraction data resolution, the DPs and the elements present in the unit cell. However, it has been observed that a proper δ value is set in such a way that the ratio between the flipped and total density tends to 0.9 [243].

In comparison with DM, CFA is an interesting method because it does not need symmetry information about the dataset and it can be approximately evaluated directly from the electron density. Furthermore, the algorithm can be expanded to a n-dimensional space by describing the electron density on a n-dimensional discrete grid, which implies that structure solutions can be directly obtained from modulated structures or quasicrystals [244, 245]. In this work, the CFA implemented in the program *SUPERFLIP* [243] and integrated in *Jana2006* [246] was used.

4.1.3.3 Simulated Annealing

When a crystal structure has a large number of atomic positions in the asymmetric unit, light elements are present, difference between reflection intensities is not so strong, the diffraction data resolution is not high and/or completeness is low, successful structure solution from the previous methods may fail. In these cases, algorithms were developed in order to find a possible crystal structure based on a priori suspected structural information. For instance, organic crystals are usually synthesized and grown from molecular knowledge. The volume for a single molecule can be approximated via the Hofmann tables [228] and the number of molecules in the unit cell can be derived from the determined unit cell volume. In this way, the molecular structure and the number of molecules in the asymmetric unit can be used as a starting model. When inorganic crystals are investigated, the coordination number of certain elements can be suggested, and tetrahedrons, octahedrons or square planes can be used as starting structural inputs.

Simulated annealing (SA) is a global optimization algorithm based on an iterative improvement scheme that looks for the minimization of a cost function [247, 248]. In crystallography problems, this function is the R value. The term "simulated annealing" comes from the progressive slow down of cooling rate applied on a melt material in order to obtain a perfect crystalline solid. When applied to a structure solution problem, the SA works as follows:

1. The structural information that comprises the sub-structural units and the space group is given as an input and the variables to change, or degrees of freedom, are identified according to the symmetry of the space group.

2. A starting change of the variables Δx_i is applied. Each individual change is evaluated with respect to the R value. If the R value is decreased, the change is retained. If the R value is increased, a probability procedure is followed. In this case, the probability associated to Δx_i is given as a Boltzmann distribution, $P(\Delta R) = \exp(\Delta R/T_{eff})$, where T_{eff} is an effective temperature without units. Then, a random number is generated from 0 to 1 and compared to $P(\Delta R)$. If $P(\Delta R)$ is higher than the random number, the change is kept, otherwise it is dismissed and a new modification to the variable is applied. This procedure is running long enough in order to reach a steady state.

3. T_{eff} is decreased in slow stages and point 2 is followed once again for each different effective temperature. This process runs as long as needed until no further changes occur.

Since the iterative scheme of SA may stagnate in local minima, several trials have to be carried out with different starting arrangements of the sub-structural units to ensure that the final structure solution corresponds to a global minimum of the R value.

The SA included in *Sir2014* was used in this work [237]. It provides an easy and friendly graphical user interface to enable the change of the different structural parameters and apply restraints to the inter-atomic distances and angles. It also checks that the crystallographic solution does not have overlapping atoms [249]. The R value used as cost function in *Sir2014* is given by

$$R_{SA} = \left[\frac{\sum_{\vec{g} \in M} (|F_{obs}(\vec{g})| - |F_{calc}(\vec{g})|)^2}{\sum_{\vec{g} \in M} |F_{calc}(\vec{g})^2|} \right]^{1/2} \tag{4.1.8}$$

4.1.4 Kinematical Refinement

After an electron density or electrostatic potential is retrieved from structure solution algorithms, the following meaningful step is to refine it. **Kinematical refinements** are referred to methods developed to complete or finely adjust the structure model based on the calculation of structure factors following the kinematical theory of diffraction.

When a crystal structure contains light and heavy atoms, an approach called **Fourier synthesis recycling** is quite useful. Here it is supposed that an initial model in which the heavy atoms are located by DM or CFA can be used in order to identify the light ones. In this way, structure factors $F(\vec{g})$ are built from the observed amplitudes and the corresponding calculated phases $\varphi_c(\vec{g})$ from the initial model. The resulting electron density will show the heavy atom positions but it will most likely reveal weak scattering parts of the structure. In general, this process has to be carried out more than one time until the structure is completed. Each cycle has to run with the calculated $\varphi_c(\vec{g})$ of the last obtained model. It is worth to point out that these Fourier cycles do not only allow to locate undiscovered atomic positions but also improves the positioning of the already found ones. In organic crystals, it can be used to look for molecular fragments in which all their elements have similar atomic number.

Another quite frequently used method to check and/or refine the structure is the **difference Fourier synthesis**. In this case, two different Fourier series are defined:

$$\rho_{calc}(\vec{r}) = \frac{1}{\Omega} \sum_{\vec{g} \in M} F_{calc}(\vec{g}) \exp(-2\pi i \vec{g} \cdot \vec{r})$$

$$\rho_{obs}(\vec{r}) = \frac{1}{\Omega} \sum_{\vec{g} \in M} F_{obs}(\vec{g}) \exp(-2\pi i \vec{g} \cdot \vec{r})$$

where

$$F_{calc}(\vec{g}) = \sum_{j=1}^{N} f_j \exp(2\pi i \vec{g} \cdot \vec{r}_j)$$

$$F_{obs}(\vec{g}) = |F_{obs}(\vec{g})| \exp(2\pi i \varphi_c(\vec{g}))$$

in which the sum of $F_{calc}(\vec{g})$ runs over the atomic positions r_j of the structure model and $\varphi_c(\vec{g})$ is the phase related to $\vec{g}$ and given by $F_{calc}(\vec{g})$. Then, the difference Fourier map $\Delta\rho$ is obtained

$$\Delta\rho(\vec{r}) = \rho_{obs}(\vec{r}) - \rho_{calc}(\vec{r}) = \frac{1}{\Omega} \sum_{\vec{g} \in M} (|F_{obs}(\vec{g})| - |F_{calc}(\vec{g})|) \exp[i(\varphi_c(\vec{g}) - 2\pi \vec{g} \cdot \vec{r})]$$

Since there is a limitation on the available observed data, the Fourier series show some ripples around peaks that are proportional to the peak height. However, the difference series will cancel out this mathematical artefact because both have the same number of terms and the truncation errors will be similar.

The inspection of the $\Delta\rho$ map allows the structure refinement. Positive peaks will appear isolated when atoms are missed because $\rho_{obs}(\vec{r})$ will theoretically give an electron density at these positions that $\rho_{calc}(\vec{r})$ is not considering. In the case of already found atomic positions, $\Delta\rho$ may show a negative minimum at these positions close to a positive peak, which indicates that the atom location has to be shifted in order to fit better the calculated density. A similar data evaluation can be carried out to isotropically or anisotropically refine the DPs for each individual atom.

Apart from these two procedures, the most used technique to make a structural refinement is based on a **non-linear least-squares method**, which uses a cost function CF in order to estimate the best refined parameters. In a crystallographic refinement, the following CF has to be minimized:

$$CF = \sum_{g \in M} w(\vec{g})(|F_{obs}(\vec{g})| - |F_{calc}(\vec{g})|)^2$$

where $w(\vec{g})$ is a weighting function dependent on the reflection. Different weighting schemes are available that depend on how the reflection intensities are detected as well as the geometry of the acquisition. Most programs allow to change these schemes , for instance, *Sir2014* includes 18 different $w(\vec{g})$ [237]. Another standard program, $SHELX$ [250], applies by default

$$w(\vec{g}) = \frac{1}{\sigma(\vec{g})^2 + q|F_{obs}(\vec{g})|^2}$$

where q is adjusted in such a way that $\langle w\Delta F^2 \rangle$ values remain constant when reflections are grouped in different manners [251]. *Jana2006* applies similar default weights.

Since an initial structure model is available, $|F_{calc}(\vec{g})|$ can be expanded in a Taylor series and CF becomes

$$CF = \sum_{\vec{g} \in M} w(\vec{g}) \left(\Delta F(\vec{g}) - \sum_{k}^{m} \frac{\partial |F_{calc}(\vec{g})|}{\partial x_k} \Delta x_k \right)^2$$

where $\Delta F(\vec{g}) = |F_{obs}(\vec{g})| - |F_{calc}(\vec{g})|$, Δx_k is the variation applied to the k parameter of the structure model and m is the total number of parameters to be refined. The derivatives of $F_{calc}(\vec{g})$ with respect to the structural parameters are usually calculated by finite-differences methods [252]. x_j are constrained according to the symmetry in order to enhance the efficiency of the method and apply structurally meaningful modifications.

Then, the so-called normal equations are obtained by using different relations related to the variance-covariance matrix from the observed reflections [250],

$$B \cdot \Delta \hat{X} = D$$

where $\Delta \hat{X}$ is the vector with the estimated changes to be applied on the refining parameters that minimize CF. The elements in the matrices B and D are, respectively,

$$b_{jk} = \sum_{\vec{g} \in M} w(\vec{g}) \left(\frac{\partial |F_{calc}(\vec{g})|}{\partial x_j} \frac{\partial F_{calc}(\vec{g})|}{\partial x_k} \right) \tag{4.1.9}$$

$$d_j = \sum_{\vec{g} \in M} w(\vec{g}) \Delta F(\vec{g}) \frac{\partial |F_{calc}(\vec{g})}{\partial x_j}| \tag{4.1.10}$$

Sometimes, the off-diagonal elements of B are set to 0 in order to perform a rough refinement on the structure, called diagonal least-squares approximation (like in the DM procedure of *Sir2014*). Such approximation is strictly wrong because the refining parameters are not statistically independent from each other, but it provides a quick way to coarsely adjust the structure model.

The process of getting $\Delta \hat{X}$ can be repeated several times until the convergence is detected according to a residual value as in equation 4.1.6. The residual value can also be used to detect wrong modifications of the structure and subsequently apply less severe changes on the parameters. In this context, a **weighted residual** R_w can also be defined as

$$R_w = \sqrt{\frac{\sum_{\vec{g} \in M} w(\vec{g}) (|F_{obs}(\vec{g})| - |F_{calc}(\vec{g})|)^2}{\sum_{\vec{g} \in M} w(\vec{g}) F_{obs}(\vec{g})^2}} \tag{4.1.11}$$

Another evaluation parameter called goodness-of-fit (GoF) is given, defined as

$$GoF = \sqrt{\frac{\sum_{\vec{g} \in M} w(\vec{g}) (F_{obs}(\vec{g})^2 - F_{calc}(\vec{g})^2)^2}{n - m}} \tag{4.1.12}$$

where n is the number of observed reflections and m the number of refined parameters. If the weights for the observed data have been correctly assessed and the number of observed reflections used for

the refinement is significantly bigger than the number of refining parameters, the *GoF* should be close to unity.

It is worth to point out here that the observed data used for the refinement is not restricted to single-crystal patterns. Poly-crystalline diffraction data can be used as well given that its profile is of good quality, i.e. non-overlapped and sharp reflections, and good signal-to-noise ratio up to high diffraction data resolution. In this case, the most known and used refining approach is the Rietveld method for XRPD data, which calculates the entire X-ray diffraction profile and compares it with the discrete observed profile, point by point, to adjust the structure parameters [253]. This procedure is frequently referred as Rietveld refinement.

4.1.5 Dynamical Refinement

This refinement is a fine adjustment of the structure model according to its calculated electrostatic potential as well, yet it is based on the calculation of reflection intensities following the dynamical theory of diffraction. This has been usually referred to as **dynamical refinement**. The probability of multiple scattering events for X-rays and neutrons is not as high as for electrons, and that is the reason why it makes sense to apply such refinement only when dealing with electron diffraction data.

A structure refinement based on the dynamical theory is not a new topic. Some programs were developed to refine structures via calculated dynamical intensities back in 1993 [254, 255], but lack of computer power and "too" dynamical reflection intensities hindered the general use of the approach. It was not until PED and the 3D ED concept started to become generally used in the electron crystallography community that the interest in a dynamical refinement appeared again [256, 257]. During these last years, a module called *dyngo* was developed and implemented by Dr. rer. nat. Lukáš Palatinus in the program *Jana2006* that has brought the dynamical refinement of precession-assisted diffraction data to a more systematic use [115, 116]. In this context, the dynamical theory of diffraction and the algorithm of *dyngo* in *Jana2006* are briefly revisited hereunder.

4.1.5.1 The Dynamical Theory of Diffraction

The relativistically corrected and time independent Schrödinger equation describing high energy electron diffraction is:

$$\frac{1}{4\pi^2}\nabla^2\Psi(r) + \left(k_0^2 + \frac{2m|e|}{h^2}V(r)\right)\Psi(r) = 0 \tag{4.1.13}$$

where $\vec{k}_0$ is the incident wavevector in free space defined as $|k_0| = (2m|e|E)/h$, and $V(r)$ is the electrostatic potential of the crystal. $V(r)$ is periodic per definition, thus it can be expanded as a Fourier series

$$V(r) = \sum_{\vec{g}} V_{\vec{g}} \exp(-2\pi i \vec{g}\cdot\vec{r}) \tag{4.1.14}$$

where $V_{\vec{g}}$ is the Fourier coefficient of the total crystal potential $V(r)$ and it fulfils $V_{\vec{g}} = V^*_{-\vec{g}}$ to be real and without inelastic scattering events, i.e. absorption effects. $V_{\vec{g}}$ (in Volts, V) is described by the structure factor of the material as

$$V_{\vec{g}} = \frac{1}{\Omega}\sum_i f_e(s)\exp(2\pi i \vec{g}\cdot\vec{r}_i)$$

where $f_e(s)$ are the atomic scattering factors for electrons in V·Å^3 units that depend on $s = \sin(\theta_b)/\lambda$ [48]. A scaled electrostatic potential $U(r)$ is defined with $U_{\vec{g}} = (2m|e|V_{\vec{g}})/h^2$ in m^{-2} units to avoid to carry out the constants during the development of the Schrödinger equation solution.

According to the Bloch's theorem [258], the wave field $\Psi(r)$ must have the periodicity of the crystal lattice, thus it can be written as a sum of plane waves

$$\Psi(r) = \exp(-2\pi i\vec{k}\cdot\vec{r})\sum_{\vec{g}} C_{\vec{g}}\exp(-2\pi i\vec{g}\cdot\vec{r})$$

Since there is no limitation to the number of reciprocal lattice points, there will be, in principle, an infinite number of solutions or Bloch waves. Therefore, the general wave field that is a solution of the Schrödinger equation is

$$\Psi_{general}(r) = \sum_j \Psi_j(r) = \sum_j c_i \exp(-2\pi i\vec{k}_j\cdot\vec{r})\sum_{\vec{g}} C_{\vec{g}}^{(j)}\exp(-2\pi i\vec{g}\cdot\vec{r}) \tag{4.1.15}$$

where $\vec{k}_j$ is the wavevector j of the Bloch wave j inside the crystal and c_j is its coefficient to take into account the contribution of each Bloch wave to the total wave field. Now, if equations 4.1.14 and 4.1.15 are introduced in the Schrödinger equation, the so-called **dispersion equations** for each reciprocal vector $\vec{g}$ are obtained

$$\left[\vec{K} - (\vec{k}_g + \vec{g})^2\right] C_{\vec{g}}^{(j)} + \sum_{\vec{h}\neq\vec{g}} U_{\vec{g}-\vec{h}} C_{\vec{h}}^{(j)} = 0$$

where $\vec{K} = \vec{k}_0 + U_0$, which can be interpreted as an incident wavevector corrected by the mean inner scaled potential. The general approach to solve this equation is to force it into an eigenvalue equation and find the eigenvalues and eigenvectors.

Let $\vec{k}_j$ be defined as $\vec{k}_j = \vec{K} + \gamma^{(j)}\cdot\hat{n}$, where $\hat{n}$ is a normal vector to the crystal surface. Distances $\gamma^{(j)}$ can be geometrically interpreted as a displacement of the true dynamical dispersion surface from spheres drawn around every lattice point with radii K. If the back-scattered beams ($\gamma << K_n = \vec{K}\cdot\hat{n}$) are neglected and the previous relationship is used, the dispersion equations become

$$\frac{2KS_{\vec{g}}}{1+(g_n/K_n)}C_{\vec{g}}^{(j)} + \sum_{\vec{h}\neq\vec{g}} \frac{U_{\vec{g}-\vec{h}}}{\sqrt{1+(g_n/K_n)}\sqrt{1+(h_n/K_n)}} C_{\vec{h}}^{(j)} = 2K_n\gamma^{(j)}C_{\vec{g}}^{(j)}$$

where $S_{\vec{g}}$ is the excitation error that follows the approximated relationship $2KS_{\vec{g}} \approx K^2 - (\vec{K}+\vec{g})^2$, and the subscript n denotes the component of the vector projected along the unit vector $\hat{n}$. The result is the fundamental eigenvalue equation to be solved,

$$A\cdot C^{(j)} = 2K_n\gamma^{(j)}C^{(j)} \tag{4.1.16}$$

where A is called the **structure matrix** whose components are

$$a_{ii} = \frac{2KS_{\vec{g}}}{1+(g_n/K_n)} \quad ; \quad a_{ij} = \frac{U_{\vec{g}-\vec{h}}}{\sqrt{1+(g_n/K_n)}\sqrt{1+(h_n/K_n)}}$$

In this way, if n-beams are included in the calculation, the structure matrix becomes a $n \times n$ matrix. Alternatively to the proposed solution of equation 4.1.15, the "Darwin representation" can be used instead [259, 260, 261]. In this view, n plane waves are propagated inside the crystal along the $\vec{K} + \vec{g}$ direction and the wave field is defined as

$$\Psi(\vec{r}) = \sum_{\vec{g}} \phi_{\vec{g}} \exp[-2\pi i(\vec{K} + \vec{g}) \cdot \vec{r}]$$

in which the amplitude ϕ_g at a thickness t is

$$\phi_{\vec{g}}(t) = \sum_{i}^{n} c_i C_{\vec{g}}^{(i)} \exp(2\pi i \gamma^{(i)} t) \tag{4.1.17}$$

In order to have a continuous wave field, the incident waves and the ones present inside the crystal have to match at the entrance surface ($t = 0$). By using this contour condition, equation 4.1.17 becomes in the matrix form

$$\begin{bmatrix} \phi_0(t) \\ \phi_{\vec{g}}(t) \\ ... \end{bmatrix} = C \begin{bmatrix} \exp(2\pi i \gamma^{(i)} t) & ... & 0 \\ ... & ... & ... \\ 0 & ... & \exp(2\pi i \gamma^{(n)} t) \end{bmatrix} C^{-1} \begin{bmatrix} \phi_0(0) \\ \phi_{\vec{g}}(0) \\ ... \end{bmatrix}$$

where matrix C corresponds to a $n \times n$ matrix of coefficients $C_{\vec{g}}^{(i)}$ and matrix $S = C\{\exp(2\pi i \gamma t)\}C^{-1}$ is the so-called **scattering matrix**, which can be interpreted as an operator defined by a periodic object of thickness t applied to a set of incident electron waves. Interestingly, the scattering matrix is related to the structure matrix as

$$S = \exp\left[\frac{\pi i t}{K_n} A\right] \tag{4.1.18}$$

therefore, the scattering operator can be described directly from the Fourier coefficients of the electrostatic potential, the thickness of the crystal and its orientation with respect to the incident beam [46]. For the general case in transmission electron diffraction, there is only one incident electron wave, hereby $\phi_0(0) = 1$ and the rest of $\phi_{\vec{G}}(0)$ are zero, and, consequently, the intensity for a given reflection $\vec{g}$ is determined by the first column of the scattering matrix

$$I_{\vec{g}} = |s_{\vec{g}1}|^2$$

One of the interesting consequences of this development is that the Friedel law is not fulfilled anymore and the determination of the correct configuration for non-centrosymmetric structures is possible [262, 263]. In X-ray diffraction, the anomalous scattering, which is a physical process linked to the absorption effect of X-rays with elements inside the crystal, allows in some cases to distinguish chirality [264]. In the case of electron diffraction, the difference in Friedel's pairs is the result of a pure elastic scattering event. Mathematically, the exponential of a matrix is $\exp^X = \sum_{k=0}^{\infty}(1/k!)X^k$, therefore each component $s_{\vec{g}1}$ will be composed of several Fourier coefficients. Physically, each reflection of a diffraction pattern depends on the structure factors of all simultaneously excited ones. Thereby, electron diffraction is presented as an alternative method to determine absolute structures by means of the calculation of reflection intensities based on the dynamical theory of diffraction [168].

4.1.5.2 The Two-beam Approximation

The two-beam condition is achieved when the crystal is tilted in such a way that only two beams are simultaneously excited. This is strictly not possible because other nodes of the diffraction space will be always excited in electron diffraction, yet it is assumed to be in this condition when the primary and a diffracted one have most of the intensity of the pattern. Moreover, this approximation is the only case in the theory of dynamical scattering from which an analytical solution can be directly obtained.

If only the excitation of the primary wave and a diffracted wave $\vec{g}$ is considered, the dispersion equations become

$$\begin{bmatrix} -2K_n\gamma & U_{-\vec{g}} \\ U_{\vec{g}} & 2KS_{\vec{g}} - 2K_n\gamma \end{bmatrix} \begin{bmatrix} C_0 \\ C_{\vec{g}} \end{bmatrix} = \begin{bmatrix} 0 \\ 0 \end{bmatrix}$$

where it has been taken into account that the surface normal is approximately perpendicular to the beam ($K_n >> g_n$). By setting the 2×2 matrix determinant to 0, the solutions for γ are obtained

$$(2K_n\gamma)^2 - 2KS_{\vec{g}}(2K_n\gamma) - |U_{\vec{g}}|^2 = 0$$

$$\gamma = \pm\frac{KS_{\vec{g}}}{2K_n}\sqrt{(KS_{\vec{g}}) + |U_{\vec{g}}|^2}$$

When these two solutions are used in the dispersion equations, the coefficients C_0 and $C_{\vec{g}}$ are retrieved

$$\begin{array}{ll} C_0^{(1)} = \cos(\beta/2)\exp(-i\varphi_{\vec{g}}) & C_{\vec{g}}^{(1)} = \sin(\beta/2)) \\ C_0^{(2)} = -\sin(\beta/2) & C_{\vec{g}}^{(2)} = \cos(\beta/2)\exp(i\varphi_{\vec{g}}) \end{array}$$

where $\cot(\beta/2) = KS_{\vec{g}}/|U_{\vec{g}}|$ and $\varphi_{\vec{g}}$ is a general phase. Finally, these coefficients are used to construct the scattering matrix and the intensities for both beams are retrieved

$$I_{\vec{g}} = \frac{|U_{\vec{g}}|^2 \sin^2\left(\frac{\pi t}{K_n}\sqrt{K^2S_{\vec{g}}^2 + |U_{\vec{g}}|^2}\right)}{K^2S_{\vec{g}}^2 + |U_{\vec{g}}|^2}$$

$$I_0 = 1 - I_{\vec{g}}$$

therefore, the intensity distribution for both beams is complementary and modulated by a sinc function that depends on the thickness of the crystal, the excitation error and the structure factor related to $\vec{g}$. Figure 4.1.5 in section 1.1.3 showed an example of such intensity modulation from a silicon (004) reflection. One way to introduce the effect of weak beams on $I_{\vec{g}}$ is via the use of the perturbation method of Bethe in which an effective $U_{\vec{g}}$ is defined, known as Bethe potential [265].

4.1.5.3 The Refining Algorithm

The key for the successful refinement on a general basis is the use of PED. Crystalline domains are never ideal, hence thickness variations, bending and differences in the beam position on the crystalline area for subsequent diffraction pattern acquisitions make the determination of the exact orientation of the crystal with respect to the beam difficult. The advantage of a precessing beam is that these effects are averaged and the refinement of the crystal orientation for each diffraction pattern becomes

much easier, thus getting a better approximation of the calculated intensities with the experimental ones [257]. Recently, the fitting of the rocking curves by means of different functions in non-precessed data has become available for successful structure dynamical refinements [13]. However, the further testing and implementation of such approach is under development and its description has been left apart since most of the electron crystallography analyses of this work were carried out with beam precession.

The reflection intensity calculation in the dynamical theory of diffraction takes into account the excitation error. This means that different intensities for a given reflection will be obtained when the orientation of the crystal with respect to the incident electron beam is slightly changed. For this reason, the *hkl* input file for a dynamical refinement is different from the one based on a kinematical refinement. It contains the orientation matrix, the geometric position of the patterns, the precession angle and the reflection intensities for each frame. Such information is used by the program to calculate the intensities of the reflections according to the unit cell orientation of each pattern, and the refinement can run over the selected intensities of the experimental data that may contain more than one intensity related to a given reflection.

When dealing with a dynamical refinement, five parameters have to be considered in order to determine the diffracted waves that are included in the scattering matrices and the reflection intensities that are going to be used for the refinement.

1. **Number of integration steps**; N_{or}. The number of steps in which a precession cycle is divided in order to calculate the scattering matrix for each of the beam tilts with respect to the orientation of the crystal. The intensities obtained from the scattering matrices for a given reflection of a diffraction pattern are then integrated to obtain the corresponding precessed reflection intensity for that pattern.

2. **Maximum diffracted wave**; g_{max}. It is the diffraction data resolution in Å^{-1} used for the calculation of the scattering matrices. It is usually set to 0.2 Å^{-1} higher than the selected diffraction data resolution for the experimental data to run the refinement. This is done to take into account the contribution of higher angle diffracted waves on the intensity of the reflections considered for the refinement.

3. **Maximum excitation error (matrix)**; S_g^{max}(matrix). This is the maximum value of the excitation error for the reflections that are considered in the calculation of the structure matrices. It is usually set to 0.01 Å^{-1}.

4. **Maximum excitation error (refine)**; S_g^{max}(refine). It is the maximum value of the excitation error for the reflections in the experimental data to be considered in the refinement. It is usually set to 0.1 Å^{-1}.

5. **Pseudo-spike length**; RS_g. This parameter is defined as $RS_g = |S_g|/|g|\alpha_{PED}$, where the relationship $2KS_{\vec{g}} \approx K^2 - (\vec{K} + \vec{g})^2$ can be used to calculate S_g for each reflection. It is usually set below 1 and it is used to filter out reflections from the experimental data that are going to be used in the refinement. The higher it is, the more reflections will be taken into account. Its exact value is generally set in an empirical way since it depends on several factors, such as material crystallinity, charge density, precession angle and/or tilt step between patterns. For a

fixed tilt step of 1° and α_{PED} of 1°, it has been observed that, in general, a RS_g of 0.7 is good for high crystalline materials, like alloys, while it can be decreased to 0.3 for low crystalline materials like organics.

Figure 4.1.7 shows the algorithm used by the refinement program that takes into account the above parameters. As a first step, reflection intensities are calculated by using the input structure model, and initial R values are obtained. Then, the cost function defined from the obtained and calculated intensities in the non-linear least-squares procedure is used to estimate the change on the structural parameters. The new reflection intensities are calculated with the modified structure model and the refinement is evaluated by the resulting R values and maximum applied changes. If no significant change is obtained in terms of maximum change over standard uncertainty, or the maximum number of refinement cycles has been reached, the refining procedure is finalized and the modified structure model is retrieved. Otherwise, the cost function is built, the new estimated structural changes are applied and the R values are re-calculated until the finalization condition is met.

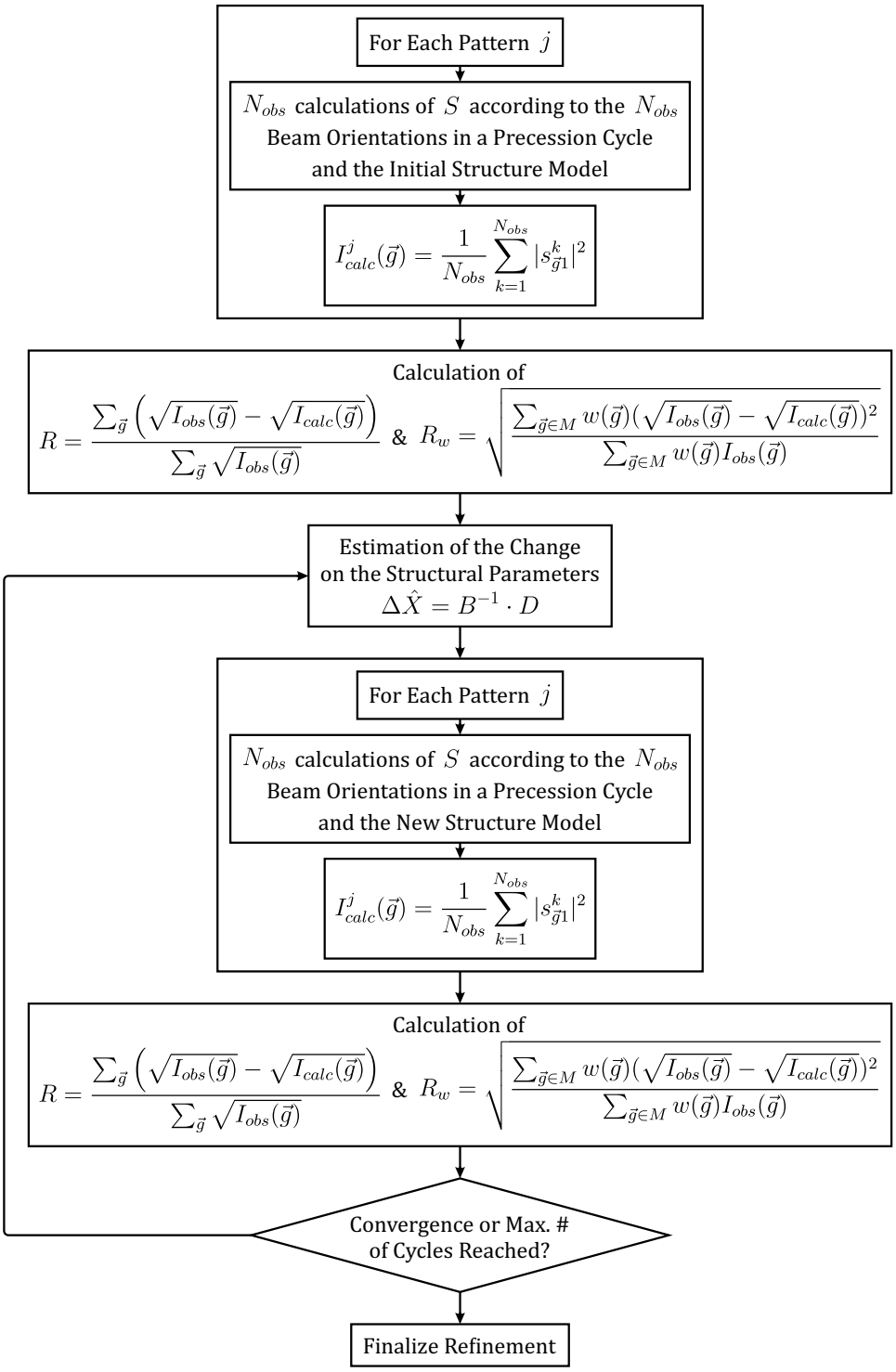

Figure 4.1.7: Workflow of the least-squares refinement following the dynamical theory of diffraction and the precession geometry. S is the scattering matrix defined by the structure matrix (equation 4.1.18) and B and D are the matrices from the normal equations of the non-linear least-squares procedure (equations 4.1.9 and 4.1.10). The sums inside the R values run over all observed reflection intensities considered for the refinement.

4.2 3D ED Acquisition Methods

Several acquisition methods to obtain 3D reconstructions of the ODS in a TEM have been developed since the invention of the technique about one decade ago [3, 4]. The initial reported technique was called **automated diffraction tomography** (ADT) and Figure 4.2.1 summarizes the steps followed by this routine.

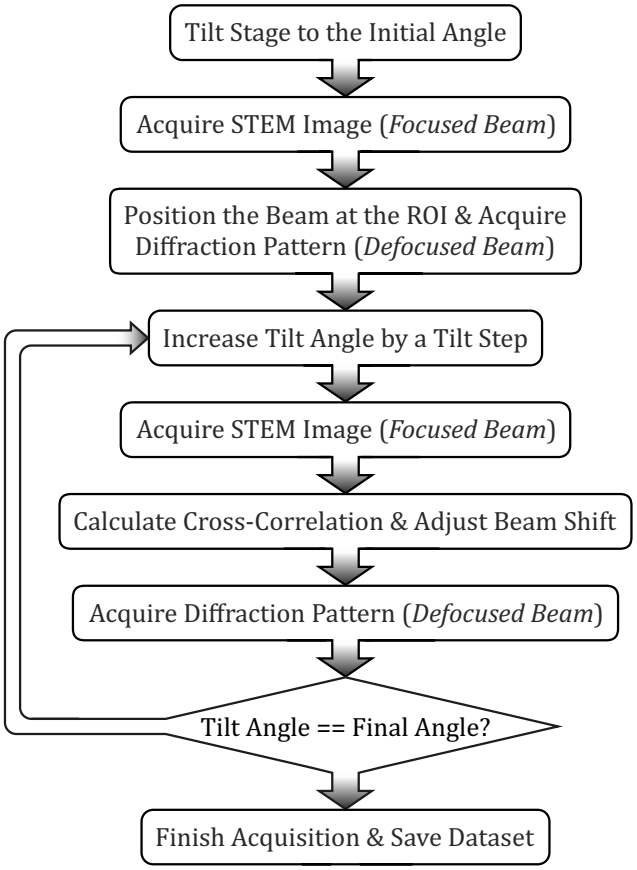

Figure 4.2.1: Steps followed by the ADT technique. Focused beam refers to the smallest probe size in order to acquire a focused STEM image. Defocused beam refers to an electron probe with the size previously set for the diffraction pattern acquisition.

ADT starts by tilting the stage to the initial angle and acquiring a first reference STEM image with a focused electron beam for high spatial resolution. Subsequently, the beam is placed at the ROI and the first diffraction pattern is acquired with a beam size previously selected. Then, the iterative and automated procedure follows; automatic tilt of the stage by an increment defined as the tilt step, generation of a reference STEM image, cross-correlation with the initially determined reference, adjustment of the beam shift according to the ROI displacement, which can be performed in a manual or automatic way, and acquisition of the diffraction pattern. This iterative scheme is repeated until the tilt angle reaches the selected final angle, when the whole diffraction dataset is stored. The usual tilt step using this methodology is 0.5° or 1°.

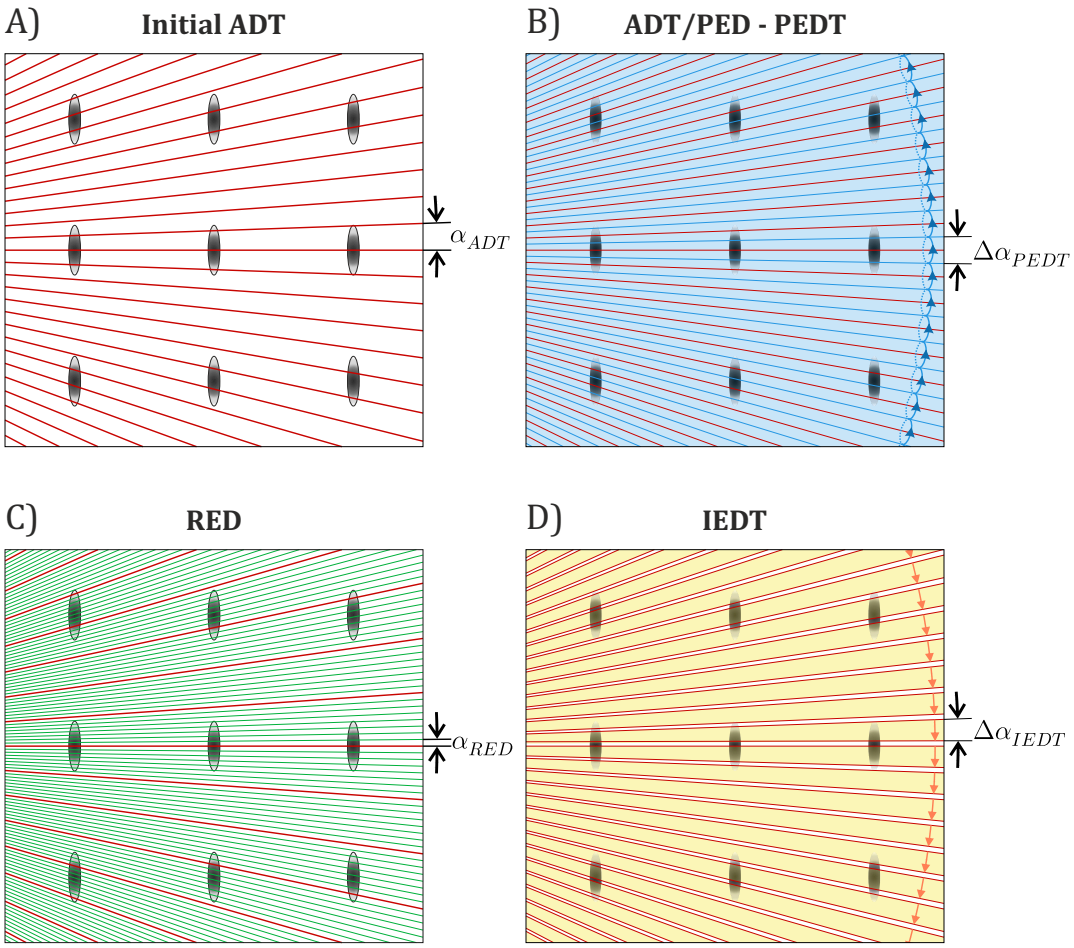

Figure 4.2.2: The sampling of the diffraction space according to the different acquisition methods. A) corresponds to the initial approach suggested by Kolb et al. [3], B) is related to the addition of precession (blue) to the initial ADT routine, called ADT/PED or PEDT [117], C) shows the technique that combines stage tilt (red) and beam tilt (green) for fine slicing, called RED [5], and D) corresponds to the method with continuous tilt of the stage that integrates the reflections through the tilting direction (yellow), called IEDT [8].

Although this technique proved to be superior in comparison to the acquisition of several zone-axis patterns [4], the missing wedge between frames induces to lose the related crystallographic information, the so-called missing step wedges. In addition, the dynamical effects are minimized with respect to zone-axis data; yet, they are still present, which makes the handling of reflection intensities by the kinematical theory difficult. For these reasons, other acquisition methods were developed to sample more from the diffraction space and retrieve better structure solutions and refinements. Some of these acquisition methods are: precession electron diffraction tomography (ADT/PED - PEDT) [117], rotation electron diffraction (RED) tomography [5] and integrated electron diffraction tomography (IEDT) [8], which in some other works is called MicroED [7] or continuous rotation electron diffraction [6, 9]. Figure 4.2.2 shows the difference in the sampling of the diffraction space according to the different techniques. Here is noted that the use of the word “rotation” for “tilt” of the goniometric stage may be misleading as rotation in a TEM is traditionally referred to the

azimuthal angle instead of the polar angle [76]. The conventional notation is the one used in this work.

PEDT couples the electron beam precession with the initial ADT technique (Figure 4.2.2B). The precession of the beam (α_{PED} usually set between 0.5° and 1.5°) induces the Ewald sphere to sweep the missing step wedge and integrate the reflection intensities on the detector, $\Delta\alpha_{PED}$, to increase the probability to measure them at their maxima and minimize the dynamical effects. In this way, averaged information of the missing step wedge is retrieved and successful structure solutions are obtained by using the same number of tilt steps as the initial ADT [266]. Since the better performance of precessed data was reported, the acronym ADT now refers to the automated acquisition of 3D ED data with precession in almost all cases. In other works, the PEDT acronym has been used independently of the automated or manual acquisition of the dataset or the use of TEM or STEM imaging to check the position of the crystal during a 3D ED data collection.

RED performs the crystal tilt in two steps; fine beam tilt steps of 0.01–0.20° combined with coarse goniometer tilt steps of 2–4° (Figure 4.2.2C). The fine slicing of the diffraction space results in finer rocking curves to determine the maximum intensity or integrate (software-wise) each reflection. Although the approach becomes better for unit cell determination, dynamical artefacts such as Kikuchi lines, double-diffraction or intensity redistributions cannot be minimized as in PEDT.

Finally, IEDT performs the acquisition while the sample is continuously tilted, resulting in a reduction of the sample beam exposure as well as an integration of the reflection intensities on the detector, $\Delta\alpha_{IEDT}$, and fine slicing of the space (Figure 4.2.2D). This technique does not apply a beam shift during the acquisition, thus relying on the crystal staying in the illuminated area. For this reason, the stage stability is the most important condition, especially in higher angular ranges. PEDT and IEDT techniques can be combined, the so-called PED-IEDT, in order to integrate reflections that are not covered when the camera is in stand-by (the time when the electronics is reading the data from the chip and saving it to the disk, i.e. the read-out time). If suitable stage velocity and precession angle are properly set, the sampled diffraction space can be maximized [8].

Another important aspect to take into account for the acquisition of 3D ED data is the detector used to collect the electron diffraction patterns. After the traditional photographic emulsions, the post-column CCD cameras were and are the most common used devices to collect diffraction patterns. The usual setup of a CCD camera consists of a scintillator, optical fibres and the CCD chip itself. The scintillator transforms the incoming electrons into photons, which are then transmitted by means of the optical fibres to the pixels of the CCD chip. These pixels are individual capacitors electrically isolated from each other by potential wells and they can accumulate charge in proportion to the incident radiation. In order to create the digital image, the charge in each pixel or cell is read by a parallel register that transfer the charge serially along a line in the chip through the modification of the applied potentials on the cells.

The higher dynamic range, linear response, uniform output, larger field of view and the direct availability of a digital frame prompted the CCD camera as the immediate preferential choice for recording images in a TEM. The only disadvantage was that its detective quantum efficiency (DQE), defined as the ratio between the square of the signal-to-noise output and input, is lower with respect to

films, yet the outlined advantages counter-balance the only significant handicap. Although reflection intensity quality is key for successful structure refinements based on dynamical intensities, the unit cell determination as well as the initial structure solution do not need such number of intensity levels. While the former needs the geometrical reflection positions, the latter was demonstrated to only need a classification or ranking of the reflection intensities as "small", "medium" and "strong" when they can be treated as *pseudo-kinematic* data, which was the methodology first implemented in X-ray techniques [267, 268, 269]. Therefore, in principle, any CCD camera could acquire 3D ED data for successful crystal structure determination given that this ranking condition is fulfilled.

The disadvantages of CCD-based detectors when applied to capture diffraction data are that they cannot work at high acquisition frame rates due to their high read-out time, and an overexposure of the primary beam may damage the camera scintillator. Furthermore, higher exposure times are needed for good signal-to-noise diffraction data, a main inconvenience for the investigation of beam sensitive materials. For these reasons, new cameras with higher frame rate and sensitivity based on the CMOS technology were launched in order to increase the number of patterns before these crystals are fully degraded as well as to make 4D-STEM acquisitions feasible. 3D ED acquisitions on such detectors through direct detection or intermediated by a scintillator and optical fibres have already reported good results [185, 270, 271]. Nevertheless, diffraction data even from beam sensitive crystals like organic compounds or metal-organic frameworks can be acquired with CCDs, and structure solutions can be successfully obtained prior to a Rietveld refinement [272, 273, 274].

4.3 Fast-ADT: The Acquisition Method

The recent IEDT acquisition methods coupled with CMOS-based cameras totally focus on operating specific microscope setups in TEM mode, which leave behind the advantages of STEM mode already demonstrated in chapter three, as well as the flexibility to implement the developed routines in other microscopes. For these reasons, this work was aimed to design a methodology implemented in both TEM and STEM microscope modes for an optimum, efficient and easy-accessible acquisition of 3D ED data in JEOL and Thermo Fisher TEMs. In other words, an all-in-one platform for systematic and routine acquisition of electron diffraction data, which has been called **fast and automated diffraction tomography** (Fast-ADT). This new technique has been designed in such a way that the initial ADT and IEDT idea for the diffraction space sampling can be selected, here called sequential and continuous approach, respectively. Furthermore, their operation does not depend on the precession of the beam, hence precession can be added in both approaches whenever it is wanted without changing any setting of Fast-ADT.

Another important point of a 3D ED acquisition is how the diffraction patterns are acquired. As shown in the second chapter, there are two ways to collect patterns in a TEM: by SAED, which uses an aperture positioned at the image plane of the OL to select the feature to be illuminated, and by NBED, which uses a nanometre-sized beam that can be placed at the region of interest through the deflector coils. The IEDT acquisition methods published up to now are based on SAED or NBED with beam sizes similar to the illuminated region of a selected aperture [6, 9, 270, 275]. Although it may be enough for microcrystals, the use of such beam settings is problematic when, for instance, individual nanoparticles in agglomerated nanoparticles have to be measured [276], or single-crystal tips of around 30 nm or less in diameter are only available for analyses [277]. Fast-ADT takes into account these possibilities by using the NBED mode with beam sizes down to the diffraction limit, which is achieved through the alignment of the TEM to produce a quasi-parallel beam following the procedures explained in the third chapter. This enables the acquisition of single-crystal diffraction data from nanometre-sized volume as well as microcrystals.

The routine followed by Fast-ADT is based on two complete stage tilts through the desired angular range. The first tilt scan is used to check and save the crystal position with respect to the tilt angle while the second one is the acquisition of the 3D ED data. Gemmi et al. first suggested this idea, although it was not fully developed neither implemented [8]. The main steps of Fast-ADT implemented in this work are summarized in Figure 4.3.1.

4.3.1 Parameters

Before starting a Fast-ADT acquisition, some parameters regarding the settings of the stage, the detector and the beam need to be defined.

4.3.1.1 Stage

The **stage parameters** correspond to the settings given to the alpha tilt of the goniometric stage. This includes the initial and final angles for the two complete stage tilts, the tilt step and the tilt

velocity for the sequential and continuous approach, respectively, and the tilt step between reference images for the generation of the crystal tracking file in the sequential approach.

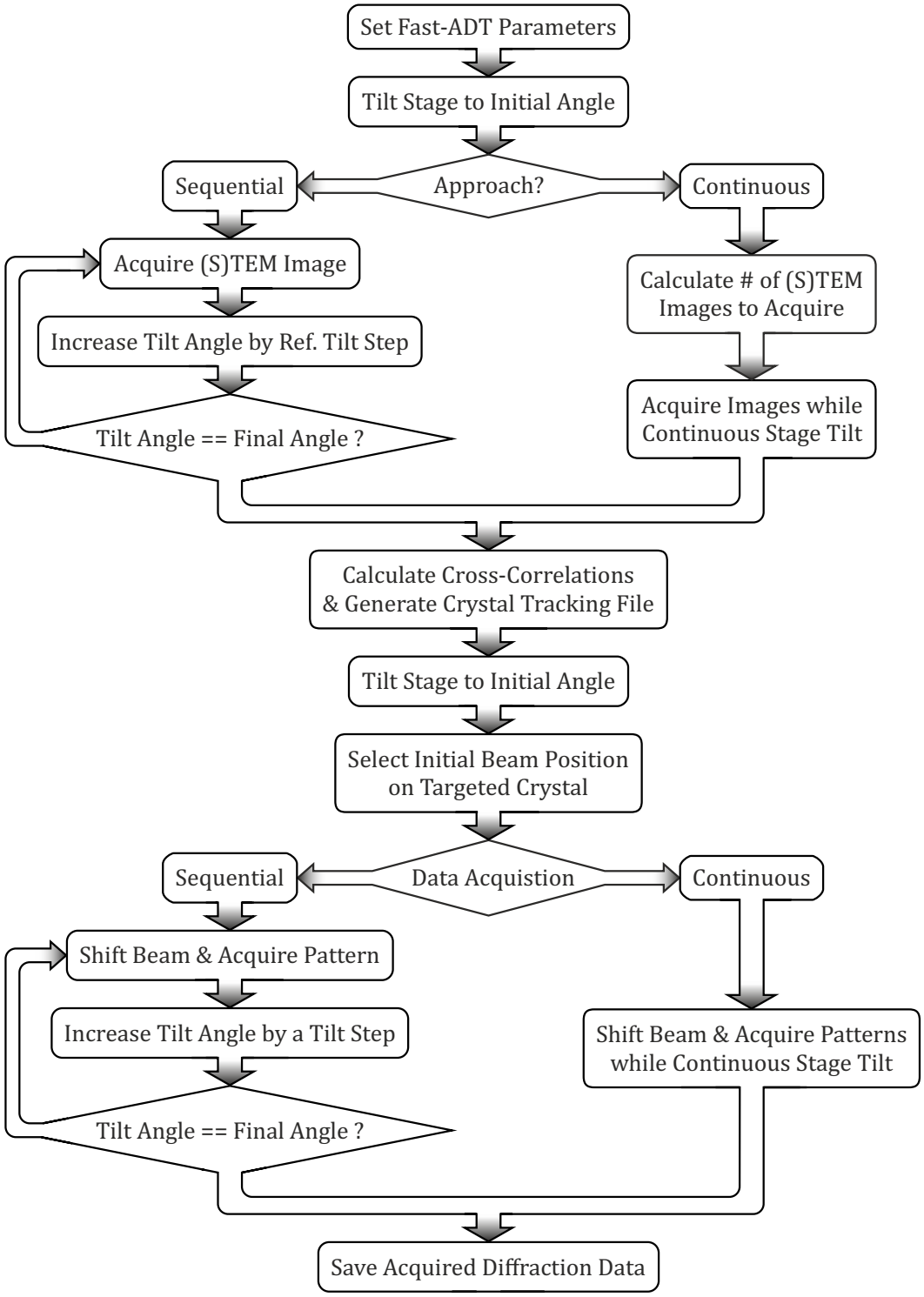

Figure 4.3.1: Steps followed by the Fast-ADT routine in TEM or STEM mode. The diffraction data acquisition approach has to be the same as the one used for the crystal tracking file generation.

4.3.1.2 Detector

The **detector parameters** refer to the settings of the camera for the acquisition of images and diffraction patterns. This includes the exposure time, binning and available frame processings. In imaging mode, the exposure can be decreased and binning increased because the acquired images are only used to generate a crystal tracking file, i.e. detector conditions that enable the visualization of the ROI are sufficient. When STEM mode is used, the exposure time of the image is changed to the dwell or pixel time. The selection of the parameters for pattern acquisition needs to consider the possible saturation and beam damage. Intensity saturation limit depends on the used detector but also on the scattering power of the crystal under the illumination. However, there is no general rule to avoid it because, intuitively, light-element crystals may give less intensity than heavy-element crystals, yet the crystallinity of the material itself has to be taken into account as well. In this situation, a testing period of time with different materials has to be spent to check which are the parameter regimes that allow good signal-to-noise reflection intensities without saturation. If the crystal is beam stable, several diffraction patterns at different orientations and camera parameters can be previously acquired to check the best conditions. When dealing with beam sensitive materials, the optimum parameters have to be available beforehand to minimize the electron dose on the sample. The exposure time and the beam diameter determine the electron dose rate of the beam, hence they have to be properly characterized as well when working with such materials.

4.3.1.3 Beam

Beam parameters refer to electron beam settings for the acquisition of reference images for crystal tracking (**imaging setting**) or diffraction patterns (**diffraction setting**). When acquiring images in STEM mode, the beam diameter is adjusted to have an electron probe with enough spatial resolution, minimized electron dose and sufficient intensity in the STEM detector. In TEM mode, the beam is defocused to illuminate the whole desired area. In this context, defocus means that the crossover of the electron probe is above the specimen plane to obtain a bigger illumination of the sample, which is different from the image defocus where it is understood as the focus or clarity of the image features. For diffraction pattern acquisitions, the beam diameter will be set in the same way in both operation modes of the TEM.

Another beam parameter that must be adjusted when working in TEM mode is the calibration of the beam shift. In STEM mode, the scanned image is used as reference to shift the beam at a desired position. The scanning system has the voltage sent to the deflector coils that corresponds to each pixel of the image available, thereby it can be applied directly. Yet in TEM this is not immediately available, and a previous calibration is required.

The beam shift is needed to determine which amount of voltage has to be sent to the DCs in order to produce a displacement of the beam selected from a reference TEM image, the so-called **beam shift calibration**. This calibration is performed by the determination of the framework that corresponds to the DCs with respect to the image framework. To do so, five images of a small beam are acquired of a non-shifted, x-positive shifted, x-negative shifted, y-positive shifted and y-negative shifted beam, all of these displacements from the DCs framework. Then, a cross-correlation of the non-shifted beam image on the other four allows to determine the coordinates (x, y) with respect to the image framework for each applied shift. The angle between the x-axis and y-axis of the DCs in image

coordinates, and the evaluation of the positive direction and length of both axes, give the necessary information to calculate the rotation angle θ_R between the displacement in the image (Δx_{img} and Δy_{img}) and DCs voltages (Δx_{DC} and Δy_{DC}), and the calibration V(a.u.)/nm along x and y (cal_x and cal_y).

$$\begin{bmatrix}\Delta x_{DC}\\ \Delta y_{DC}\end{bmatrix} = \begin{bmatrix} cal_x \cdot \cos\theta_R & cal_x \cdot \sin\theta_R \\ -cal_y \cdot \sin\theta_R & cal_y \cdot \cos\theta_R\end{bmatrix} \begin{bmatrix}\Delta x_{img}\\ -\Delta y_{img}\end{bmatrix} \tag{4.3.1}$$

where Δy_{img} is negative because the image framework considers the origin as the first pixel of the image at the top left corner, which would result in an inverted reference with respect to the DCs if not sign changed.

Generally, the setting of the beam parameters ends up here. However, there are some cases in which a correction by the projector coils to keep the primary beam of the diffraction pattern in the detector centre during a Fast-ADT acquisition is needed. It is not mostly required because the common observed pattern shift does not cut down significantly the diffraction data resolution. But it may happen if the electron beam is not well aligned to shift without tilt for the desired value of DL (diffraction pattern fine focus), thus the alignment should be followed once again to avoid it. In some microscope setups, such alignment is restricted to manufacturer engineers and an alternative method has to be implemented if the pattern shift is too large, called in this work as **diffraction shift calibration**. It is worth to point out that this inconvenience could appear in both TEM and STEM modes.

Initially, the pattern shift amount has to be identified for the deflector coils and projector coils, i.e. calibrate them. The procedure is the same as for beam shift calibration but this time the cross-correlation is done with the primary beam of the diffraction pattern for the two different coils. In this way, the rotation operation for the deflector coils between the image and coils framework is

$$\begin{bmatrix}\Delta x_{DC}(a.u.)\\ \Delta y_{DC}(a.u.)\end{bmatrix} = \begin{bmatrix} cal_x^{DC} \cdot \cos\theta_R^{DC} & cal_x^{DC} \cdot \sin\theta_R^{DC} \\ -cal_y^{DC} \cdot \sin\theta_R^{DC} & cal_y^{DC} \cdot \cos\theta_R^{DC}\end{bmatrix} \begin{bmatrix}\Delta x_{img}(nm^{-1})\\ -\Delta y_{img}(nm^{-1})\end{bmatrix}$$

and, equivalently, the one for the projector coils is

$$\begin{bmatrix}\Delta x_{PC}(a.u.)\\ \Delta y_{PC}(a.u.)\end{bmatrix} = \begin{bmatrix} cal_x^{PC} \cdot \cos\theta_R^{PC} & cal_x^{PC} \cdot \sin\theta_R^{PC} \\ -cal_y^{PC} \cdot \sin\theta_R^{PC} & cal_y^{PC} \cdot \cos\theta_R^{PC}\end{bmatrix} \begin{bmatrix}\Delta x_{img}(nm^{-1})\\ -\Delta y_{img}(nm^{-1})\end{bmatrix}$$

Once these calibrations are done, θ_R^{DC}, θ_R^{PC}, cal_x^{DC}, cal_y^{DC}, cal_x^{PC} and cal_y^{PC} are obtained, and the following expression can be used to determine the amount of voltage that needs to be sent to the projector coils in order to compensate the shift of the deflector coils

$$\begin{bmatrix}\Delta x_{PC}(a.u.)\\ \Delta y_{PC}(a.u.)\end{bmatrix} = \begin{bmatrix} cal_x^{PC} \cdot \cos\theta_R^{PC} & cal_x^{PC} \cdot \sin\theta_R^{PC} \\ -cal_y^{PC} \cdot \sin\theta_R^{PC} & cal_y^{PC} \cdot \cos\theta_R^{PC}\end{bmatrix} \times \begin{bmatrix} \cos\theta_R^{DC}/cal_x^{DC} & -\sin\theta_R^{DC}/cal_y^{DC} \\ \sin\theta_R^{DC}/cal_x^{DC} & \cos\theta_R^{DC}/cal_y^{DC}\end{bmatrix} \times \begin{bmatrix}\Delta x_{DC}(a.u.)\\ \Delta y_{DC}(a.u.)\end{bmatrix}$$

4.3.2 Acquisition Routine

Once the parameters are settled, a crystal has been targeted and its eucentricity has been found to minimize the x and y displacement with respect to the tilt angle, the Fast-ADT acquisition routine can start.

The stage is tilted to the selected initial angle and the acquisition of the crystal-tracking images starts. Since there are two different acquisition approaches, two different ways are implemented. The sequential approach acquires a (S)TEM image every reference tilt step, which is set to 5° by default, until the final angle is reached. In the continuous approach, the initial and final angles are used to calculate the number of frames to acquire according to a reference tilt velocity. Such velocity is calculated with respect to the desired exposure or pixel time in order to acquire a (S)TEM image every $\sim 5°$ while the stage is continuously tilting.

After the acquisition of the crystal-tracking images, a cross-correlation calculation is performed using the middle of the angular range as reference. Instead of using the whole image for the cross-correlation, which does not work properly due to the change of the crystal projection, a sub-image selected by a ROI is used in order to have more accuracy on the part of the crystal that the beam should follow. Sobel filter together with smooth filters are applied to the images to highlight the crystal edges and get more precise crystal positions. Figure 4.3.2 shows the use of different methods for the cross-correlation of a reference image at 0° with two other images at -40° and 40°.

The cross-correlation of the whole reference image with the other images results in a misfit of the ROI with respect to the targeted area (Figure 4.3.2 left row). The geometrical shrinking or enlargement perpendicular to the tilt axis caused by the projection of the crystal at different tilt angles is more evident for large features. Resizing of the targeted images provides a better positioning of the ROI (Figure 4.3.2 middle row). Here the images are expanded along the tilt axis direction according to the tilt angle in order to appear geometrically similar to the reference. After the cross-correlation, the resulting shift coordinates are translated back to the original non-modified image. This is more accurate and it definitely positions the ROI at the volume determined in the reference image. However, in case that the ROI for measurement would be at the rim of the crystal, the amount of electrons penetrating the crystal and thus the total intensity of the diffracted waves would be reduced. For this reason, the use of a sub-image subtracted from the full image using the ROI to cross-correlate with the other images provides a better solution (Figure 4.3.2 right row). It avoids the contribution of background artefacts, when they are not big but high contrasted features, and it keeps similar illuminated areas through the tilt scan granting a uniform total diffracted intensity. Nevertheless, the position of the ROI in all the crystal-tracking images should be carefully checked and, if necessary, modified after the automatic positioning of the cross-correlation. The use of the continuous approach produces blurred reference images along the direction perpendicular to the tilt axis, which increases the probability of a wrong cross-correlation positioning and makes subsequent position check almost mandatory for a successful Fast-ADT dataset.

Once the crystal positions have been found at each reference tilt step or velocity, the crystal-tracking file is generated. This file contains the beam shifts that need to be sent to the DCs in order to follow the crystal for each tilt angle of the desired 3D ED acquisition. In TEM mode, the positions

from the reference images are used to calculate the displacements in nm units, and equation 4.3.1 is used to transform these spatial displacements into electronic shifts of the DCs. In STEM mode, the transformation is not needed and the displacement amount in nm related to the framework of the scanned image is directly used. Since the tilt step or velocity is smaller than the one used for the crystal-tracking images, the values in-between the reference ones are linearly interpolated. When the diffraction shift is calibrated, the crystal-tracking file includes the compensation applied by the projector coils to correct the shift of the diffraction pattern.

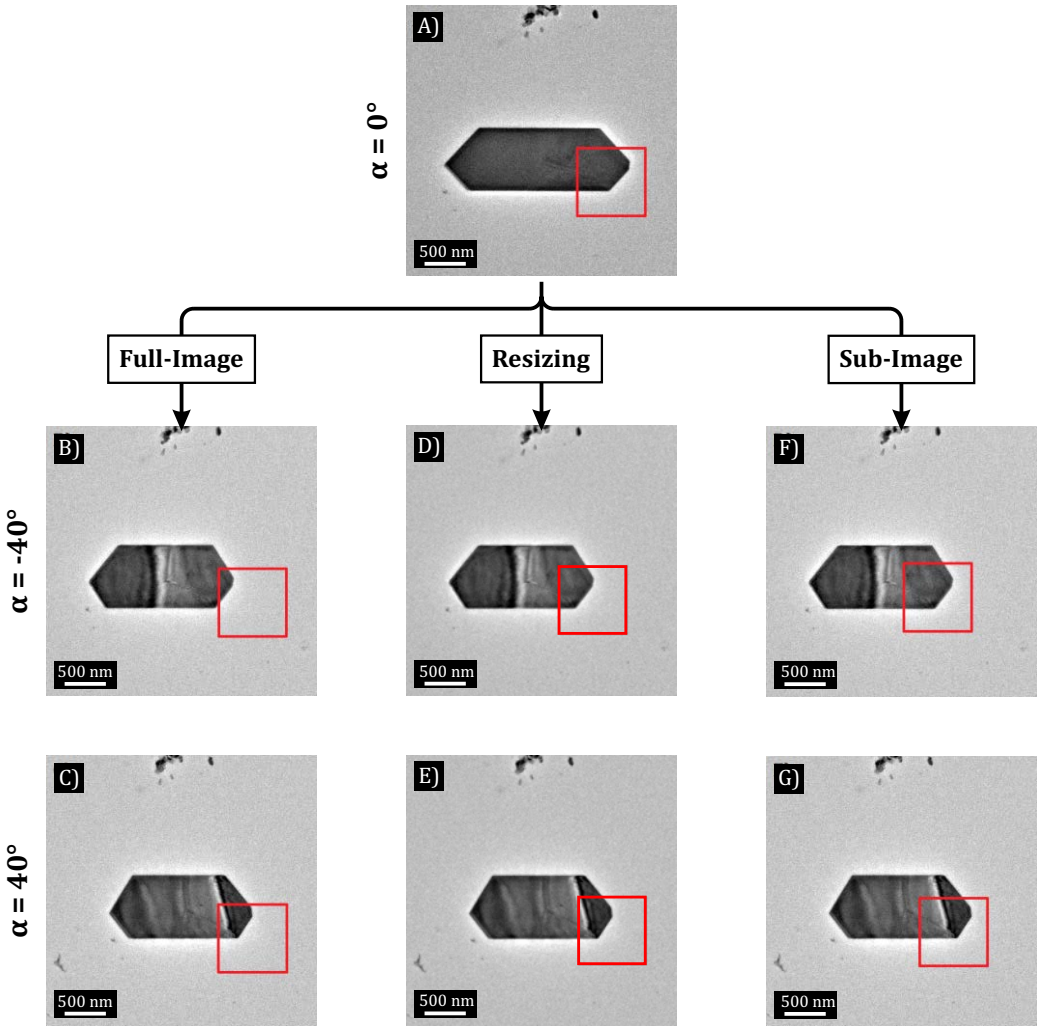

Figure 4.3.2: TEM images of a MoO_2 crystal at 0°, -40° and 40° of α-tilt angle with ROIs marked by red squares. A) is the reference image for the cross-correlation, B) and C) correspond to the resulting position of the ROI using the cross-correlation with the whole reference image, D) and E) by taking into account the shrinking effect of the projected crystal image, and F) and G) using the sub-image marked by the ROI on the reference image. The tilt axis is approximately along the vertical line of the image.

Then, the stage is tilted to the initial angle and a (S)TEM image is acquired that is used as a reference to select the desired starting position for the 3D ED acquisition. This position is stored and the electron beam is brought there only when the diffraction pattern collection begins, ensuring that the ROI is only illuminated when necessary to minimize the possibility of beam damage. Now, the beam setting is changed from imaging to diffraction. In TEM mode, the current position of the beam is obtained by a vertical and horizontal intensity integration of a TEM image with the diffraction setting selected, and the search for the maximum in these two intensity vectors that correspond to the x and y axes, respectively, gives the current beam position. In STEM mode, the position of the beam is immediately available in the last acquired STEM image.

Finally, the 3D ED acquisition can start. In the discrete approach, the alpha tilt of the stage is increased by the selected tilt step, the beam shift (and, if calibrated, the diffraction shift) is applied, according to the crystal-tracking file, and the diffraction pattern is acquired. This iterative process is performed until the tilt angle meets the selected final angle. When the continuous approach is used, the continuous tilt of the stage triggers the first diffraction pattern acquisition and, subsequently, electronic shifts of the beam according to the crystal-tracking file and the pattern acquisitions are followed until the total number of patterns, determined by the angular range and tilt velocity, is reached. It has to be noted that the approach used for the crystal-tracking file and the 3D ED acquisition has to be the same, as the tracking file is created by the step or velocity tilt parameter, and the stage does not produce the same x and y displacement when sequentially or continuously tilted. Once all diffraction patterns are collected, the diffraction dataset is stored and ready for processing.

4.3.3 Mechanical Limitations

The x and y movement of a feature of interest in a TEM grid with respect to the tilt angle is almost linear or non-existent when small angular ranges such as 60° (± 30°) or 80° (± 40°) are considered, but it becomes non-linear when angular ranges are as high as 120° (± 60°) [278]. An important step in the high angular regimes is to accurately find the eucentricity of the targeted crystal. This ensures that the crystal is moving as little as possible while it is kept in focus, otherwise it might not be possible to track it, even with the smallest magnification available in the *SA* optical regime of the projector system. Needless to say that the stage should be optimized for tomography experiments by the TEM manufacturer engineers. Furthermore, the crystal displacement depends on the position of the particle on the grid as well, thus the eucentricity has to be checked for new targeted crystals and a new set of crystal-tracking images has to be acquired for proper tracking.

Goniometric stages unfortunately have hysteresis behaviours produced by stage motors, holder design and holder mechanical condition, e.g., bending of the tip or holder axis not optimized for eucentric height at low values of z (middle of the pole piece gap). Therefore, the x and y movements of a crystal during the crystal-tracking file generation and 3D ED acquisition are never the same. This is the main limiting factor for the beam size because it determines when the beam will not illuminate the targeted crystal. For this reason, tilt-scan reproducibility tests for a given stage and holder have to be performed in order to assert the minimum beam size that ensures the acquisition of any pattern from the targeted crystalline domain during the two subsequent tilt scans.

A tilt-scan reproducibility plot shows the difference of the x and y position of a crystal between two consecutive tilt scans. Firstly, a reference feature is located on one of the tilt scan images and the positions of this feature on all the images are saved; $(x,y)_i^{1st\ Tilt\ Scan}$ and $(x,y)_i^{2nd\ Tilt\ Scan}$. Then the x_0 and y_0 position of the feature at the initial angle is subtracted to all the positions $(x,y)_i$ to obtain displacement values referred to the initial one ($x_i^s = x_i - x_0$, $y_i^s = y_i - y_0$). Finally these displacements are compared between the two tilt scans ($\Delta x_i = x_i^{(s:\ 2nd\ Tilt\ Scan)} - x_i^{(s:\ 1st\ Tilt\ Scan)}$, $\Delta y_i = y_i^{(s:\ 2nd\ Tilt\ Scan)} - y_i^{(s:\ 1st\ Tilt\ Scan)}$) and the hysteresis shift is calculated ($\Delta r_i = \sqrt{\Delta x_i^2 + \Delta y_i^2}$). In this context, the minimum beam size depends on the maximum hysteresis shift, Δr_{max}, and the size of the investigated crystal, $\sigma_{crystal}$, defined as the distance between the selected position for the actual measurement of the crystal and its end along the maximum shift direction. There are two different situations to determine the minimum beam diameter, which are sketched in Figure 4.3.3.

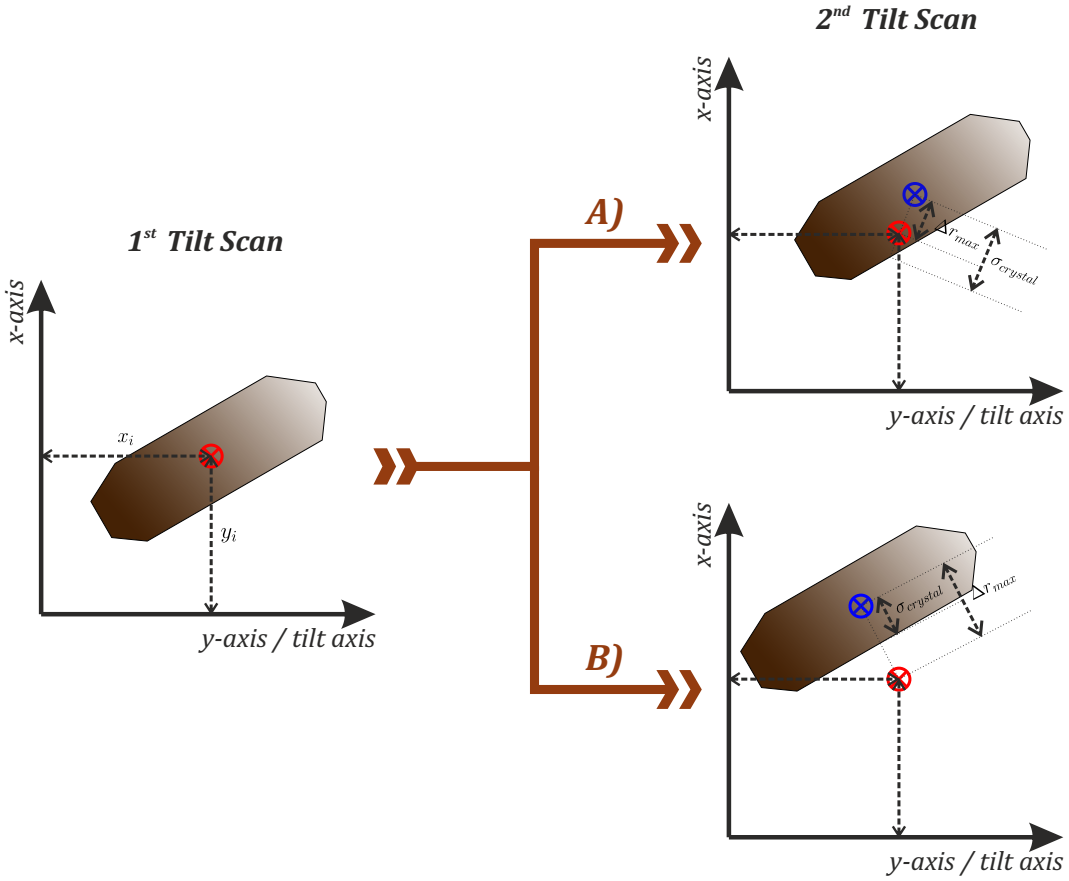

Figure 4.3.3: Schematics for the two possibilities A) and B) to determine the minimum beam size to illuminate a crystal during the Fast-ADT routine. The red-crossed circle is the position selected on the first tilt scan and the blue-crossed circle is the previously selected crystal position on the second tilt scan. Both tilt scan displays correspond to the same tilt angle.

If a targeted crystal has a $\sigma_{crystal}$ higher than Δr_{max}, the minimum beam size is the diffraction limit, which corresponds to case A) in Figure 4.3.3. On the other hand, if $\sigma_{crystal}$ is smaller than Δr_{max},

the minimum beam diameter is limited to the difference between Δr_{max} and $\sigma_{crystal}$, that is the case B) in Figure 4.3.3. This can be mathematically summarized in the following conditions:

$$\sigma_{crystal} \leq \Delta r_{max} \quad \rightarrow \quad \phi_{beam} > \begin{cases} 2(\Delta r_{max} - \sigma_{crystal}) & \text{if} \quad (\Delta r_{max} - \sigma_{crystal}) \geq \left(0.259\frac{\lambda}{\alpha}\right) \\ 0.517\frac{\lambda}{\alpha} & \text{if} \quad (\Delta r_{max} - \sigma_{crystal}) < \left(0.259\frac{\lambda}{\alpha}\right) \end{cases}$$

$$\sigma_{crystal} > \Delta r_{max} \quad \rightarrow \quad \phi_{beam} \geq 0.517\frac{\lambda}{\alpha}$$

where ϕ_{beam} is the beam diameter, λ is the electron wavelength and α is the convergence angle. 0.517 (λ/α) is the diffraction limit calculated as the FWHM of the Airy disk [107]. Figure 4.3.4 shows tilt-scan reproducibility plots for four different holders in three different TEMs mechanically aligned for tomography experiments.

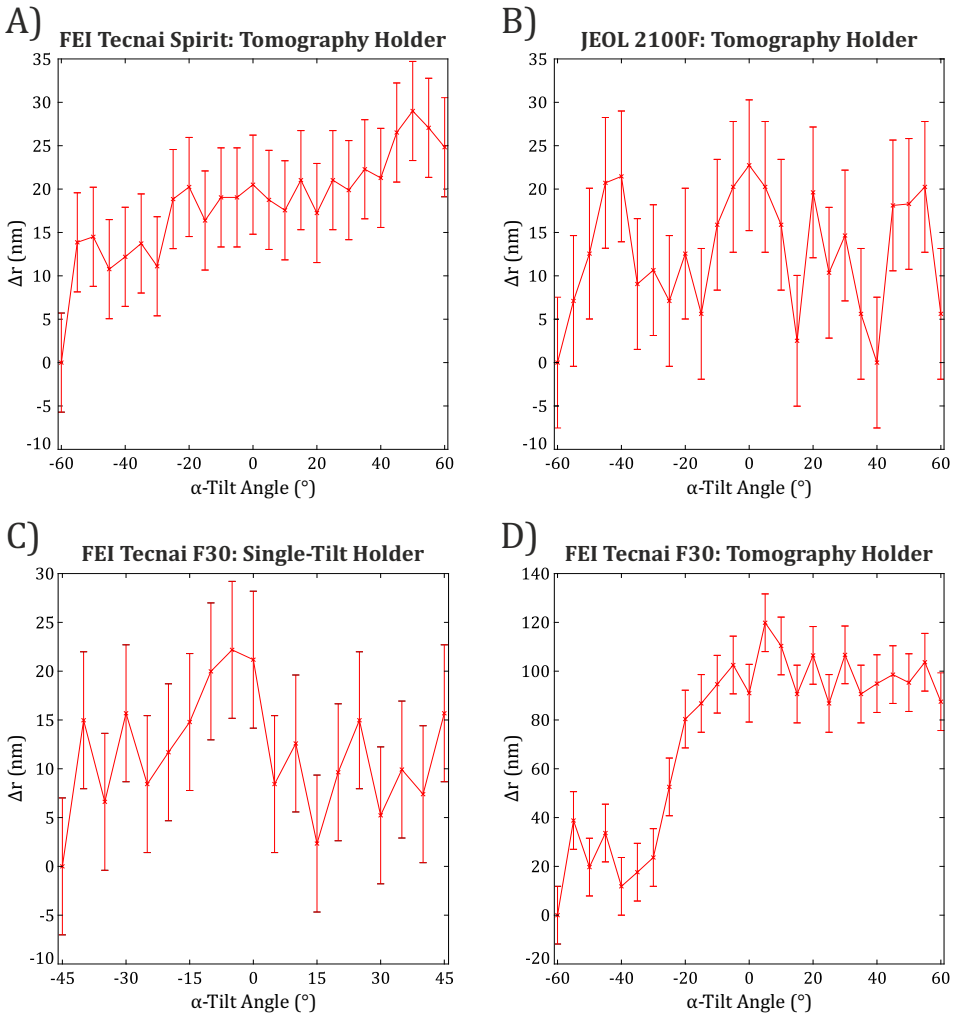

Figure 4.3.4: Tilt-scan reproducibility plots from A) a FEI tomography holder in a FEI Tecnai Spirit 120 kV, B) a Fischione tomography holder in a JEOL 2100F 200 kV, and a C) FEI single-tilt holder and D) a Fischione tomography holder in a FEI Tecnai F30 300 kV. The first tilt scan was performed with 5° of tilt step and the second one with 1° of tilt step. The same tilt angle positions were only selected for the plots.

Figure 4.3.4A corresponds to the FEI tomography holder in a FEI Tecnai Spirit at 120 kV and it has a Δr_{max} of about 30 nm, which means, for instance, that a beam size bigger than 40 nm will be needed for a successful Fast-ADT acquisition on a crystal of 10 nm in lateral size. Figure 4.3.4B shows the tilt reproducibility plot for a Fischione tomography holder in a JEOL 2100F at 200 kV, which results in a Δr_{max} of around 20-25 nm. The FEI single-tilt holder in a FEI Tecnai F30 at 300 kV shown in Figure 4.3.4C also has similar Δr_{max} and, in these setups, the beam size needs to be bigger than 20 nm following the previous crystal example. Figure 4.3.4D shows another plot for the FEI Tecnai F30 but using an intensively used Fischione tomography holder. In this case, Δr_{max} is of 120 nm due to a non-reproducible jump of the stage along the perpendicular direction of the tilt axis. Therefore, to analyse the same crystal size of 10 nm, the beam size needs to be bigger than 220 nm. However, this beam size could be unsuitable for some challenging samples.

One way to overcome this size-limitation is to position the centre of the beam at the edge of the crystal before starting the 3D ED acquisition, but the crystal-tracking file is created selecting the desired position of the crystal. In this way, the minimum beam size would be $2 \times (\Delta r_{max} - 2\sigma_{crystal})$, thus 200 nm for the tomography holder following the example above. In order to reduce this size limitation even more, other solutions have to be applied. One possibility is to acquire more than one pattern per tilt angle; the beam is shifted to pre-selected regions on the crystal-reference images, restraining the minimum beam shift to the beam diameter in order to avoid the illumination of already exposed areas. Furthermore, this idea allows the acquisition of diffraction datasets from different crystals or different parts of a "big" crystal with only one tilt scan, given that they are properly visible in all the crystal-tracking images. Another possibility is to use the ADT method, which allows a precise positioning of the beam for each tilt angle. The main disadvantage for both possibilities is the acquisition time, which is multiplied according to the number of patterns per tilt angle for the former alternative, and the STEM image acquisitions between patterns for the latter.

4.3.4 Experimental Setups

During the development of this doctoral work, two different programs were developed to acquire 3D ED datasets following the Fast-ADT acquisition routine.

The first one is based on the scripting language of the *Digital Micrograph* environment (DME), which enables the control of Gatan cameras, electron beam settings and alpha-tilt angles of the stage in one single ready-to-use platform. The DigiScan unit also provided by Gatan is used to generate the STEM images. In the case of the continuous approach, external software tools to control the tilt velocity of the stage (*Temspy* for Thermo Fisher microscopes and *GonioTool* for JEOL microscopes) are synchronized with the DME program. The resulting DME plug-in has been successfully tested in a FEI Tecnai F30 FEG operated at 300 kV, a JEOL 2100F FEG operated at 200 kV and a FEI Tecnai Spirit LaB_6 operated at 120 kV.

In this work, the Gatan UltraScan 4000 (US4000, 4096 × 4096 pixels) and UltraScan 1000 (US1000, 2048 × 2048 pixels) were used with the Fast-ADT program. The advantage of this detector series is its good quality reflection intensities for diffraction, but its main disadvantage is its high read-out time; $\sim$ 3.6 s for binning 2 of the US4000 and $\sim$ 1.6 s for binning 1 of the US1000. Although these times are feasible for the continuous approach, there is no real benefit when compared to the sequen-

tial one in terms of experimental time and data quality. The tilt velocity has to be reduced down to ~ 0.09 °/s for 4 s of exposure and binning 2 on the US4000, which is the usual camera setting for low-dose experiments [134]. For this reason, a second program was developed in *Matlab*-environment in order to take control of other fast frame-rate detectors for an optimum continuous approach.

This second design is based on the setup used by the precession-assisted crystal orientation and phase mapping technique provided by NanoMegas SPRL, commercially called ASTAR. It uses an external optical CCD camera mounted on the binocular position of the TEM to capture the diffraction patterns that are projected at the small or big fluorescent screen. The major advantage of such cameras is the high frame-rate, which means that acquisitions of a PED-IEDT experiment between $\pm$ 60° can be performed in less than 1 minute. The signal generator unit of ASTAR system is used to produce the beam shift and a self-modified tilt controller -following the design of Shi et al. [270]- is used to trigger the start of the continuous tilt. The use of external equipment specifically designed for this approach allows the direct synchronization of the camera acquisition, crystal tracking and stage tilting in a single environment. The resulting *Matlab* program has been successfully tested in a FEI Tecnai F30 FEG operated at 300 kV and a FEI Tecnai Spirit LaB_6 operated at 120 kV.

Finally, the traditional ADT routine has been re-programmed as a DME plug-in that works in TEM and STEM mode in order to meet the most challenging nanocrystal problems as exemplified in the previous subsection. In this case, it has been tested in a FEI Tecnai F30 operated at 300 kV and a JEOL 2100F operated at 200 kV.

4.3.4.1 The DME-based module

The advantage of this experimental setup is that it can be applied to any microscope with an available Gatan camera and the version 3 of *Digital Micrograph*. This program contains a C++-like object-oriented language that is able to take control of all camera parameters as well as the main functions of the TEM, thus a microscope control program can be developed inside *Digital Micrograph*. Although the code is interpreted instead of compiled like C++, the program is fast enough to synchronize the different routine parts.

Beam settings and shifts are controlled through the functions available in the *EMControl* library, which may change the functions depending on the software version. For instance, the function called *EMBeamShift()* is present with the old program versions, which uses relative values for the coil currents, while the function called *EMSetBeamShift()* is in the newer versions and uses absolute ones. The module developed here uses the *EMBeamShift()* because it creates the crystal tracking file with relative values, thus it does not depend on the exact same position of the crystal to perform the Fast-ADT routine. The *EMSetBrightness()* function is used to set the two different beam configurations for imaging and diffraction. When STEM mode is considered, the DigiScan scanning generator unit provided by Gatan is used, as it allows an easy acquisition of fast and low-dose scanned images and beam positioning through a STEM detector. In this case, the functions available in the *DigiScan* library are used for beam shift, because the change of the reference system between image coordinates and coils coordinates is internally calculated.

Although the control of the tilt velocity is not currently available in the *EMControl* library, the alpha-tilt angle can be set with the function *EMSetStageAlpha()* or *CMTiltGoniometerTo()*, which depends on the DM version as well. Therefore an automatic and totally DM-integrated Fast-ADT acquisition can be performed following the sequential approach. This impressively decreases the experiment acquisition time from the usual 1 hour to slightly more than 10 min, while using the same microscope tools and angular ranges. When the continuous approach is selected, the *Temspy* (Thermo Fisher) or *GonioTool* (JEOL) program has to be used. Here the module is prepared to synchronize with these manufacturer-dependent stage controller programs through a countdown for triggering the continuous tilt and frame acquisitions both in TEM and STEM mode.

As mentioned above, US1000 and US4000 Gatan cameras with 15 µm of pixel size are used for the present work. As the read-out time for the 4k x 4k chip is around 7.7 s, binning 2 is applied to decrease it and obtain a faster retrieve of the diffraction patterns. In the case of the 2k chip, the read-out is lower ($\sim$ 1.6 s) and binning 2 does not decrease it so strongly ($\sim$ 1.1 s). Binning 4 on both cameras is used for the acquisition of the crystal tracking images in order to speed up the whole Fast-ADT routine. The pre-specimen shutter is active during the read-out time in order to decrease the electron dose on the sample. The advantage of such big chips is the recording of patterns at high resolution with well-resolved reflections to properly solve structures of more than 100 Å of unit cell parameters, like pharmaceuticals or proteins.

4.3.4.2 The Matlab-based module

The optical CCD camera used in this setup is the Stingray F-145B provided by Allied Vision GmbH, which is plugged to the PC through a FireWire interface of a PCI card. The sensor has 1388 × 1038 pixels with a cell size of 6.45 µm x 6.45 µm and a 14-bit analogue-to-digital converter. This allows the acquisition of 14-bit data at a maximum frame rate of 16 fps at full resolution. *Matlab* was used in this setting as it has an easy accessible user interface to program the needed features: full control of the camera as well as signal generation and triggering through the hardware unit of the ASTAR system.

Images projected at the tilted fluorescent screen are distorted. The screen and binocular position are designed in such a way that the view of the binocular is perpendicular to the screen, thus the screen is usually tilted about 45° with respect to the TEM horizontal plane. This angle introduces a $\sqrt{2}$ image enlargement along the vertical direction and a magnification difference effect between the top and bottom part of the image, which is enhanced by large field of views. 2D homographies (projective transformations) have to be applied in order to recover the non-distorted image.

A homography is a non-singular, line preserving and projective application from a n-space to itself, $\Delta : E^n \rightarrow E^n$. It is represented by a square matrix of $(n + 1)$ dimensions, δ, which has $(n + 1)^2$ - 1 degrees of freedom. In this way, the more general form of the projective transformation is

$$\vec{r'} = \begin{bmatrix} x' \\ y' \\ z' \end{bmatrix} = \delta \cdot \vec{r} = \begin{bmatrix} d_{11} & d_{12} & d_{13} \\ d_{21} & d_{22} & d_{23} \\ d_{31} & d_{32} & d_{33} \end{bmatrix} \begin{bmatrix} x \\ y \\ z \end{bmatrix}$$

If a small field of view is used, like a small portion of the small fluorescent screen, the magnification difference effect is not significantly strong. This allows a simplification of the homography that has

to be applied to correct the geometrical distortions; $d_{31} = d_{32} = 0$ and $d_{33} = 1$. This is a type of homography called affine transformation that has 6 degrees of freedom, which includes 2 of scaling, 2 of rotation and 2 of translation. The simplified application for this particular case using homogeneous image coordinates is

$$\begin{bmatrix} x' \\ y' \\ 1 \end{bmatrix} = \begin{bmatrix} a_{11} & a_{12} & t_{13} \\ a_{21} & a_{22} & t_{23} \\ 0 & 0 & 1 \end{bmatrix} \begin{bmatrix} x \\ y \\ 1 \end{bmatrix}$$

where the t_i components correspond to the translation and a_{ij} components to the rotation and scale factors.

When a bigger area of the fluorescent screen is viewed, the image magnification is reduced and the projecting distortion clearly appears. This image distortion is shown as a vanishing point due to the higher difference of the image plane distance from the projector system between the top and the bottom of the acquired area. In other words, the optical system projects the image at the tilted screen with less magnification at the top of the image than at the bottom. For such cases all the components of the projective transformations are needed in order to take into account two more degrees of freedom that correspond to the control of the vanishing point.

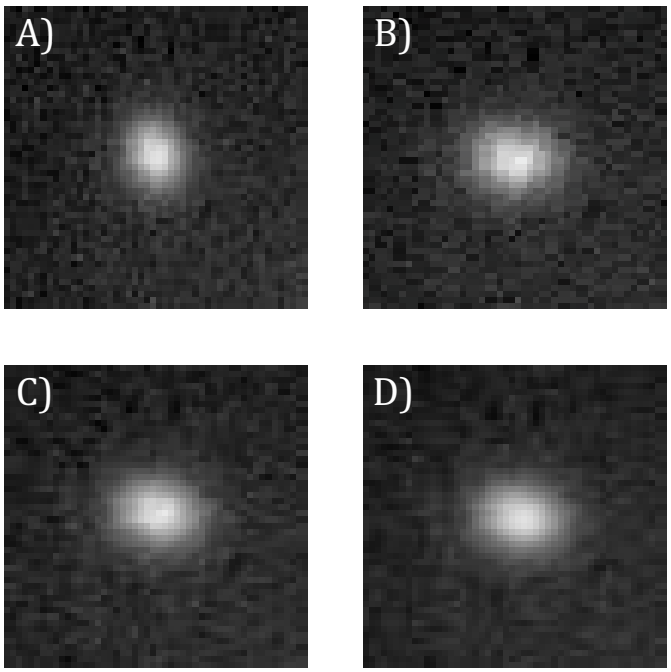

Figure 4.3.5: Images of a non-saturated silicon reflection A) without geometrical correction, and corrected and intensity interpolated by the B) nearest neighbour, C) bilinear and D) bicubic mapping.

The following step is to assign an appropriate intensity value to the new set of pixels created by the homography with respect to the distorted image. These intensity values are found using interpolation algorithms, which take the positions of the corrected image, calculate the theoretical positions in the original image using the applied factors and, finally, use their specific algorithm to assign the intensity. The interpolation algorithms in image processing are known as texture mapping and the

most common ones are the nearest neighbour, bilinear and bicubic. The first one assigns the intensity value of a pixel on the corrected image with respect to the nearest pixel from the theoretical position at the distorted image. The bilinear interpolation uses the 2 × 2 known nearer neighbour pixels for these theoretical positions. It weights each of these positions with the related computed pixel distance through two linear interpolations:

$$J(x'', y_1) = \frac{x_2 - x''}{x_2 - x_1} I(x_1, y_1) + \frac{x'' - x_1}{x_2 - x_1} I(x_2, y_1)$$
$$J(x'', y_2) = \frac{x_2 - x''}{x_2 - x_1} I(x_1, y_2) + \frac{x'' - x_1}{x_2 - x_1} I(x_2, y_2)$$
$$J(x'', y'') = \frac{y_2 - y''}{y_2 - y_1} J(x'', y_1) + \frac{y'' - y_1}{y_2 - y_1} J(x'', y_2)$$

where (x'', y'') are the coordinates of the distorted image transformed back to the reference system of the original image, and x_1, x_2, y_1 and y_2 are coordinates of the original image that correspond to the four nearest pixels to the position (x'', y''). $I(x_i, y_j)$ is the intensity value from the distorted image at the x_i and y_j position, and $J(x''_i, y''_j)$ is the interpolated intensity value for the corrected image position, (x'_i, y'_j). When the bicubic interpolation is applied, the 4 × 4 known nearer neighbour pixels from the theoretical position are used to determine the intensity for the corrected position.

Figure 4.3.5 shows the use of these interpolation algorithms on a non-saturated reflection acquired with the described experimental setup. Bilinear interpolation is preferred because it reduces the visual distortions when the scale factors are not integer values. Nearest neighbour interpolation lets some pixels appear larger than others and bicubic interpolation gives smoother intensity values because of the bigger area used to assign the intensity. Although bicubic could be interesting for smooth changes of intensity profiles, a small interpolation area is preferred to have a more step-like intensity profile for a reflection. Moreover, Figures 4.3.5C and 4.3.5D show that the difference between bilinear and bicubic is not significant, but bilinear is chosen because of its faster calculation and almost identical result.

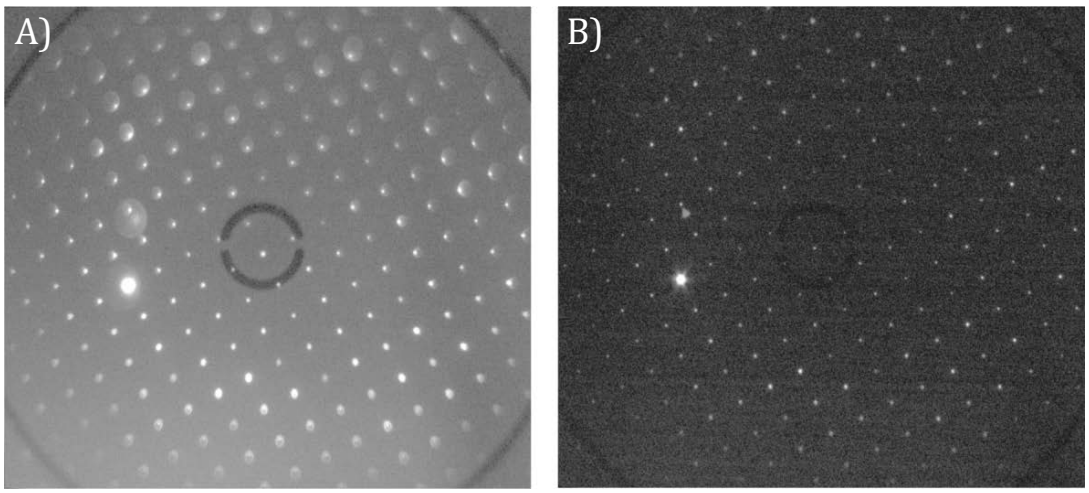

Figure 4.3.6: Diffraction patterns acquired from the big fluorescent screen of a FEI Tecnai Spirit TEM with the Stingray F-145B at A) low and B) large focus depths. Both images are geometrically corrected.

The different binocular geometries by the TEM manufacturers require the design of specific and different supports in order to place the camera and acquire images from the viewing chamber. Moreover, the C-mount optical lens for the camera also changes depending on the focused screen and the desired field of view. If the camera is focused on the small fluorescent screen, an optical lens of 50 mm of focal distance is enough to cover the whole area of the screen. If the camera is focused on the big fluorescent screen and a large field of view is needed, an optical lens of 25 mm of focal distance may be used. The big screen case scenario also requires a closed diaphragm for the optical lens; otherwise the focus depth is too small for the whole frame to be properly focused (see Figure 4.3.6). This is because of the relative tilt of the screen with respect to the plane of the CCD sensor, which on the small fluorescent screen is almost 0°. In JEOL microscopes the big fluorescent screen can be tilted 7° with respect to the TEM horizontal plane in order to minimize this image defocusing, while in Thermo Fisher microscopes it is not possible to do so at the present moment. Nevertheless, the 50 mm optical lens focused on the small screen was used in this setup. When a camera length that provides a diffraction data resolution of 0.8 Å and a reflection size of 15 pixels for proper reflection intensity integration are considered, the maximum measurable unit cell parameter is around 45 Å, which is suitable for most of the materials to be studied with this experimental setup. The big screen and bigger size sensors may be considered in order to deal with bigger unit cells. It is worth to say that a fast decay phosphor (type P46; Gd_2O_2S:Tb) should be used, instead of the high conversion efficiency and spatial resolution one (type P43; $Y_3Al_5O_{12}$:Ce), to vanish as fast as possible the remaining reflection intensities when high tilt velocities are used.

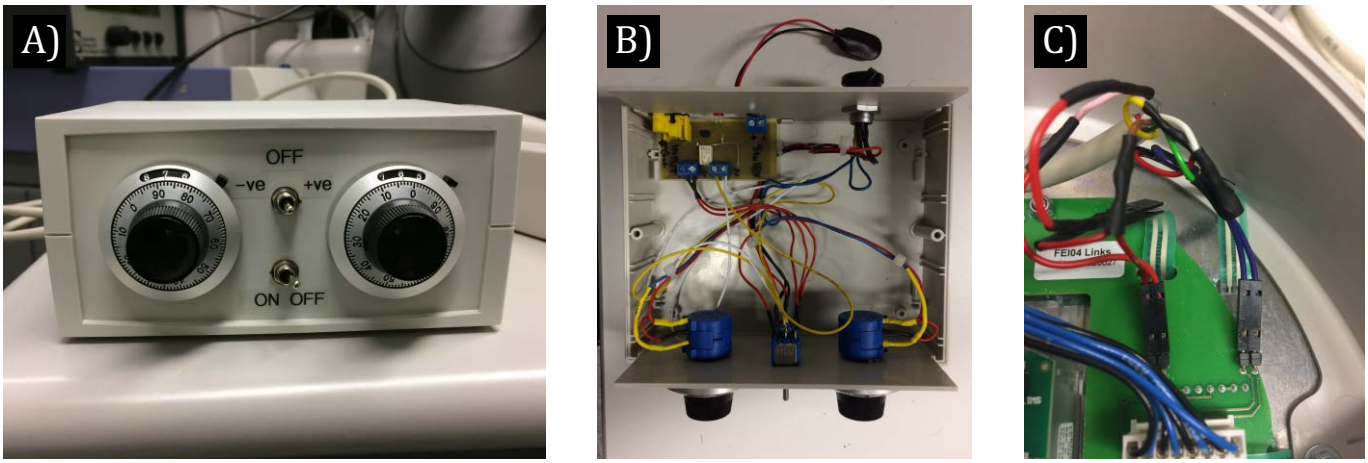

Figure 4.3.7: A) Image of the continuous tilt stage controller, B) the internal electronic circuitry and C) the connections to the left control panel of any modern FEI or Thermo Fisher Tecnai series TEM.

The shift of the electron beam is generated through an external voltage output device. The Fast-ADT program sends digital signals to the USB-3101FS voltage generator from the Measurement Computing company, which in turn sends analogue signals to the P1000 hardware unit provided by NanoMegas SPRL. Then, this external signal generator merges the shifting signal with the precession signal and sends the resulting mix to the DCs and ICs of the microscope.

The continuous tilt of the stage is produced by means of the continuous tilt controller shown in Figure 4.3.7. A self-made electronic circuit based on the design of Shi et al. [270] is used to shortcut

the resistance values produced by the pressure-sensor buttons of the control panel. Here, a relay, which triggers the use of the external resistances (properly calibrated for different tilt velocities) by means of a small electronic board that is energized through one of the available outputs of the USB-3101FS, is added for the initial synchronization of continuous tilt, detector acquisition and beam shift. Special acknowledgement is given here to Spiros Panaretos from NanoMegas SPRL to help in the design and manufacturing of this board. The electronic circuits of the resulting hardware are shown in Figure 4.3.8. This controller can be used on any FEI or Thermo Fisher microscope that uses the same control panel as the modern Tecnai series. It could be similarly implemented in JEOL microscopes after some hardware modifications.

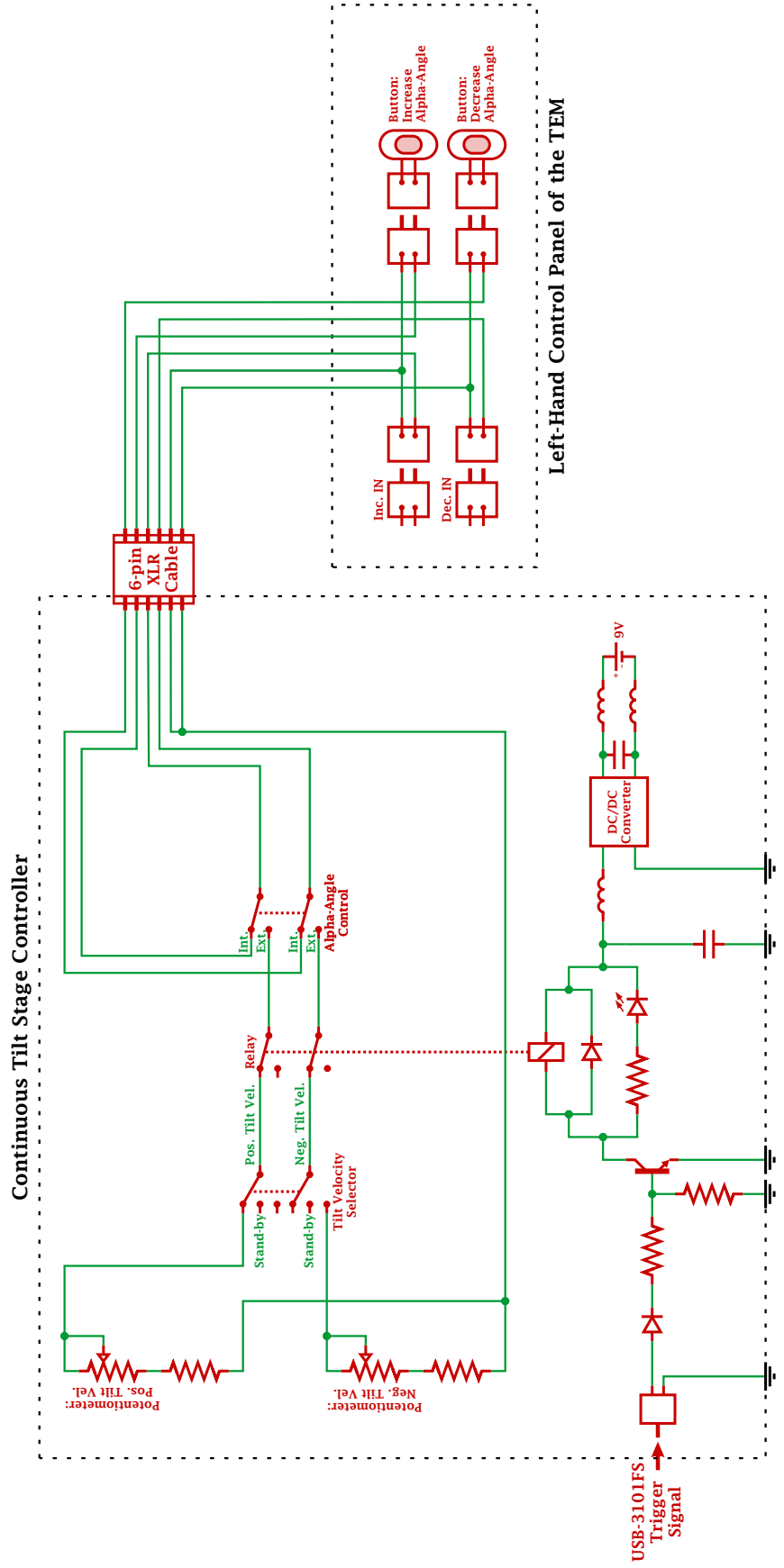

Figure 4.3.8: Electronic circuits for the continuous tilt stage controller and its connections to the control panel to shortcut the resistances determined by the pressure-sensor buttons.

4.4 Conclusions

Electron diffraction has been shown through this chapter as a consolidated method to structurally characterize different materials. A historical perspective has been explained in order to introduce the 3D ED technique, which is currently being used in several laboratories and it is continuously attracting attention due to its capability to acquire individual diffraction data from single nanocrystals. Most of the reported acquisition methods have been introduced and its advantages and disadvantages have been discussed to justify the motivation to develop the new Fast-ADT routine.

Fast-ADT is based on two tilt scans of the goniometric stage in which the first one is used to generate a crystal tracking file by acquiring images at the different tilt angles, and the second one is the 3D ED acquisition itself that tilts the stage, shifts the electron beam according to the tracking file, and acquires the diffraction pattern over the desired angular range in an automatic and optimum way. This acquisition routine has been implemented both in TEM and STEM mode and the acquisition can be performed by using the continuous or discrete tilt of the stage. In this context, an all-in-one platform has been developed with the aim to provide an acquisition software that can be adapted to the different technical characteristics of any TEM or the requirements of the material under study, and boost the use of electron diffraction in the scientific community. Figure 4.4.1 shows the icon used for the Fast-ADT programs.

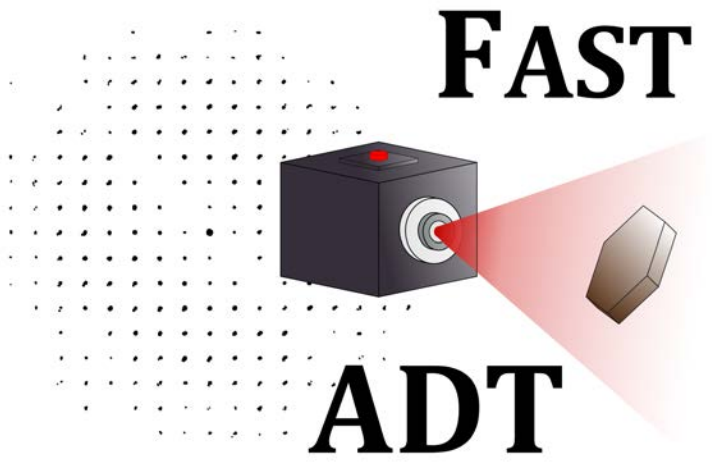

Figure 4.4.1: Fast-ADT program icon.

Fast-ADT was initially designed in STEM mode to overcome the limitations of previous approaches developed in TEM mode, while speeding up the traditional acquisition times of 3D ED datasets. Another software called *Instamatic* and written in *Python* has been freely available during these last years with a similar scope as the one presented in this work [279]. This program implements the RED and IEDT techniques as well as the serial crystallography approach in TEM mode [280, 9]. Although it has been demonstrated to work quite well for microcrystals [281, 282], it is not the most suitable option for acquiring individual diffraction data from the most nanometre-sized crystallites. That is

because of the beam registration problem, i.e., the positioning of the beam at the nanometre scale in TEM mode suffers from the aberrations of the projector system [173], and an optimum tracking tool is not available for the IEDT technique.

It is true that the Fast-ADT routine is not as fast as the automatic procedures implemented in *Instamatic*, which claims to acquire several 3D ED datasets from different crystals in less than an hour [9, 275], but the accuracy of the presented technique to position the nanometre-sized beam at the desired place of the crystal through the whole angular range of a 3D ED acquisition ensures that the measurement of a few crystals in one to three hours is sufficient to obtain good and reliable results of the specimen under study. In general, a few good single-crystal datasets are better than several textured or poly-crystalline ones that come from a full illumination of expected individual particles that are then found to be aggregates.

It is worth mentioning that all diffraction datasets acquired for crystal structure analysis in this work have been obtained without using the microscope where the quasi-parallel beam alignment was tested and characterized, the JEOL 2100 LaB_6. That is because the goniometric stage was not specifically aligned for tomography experiments and a slight tilt of the sample holder places the specimen out of the eucentricity, which makes the acquisition of 3D ED datasets complicated, since automatic procedures for x, y and z position adjustments similar to the ones implemented in image tomography software should be added that would increase the acquisition time as well as the total accumulated electron dose on the sample. Nevertheless, some of the author's PhD-candidate colleagues are using a JEOL 2100F FEG following the alignment steps explained in this work and good results have been obtained for phase and orientation maps as well as crystal structure determinations using the Fast-ADT technique [283, 284].

Up to this point, this work has shown how to align the TEM for an optimum acquisition of diffraction patterns according to the instrumentation available as well as the material under study, and a novel acquisition method has been presented to efficiently acquire 3D ED datasets. In this context, the TEM is enabled for its optimum application to the crystallographic characterization of different materials based on the diffraction space. The following chapters detail the use of such setup in several compounds to prove the high potential of electron diffraction for the study of crystal structures.

Chapter 5

Fast-ADT: Applications

We pay more attention to the content of messages than to information about their reliability.

Thinking, Fast and Slow
Daniel Kahneman

The previous chapter has described the Fast-ADT technique and the different experimental setups that can be used in order to run its acquisition method. Here, the technique is applied to three different crystallographic analyses to demonstrate its potential for structure characterization. The first one is a proof-of-concept on barium sulfate, a material stable under the illumination of the electron beam that is used to show how accurate a crystal structure determination can be by using the two Fast-ADT experimental setups. The second example is related to the quantitative study of diffuse scattering in a layer silicate and it serves for the comparison of these setups to point out the different benefits of specifically TEM-designed and external CCDs. Finally, the Fast-ADT technique is used to acquire a dataset from a new ferrosilicide to show the capability of electron diffraction to distinguish chirality in non-centrosymmetric crystal structures.

5.1 Interplay of Detectors & Acquisition Approaches

The aim of this section is to show how diffraction data acquired with the Fast-ADT technique provides good reflection quality for structure determination and refinement using particles of barite, as well as its suitability for disorder investigations by presenting the case example of the RUB-5 layer silicate. A post-column CCD detector with the sequential approach is compared to an external CCD camera with the continuous approach in order to highlight the differences in their use and show the different possibilities of the acquisition method.

5.1.1 Barite: Data Acquisition

Particles of barite ($BaSO_4$), an inorganic salt with an orthorhombic crystal system (*Pnma*) mostly used in oil and gas exploration that is stable under the electron beam, were chosen as a basic test sample [285, 286, 21]. Fine powder of the specimen was dispersed in ethanol and sprayed on a carbon-coated copper grid with a UIS250v Hielscher sonifier. The copper grid was loaded on a Fischione tomography holder and inserted in a FEI Tecnai F30 FEG operated at 300 kV. STEM images were acquired with a Fischione HAADF detector mounted at the side port of the TEM column. Three crystals were selected from this grid and two Fast-ADT datasets were acquired on each one with 1° of precession angle generated by the DigiStar unit provided by NanoMegas SPRL. One dataset was acquired with the Gatan US4000 post-column CCD camera and an electron beam set with spot size 6, gun lens 8 and a 10-µm CA. The other dataset was collected with the Allied Vision Stingray F-145B external CCD camera and spot size 6, gun lens 4 and a 10-µm CA were selected. A 200 nm quasi-parallel beam in STEM mode and Microprobe illumination mode was chosen in both cases. Figure 5.1.1 shows the images of the three crystals used for this Fast-ADT proof-of-concept.

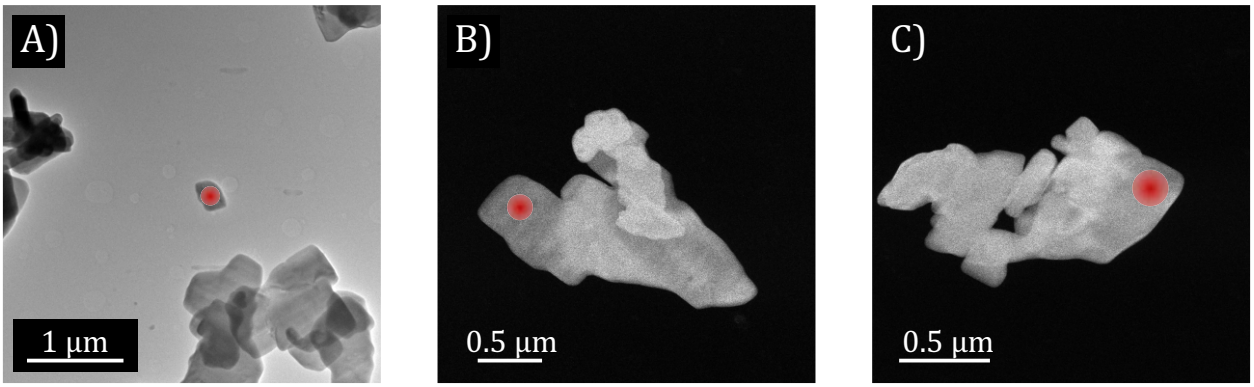

Figure 5.1.1: TEM image (A) and STEM-HAADF images (B and C) of the three barite crystals used for the Fast-ADT proof-of-concept. The filled red circles represent the position of the 200 nm beam for the 3D ED acquisitions.

The post-column CCD dataset was acquired through the sequential approach with 1° of tilt step. An exposure time of 0.5 s was selected, which resulted on a 3D ED acquisition time of around 10 min. The external CCD dataset was acquired with the continuous approach. The tilt velocity was set to 1.77 °/s for the first crystal and 1.5 °/s for the other two. The exposure time was set to 100

ms, which translated to around 1 min for the whole diffraction data acquisitions. In this second case, special care was taken to avoid saturated reflections because the exposure time and the gain of the camera can be changed over a large range without any danger to damage the sensor. The use of such low velocity and exposure time resulted in a reflection integration of 0.15–0.18° per pattern. Since the integration due to 1° of precession movement has a higher integration effect than the reflection integration by the continuous tilt of the stage, the dataset can be later analysed as one acquired with the sequential approach for proper comparison between detectors. Table 5.1.1 shows the acquisition parameters for the six acquired datasets. The initial angle of crystal 1 datasets was limited to -45° because of crystal overlapping from close-by particles.

	Crystal 1		**Crystal 2**		**Crystal 3**	
	US4000	*F-145B*	*US4000*	*F-145B*	*US4000*	*F-145B*
Tilt Range (°)	-45/60	-45/60	-60/60	-60/58	-60/60	-60/59
Tilt Step (°)	1	-	1	-	1	-
Ref. Tilt Step (°)	5	-	5	-	5	-
Tilt Vel. (°/s)	-	1.77	-	1.5	-	1.5
Ref. Tilt Vel. (°/s)	-	2.3	-	2.3	-	2.3
Acq. Patterns (#)	106	580	121	796	121	802
Exp. Time (s)	0.5	0.1	0.5	0.1	0.5	0.1
3D ED Acq. Time (s)	592	58	678	80	670	80

Table 5.1.1: Fast-ADT acquisition parameters from the US4000 and F-145B CCD cameras for the three different barite crystals. "Ref." stands for reference.

5.1.2 Barite: Data Processing & Crystal Structure Analysis

5.1.2.1 Initial Considerations

The acquired diffraction patterns with the US4000 do not require any major pre-processing in order to start the crystallographic procedures. On the other hand, datasets from the F-145B need to be processed prior to any reliable structure analysis. Two main operations have to be applied: the correction of the geometrical distortion and the subtraction of the high background level.

The projective transformation matrix for the geometrical correction is obtained from a non-distorted and a distorted reference pattern. On the non-distorted pattern, two Friedel pairs are selected and the length ratio and the angle between the lines drawn for each Friedel pair are stored as the reference parameters. Then, the same Friedel pairs are selected in the distorted pattern and their pixel coordinates are modified in order to meet the reference parameters. These initial and corrected positions allows the determination of the projective transformation matrix that can be applied to all the other frames given that the geometry of the acquisition has not been changed. Figure 5.1.2

shows the reference patterns from the US4000 and F-145B that enabled the calculation of the matrix components for the Fast-ADT acquisition of crystal 2. Since frames acquired with the US4000 do not contain strong geometric distortions, these can be used as the references for the frames collected at the tilted fluorescent screen. The Fast-ADT software developed in *Matlab* includes a graphical user interface (GUI) that facilitates the selection of these positions and automatically retrieves the geometrical correcting matrix.

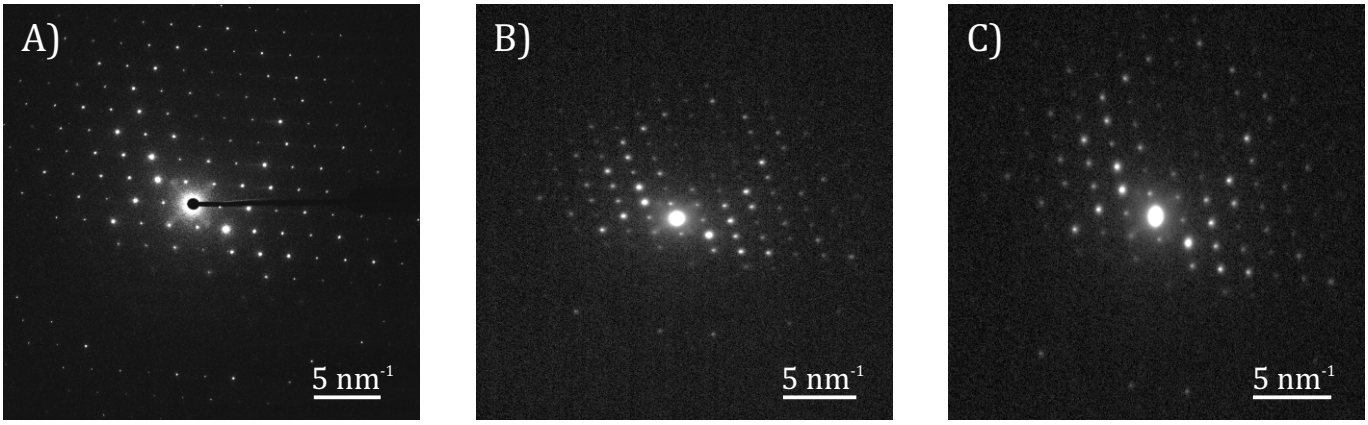

Figure 5.1.2: A) Reference diffraction pattern acquired with the US4000, B) raw pattern from the F-145B and C) geometrically corrected pattern from the F-145B. The *Matlab*-based Fast-ADT software was used for the geometrical correction.

One of the main key points for successful structure refinement is the characterization of the detector noise. The US4000 provides a background with almost all pixels at 0 intensity, thus any processing of the patterns to minimize this weak noise not related to the measurement itself is not necessary. On the other side, the F-145B data contains a lot of noise in the background that reaches around 2000 counts on average. In order to take into account this huge noise, a histogram of the dark reference acquired with the same settings as the 3D ED acquisition is analysed to find the best constant value to subtract on all patterns. Figure 5.1.3 shows the histograms for the intensity levels of a dark reference and a background area near the edge of the screen from a pattern of the crystal 2 dataset, both acquired with the same camera parameters.

The two histograms are very similar and it can be concluded that neither the excitation of the fluorescent screen nor the reflection of photons on the glasses between the CCD chip and the screen increase the intensity levels of the background. In this way, a subtraction of 5000 counts to the whole frame while keeping the negative values to 0 would suppress all noise in the background. However, careful inspection of the pattern reveals that weak reflection intensities are above the 4000 level and a subtraction of 5000 would bias their intensity. Therefore, in this case, 4000 is selected to subtract the pattern background, which corresponds to $\sim 98\%$ of the background pixels. The same procedure was applied to the datasets of crystal 1 and crystal 3, which results in a subtraction of 5000 and 4000 counts, respectively. This kind of frame processing may be biased due to the fact that the weakest reflections not detected by usual profile inspection may be at the noise level, but they are still forming pixel clusters that can be found by 2D reflection search routines and their related intensity can be ex-

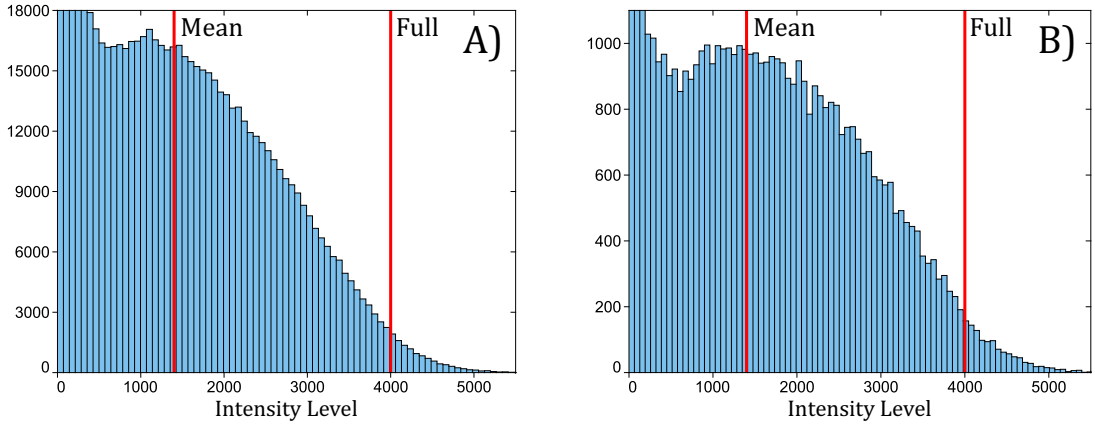

Figure 5.1.3: Histograms for the intensity levels of A) a dark reference image of 886 × 886 pixels and B) a background area of 230 × 230 pixels near the edge of the screen when a diffraction pattern is projected into the fluorescent screen. Both acquired with the Stingray F-145B CCD and the camera parameters used for the 3D ED acquisition of crystal 2. Red lines mark the cut-off for the mean and full background subtraction of the datasets.

tracted subsequently. For this reason, a less aggressive processing was carried out by subtracting the mean intensity value of the pattern background, which turns out as 2800 counts for crystal 1 and 1400 counts for crystal 2 and 3. Nevertheless, structure solution algorithms focus on strong reflections to solve the phase problem, hence the former background subtraction was used in this case. During the structure refinement, both processed data have been used for comparison and discussion. The former will be referred as *full-background subtracted dataset* and the latter as *mean-background subtracted dataset* hereby. It is worth to note, that independent background fitting and subtraction for each reflection in each coarse-processed pattern is performed later on through the data processing programs.

Another point to mention is the α-tilt assigned to each frame. This is clear for the sequential approach of the US4000 data since it is the tilt angle in which the stage stops to acquire the respective pattern. In the case of the continuous approach of the F-145B, the α-tilt assigned to each frame was selected to be the starting angular position of its continuous tilt integration. The middle tilt angle of each continuous integration could be selected as well yet the resulting structure solutions will be quite similar, because the integration by beam precession of 1° shades the integration effect of the continuous tilt of 0.15-0.18° per pattern.

5.1.2.2 Unit cell Determinations & Structure Solutions

At this point, the crystallographic data processing can start. The unit cell determination for all six datasets was carried out with the *eADT* program and the resulting cells are shown in Table 5.1.2. The maximum a, b and c difference of the same crystal between both cameras is around 0.8 %, and all angles approach to 90° with a maximum difference of 0.7° for crystal 1 and crystal 2 of the F-145B data. Such differences are acceptable for electron diffraction data [266] and demonstrate that the geometrical corrections applied to the distorted frames are suitable inside the regime of standard analyses.

The reconstruction of the ODS in all datasets allow to determine the extinction symbol Pn - a by means of the identification of systematic absences. Figure 5.1.4 shows the $0kl$ section of crystal 2 from both detector acquisitions where the $k + l = 2n$ reflection condition confirms the existence of the n-glide plane perpendicular to the a-axis. Some violations of this condition are seen (blue circles) yet they are weak and they are likely coming as a result of the dynamical interaction of electrons with the crystal. The section that belongs to the F-145B data does not show so clearly these violations due to the much lower sensitivity of the experimental setup.

	Crystal 1		**Crystal 2**		**Crystal 3**	
	US4000	*F-145B*	*US4000*	*F-145B*	*US4000*	*F-145B*
a (Å)	8.880	8.841	8.883	8.882	8.899	8.842
b (Å)	5.474	5.454	5.460	5.434	5.471	5.483
c (Å)	7.127	7.185	7.143	7.179	7.116	7.145
α (°)	90.6	90.2	90.4	89.3	89.7	89.7
β (°)	89.7	89.4	90.2	89.7	90.2	90.2
γ (°)	90.3	89.3	90.0	90.1	89.7	90.4

Table 5.1.2: Unit cell parameters determined with *eADT*. a, b and c are scaled by the averaged factor obtained from the values reported by Jacobsen et al. (8.879 Å, 5.454 Å and 7.154 Å) [21].

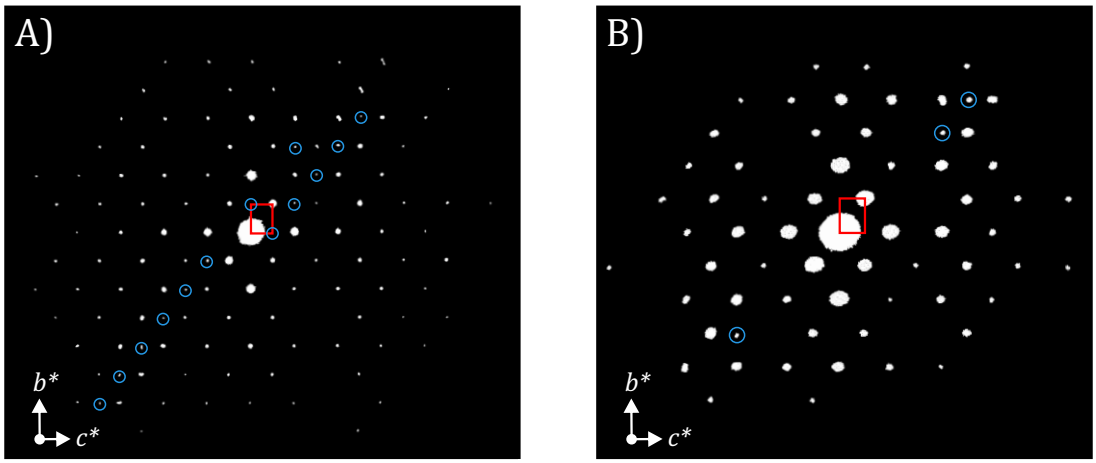

Figure 5.1.4: $0kl$ sections of the reconstructed ODS of crystal 2 from A) the US4000 data and B) F-145B data. The red rectangles overlaid on the sections correspond to the projection of the unit cell, and blue circles indicate reflections that violate the systematic extinctions. Both reconstructions were carried out with the *eADT* program.

Structure solution followed the unit cell and space group determination using DM for electron diffraction implemented in *Sir2014*. The obtained structure solutions reveal all atomic positions except for

one oxygen at a 4*c* site in the F-145B dataset of crystal 2. Nevertheless, similar and positive DPs are obtained in all cases and the peak heights are differentiated enough to automatically distinguish the three elements composing the crystal. Output parameters of the DM runs are shown in Table 5.1.3. The low number of reflections in the F-145B dataset of crystal 1 are caused by a larger camera length used for pattern acquisition. As a consequence, reflections that belong to the diffraction data resolution between 0.7 Å and 1.0 Å are only acquired at the frame corners and a significant number of reflections covered from the other datasets are not present in this one. The low number of independent reflections in the US4000 dataset of crystal 3 is due to the use of a lower diffraction data resolution. In this particular case, the use of more reflections by increasing the resolution to 0.7 Å resulted in a structure model with one missing oxygen.

	Crystal 1		**Crystal 2**		**Crystal 3**	
	US4000	*F-145B*	*US4000*	*F-145B*	*US4000*	*F-145B*
Num. of Reflections (#)	4651	1728	4826	5304	4464	5684
Used Diff. Data Res. (Å)	0.7	0.7	0.7	0.7	0.8	0.7
Num. of Ind. Refl. (#)	480	398	480	498	319	494
Completeness (%)	82.2	68.2	82.2	85.2	82.0	84.6
Refl./Param. Ratio (-)	12.4	10.8	12.7	12.5	8.5	13.4
Overall B (Å^2)	1.49	2.75	1.42	2.05	1.32	2.54
R_{int} (%)	18.5	13.7	13.8	16.3	12.8	14.8
R (%)	15.2	16.5	11.8	15.8	12.6	16.0

Table 5.1.3: Output parameters for the successful structure solutions obtained from DM of *Sir2014*. The used diffraction data resolution filters the number of reflections that are used for the subsequent parameters of the table. R_{int} is based on structure factors and R is based on structure factors and the BEA algorithm.

5.1.2.3 Structure Refinements

Structure refinements based on calculated dynamical intensities were carried out with the structure models found in *Sir2014*. Here, *PETS2* was used to extract the reflection intensities by fitting the double-peaked profile and refine the orientation angles of each pattern with respect to the orientation matrix. Figure 5.1.5 shows the obtained fittings for the datasets of crystal 1. Note that the fitting on the US4000 data is smooth up to the highest diffraction data resolution, while the F-145B data starts to be noisier at the largest resolutions. When the full-background subtracted and mean-background subtracted datasets are compared (Figures 5.1.5B and 5.1.5C), the former has larger deviations at this high resolutions. That is because the weakest reflections at this region have lost some of their intensity and the remaining is similar to the background noise. On the other side, the mean-background subtracted data has cut some of the background but still leaves meaningful intensity for the weakest reflections, hence the smoother fitting.

Noise parameters to calculate the $\sigma(\vec{g})$ in *PETS2* were set to 50 and 28 for US4000 data, and 35 and 3000/500000 for the full/mean background subtracted F-145B data. The first value corresponds to the gain of the detector (counts/e$^-$) multiplied by a cascade factor (fixed to 1.3) and the second one is the variance of the dark reference of the detector [287]. The former was obtained through the specifications of the experimental setups, while the latter was calculated by the acquisition of dark references. Due to the still high background intensities that remain after subtracting the constant value on the patterns, the variance of the F-145B dark reference is significantly higher than the US4000. That is not due to the CCD chip but to the experimental setup, which has a constant signal background even when the TEM room is kept fully dark. The constant-value subtraction helps to decrease this effect but it is comprehensively higher than TEM-designed CCD detectors.

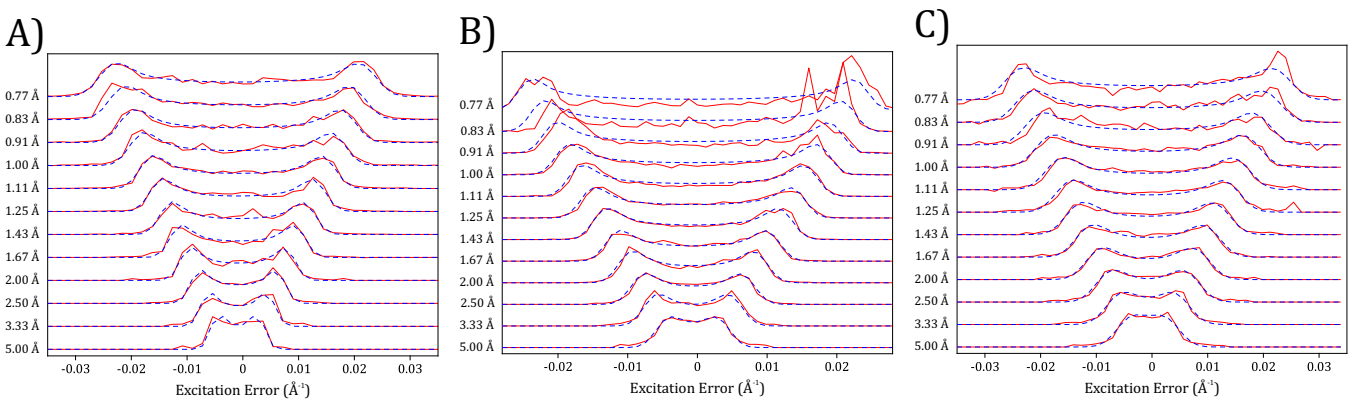

Figure 5.1.5: Averaged rocking-curves of the strongest reflections at different diffraction data resolutions intervals (red curves) and fitted by the precession-dependent double-peaked profile (blue dashed curves). A) corresponds to the US4000 dataset, B) to the full-background subtracted F-145B dataset, and C) to the mean-background subtracted F-145B dataset, all from crystal 1.

The extracted intensities and the found structure model from DM were imported to *Jana2006* to run the *dyngo* module. N_{or} was set to 128 and 256, for the F-145B and US4000 datasets, respectively. S_g^{max} (matrix) of 0.01 Å^{-1} , S_g^{max} (refine) of 0.1 Å^{-1}, RS_g of 0.4 and g_{max} of 1.6 Å^{-1} were kept for all datasets except the US4000 dataset of crystal 3, for which g_{max} was set to 1.45 Å^{-1}. For the F-145B data, all frames of crystal 1 were initially used while each second one of crystal 2 and 3 were chosen to speed up the procedure. In all nine datasets, the worst fitting patterns were checked and removed from the least-squares refinements.

The structure refinement in all datasets followed the same procedure; initial refinement with all structural parameters fixed to find the best scale factor for each frame and the thickness of the crystal, second refinement with atomic positions and isotropic DPs unconstrained, third one with DPs changed to anisotropic for those atomic positions that are not negative, and a final refinement with the same unconstrained parameters of the previous one but after optimizing the orientation angles for each pattern based on the calculated dynamical intensities. Tables 5.1.4 and 5.1.5 show the resulting figures of merit for the US4000 and F-145B datasets, respectively, and Tables 5.1.6, 5.1.7 and 5.1.8 at the end of this subsection show the final refined structural parameters.

	Crystal 1	**Crystal 2**	**Crystal 3**
Reflections (#)	2045/2752	2674/2973	1884/2009
GoF (-)	2.44/2.16	3.22/3.09	3.68/3.58
R (%)	6.41/7.86	7.15/7.62	7.65/7.94
R_w (%)	6.94/7.14	8.10/8.18	8.80/8.85

Table 5.1.4: Resulting figures of merit (obs/all) from the dynamical refinement of *Jana2006* on the US4000 datasets. The criterion for observed (obs) reflections was $I(\vec{g}) > 3\sigma(\vec{g})$. R and R_w are based on the square root of reflection intensities.

	Full-Bckg Subtracted			**Mean-Bckg Subtracted**		
	Crystal 1	*Crystal 2*	*Crystal 3*	*Crystal 1*	*Crystal 2*	*Crystal 3*
Reflections (#)	6279/12394	5354/10631	6415/11547	6907/12402	5657/9620	6617/11075
GoF (-)	9.12/6.74	8.23/6.08	8.95/6.86	3.34/2.65	3.06/2.48	3.62/2.94
R (%)	14.2/25.0	13.2/25.2	15.1/25.6	11.2/25.4	10.0/21.3	11.7/24.4
R_w (%)	14.4/15.0	13.3/13.8	15.0/15.5	8.79/9.32	8.42/8.91	10.0/10.5

Table 5.1.5: Resulting figures of merit (obs/all) from the dynamical refinement of *Jana2006* on the F-145B datasets. The criterion for observed (obs) reflections was $I(\vec{g}) > 3\sigma(\vec{g})$. R and R_w are based on the square root of reflection intensities.

The refined structures from US4000 data show an accurate agreement with respect to the reference structure model of Jacobsen et al. [21], up to only 3 pm difference in the positioning of the atoms (see Appendix for the position differences of all atoms). All atomic positions have been refined with anisotropic DPs, from which all the principal components of the tensor are positive and around 1 Å^2. Figure 5.1.6A displays a projection of the structure model after the dynamical refinement from the dataset of crystal 1. The residual values R and R_w also show low and good percentages for electron diffraction data that confirms the correct determination of the model with respect to the experimental data. *GoF*s are also close to the unity, thus the $\sigma(\vec{g})$ assigned to the extracted intensities have been correctly assessed. A characteristic of these structure refinements is that the DPs of sulphur are the smallest in the three datasets. If the difference Fourier map is checked with the final models, some positive potential is seen in these positions, which indicates that perhaps their DPs should be increased yet the least-squares method determines that these are the best estimated parameters. Although the actual DP values in electron diffraction cannot be physically interpreted as accurate as in neutron diffraction, the remaining potential at these positions does not exceed 3σ and it could be concluded that this atom is highly fixed in such position. From a chemical point of view, the four oxygen atoms that surround sulphur and form the tetrahedron geometry are covalently bonded. This environment provides a balance of forces that allows the small movement of sulphur in comparison to the oxygen as well as barium atoms, which explains the obtained DPs and they are confirmed

by the comparable trend of these parameters in the structure refined by Jacobsen et al. in XRPD [21] (see Table 5.1.9). In the case of oxygen, O1 and O2 atoms exhibit higher DPs in comparison to O3, but here the origin of such values come from the symmetry-constrained positions related to the mirror plane, since atoms in nature are not exactly fixed in these positions and the refinement increases their DP values to fit better the experimental electrostatic potential.

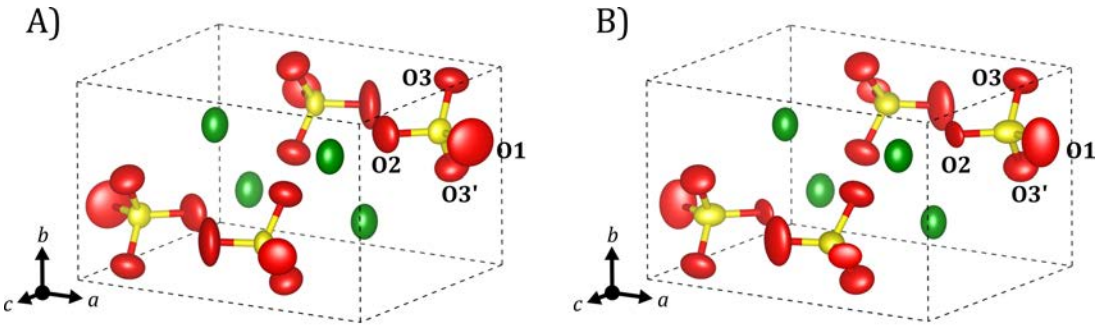

Figure 5.1.6: Projections of the dynamical refined models from the A) US4000 dataset and B) full-background subtracted F-145B dataset of crystal 1. Red atoms correspond to oxygen, yellow ones to sulphur and green ones to barium. Atom volumes are scaled according to the principal components of the anisotropic DPs.

The refined structures from F-145B data also match the reference XRPD model quite well but with a higher discrepancy in the atomic positions; up to 6 pm and 8 pm for the full and mean-background subtracted datasets, respectively (see Appendix for the position differences of all atoms). Figure 5.1.6B shows a projection of the structure model of crystal 1 from the full-background subtracted data after the dynamical refinement. In this case, the way to process the frames before the refining procedures plays a major role. The figures of merit for the full-background subtracted datasets are worse than the ones from the mean-background subtracted, yet the ratio between observed and all reflections in both cases is approximately the same. The resulting lower GoF, R and R_w may come from the fact that the processed reflection intensities have relative values that are better adjusted to the reality of the measurement, i.e. counts related to the reflections are not being strongly removed as in the full-background subtracted datasets. In the same way, the variance calculated from the processed dark reference images is closer to the performance of the camera, even if it is extremely high compared to TEM-specific detectors. The effect of the high $\sigma(\vec{g})$ can be seen in the ratio of observed reflections (reflections with intensities above three times $\sigma(\vec{g})$) over all reflections between the two different detectors data (see Tables 5.1.4 and 5.1.5). While it is 85% on average for the US4000 data, it goes down to around 55% for the F-145B data, which is a clear indication that the noise of the camera filters a big number of reflections because they are not statistically meaningful, which is also seen in the jump of the GoF, R and R_w between the use of the observed and all reflection intensities. Another significant difference is the estimated DPs according to the frame processing. The structure models from the full-background subtracted data can be refined with anisotropic DPs and they result in positive values, albeit bigger than the standard 1-2 Å^2. On the other side, the structures from the mean-background subtracted datasets allow to refine the barium and oxygen atoms anisotropically but some principal components become negative, even if not significantly, and the sulphur positions have to be kept isotropic because they become negative.

Crystal 1

	x/a	y/b	z/c	B_{eq} (Å^2)
Ba	0.1842(1)	0.25	0.1583(1)	1.24(2)
S	0.0628(3)	0.25	0.6898(3)	0.77(5)
O1 ($4c$)	0.5876(5)	0.75	0.1069(5)	2.3(1)
O2 ($4c$)	0.3175(5)	0.75	0.0486(5)	1.43(9)
O3 ($8d$)	0.4195(4)	0.9684(5)	0.3109(4)	1.33(6)

Crystal 2

	x/a	y/b	z/c	B_{eq} (Å^2)
Ba	0.1848(2)	0.25	0.1584(1)	1.07(2)
S	0.0634(4)	0.25	0.6917(2)	0.59(7)
O1 ($4c$)	0.5883(9)	0.75	0.1109(6)	2.3(2)
O2 ($4c$)	0.3163(7)	0.75	0.0502(4)	1.3(1)
O3 ($8d$)	0.4199(5)	0.9679(4)	0.3109(3)	1.08(8)

Crystal 3

	x/a	y/b	z/c	B_{eq} (Å^2)
Ba	0.1852(2)	0.25	0.1583(1)	1.33(4)
S	0.0628(5)	0.25	0.6903(4)	0.89(9)
O1 ($4c$)	0.5845(1)	0.75	0.1081(8)	2.6(2)
O2 ($4c$)	0.3163(1)	0.75	0.0496(6)	1.3(2)
O3 ($8d$)	0.4178(6)	0.9679(6)	0.3120(4)	1.1(1)

Table 5.1.6: Structural parameters of barite after the structure refinement for the datasets acquired with the US4000. Unit cell parameters were fixed to the ones reported by Jacobsen et al. [21] for the refinement. The values in parentheses for the different parameters are the estimated standard deviations. $4c$ and $8d$ refers to the Wyckoff positions. B_{eq} is calculated from the anisotropic DPs as $B_{eq} = 1/3 \sum\sum B_{ij} a_i^* a_j^* \vec{a}_i \vec{a}_j$. See Appendix for all the anisotropic components.

Crystal 1

	x/a	y/b	z/c	B_{eq} (Å^2)
Ba	0.1837(1)	0.25	0.1559(1)	3.16(3)
S	0.0617(3)	0.25	0.6849(3)	2.74(7)
O1 ($4c$)	0.5904(7)	0.75	0.1087(6)	5.3(2)
O2 ($4c$)	0.3175(5)	0.75	0.0438(4)	2.3(1)
O3 ($8d$)	0.4147(5)	0.9663(4)	0.3141(4)	3.5(1)

Crystal 2

	x/a	y/b	z/c	B_{eq} (Å^2)
Ba	0.1846(2)	0.25	0.1571(1)	2.46(3)
S	0.0635(4)	0.25	0.6891(2)	1.56(7)
O1 ($4c$)	0.5922(8)	0.75	0.1133(5)	3.3(2)
O2 ($4c$)	0.3159(6)	0.75	0.0482(4)	2.1(1)
O3 ($8d$)	0.4214(5)	0.9646(4)	0.3135(3)	2.8(1)

Crystal 3

	x/a	y/b	z/c	B_{eq} (Å^2)
Ba	0.1840(2)	0.25	0.1574(1)	2.90(3)
S	0.0657(4)	0.25	0.6888(2)	1.81(8)
O1 ($4c$)	0.5872(9)	0.75	0.1158(5)	4.3(2)
O2 ($4c$)	0.3154(6)	0.75	0.0460(4)	2.1(1)
O3 ($8d$)	0.4250(5)	0.9675(4)	0.3163(3)	3.1(1)

Table 5.1.7: Structural parameters of barite after the structure refinement for the datasets acquired with the Stingray F-145B and full-background subtracted. Unit cell parameters were fixed to the ones reported by Jacobsen et al. [21] for the refinement. The values in parentheses for the different parameters are the estimated standard deviations. $4c$ and $8d$ refers to the Wyckoff positions. B_{eq} is calculated from the anisotropic DPs as $B_{eq} = 1/3 \sum\sum B_{ij} a_i^* a_j^* \vec{a}_i \vec{a}_j$. See Appendix for all the anisotropic components.

Crystal 1

	x/a	y/b	z/c	B_{eq} (Å^2)
Ba	0.1848(1)	0.25	0.1565(1)	0.19(2)
S	0.0644(3)	0.25	0.6905(2)	-0.73(3)*
O1 ($4c$)	0.5914(7)	0.75	0.1064(7)	2.8(2)
O2 ($4c$)	0.3101(7)	0.75	0.0522(6)	2.1(1)
O3 ($8d$)	0.4215(4)	0.9698(4)	0.3149(3)	0.33(8)

Crystal 2

	x/a	y/b	z/c	B_{eq} (Å^2)
Ba	0.1843(1)	0.25	0.1583(1)	0.36(2)
S	0.0657(3)	0.25	0.6939(2)	-0.49(3)*
O1 ($4c$)	0.581(1)	0.75	0.1141(5)	2.8(2)
O2 ($4c$)	0.3176(7)	0.75	0.0574(5)	1.1(1)
O3 ($8d$)	0.4208(5)	0.9639(4)	0.3127(3)	0.9(1)

Crystal 3

	x/a	y/b	z/c	B_{eq} (Å^2)
Ba	0.1845(1)	0.25	0.1581(1)	0.18(2)
S	0.0665(4)	0.25	0.6903(2)	-0.34(3)*
O1 ($4c$)	0.5903(9)	0.75	0.1147(5)	1.3(2)
O2 ($4c$)	0.3093(9)	0.75	0.0489(6)	1.7(2)
O3 ($8d$)	0.4261(5)	0.9750(4)	0.3122(3)	0.2(1)

Table 5.1.8: Structural parameters of barite after the structure refinement for the datasets acquired with the Stingray F-145B and mean-background subtracted. Unit cell parameters were fixed to the ones reported by Jacobsen et al. [21] for the refinement. The values in parentheses for the different parameters are the estimated standard deviations. $4c$ and $8d$ refers to the Wyckoff positions. B_{eq} is calculated from the anisotropic DPs as $B_{eq} = 1/3 \sum\sum B_{ij} a_i^* a_j^* \vec{a}_i \vec{a}_j$. See Appendix for all the anisotropic components.
*This value corresponds to the isotropic value of the DP.

	x/a	y/b	z/c	B_{eq} (Å^2)
Ba	0.18453	0.25	0.15843	0.833
S	0.06251	0.25	0.69082	0.705
O1 ($4c$)	0.5870	0.75	0.1072	1.782
O2 ($4c$)	0.3176	0.75	0.0498	1.390
O3 ($8d$)	0.4194	0.9704	0.3118	1.056

Table 5.1.9: Structural parameters of barite from the Rietveld refinement of Jacobsen et al. [21]. $4c$ and $8d$ refers to the Wyckoff positions. B_{eq} is calculated from the anisotropic DPs as $B_{eq} = 1/3 \sum \sum B_{ij} a_i^* a_j^* \vec{a}_i \vec{a}_j$.

5.1.3 Layer Silicate: Data Acquisition

RUB-5 ($Si_{42}O_{84}$) is a recently solved new layer silicate structure that exhibits a new silica polymorph in a monoclinic crystal system [22]. Crystals of this material exhibit a high degree of stacking disorder with intergrowths of different polymorphs due to its layer-like building units. Figure 5.1.7 shows a projection of the crystal structure along $[\bar{1}\bar{1}0]$ direction in which two of these structural layers are indicated. The plate-like morphology of these particles makes the disorder analyses difficult due to a strong preferred orientation. Since these layer-like building units lay always parallel to the carbon film of the TEM Cu-grid, most of the streaks do not appear on single frames and they need to be obtained from sections of the reconstructed ODS, thus making the tilt step the main critical experimental parameter. This particular characteristic is interesting in order to compare the performance of the different CCD-based detectors to approach such investigations.

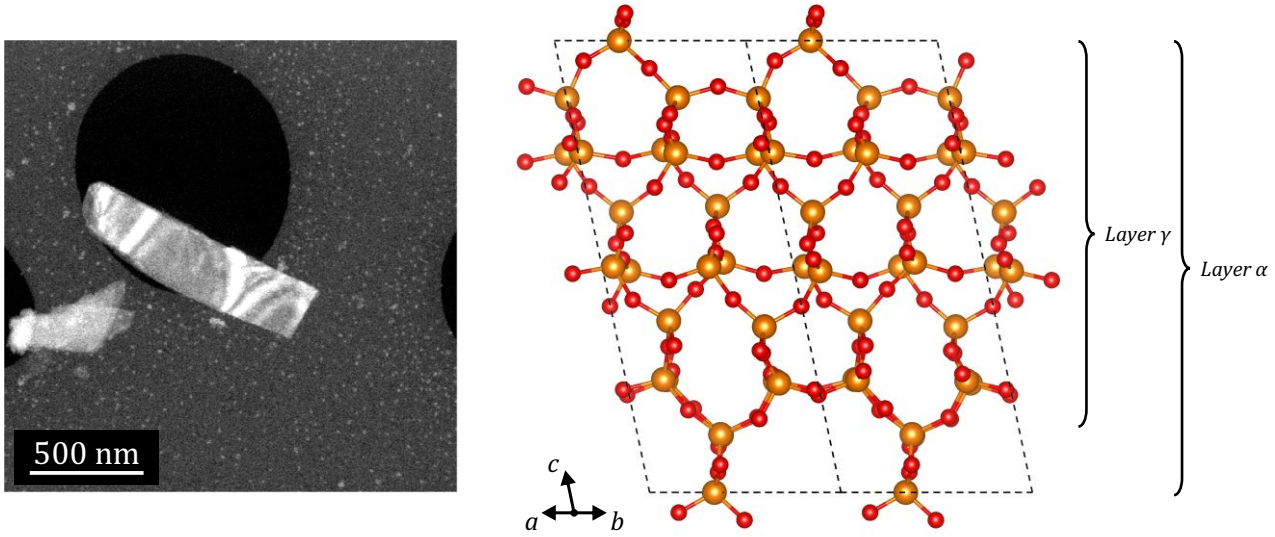

Figure 5.1.7: STEM-HAADF image of a RUB-5 crystal (left) and its crystal structure projected along the $[\bar{1}\bar{1}0]$ direction (right). The orange atoms correspond to silicon and the red ones to oxygen. Structural layers α and γ correspond to the building units of the different polymorphs according to the notation of Krysiak et al. [22].

ADT datasets were acquired using the US4000 camera and Fast-ADT datasets were collected with the Stingray F-145B by means of the continuous approach, both in a FEI Tecnai F30 FEG operated at 300 kV in STEM mode and Microprobe illumination. A 10-µm CA, gun lens 8 and spot size 6 were used to produce a quasi-parallel beam of 100 nm in diameter for the US4000 data. A 50-µm CA, gun lens 4 and spot size 7 were set to produce a 300 nm quasi-parallel beam for the F-145B data. The beam size is bigger for the F-145B data in order to reduce the electron dose on the crystal. Several datasets were acquired at different angular ranges and camera parameters, but here only two datasets are included for comparison. The ADT dataset is composed of 121 patterns acquired with 4 s of exposure time and a tilt step of 1° between -60° and 60° of α-tilt that took around 1 hour to acquire. The F-145B dataset took about 1 minute to entirely acquire it and it contains 1018 patterns acquired with 30 ms of exposure time and a tilt velocity of 1.75 °/s between -50° and 60° of α-tilt.

Prior to the reconstruction of the F-145B diffraction data, single frames were background corrected with the rolling-ball option of the *eADT* [12]. For both kinds of datasets, the reconstruction of the ODS was carried out with the *eADT*.

5.1.4 Layer Silicate: Comparison on ODS Reconstructions

Figure 5.1.8 shows the same 2D section from the ODS reconstruction of the two different acquisitions, and the zoom-in of three selected regions that contain diffuse scattering. As exemplified in this figure, the use of smaller tilt steps in the F-145B dataset clearly provides a better way to sample the streaks, which is evidently seen the higher the diffraction data resolution is (see Figure 5.1.8C). It also demonstrates that the intensity coming from the fluorescent screen is enough to detect such features. Although the beam dose was higher in the F-145B case to obtain enough intensity from the screen, it was not strong enough to deteriorate the crystallinity of the particle. One problem that could lead to the hampering of the analysis is the reminiscence of the phosphor. For this reason, the screen should be coated with the fast-decay phosphor and special care should be taken on the beam settings to not overexpose the screen and avoid saturation of reflection intensities as much as possible. Nevertheless, the low intensities between reflections observed in this dataset come from diffuse scattering as other intense reflections do not have such reminiscence effect.

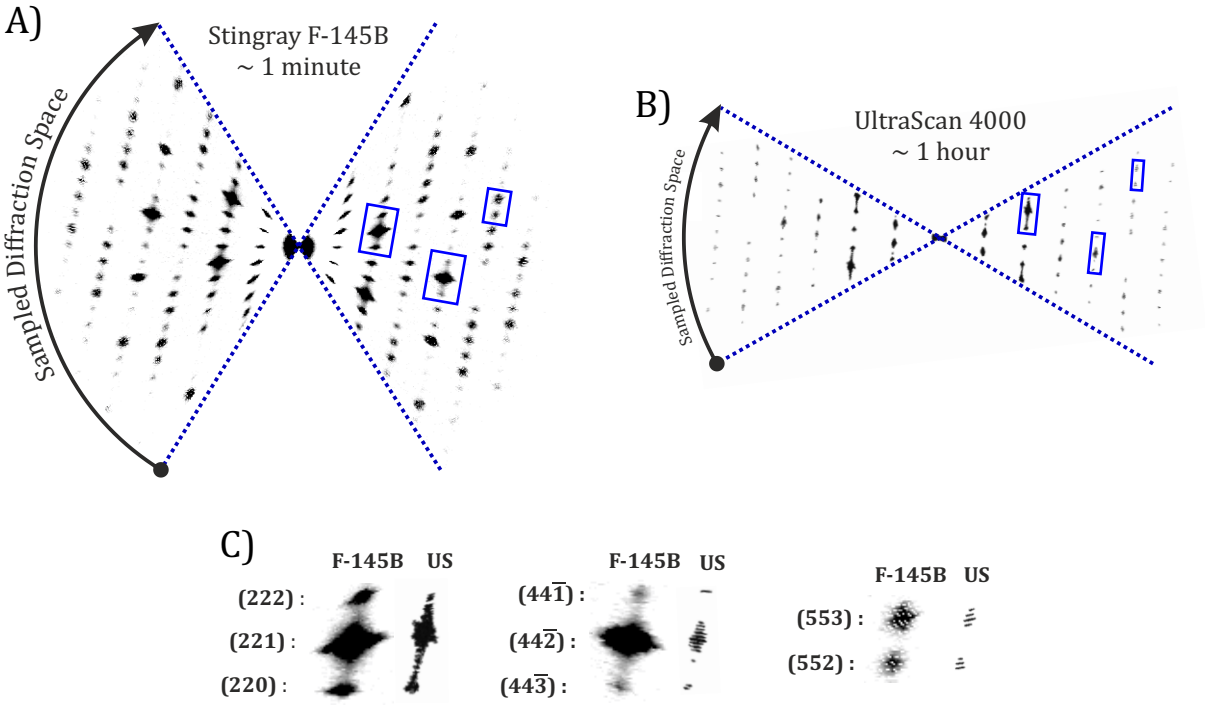

Figure 5.1.8: A) and B) *hhl* sections from the ODS reconstruction of two different RUB-5 particles. A) corresponds to F-145B data acquired with the continuous approach from -50° to 60°, and B) with the US4000 and the sequential approach from -60° to 60°. C) shows zoomed images of the reflections from the blue rectangles of A) and B) together with the respective indices.

5.1.5 Discussion

The US4000 datasets show that the use of such detector for accurate and reliable crystal structure determination is appropriate. Although its main disadvantage is its long exposure times for good signal-to-noise levels and read-out times, the sensitivity and especially tuned electronics to measure diffraction patterns result in diffraction data quality suitable for precise characterization of crystal structures. Its coupling with the Fast-ADT acquisition routine optimizes the efficiency of these diffraction acquisitions in a routine basis.

The use of the F-145B for these crystal structure analyses is feasible but it is not as good as the US4000. The reason behind this statement is the low signal-to-noise ratio of the detector on such an experimental setup. The high background intensities hinder the reliable acquisition of weak reflection intensities, which are the majority of reflections in a diffraction dataset. Furthermore, this CCD camera is prone to saturation and previous checks have to be carried out to ensure acquisitions of non-saturated diffraction data, thus it complicates the enhancement of weak reflections. The data processing shown here demonstrates that crystal structure determination and dynamical refinement is possible with this camera in an accurate way, which can be seen in the low maximum deviation of the atomic positions and the low figures of merit. On the other hand, the variation of the DPs according to the background processing of the frames shows that a high reliability of such characterization cannot be assessed, yet the crystal model is still correct. In this way, it can be concluded that this experimental setup can be used to determine crystal structures of high crystalline and beam stable materials, yet the found structure models have to be further refined with other experimental setups and/or techniques.

One main advantage of the F-145B setup in comparison to the US4000 is the faster fine sampling of the ODS for the accurate acquisition of diffuse scattering. Although the use of the US4000 works for the characterization of disorder [135], in this case the need of a tilt step smaller than 0.5° and higher exposure times for good signal-to-noise ratio would result in 2-3 hours of data acquisition for a single particle (± 60° of angular range). The acquisition of low angular ranges would be feasible, but the preferred orientation of these crystals necessitate high tilt angles in order to have a better display of lines containing diffuse scattering and select the best regions. The use of Fast-ADT with a fast frame rate camera facilitates the acquisition of such large 3D ED datasets, and allows the accurate description of such disorder effects by the analysis of the diffuse streaks from the ODS . The Stingray F-145B is not a very sensitive camera due to the remaining noise of the experimental setup, but it has been demonstrated that it can be used to perform these quantitative analyses when dealing with crystal structures that contain strong diffuse scattering [22].

5.2 The Absolute Structure of a Ferrosilicide

The aim of this section is to show how electron diffraction data acquired with the Fast-ADT technique allows the determination of the absolute structure of a Fe-Cr-Ni silicide by means of dynamical refinements.

5.2.1 The Fe-Cr-Ni Silicide Phase

The structure determination of the new silicide phase present in the RR2450 alloy was carried out by electron diffraction, since the strong reflection overlapping present in the XRPD pattern hindered its use to find the structure solution. Interestingly, it was found that a uniformly solved carbon (around 1.2 weight %) considerably enhances the alloy strength and enables its use in extreme environments like in a nuclear reactor, thus the crystal structure was characterized from samples with and without carbon to check any possible difference between them. The π-ferrosilicide phase was solved by DM of *Sir2014* with the cubic space group $P2_13$, determined by *eADT*, and a lattice parameter of 6.1908(1) Å with carbon and 6.1669(2) Å without carbon, obtained from the XRPD pattern. The dynamical refinement with partially occupied positions by silicon or iron-nickel-chromium showed that the final chemical formula was $(Fe,Ni,Cr)_{4.18}Si_{0.82}$ with carbon and $(Fe,Ni,Cr)_{3.92}Si_{1.08}$ without carbon. Since Fe, Ni and Cr have similar scattering factors due to the consecutive atomic numbers and they occupy the same atomic positions, Fe was used as the reference element to consider their whole contribution. The main difference found between both final structure models was the unit cell parameters, hence it was concluded that the carbon was uniformly located in interstitial positions within the crystal structure [25]. The only question left over was the chirality of the structure due to the use of a non-centrosymmetric space group, from which two different arrangements of the atoms inside the unit cell, that are differentiated by the application of an inversion centre, are possible.

5.2.2 Data Acquisition

A 10 µm by 5 µm lamella was prepared from a carbon-free ingot of the RR2450 alloy by David Bowden from the university of Manchester with a focused ion beam (see Figure 5.2.1) [25].

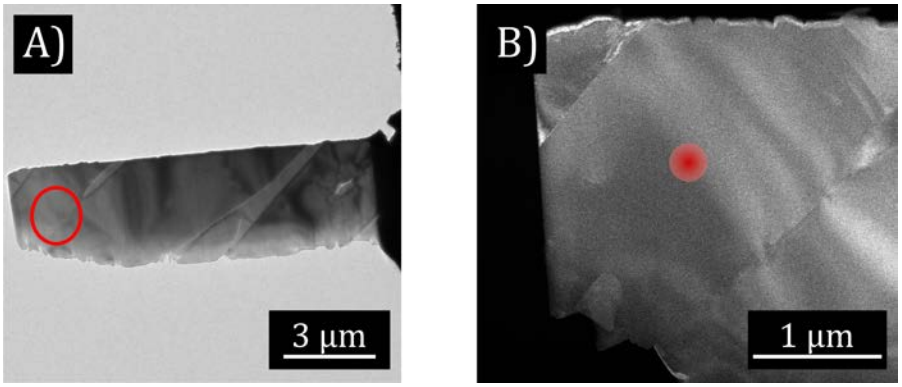

Figure 5.2.1: A) TEM and B) STEM-HAADF images of the lamella used for the Fast-ADT acquisition. The filled red circle in B) represents the position of the 300 nm beam for the 3D ED acquisition.

The sample was mounted in a FEI tomography holder and inserted in a FEI Tecnai Spirit LaB_6 operated at 120 kV. The Gatan US1000 post-column CCD camera was used to acquire the diffraction patterns with an exposure time of 0.25 s. Microprobe illumination, spot size 8 and a 10-µm CA were used to produce a 300 nm quasi-parallel beam. The Fast-ADT DME-based program was used in TEM mode to collect a 3D ED dataset between -60° and 60° of α-tilt with 1° of tilt step. 1° of precession was applied by the DigiStar unit provided by NanoMegas SPRL.

5.2.3 Structure Refinement

The reflection intensities were extracted from *PETS2* by the double-peaked profile fitting after the optimization of the orientation angles. The resulting *hkl* file was imported to *Jana2006* and the crystal structure obtained from the charge-flipping algorithm was used as the initial model for the structure refinement.

First, kinematical refinement was carried out to coarsely refine the found model. The correct enantiomer for the measured crystal cannot be determined through the kinematical theory because of the Friedel pairs. The calculated reflection intensities related to the two structural configurations of a non-centrosymmetric crystal are exactly the same, thus the least-squares method with both settings lead to the same result.

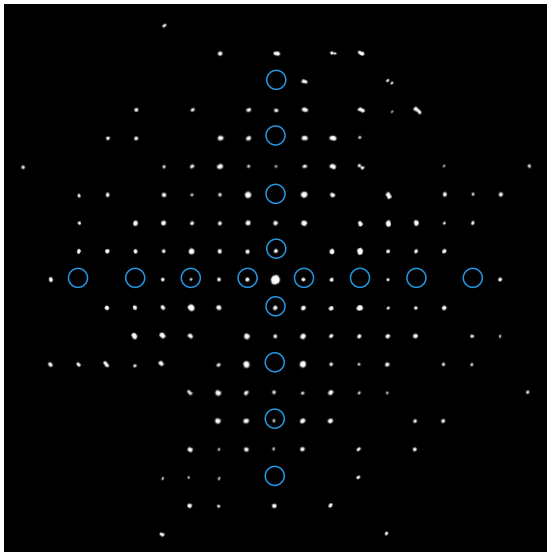

Figure 5.2.2: $0kl$ section of the reconstructed ODS of the π-ferrosilicide dataset. Blue circles indicate the positions of the systematic extinctions according to the $P2_13$ space group.

A dynamical refinement is not always necessary, but when the material under study contains heavy elements and it is highly crystalline, dynamical effects are more likely to occur. This is the case of this structure from which reflection intensities could be collected up to 0.33 Å in diffraction data resolution. Moreover, even if the lamella thickness was estimated to be around 40 nm [25], the dynamical nature of electron diffraction phenomena is significant, which can be seen in the strong violation of the systematic extinctions in the $0kl$ section of the reconstructed ODS in Figure 5.2.2. For this reason, it makes sense to perform a dynamical refinement and improve the accuracy of

the retrieved crystal structure. In fact, the kinematical refinement results in one Fe position with negative isotropic DP, which is an indication of partial occupation of silicon but also of strong dynamical effects that difficult the match between experimental and theoretical potential maps used by the least-squares method. The resulting figures of merit from the refinements are shown in Table 5.2.1.

	Kin. Refinement	**Dyn. Refinement**	
		Incorrect Enantiomer	*Correct Enantiomer*
Reflections (#)	873/875	2374/2386	2358/2370
GoF (-)	21.5/21.5	7.08/7.07	3.54/3.53
R (%)	22.9/22.9	9.89/9.91	5.10/5.11
R_w (%)	30.4/30.4	12.8/12.8	6.41/6.41

Table 5.2.1: Resulting figures of merit (obs/all) from the kinematical and dynamical refinements of the π-ferrosilicide from *Jana2006*. The criterion for observed (obs) reflections was $I(\vec{g}) > 3\sigma(\vec{g})$. R and R_w are based on structure factors for the kinematical case and the square root of reflection intensities for the dynamical one. Dynamical refinements were carried out with N_{or} of 128, g_{max} of 1.6 Å^{-1}, RS_g of 0.4, S_g^{max}(refine) of 0.1 Å^{-1} and S_g^{max}(matrix) of 0.01 Å^{-1}.

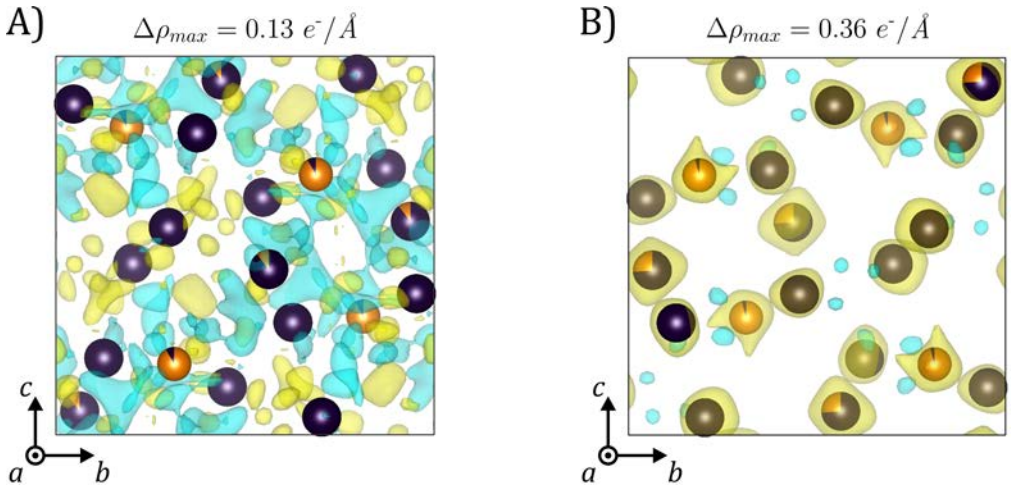

Figure 5.2.3: Difference Fourier map along the a-axis of the A) correct and B) incorrect enantiomer for the measured π-ferrosilicide phase. The cut-off value for the electrostatic potential, $\Delta\rho_{max}$, is set to 2σ in both cases. Positive potentials are displayed in yellow and negative ones in light blue. The dark blue atoms correspond to Fe-Ni-Cr positions and the orange ones to the Si positions.

From the decline of about 18% in the residual R value, it is clear that the dynamical refinement improves the reliability of the retrieved model. The ratio between observed and all reflections that is close to the unit also points out that the scattering power of the crystal is high, and the dynamical interactions are increased in consequence. It is statistically meaningful as well the drop in the three figures of merit between the dynamical refinements of the enantiomers, which suggests the crystal structure with lower figures of merit as the correct one according to this diffraction dataset.

Furthermore, the difference Fourier maps displayed in Figure 5.2.3 show remaining potential related to noise for the low figures of merit enantiomer, while the other model produces a map with remaining potential at the atomic positions, hence indicating the wrong selection of the crystalline configuration. In this way, these two analyses of the resulting structure refinements determine in good agreement the correct non-centrosymmetric crystal structure for the measured π-ferrosilicide phase.

5.2.4 Discussion

The resulting figures of merit from the dynamical refinements carried out from the acquired Fast-ADT dataset allows the reliable determination of the absolute structure of the π-ferrosilicide phase. The difference Fourier maps graphically facilitate this characterization due to the appearance of remaining potentials at the atomic positions when the wrong structural setting is chosen. It is also worth to say that such clear result is product of the enhanced dynamical effects due to the nature of the measured crystal. While the kinematical refinement was only possible with isotropic DPs and one of the Fe-Cr-Ni positions resulted in a negative DP, the dynamical refinement allowed a structure refinement with meaningful partial occupancy factors and low and positive anisotropic DPs. The difference between both non-centrosymmetric configurations of the structure plays a role as well, since both structural settings are significantly different and therefore its related reflection intensities. This is not always the case and as a result the refinement parameters are not very different between enantiomers. For instance, pharmaceutical compounds where the determination of the absolute structure is key for efficient use of the drug are formed by light elements, the scattering differences between enantiomers are not high and the electron beam is damaging the crystal during the measurement. It has been demonstrated that it is possible to distinguish them [168], although the same confidence shown here cannot be obtained and such result may not be that easy to retrieve in a routine basis. For this reason, the acquired diffraction data have to be carefully analysed and the nature of the material under study properly understood in order to carry out such fine crystallographic analyses.

5.3 Conclusions

This chapter has demonstrated the utility of the Fast-ADT technique to acquire diffraction datasets suitable for three different crystallographic problems: the determination and refinement of a crystal structure, the analysis of diffuse scattering to explain disorder, and the retrieval of the absolute configuration of chiral structures.

Two different CCD cameras have been compared for the Fast-ADT acquisition method. The use of slow refreshing CCD cameras like the US1000 or US4000 in the TEM limits the performance of the continuous acquisition approach and, for this reason, the Fast-ADT routine was coupled to the faster Stingray F-145B optical CCD mounted in the binocular position to evaluate the use of the continuous approach. Both experimental setups have been compared by two different case studies; a proof-of-concept crystal structure determination from the well-known barite and a disorder analysis of the recently-solved RUB-5 layer silicate.

The results from section 5.1 on barite crystal structure determinations show that both experimental setups can be used to obtain accurate structure models, up to 3 pm difference with respect to the XRPD model for the US4000 data and 8 pm for the F-145B data. The major disadvantage of the F-145B experimental setup is its remaining background noise that decreases its signal-to-noise ratio and lowers its sensitivity. Different image processings have been applied to the frames but it has been shown that this can significantly change the DPs related to the atomic positions. Traditionally, DPs from electron diffraction have been considered figures of merit (around 1-2 $Å^2$) rather than real measurable physical properties like in neutron diffraction. In fact, the resulting atomic positions from the F-145B dataset are found to be in good agreement with the XRPD model, even if the DPs are totally different. Nevertheless, a reliable structure determination has to be further confirmed using a different technique if only this kind of data is available. On the other hand, since the US4000 is a specifically TEM-designed CCD detector that has an almost negligible and flat background noise of low variance, all reflection intensities can be reliably taken into account and accurate crystal structures can be determined.

The Fast-ADT acquisitions on the RUB-5 structure has shown that, even if the F-145B experimental setup is not very sensitive, diffuse scattering can be investigated to resolve the probability of layer stacking in such crystals, thus disorder problems. In this case, the major advantage of the F-145B setup with respect to the US4000 setup is its fast retrieval of the diffraction data, together with the fine slicing of the diffraction space required for proper sampling of the streaks between Bragg reflections.

At this point, it is worth to mention that the combination of CMOS-based detectors via the intermediation of a scintillator and optical fibres (like the XF416 from TVIPS or the OneView from Gatan) or direct detection (like the Medipix-based detectors from ASI or QD, the Quadro from Dectris or the EMPAD from Thermo Fisher) with the Fast-ADT technique could be the optimum experimental setup to deal with any crystallographic analysis of the diffraction space, mainly because of its higher sensitivity and fast acquisition frame rate. However, careful tests should be made to check the best pixel counting setting in order to suppress most of the noise but still retain the weakest intensities. In the case of direct detection cameras, additional studies on the influence of bigger pixel size should

be made to analyse the shape of reflections, their sensitivity to diffuse scattering and the maximum attainable diffraction data resolution before reflection overlapping.

Finally, the crystallographic analysis of the ferrosilicide phase from data acquired with the Fast-ADT routine has shown that electron diffraction can be processed to reliably determine the absolute structure for crystals that crystallize in non-centrosymmetric space groups. This result has been obtained because of the significant difference between the two enantiomorphs of the structure, and the corresponding calculated intensities based on the dynamical theory used for the structure refinement. This is a very important finding, mostly for the pharmaceutical field, because of the major role that chirality plays in drug effectiveness.

To sum up, the Fast-ADT technique together with the already available data processing tools have demonstrated that reliable and accurate crystal structure characterizations can be carried out with electron diffraction. In this way, the following two chapters use the proven validity of this approach in order to determine the crystal structure of an organic dye and the incommensurately modulated structure of an inorganic industrial mineral in cement.

Chapter 6

A New Crystal Structure of DRED1

τὴν δὲ εὐμάρειαν οὐδὲν ἄλλο λέγω
ἢ εὐκοσμίαν.
[Tranquility is nothing else than the good ordering of the mind.]

Τὰ εἰς ἑαυτόν *[Meditations]*
Marcus Aurelius

Previous chapters have shown how a TEM can be aligned to set up a quasi-parallel beam, with and without precession, that coupled with the Fast-ADT technique provides a suitable combination for the systematic acquisition of 3D ED datasets. Such setting has been proved to fit for reliable crystal structure determinations as well as for the retrieval of fine crystallographic details. In this chapter, the Fast-ADT technique is applied to characterize an unknown polymorph of the DRED1 molecular crystal. This is an organic compound that loses its crystallinity under the illumination of the electron beam, thus the challenge consists on getting enough reflections with good signal-to-noise ratio for a successful structure determination. Although several Fast-ADT datasets are collected and their data processing reveals a triclinic crystal system, the standard tools for intensity extraction are not enough in order to get a complete structure solution. For this reason, the reflection intensities are extracted by means of the fitting of the double-peaked profile on the rocking curves, and different *hkl* files are merged in order to increase the completeness. This approach allows the *ab initio* determination of all 46 non-hydrogen atom positions related to two independent DRED1 molecules in the asymmetric unit of the $P\bar{1}$ space group. Finally, a Rietveld refinement against XRPD data and a dynamical refinement on Fast-ADT datasets confirm the new structure model for DRED1.

6.1 The Disperse Red 1 Dye

Disperse red 1 (DRED1: $C_{16}H_{18}N_4O_3$) is an azobenzene derivative from the family of dye molecules. Dyes belong to the general family of colourants together with pigments, but the difference is that dyes are soluble coloured compounds that are designed to bond strongly to polymer molecules for textile applications, while pigments are insoluble and they are mainly used in paints, printing inks or plastics [288]. The molecule of DRED1 is shown in Figure 6.1.1.

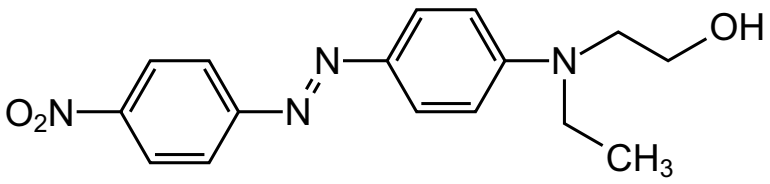

Figure 6.1.1: DRED1 molecule.

The DRED1 molecule is formed by a nitro group (-N_2O) at the para position of one of the benzenes, while there is a nitrogen at the other benzene linked to an ethanol group (-C_2H_6O) and an ethyl group (-CH_2CH_3) positioned above and below the azobenzene plane. This compound has a characteristic red colour that gives name to the dye.

DRED1 has been intensively characterized with spectroscopic tools (such as Fourier-transform infrared spectroscopy, visible-ultraviolet spectroscopy, Raman spectroscopy and nuclear magnetic resonance) in different chemical environments [26, 27, 28, 29], but few studies are found regarding its crystalline structure [289, 290]. Electron diffraction has already been used in combination with other characterization tools for structural studies in these kinds of organic compounds, mainly pigments, during the last decades, especially since the invention of the 3D ED technique [164, 291, 292, 293, 294, 295]. In this context, a new crystallographic study is carried out on the basis of electron diffraction in order to get a clearer picture of the crystal structure of DRED1 in comparison to the reported ones.

6.2 Crystal Structure Determination

DRED1 powder was purchased from Sigma-Aldrich and a recrystallization procedure with toluene was followed in order to improve the crystallinity of the compound. Figure 6.2.1 shows the XRPD patterns of the as-made and recrystallized DRED1 in normalized intensity scale. This plot displays reflections with higher signal-to-noise ratio for the recrystallized one that indicates a better crystallinity of the material. Then, the re-crystallized powder was mixed with a very small amount of barite, dispersed in n-hexane and sprayed with a UIS250v Hielscher sonifier on carbon-coated copper grids for their subsequent use in the TEM. The small amount of barite is used as a reference to accurately calibrate the diffraction patterns.

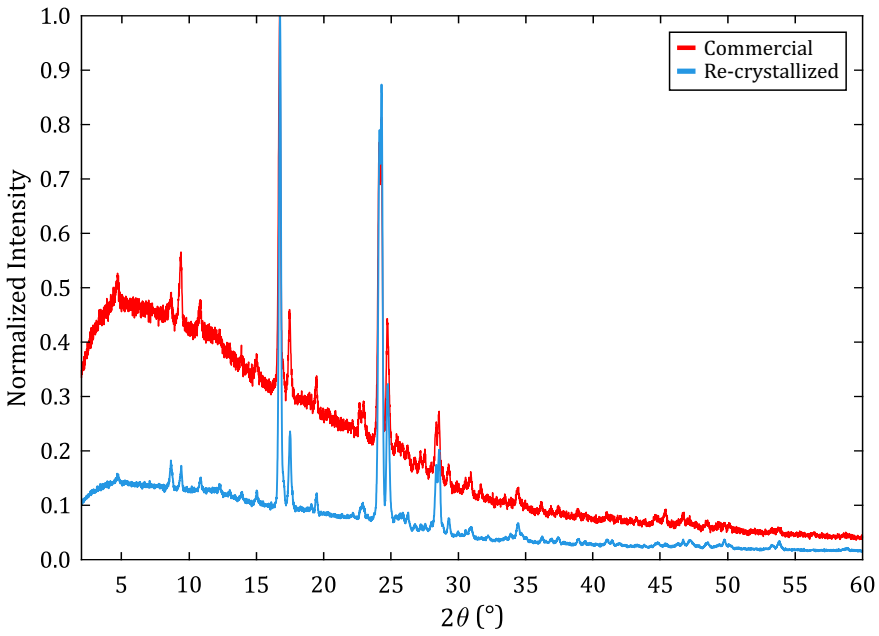

Figure 6.2.1: XRPD patterns of the commercial DRED1 powder (red) and the re-crystallized one with toluene (blue).

6.2.1 Data Acquisition

Fast-ADT datasets were acquired with a FEI Tecnai F30 FEG operated at 300 kV in STEM mode. Spot size 8, gun lens 8 and a 10-µm CA in the Microprobe illumination was used to produce a 200 nm beam with an electron dose rate of 0.21 $e^-/Å^2s$ (at FWHM) for the acquisition of the diffraction patterns. A 5 nm beam with an electron dose rate of 293 $e^-/Å^2s$ (at FWHM) was set for STEM imaging. 1° of precession was applied for the acquisition of the 3D ED datasets with the DigiStar unit provided by NanoMegas. The Gatan US4000 CCD with binning 2 and exposure times of 2 and 4 seconds were used for the collection of the patterns. Camera length of 1 and 1.2 m were chosen to take advantage of the full CCD field of view as the material diffracts up to 0.8 Å at maximum. The crystal tracking files were generated from STEM-HAADF images (1024 × 1024) with a dwell time of 4 µs per pixel. A final accumulated dose of $\sim$ 100 $e^-/Å^2$ was obtained per Fast-ADT dataset. Initially, three datasets were acquired at room temperature (RT) using a Fischione tomography holder.

Later, three other crystals were measured with a Gatan cryo-transfer tomography holder (model 914) at liquid N_2 temperature (LT) in order to increase the stability of the sample [296]. The holders were tilted from -60° to 60° in all cases. Figure 6.2.2 shows STEM-HAADF images of two measured crystals.

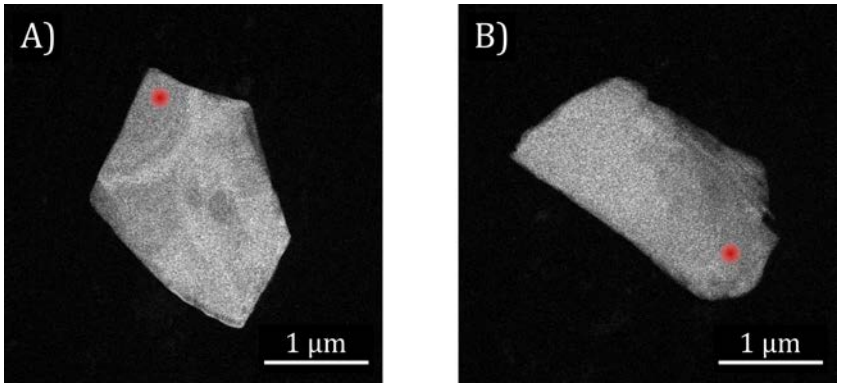

Figure 6.2.2: STEM-HAADF images of two measured plate-like crystals. The red filled circles represent the size and position of the electron beam for the acquisition of the diffraction data.

XRPD measurements were carried on a STOE transmission powder diffraction system (STADI P) equipped with a Ge (111) monochromator (Cu-Kα_1 radiation, λ =1.54056 Å) and a linear position sensitive director. A borosilicate glass capillary of 1 mm in diameter was filled with the microcrystalline powder, which was cooled down to 140 K during the measurement by an Oxford Cryostream 700Plus.

6.2.2 Unit Cell Determination & Structure Solution

The six acquired diffraction datasets were imported to the *eADT* program for unit cell determination and intensity extraction. All datasets revealed a triclinic unit cell with the following averaged parameters: a = 7.8(1) Å, b = 11.20(9) Å, c = 19.7(1) Å, α = 74.0(8)°, β = 83.8(9)°, γ = 70.4(6)° and Ω = 1569(26) Å^3 (see Appendix for each determined unit cell). The DRED1 molecule occupies $\sim$ 395 Å^3 according to the approximated elemental volumes reported in the Hofmann tables [228], which means that approximately four molecules can sit inside the found unit cell. Molecular crystals tend to crystallize in low-symmetry settings because molecules constitute the basic structural unit of the crystal and occupy a large volume, thus the resulting crystal has to keep an energy-balanced packing without overlapping of molecules. However, when main sections of the reconstructed ODS are inspected, systematic extinctions appear along the a^*-axis that could hint the possibility of a higher symmetry cell. Figure 6.2.3 shows these sections for crystal 3 at RT and crystal 4 at LT. In this scenario, *Lepage* [297] was used to look for other cells, but only monoclinic cells with different centrings and face-centred orthorhombic cells were suggested that match the metric of the found triclinic cell. Initial trials with space groups following these translational symmetries using DM in *Sir2014* showed high R_{int} values, which indicate wrong choices of symmetry, and the structure solutions did not provide a model that could resemble a packing of DRED1 molecules. For these reasons, the triclinic setting with four DRED1 molecules was chosen for further structural analysis (see Appendix for the projections along the main axes of the reconstructed ODSs from crystal 3 and crystal

4 datasets). The XRPD pattern was indexed in *DICVOL* [298] based on the averaged *eADT* unit cell parameters and a Pawley refinement [299] was followed to accurately obtain the lattice parameters: $a = 7.72170(2)$ Å, $b = 11.13973(4)$ Å, $c = 19.57525(8)$ Å, $\alpha = 73.8003(28)°$, $\beta = 83.0396(38)°$, $\gamma = 70.4982(13)°$ and $\Omega = 1523.465(9)$ Å^3.

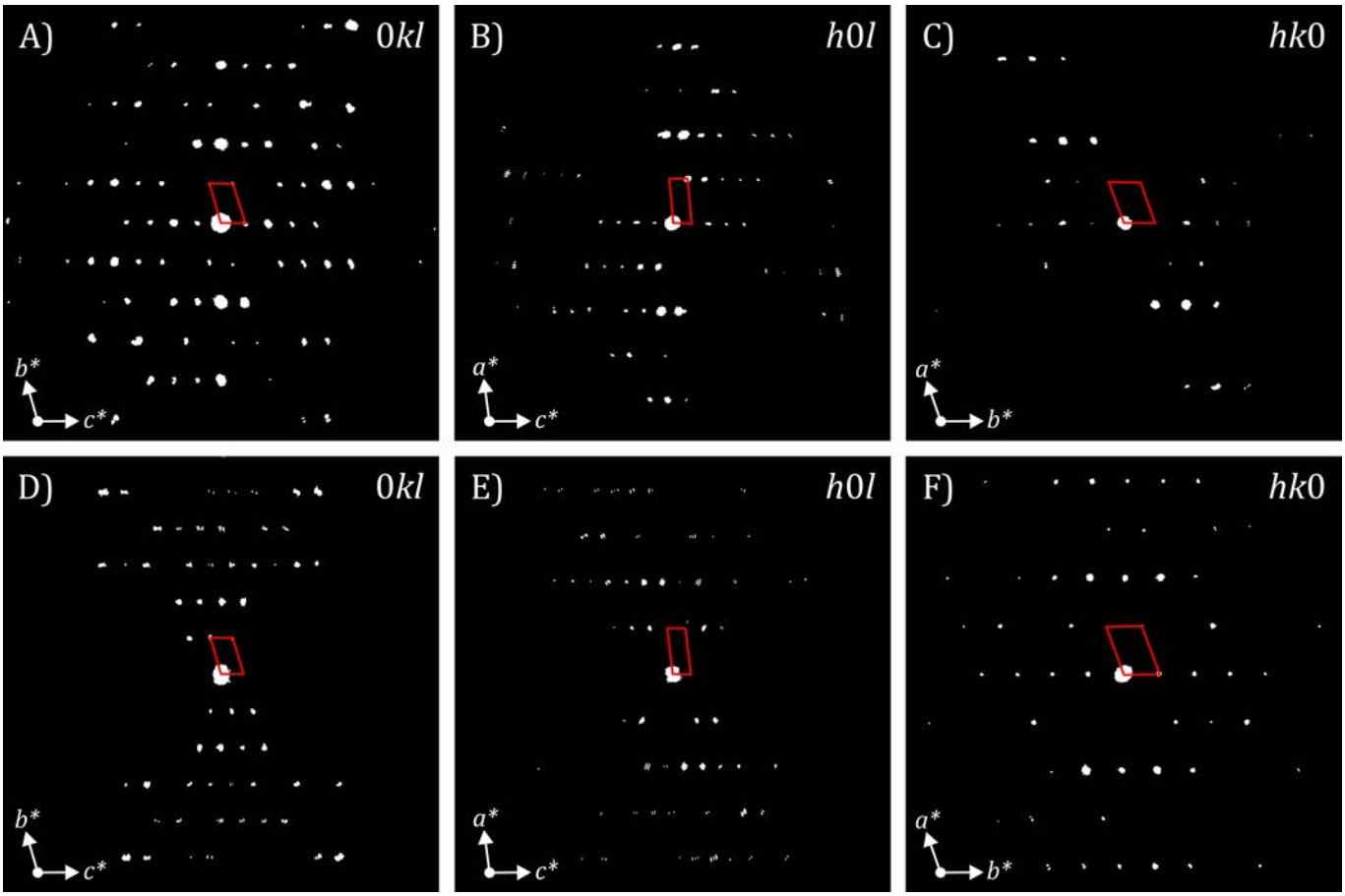

Figure 6.2.3: 0*kl*, *h*0*l* and *hk*0 sections of the reconstructed ODS from crystal 3 at RT (upper figures) and crystal 4 at LT (lower figures). The red rhomboids correspond to the projections of the unit cell.

Figure 6.2.4 shows the projections of the reconstructed ODS along the c^*-axis of the triclinic setting for two crystals measured at RT and LT. Here, it is worth noting how the use of liquid nitrogen improved the quality of the dataset. The sensitivity of the DRED1 crystals under the illumination of the electron beam is not that high in comparison to other organic materials or metal-organic frameworks [181, 300]. However, the illuminated areas did not show intense reflections anymore after a Fast-ADT dataset was acquired, i.e. a $\sim$ 100 e$^-$/Å^2 electron dose was enough to considerably deteriorate the ordering of the solid. The sample cooling with liquid nitrogen proved to stabilize the particles because reflections at higher diffraction data resolutions could be acquired, and a good signal-to-noise ratio for the reflection intensities was kept until the dataset acquisition was finalized. In this way, the maximum electron dose before the crystallinity is lost was increased and more statistically-meaningful reflections were acquired. For instance, the number of reflections with intensity above 3σ for the crystal 3 dataset using all acquired frames (121) is 2042, while crystal 4 dataset using 111 of the acquired patterns provides 2470 above this threshold.

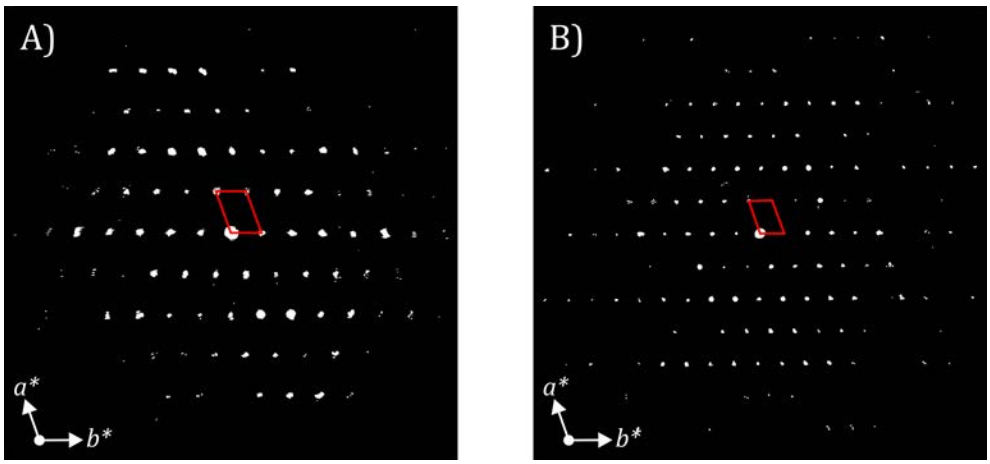

Figure 6.2.4: Projections along the c^*-axis from A) crystal 3 at RT and B) crystal 4 at LT. The red rhomboids correspond to the projections of the unit cell.

Reflection intensities were then extracted with *eADT* by the assignment of the maximum value of the rocking curve as the reflection intensity. Since the diffraction data may have slight geometrical distortions due to the optical system of the TEM as well as the different morphology of the measured crystals, the found *eADT* unit cell in each dataset was used here instead of the XRPD-refined one. In this way, the reflection positions in the diffraction patterns and the positions calculated by the *UB* fit better and their intensity can be accurately integrated.

The obtained *hkl* files were imported to *Sir2014*, a composition of four DRED1 molecules was set for the normalization of the structure factors, and the $P\bar{1}$ space group was selected to run DM to retrieve *ab initio* structure solutions. The resulting electrostatic potentials showed some hints on the approximate positions of the azobenzenes but they differed between different datasets. One of the reasons of such poor results comes from the low completeness of the diffraction data. Although an angular range of 120° was covered for each dataset, the percentage of independent reflections ranges between 55% and 70% because of the low symmetry. Furthermore, DRED1 crystals exhibit preferred orientation with the *a* and *b* axes sitting in the plane of the TEM grid, and only one of the datasets covered the *c*-axis. This means that most missed reflections are along the *c*-axis direction, thus producing an elongation of the resulting electrostatic potential through this direction that makes the determination of the ethanol and ethyl positions difficult [301].

In order to increase the completeness and improve the possibility of a successful structure solution, one dataset covering the *a* and *b* axes was completed with a second one including the *c*-axis. The *hkl* files of both datasets were merged by a Matlab script courtesy of Yaşar Krysiak. This code takes both *hkl* files, looks for reflections that appear in both files and obtains a scale factor through a linear fitting. Then, the scale factor is applied to the reflections of the second file that are not present in the first one, and the final *hkl* file is generated with all reflections of the first one plus the scaled reflections of the second one. Table 6.2.1 shows the parameters of the *hkl* files from the two used diffraction datasets and the final merged *hkl* file. The slight increase of the R_{int} indicates the good merge of both reflections files.

	Crystal 3 (RT)	**Crystal 4 (LT)**	**Merged**
Used Tilt Range (°)	-60 to 60	-50 to 60	-
Num. of Reflections (#)	5979	10203	12702
Ind. Refl. at 0.8 Å (#)	3508	4180	5530
Completeness (%)	56.4	67.1	88.8
R_{int} (%)	17.5	20.0	20.6

Table 6.2.1: Parameters of two diffraction datasets and their merged *hkl* file. R_{int} is based on structure factors from *Sir2014*.

Ab initio structure solutions were tried once again with the merged *hkl* file in DM of *Sir2014*, yet the results did not improve significantly. In this situation, SA from *Sir2014* was used instead. The molecule was imported as a *.mol* file obtained by drawing the molecule and the application of a forcefield geometry optimization in *Materials Studio* [302]. In the SA algorithm, the x, y and z translation as well as its whole rotation were set free to move. Regarding the torsion angles, only the ones related to the movement of the end groups were flexible (5 in total), while the ones linked to hydrogens were fixed (see Figure 6.2.5). SA was executed 10 times with space groups $P1$ and $P\bar{1}$ with four and two independent molecules, respectively. The resulting models showed the positions of the azobenzenes in both space groups, and the small difference found between them suggested that the crystal could be well described in $P\bar{1}$. However, the correct orientation of the nitro, ethyl and ethanol groups was more difficult to retrieve as they have more freedom to move, and the comparison of the XRPD pattern against the simulated powder based on the model from SA showed some significant discrepancies (see Appendix).

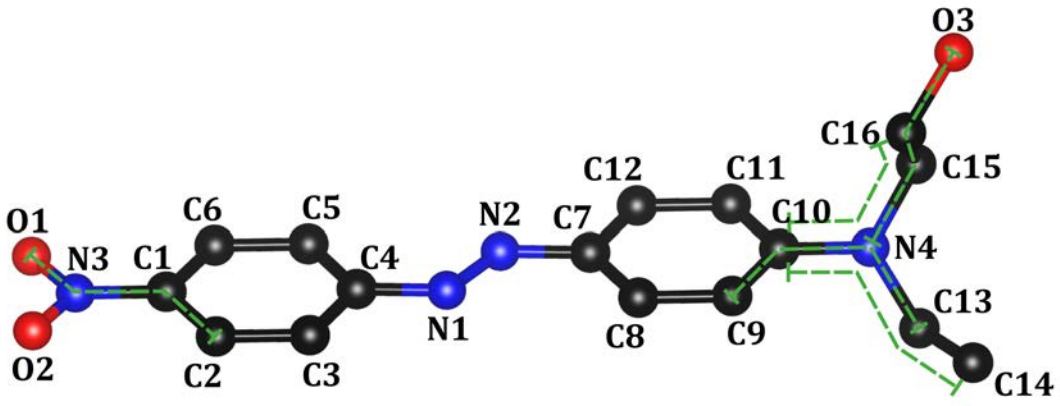

Figure 6.2.5: Sketch of the DRED1 molecule with the labels for the different atoms and the 5 torsion angles (marked in green dashed lines) used for the structure solutions of SA from *Sir2014*.

At this point, the reflection intensities from the two datasets used for the merged file were extracted with *PETS2* [13]. The intensities were initially extracted through the fitting of the double-peaked profile, then the orientation angles were refined using least-squares methods via the fitting of the experimentally determined rocking curves with the modelled curves, and, finally, reflection intensities were extracted based on the new orientation and a scale factor refined as well on the rocking curves of each diffraction pattern (see Appendix for the results on the fitting of the double-peaked profiles on the averaged rocking-curves from the different datasets). The unit cell determined from XRPD was used and constrained here to prevent the triclinic lattice to partially compensate the misorientation of the patterns. The extracted *hkl* files were then merged to obtain a new *hkl* file with R_{int} of 21.1 % and completeness of 87 %, which was subsequently used for *ab initio* structure solutions with DM in *Sir2014* as well as with the CFA in *SUPERFLIP* [243] in the $P\bar{1}$ space group using a fixed composition of four molecules (B_{iso} was fixed to 2 Å^2 in *SUPERFLIP*). In both cases, the crystal structure determination was successful and a structure model with all 46 non-hydrogen atoms of the two DRED1 molecules in the asymmetric unit was directly retrieved. Table 6.2.2 shows the resulting parameters for the structure solutions according to the different intensity extractions and algorithms used. Figure 6.2.6 shows the electrostatic potential and the as-found structure models with *SUPERFLIP* and *Sir2014* revealing a molecule stacking similar to the one found in the previous SA. Some of the elements were not properly assigned and they were manually changed according to the DRED1 molecule.

	Max. Int. / SA	**Profile Fit / DM**	**Profile Fit / CFA**
Used Diff. Data Res. (Å)	2.0	0.8	0.8
Completeness (%)	95.2	87.1	87.5
Refl./Param. Ratio	17.2	15.3	8.07
Overall B (Å^2)	13.66	0.03	1.88
R_{int} (%)	7.98	21.1	20.9
R^* (%)	45.9	35.4	44.2

Table 6.2.2: Output parameters of the structure solutions according to the different intensity extractions (Maximum intensity in *eADT* and the fitting of the double-peaked curved in *PETS2*) and algorithms (SA and DM from *Sir2014*, and CFA from *SUPERFLIP*). R_{int} is based on structure factors.
* The R values reported here correspond to R_{SA}, R based on structure factors and the BEA algorithm, and R_{cf}, respectively.

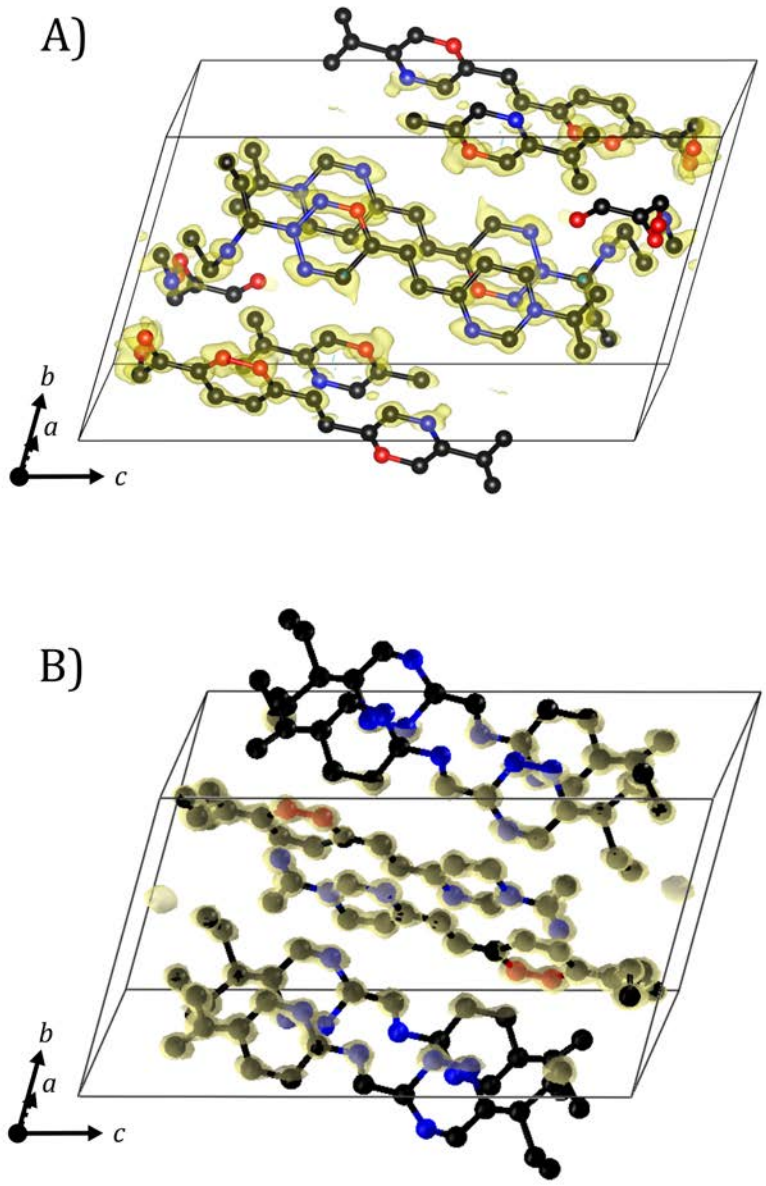

Figure 6.2.6: Projections of the as-found structure solutions in A) *SUPERFLIP* and B) *Sir2014* overlapped with their related electrostatic potential at 2σ (displayed in transparent yellow). The potentials that are not filled in B) correspond to the atoms of molecules from subsequent unit cells. Black atoms correspond to carbon, blue ones to nitrogen and red ones to oxygen.

6.2.3 Structure Refinements

The obtained structure solution was used as the initial model for its refinement against XRPD through the Rietveld method from the program *TOPAS* [303]. The table in Figure 6.2.7 shows some of the input parameters and the resulting figures of merit for the refinement of the DRED1 structure model against the XRPD data.

Rietveld Refinement	
Formula	$C_{16}H_{18}N_4O_3$
ρ_{calc} (g/cm^3)	1.371
Space Group	$P\bar{1}$
Z, Z' (#)	4, 2
θ_{max} (°)	40
B_{iso}-C (Å^2)	1.15(7)
B_{iso}-N (Å^2)	1.36(15)
B_{iso}-O (Å^2)	1.89(14)
B_{iso}-H (Å^2)	1.38(8)
GoF (-)	1.13
R (%)	1.72
R_w (%)	2.30

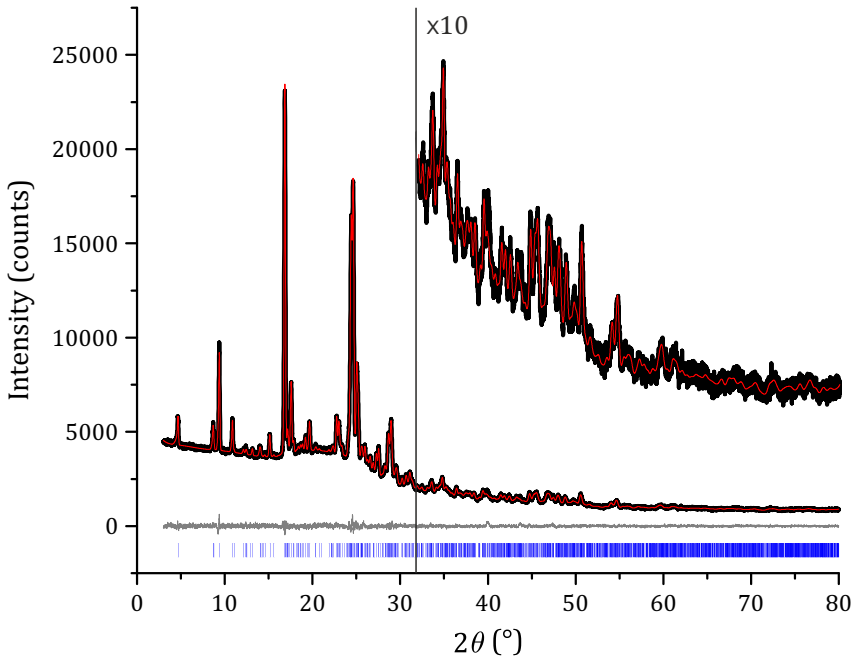

Figure 6.2.7: Rietveld refinement in *TOPAS* of the new polymorph of DRED1 on the XRPD pattern taken at 140 K. Z refers to the number of molecules inside the unit cell and Z' is the independent number of molecules according to the space group. R and R_w are based on structure factors. Black profile corresponds to the measured intensities, red profile to the calculated ones, and grey profile to their difference. Blue tick marks represent the reflection positions according to the Pawley refined unit cell parameters.

The hydrogen atoms were initially positioned at $\sim$ 1.09 Å of carbons in the benzenes, at $\sim$ 1.10 Å of carbons in the -CH_2 and -CH_3 groups, and at $\sim$ 0.86 Å of the oxygen in the ethanol end-group. Their initial orientation with respect to the other elements was given according to the forcefield geometry optimized molecule created in *Materials Studio*. Angles, distances and geometries were restrained by chemical reasons according to similar structures found in the Cambridge structural database [304]. Three isotropic DPs were defined for each atom type and refined separately, whereas hydrogen was fixed to be 1.2 times the carbon DP. The reported low figures of merit demonstrate the reliability of the crystal structure and Figure 6.2.7 shows the resulting calculated reflection intensities against the experimental ones after the Rietveld refinement that proves the correctness of the structure model for the new polymorph of DRED1. The position of all symmetrically-independent atoms obtained from this refinement are provided as a *Cif* file in the Appendix.

Although the refined structure gave a good fitting, the hydrogens of the OH- groups were not that clear because the oxygens of four molecules were close and they generated a hydrogen-bond (H-bond) network between them. In order to verify the formation of this network, crystal 4 and crystal 5 electron diffraction datasets were used, as single datasets as well as for a combined refinement, to perform a dynamical refinement with the XRPD-refined model. Initially, a difference Fourier map without the hydrogens was calculated from these datasets in order to check if extra potentials appear at these positions. Figure 6.2.8A shows this map with the structure model from the Rietveld refinement in which an enlarged extra potential at 3σ is seen close-by one of the hydrogens. In this way, the dynamical refinement was carried out using the XRPD-refined structure as the initial model, applying similar restraints as the Rietveld refinement (see Appendix), and following the same procedure described for the barite example in the previous chapter. Table 6.2.3 shows the resulting figures of merit of the refinement. Figure 6.2.8B shows the difference Fourier map with the final dynamical refined model where the map was calculated without the hydrogens of the network. The extra potential seen in Figure 6.2.8A is enhanced in this case because there is still remaining potential at 4σ, which significantly indicates that the hydrogen needs to be placed at this position and thus confirms the formation of the square-like network suggested from the Rietveld refinement. The *Cif* file of the resulting refined structure is provided in the Appendix.

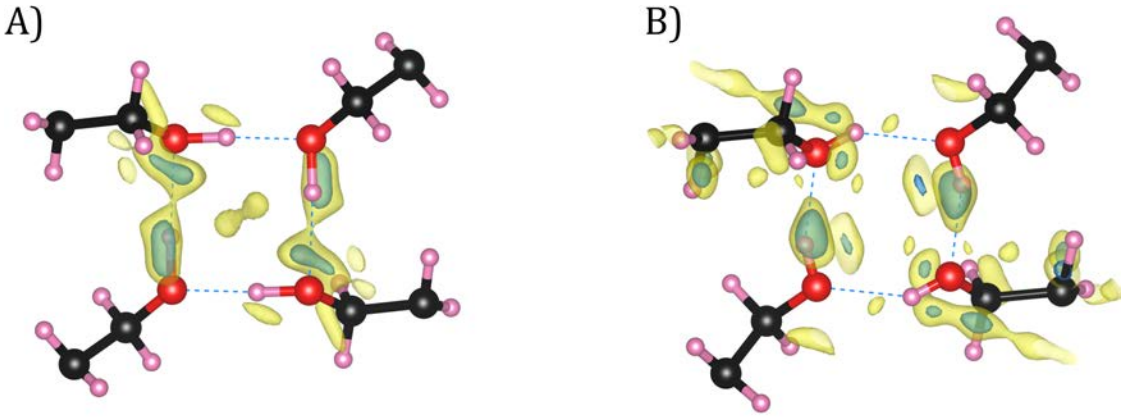

Figure 6.2.8: Difference Fourier maps from the area of the H-bond network A) before and B) after the dynamical refinement. The structure model in A) corresponds to the one obtained from the Rietveld refinement, and B) corresponds to the model retrieved at the end of the dynamical refinement. Electrostatic potentials at 2σ and 3σ are displayed in yellow and blue, respectively. $2\sigma = 0.29$ e$^-$/Å and $3\sigma = 0.43$ e$^-$/Å for A), $2\sigma = 0.21$ e$^-$/Å and $3\sigma = 0.31$ e$^-$/Å for B). Pink atoms correspond to hydrogen, black ones to carbon and red ones to oxygen.

The found crystal structure corresponds to a new polymorph that is different to the two reported ones from XRPD. It was first characterized in a hydrated form by Lacroix et al. with a triclinic crystal system ($P\bar{1}$) and two independent molecules ($Z = 4$) [289]. Subsequently, Nath et al. showed a dehydrated form with a monoclinic crystal system ($P2_1/n$) and two molecules in the asymmetric unit ($Z = 8$) [290]. In this case, both molecules exhibit statistical disorder for the ethanol and ethyl groups and the Rietveld refinement results in partial occupation of both groups in their respective positions. Table 6.2.4 shows the unit cell parameters for these two published structures and the one found in this work.

	Crystal 4	**Crystal 5**	**All Reflections**
Reflections at 0.91 Å(#)	2507/12946	1387/11560	3894/24506
Refl./Param. (-)	6.93	3.83	10.8
GoF (-)	2.27/1.20	2.87/1.17	2.51/1.19
R (%)	10.6/29.2	12.2/37.5	11.2/32.7
R_w (%)	11.5/13.7	13.6/16.3	12.3/14.7

Table 6.2.3: Resulting figures of merit (obs/all) from the dynamical refinements in *Jana2006*. The criterion for observed (obs) reflections was $I(\vec{g}) > 3\sigma(\vec{g})$. The "Refl./Param." parameter refers to the number of observed reflections over the number of refined parameters. R and R_w are based on the square root of reflection intensities. N_{or} of 128, g_{max} of 1.3 Å^{-1}, S_g^{max} (matrix) of 0.01 Å^{-1} , S_g^{max} (refine) of 0.1 Å^{-1} and RS_g of 0.8 were used for the refinement.

	$\boldsymbol{a}$ **(Å)**	$\boldsymbol{b}$ **(Å)**	$\boldsymbol{c}$ **(Å)**	$\boldsymbol{\alpha}$ **(°)**	$\boldsymbol{\beta}$ **(°)**	$\boldsymbol{\gamma}$ **(°)**	$\boldsymbol{\Omega}$ **(Å^3)**
Lacroix et al. [289]	7.539(1)	11.365(1)	19.358(3)	83.58(2)	83.77(2)	73.81(1)	1578
Nath et al. [290]	10.152(2)	7.769(2)	38.639(3)	90	92.863(3)	90	3043.61
Plana-Ruiz et al. [305]	7.72170(2)	11.13973(4)	19.57525(8)	73.8003(28)	83.0396(38)	70.4982(13)	1523.465(9)

Table 6.2.4: Unit cell parameters of the crystalline structures of DRED1.

The only left over question was whether water is present inside the crystal given that the hydrated triclinic structure of Lacroix et al. incorporates two water molecules inside the unit cell. Half cell of the dehydrated monoclinic phase has a volume of $\sim$ 1521 Å^3, which is close to the cell found in this work ($\sim$ 1523.5 Å^3). The hydrated triclinic one has a volume of $\sim$ 1578 Å^3. According to the increment method of Hofmann [228], H_2O has an average volume of 43.1 Å^3, which shows that if the determined crystal structure would have water, its volume would be increased about 50 Å^3 and it would fit to the volume of the reported hydrated structure. This indicates that the crystalline volume of the solved structure is not big enough to place water molecules. To confirm this, differential thermal analysis (DTA) and thermogravimetric analysis (TGA) were carried out to have an experimental proof that the structure does not contain water.

TGA and DTA are experiments that measure the weight of the sample and the temperature difference that the sample could undergo with respect to a reference inner material, respectively, through a temperature cycle. The usual combination of both techniques allows, for instance, the identification of phase transitions, crystallization processes or solid state reactions [306]. Figure 6.2.9 shows the TGA and DTA curves for the re-crystallized DRED1 powder through a temperature cycle between 28 °C and 510 °C. Around 100 °C there is a smooth decrease on the DTA curve but the TGA does not show any decrease on the mass of the sample, thus no water is present inside the structure. Interestingly, an exothermic reaction happens around 160-170 °C that indicates a phase transition of the crystalline structure before the sample melts at around 310 °C.

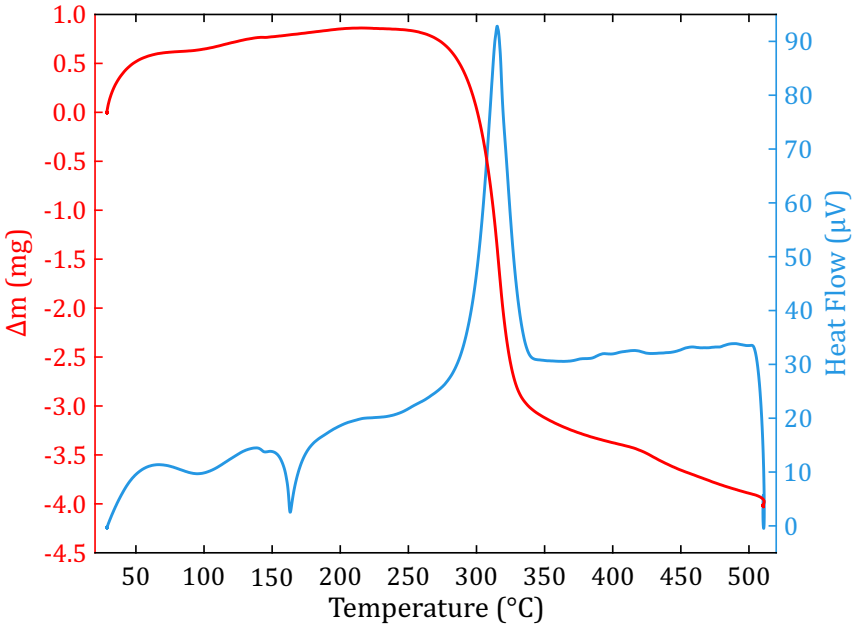

Figure 6.2.9: TGA (red) and DTA (blue) curves on the re-crystallized DRED1 powder through a temperature cycle between 28 °C and 510 °C.

In this way, the combination of the refinements on diffraction data and the thermal analysis demonstrates that the new polymorph of DRED1 is well characterized and reliably fits the available experimental data. Figure 6.2.10 shows a projection of the refined crystal structure which only displays the two symmetrically independent molecules inside the unit cell for their better visualization.

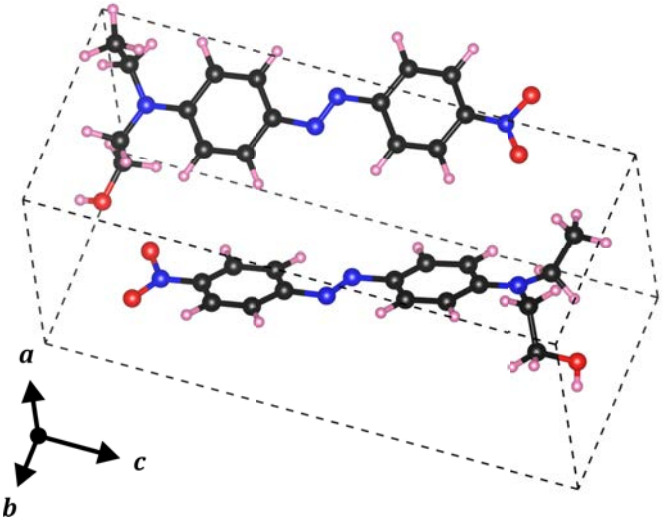

Figure 6.2.10: Projection of the new crystal structure of DRED1 from the dynamical refinement with the two asymmetric molecules only. Pink atoms correspond to hydrogen, black ones to carbon, blue ones to nitrogen and red ones to oxygen.

6.2.4 Crystal Structure Description

The crystal structure in $P\bar{1}$ is formed by two independent DRED1 molecules of different conformation and not fully planar azobenzenes. Figure 6.2.11 shows the two molecules with the different torsion angles obtained from the dynamical refined crystal structure.

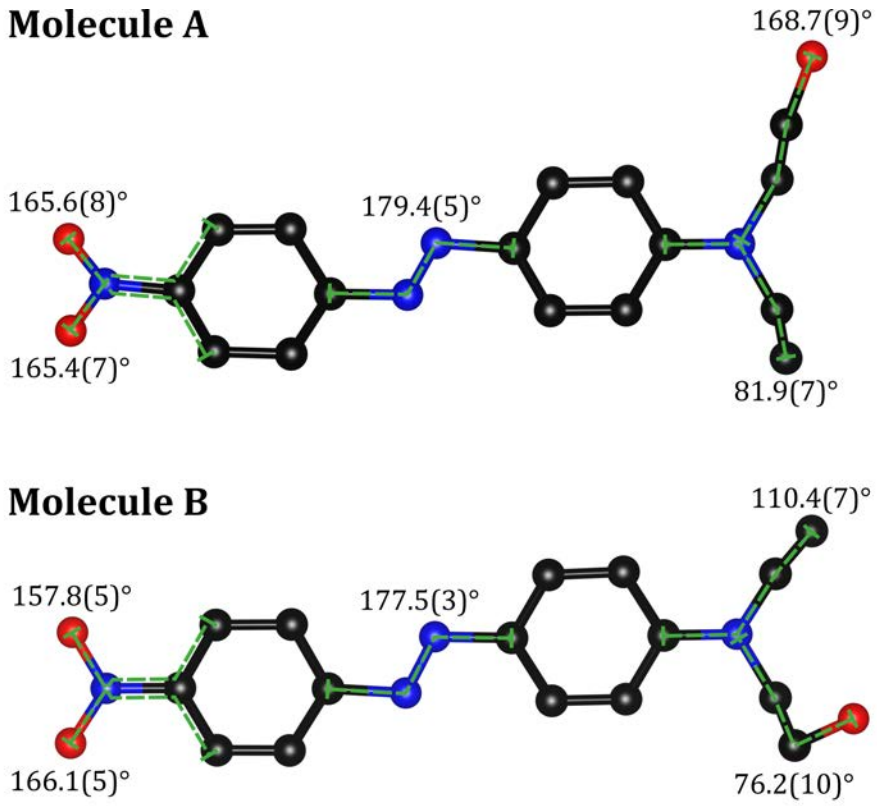

Figure 6.2.11: The two symmetrical independent molecules of the dehydrated DRED1 crystal structure. Torsion angles according to the dynamical refined model are indicated with green dashed lines.

The planes formed by the azobenzenes and nitro groups are deviated from a perfect plane. The two phenyl rings linked by the N=N bond result in torsion angles of 179.4(5)° and 177.5(3)°, which show that the two phenyl rings are not totally co-planar in both molecules, but the phenyl rings are not completely flat either since a deviation up to 1.2(11)° is observed. Para positioned nitro groups are tilted with respect to the plane of their linked phenyl rings as well with torsion angles of 165.6(8)° and 165.4(7)° for the first molecule, and 157.8(5)° and 166.1(5)° for the second one. The lengths of the two symmetrically independent azobenzene planes are approximately oriented along the *c*-axis and their planes are tilted $\sim 126°$ with respect to each other. When several molecules are projected approximately along the *c*-axis, a herringbone-like packing is observed (see Appendix).

However, the biggest difference between the independent molecules lies in the orientation of the ethyl and ethanol groups. In both molecules, they point in opposite directions along the *a*-axis, i.e. while the ethyl group is oriented along the positive direction of the *a*-axis, the ethanol group is pointing

towards the negative one. This structural arrangement is followed by the two molecules but their specific orientations with respect to their linked phenyl groups are different. The torsion angles are 81.9(7)° and 110.4(7)° for the ethyl groups, and 168.7(9)° and 76.2(10)° for the ethanol groups. Due to the positioning of the ethanol groups, the compound exhibits four O-H··O hydrogen bonds with distances between oxygens of 2.624(15) Å and 2.633(10) Å, which leads to a square-like network between four molecules. Figure 6.2.12A shows the H-bond network, its oxygen to oxygen distances and the angles of the hydrogen with respect to the oxygens (see Appendix for the whole orientation of the molecules).

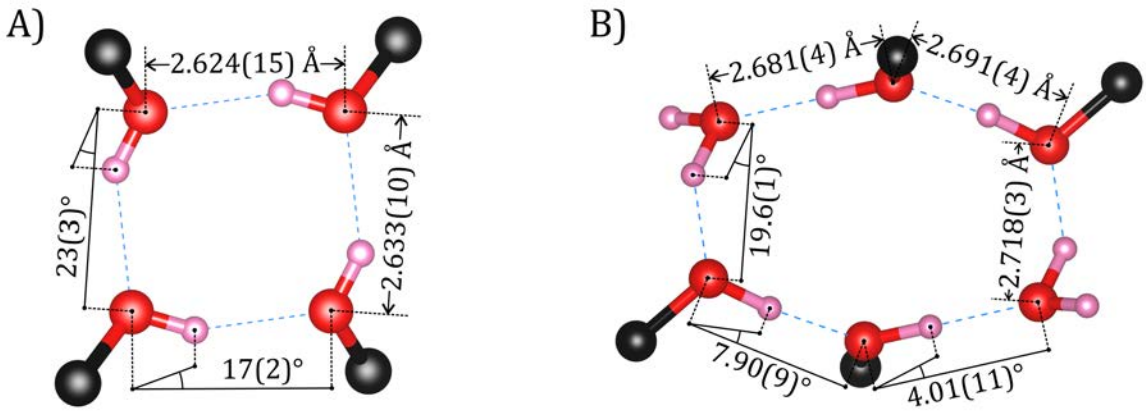

Figure 6.2.12: H-bond network together with the oxygen to oxygen distances and angles of the hydrogens with respect to the oxygens from A) the dynamical refined model reported in this work and B) the one reported by Lacroix et al. [289]. Pink atoms correspond to hydrogen, black ones to carbon and red ones to oxygen. The dashed blue lines represent the hydrogen bonds.

Unit cell parameters and molecular packing are comparable to the structure reported by Lacroix et al. [289]. The structural arrangement of the two independent molecules is quite similar, yet some differences are observed. The torsion angles related to the N=N bonds are smaller, the para positioned nitro groups are less tilted with respect to the azobenzenes and the carbons of the phenyl rings are not as flat, up to a torsion angle of 3.7(4)°. When the two symmetrically-independent azobenzene planes are considered, the angle between both planes is about $\sim 128°$. The ethyl groups are oriented more perpendicular to the azobenzene planes, 82.8(4)° and 77.1(3)°, and the ethanol groups are much more tilted towards their respective azobenzene planes, 62.6(3)° and 175.6° angles. These arrangements of the ethanol groups and the presence of the water molecules result in six hydrogen bonds (2.681(4) Å, 2.718(3) Å and 2.691(4) Å oxygen to oxygen distances) that form an hexagonal-like network as shown in Figure 6.2.12B.

The comparison with the Nath et al. structure is more difficult because of the disorder of the end-groups in both symmetrically-independent molecules [290]. If only the azobenzenes are considered, their planes are the most planar in comparison to the other two crystal structures, and the orientation angle between each of them is decreased down to $\sim 89°$. When the ethanol groups are considered, their arrangement can be described in one of the molecules as partially occupying the position of the ethyl group with the oxygen approximately pointing towards the positive direction of the a-axis in both cases, while in the other molecule it partially occupies four different positions taking into account the position of the ethyl group and the orientation of the oxygen approximately pointing through the positive or the negative direction of the a-axis. Nevertheless, although there are several possible orientations of these groups, no hydrogen-bond network similar to the ones of Figure 6.2.12 is detected in this case. A search in *Lepage* for possible lower symmetry cells suggests another primitive monoclinic cell ($a = 10.15$ Å, $b = 7.77$ Å, $c = 19.32$ Å, $\beta = 92.86°$ and $\Omega = 1521.78$ Å^3). Although the same volume is obtained, the unit cell is quite different to the one reported in this work. Therefore, it is clear that the determined crystal structure is another dehydrated polymorph of DRED1.

6.3 Conclusions

The structure characterization of organic materials is a field that is mostly addressed by X-ray techniques due to its systematic and routine acquisition methods and data processing tools. However, the further development of electron diffraction in terms of detectors as well as acquisition methods has brought the gap between X-ray and electron diffraction closer. In this context, this chapter has shown how electron diffraction data acquired through the Fast-ADT acquisition routine is suitable for the determination of beam sensitive materials.

DRED1 crystals are not as beam sensitive as other organic materials since Fast-ADT datasets could be acquired through angular ranges of 120°. However, the intensity of reflections was strongly decreasing while acquiring the 3D ED dataset and the last diffraction patterns did not contain that much reflections in comparison to the initial ones. In this context, the use of liquid nitrogen proved to be essential in order to stabilize the particle and increase the number of statistically-meaningful reflections acquired through the whole dataset. As a consequence, the different algorithms had more reliable reflections to be used that increased the possibility to retrieve a chemically-valid model.

The data processing of the acquired datasets by using two different structure solution algorithms directly revealed the 46 non-hydrogen atoms in $P\bar{1}$ from the obtained electrostatic potential map. Here, the merging of two datasets in order to obtain a high number of independent reflections, as well as the fitting of the double-peaked curve on the rocking curves for reflection intensity extraction were key for this result. After the initial *ab initio* structure solution was obtained, the structure model was further completed and validated by a Rietveld refinement on XRPD data and a dynamical refinement on two electron diffraction datasets. It is important to remark the sensitivity of electron diffraction to validate the hydrogen positions of the H-bond network and reliably determine one of them for further refinement. In fact, if the R value is calculated according to a structure model with and without hydrogens, the $R(obs)$ increases from 11.2% (with H) to 14.4% (without H), a significant difference that proves the high sensitivity of electron diffraction. Nevertheless, the combination of these two different refinements shows that electron and X-ray diffraction techniques are complementary and provide a strong confirmation of the reported structure.

The structure determination of a triclinic system demonstrates the reliability of electron diffraction for the crystallographic characterization of beam sensitive materials. The structure was characterized by the combination of electron and X-ray measurements, yet it has to be pointed out that the structure solution was directly obtained from single-crystal electron diffraction data. Furthermore, the approach followed in this study also proves that a high-end TEM or camera is not mandatory to reliably determine the structure of beam sensitive materials, since the key point is to acquire good quality datasets and process them in an accurate way to get the most of it.

Chapter 7

The Modulated Structure of Belite

We must use time as a tool,
not as a couch.

Address in NYC to the NAM, 1961
John F. Kennedy

Traditional X-ray methods are extensively applied to cement samples, yet reflection overlapping caused by the high number of different crystal phases in powder patterns, and the necessity to grow large enough crystals for single-crystal analysis, turn out to be non-optimum for the proper characterization of real cement specimens. A TEM coupled with the Fast-ADT routine is advantageous because it enables the fast and systematic acquisition of diffraction datasets from individual particles of well-dispersed powders. For this reason, the approach has been used on the investigation of the different crystalline phases of cement clinkers manufactured by Schwenk Zement KG. Such acquisition procedure and later data processing enables the structural characterization of the different crystalline phases, from which the α'_H polymorph of belite (Ca_2SiO_4) exhibits satellite reflections at an incommensurate reciprocal distance from main reflections. The crystal structure of such polymorph has been known since 1971, but the observed modulation has never been fully studied. Further crystallographic analysis reveals for the first time that the incommensurately modulated structure can be solved and refined by using harmonic and crenel functions [157] in the superspace group $Pnma(\alpha 00)0ss$.

7.1 The Polymorphs of Belite

Belite (Ca_2SiO_4) is one of the major constituents of clinker, thus the structure characterization of the different polymorphs is key to foresee and understand the performance of the resulting cement. Figure 7.1.1 shows a scheme of the different crystal structures, that dicalcium silicate (C_2S) transitions to, with respect to temperature.

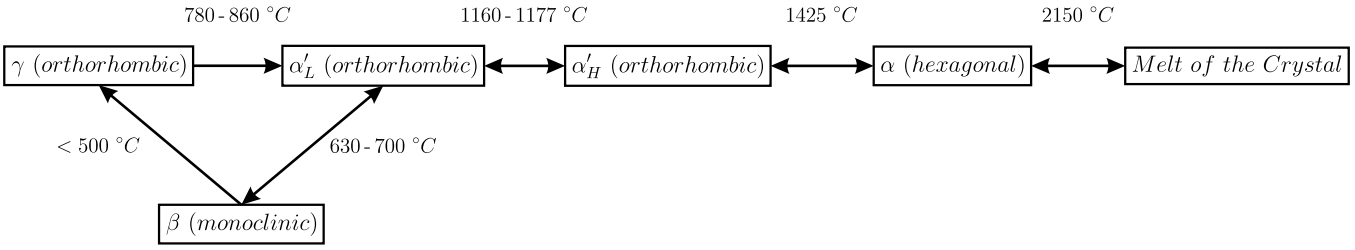

Figure 7.1.1: Schematic of the dicalcium silicate phase transitions between the different polymorphs with respect to temperature [16, 18].

The only phase that is thermodynamically stable at room temperature is the orthorhombic γ-C_2S [307]. All other polymorphs require the addition of dopants that partially substitute the silicon anions by phosphates and/or the calcium by potassium or strontium, as well as the precipitation of minor oxides that induce strain to the crystal structure [307, 308]. In the case of the manufacturing process of the clinker, belite grains contain these different crystal phases and the interest is to preserve the high-temperature polymorphs because of their higher reactivity at room temperature. Table 7.1.1 summarizes the crystallographic information of C_2S-polymorphs according to the literature.

Polymorph	**Crystal System**	**Lattice Parameters**	**Space group**
γ	Orthorhombic	a = 5.081 Å; b = 6.778 Å; c = 11.244 Å [309]	*Pcmn* [309, 310]
β	Monoclinic	a = 5.502 Å; b = 6.745 Å; c = 9.297 Å β = 94.59° [312]	$P12_1/n1$ [311, 312]
α'_L (2a,b,2c)	Orthorhombic	a = 11.184 Å; b = 6.837 Å; c = 18.952 Å [313]	*Pcnb* [313] *Pmnb* or *Pmnn* [314]
α'_L (a,3b,c)	Orthorhombic	a = 5.601 Å; b = 20.863 Å; c = 9.500 Å [315]	$P2_1nb$ [315] *Pmnb* [316]
α'_H	Orthorhombic	a = 5.519 Å; b = 6.767 Å; c = 9.303 Å [317]	*Pmnb* [313, 316, 317]
α	Hexagonal / Trigonal	a = 5.579 Å; c = 7.150 Å [318]	$P6_3/mmc$ [318] $P\bar{3}m1$ [319]

Table 7.1.1: Crystal structure information of the different polymorphs of dicalcium silicate obtained by X-ray single-crystal or powder diffraction. The notation in the α'_L polymorphs refer to the number of α'_H unit cells along the different directions needed to obtain the superstructures.

γ-C_2S is an orthorhombic crystal that resembles the olivine-type structure and contains two independent calcium cations surrounded by six-oxygen environments [309]. When temperature is increased, different superstructures are obtained that are generally referred to as α'_L-C_2S [313, 315]. These can be understood as intermediate phases between γ-C_2S and α'_H-C_2S since their superstructure can be derived from the basic unit cell of α'_H-C_2S, where oxygen and calcium have split positions and calcium cations are surrounded by eight and ten oxygen environments [317]. α-C_2S crystallizes in the hexagonal or trigonal crystal system and, in this case, six and seven oxygen-coordinated environments for calcium cations are observed [318]. When temperature is decreased from 700 °C or higher to around 600 °C, the monoclinic β phase is formed with calcium coordinated by six and eight oxygen anions. If temperature is then decreased further down to room temperature, γ-C_2S is retrieved once again. When enough dopants are added or belite crystals are sufficiently small, the β polymorph is stabilized and it is prevented from reducing to γ-C_2S. Since the latter crystal phase is less dense, the clinker production tries to minimize this transformation because it would produce a more voluminous powder on cooling that results in less strength, an effect called dusting [16].

β, α'_L, α'_H and α phases are classified as glaserite-type structures and they can be subsequently described by the movement of calcium anions and the change of the silicon tetrahedra orientations. The lower the temperature, the lower the symmetry of the related crystalline phase. The nature of the transition between α'_L and α'_H C_2S also leads to the observation of modulated features in the form of extra reflections in zone-axis electron diffraction patterns [307, 320, 321]. Although these features have been investigated through the use of supercells and chemically and crystallographically meaningful descriptions for more than half a century, crystal structure refinements including incommensurate modulations still remain to be done to fully comprehend the compound.

7.2 TEM Study on Calcium Silicate Enriched Samples

7.2.1 Motivation

Almost all crystal structure determinations from the works cited in the previous section were carried out by X-ray diffraction. This means that single-crystal studies had to be done with crystalline domains grown in laboratory conditions, and powder investigations on "real" clinkers or cement samples resulted in diffractograms full of reflection overlapping. The former results in good Rietveld refinements that properly determines the crystal structure of the material under study, but it may hinder other crystallographic effects produced in the manufacturing process. XRPD gives good and accurate phase quantification of the different crystal phases inside the mixture, but it requires the input of all the structures that are thought to be inside in order to run the Rietveld method [322]. In this context, TEM appears as an alternative and complementary characterization tool that can give very useful insights about these kind of samples.

TEM has been used to visualize the morphology, twinning and crystalline structures since the initial studies on cement [323]. In particular, electron diffraction was frequently used to identify superstructure reflections and suggest different hypothetical structures that were subsequently fit in powder or single-crystal X-ray patterns [307, 321, 324]. However, electron diffraction analyses were restricted to pure geometric descriptions and its potential for further crystallographic investigations was left apart due to the lack of the necessary tools.

At this point, the full development of the 3D ED technique together with the systematic acquisition by the Fast-ADT routine is presented here as a new reliable way to study the different crystalline phases of clinkers. Such approach allows to accurately identify crystallographic features from individual crystals inside these mixtures that may be difficult to observe and properly analyse in XRPD, thus increasing the reliability of the models that can be later used in the quantification of powder patterns.

7.2.2 Sample Preparation & Data Acquisition

Three different clinker samples were obtained from the Schwenk Zement KG plant in Bernburg, Germany. They were differentiated by the amount of sewage that was ejected from the burner pipe inside the rotary kiln (a cylindrical oven that is slowly rotating and it is tilted between 1° and 4° from the horizontal ground where the clinker is produced); 0, 2.5 and 5 tonnes per hour, referred in this work as "clinker_0", "clinker_2.5" and "clinker_5", respectively. In all cases, the final amount of sewage used during their production was the same since the amount that was not shot from the pipe was introduced at the input mixture of the kiln. The ground clinkers were then chemically treated by BASF Construction Solutions GmbH to dissolve the aluminates and ferrites in order to easily identify the calcium silicate phases. The resulting powders were dispersed in ethanol and sprayed on TEM carbon-coated copper grids with a UIS250v Hielscher sonifier. Cu grids were cleaned with argon plasma during one minute before and after the powder was sprayed on them in order to eliminate remaining organic compounds and minimize carbon contamination during TEM measurements.

The prepared copper grid samples were loaded on a FEI single-tilt holder as well as a Fischione tomography holder and inserted in a FEI Tecnai F30 FEG operated at 300 kV. The microscope was

aligned in STEM mode with the Microprobe illumination. The same data acquisition procedure was carried out for all samples: initial EDS measurements to identify particles with calcium and silicon followed by a 3D ED acquisition by means of the Fast-ADT routine. Spot size 6, gun lens 1 and a 50-µm CA were used to acquire the EDS spectra with a EDAX EDAM III detector. Spot size 6, gun lens 8 and a 10-µm CA were selected to set a quasi-parallel beam between 150 and 200 nm of diameter in order to check the particles crystallinity and acquire the diffraction data. STEM images were acquired with a Fischione HAADF detector mounted at the side port of the TEM column and diffraction patterns were collected with a Gatan US4000 with binning 2 and different exposure times. Five crystals were investigated in "clinker_0", six in "clinker_2.5" and three in "clinker_5" from which 3D ED datasets with and without 1° of precession angle were acquired for each particle.

7.2.3 Data Analysis

EDS spectra allowed a direct identification of the calcium silicate phases, and the quantification of the Ca/Si ratio was accurate enough to distinguish between alite and belite crystal phases. Table 7.2.1 exemplarily shows the EDS spectra quantification for the "clinker_0" sample from which four crystals correspond to belite and one crystal to alite. Aluminium and magnesium were included in the quantification because they are sometimes incorporated in the structures as dopants.

	Crystal 1	**Crystal 2**	**Crystal 3**	**Crystal 4**	**Crystal 5**
O	60.0	55.8	58.0	55.2	49.9
Mg	2.0	1.6	0	0	0
Al	2.2	1.8	0	0	0
Si	11.1	13.6	15.2	13.8	12.3
Ca	24.6	27.2	26.8	31.0	37.8
Ca/Si	2.2	2.0	1.8	2.2	3.1

Table 7.2.1: EDS spectra quantification in atomic % for the "clinker_0" measured particles. The K edge was used for the quantification of all elements.

Since this work was focused on the polymorphs of belite (C_2S), 3D ED datasets were analysed from crystals that have Ca/Si ratio ~ 2 in the EDS quantification. In this way, three, one and two β-C_2S were identified in "clinker_0", "clinker_2.5" and "clinker_5", respectively, and one α'_H-C_2S was found in each sample. Their unit cells were determined from the nine non-precessed datasets in the *eADT* program, which are shown in Table 7.2.2. Here, the unit cell parameters were scale-corrected by the averaged factor obtained from the parameters of the best quality β-C_2S dataset and the values reported by Jost et al. [312]. The β polymorph was used for this scaling because it is better understood than the α'_H phase. One scale factor was retrieved and applied for each clinker sample.

The ODS reconstruction on the β-C_2S datasets revealed that all measured specimens contained at least one crystal with a typical twin along the [100] direction of the monoclinic cell. This means

that crystalline domains are grown together but they are crystallographically differentiated by a two-fold rotation around the a-axis. Figure 7.2.1 shows a STEM-HAADF image of one of the measured twinned crystals and the projections along the b^*-axis of the three ODS reconstructions. The diffraction contrast in the STEM image enables the direct visualization of the twin boundaries, and two monoclinic unit cells with the same unit cell parameters but differently oriented are needed to index all reflections.

	a (Å)	b (Å)	c (Å)	α (°)	β (°)	γ (°)
"clinker_0"						
Crystal 1 (β)	5.537	6.717	9.278	90.4	94.3	90.3
Crystal 2 (β)	5.525	6.750	9.274	89.6	94.1	90.3
*Crystal 3 (β)**	5.497	6.780	9.246	90.3	94.3	90.0
Crystal 4 (α'_H)	5.496	6.776	9.252	89.9	89.9	89.5
"clinker_2.5"						
*Crystal 1 (β)**	5.544	6.690	9.306	90.0	94.2	89.5
Crystal 2 (α'_H)	5.514	6.765	9.250	90.5	89.5	89.8
"clinker_5"						
*Crystal 1 (β)**	5.538	6.783	9.279	89.9	94.6	90.8
Crystal 2 (β)	5.478	6.751	9.334	89.6	94.2	90.2
Crystal 3 (α'_H)	5.444	6.775	9.348	90.4	90.3	89.8
Literature						
β-C_2S [312]	5.502	6.745	9.297	90.0	94.59	90.0
α'_H-C_2S [317]	5.519	6.767	9.303	90.0	90.0	90.0

Table 7.2.2: The determined unit cells from *eADT* for all measured belite crystals in the different clinker samples and the literature unit cells.
* twinned crystal from which one of the unit cells is reported.

Reflection intensity integration and extraction of the β-C_2S datasets was carried out with *eADT*. In the case of twinned crystals, two separate *hkl* files were obtained for each unit cell. The observation of the reflection condition $h + l = 2n$ in the $h0l$ section of the reconstructed ODS for all of the diffraction datasets pointed to the already reported $P12_1/n1$ space group [312]. Structure solution via DM and a kinematical refinement performed with *Sir2014* provided in all cases the reported crystal structure (see Appendix for the different quality parameters of the solutions). Interestingly, since the twinned crystal datasets have low reflection overlapping, which is mainly seen at low diffraction data resolutions, both *hkl* files in the three cases result in successful structure determination without significant structural differences between them.

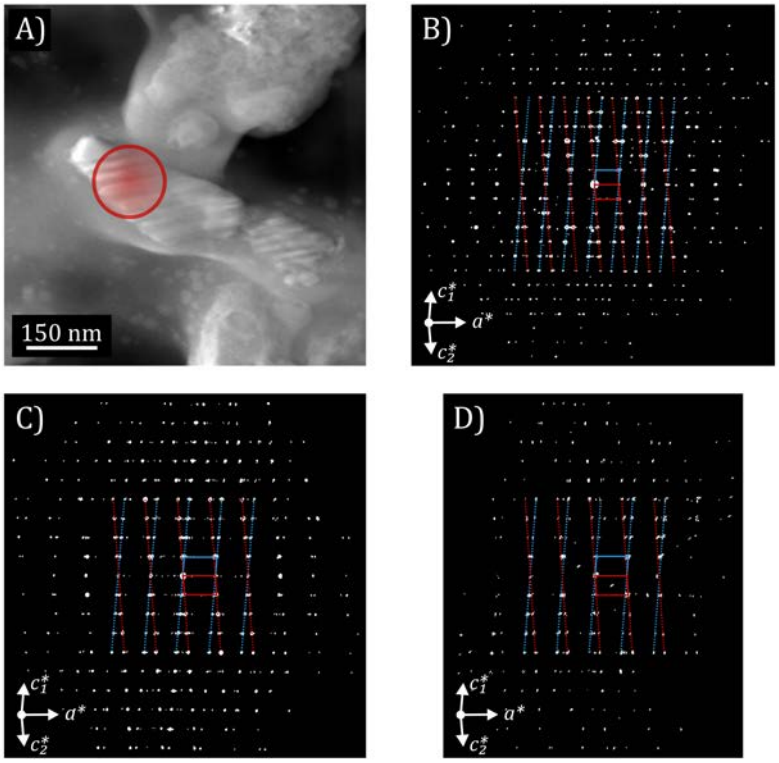

Figure 7.2.1: A) STEM-HAADF image of the twinned β-C_2S crystal in "clinker_0". The red-circle marks the region illuminated by the electron beam for the acquisition of the diffraction datasets. B), C) and D) are projections of the reconstructed ODS along the b^*-axis acquired from the twinned β-C_2S crystals of "clinker_0", "clinker_2.5" and "clinker_5", respectively. The red and blue overlapped rhomboids represent the projected monoclinic unit cells for the two differently oriented cells, and the dashed lines are displayed to show which reflections belong to the different twins.

In the case of α'_H-C_2S datasets, the ODS reconstructions revealed extra reflections that do not fit to the reported α'_L superstructure or α'_H structure. These extra reflections are located along the b^*-axis of the *Pmnb* setting at $\pm$ 0.3725, $\pm$ 0.3795 and $\pm$ 0.3563 of $\vec{b^*}$ for "clinker_0", "clinker_2.5" and "clinker_5", respectively. The values tend to approach an irrational number, thus big supercells would be required in order to have lattices that fit well all observed reflections, yet the number of structural parameters would be really large and the description would not be accurate. Such features were initially reported in 1982 by Jelenić et al [321], who identified extra reflections at $\sim$ 3/8 and $\sim$ 5/8 from the main ones. However, no further structural investigations were undertaken. If these reflections are momentarily ignored, the systematic absences in the $h0l$ and $hk0$ ODS sections confirm the *Pmnb* space group, and the retrieved structure solutions via DM from *Sir2014* correspond to the crystal structure reported by Mumme et al. [317] (see Appendix for the different quality parameters of the solutions). Nevertheless, the satellite reflections are not weak as it is shown in Figure 7.2.2, and they cannot be ignored for a proper crystal structure determination. For this reason, the procedure to determine the crystalline phase has to include the significant incommensurate characteristic of the acquired diffraction patterns.

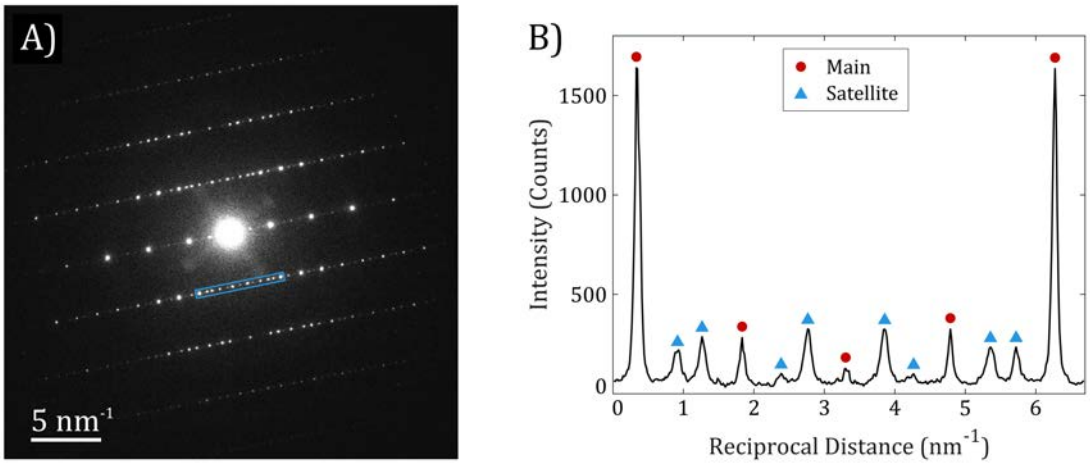

Figure 7.2.2: A) Precessed diffraction pattern along $[10\bar{2}]$ from the α'_H-C_2S crystal of "clinker_0" that shows strong extra reflections, and B) an intensity histogram of $(\bar{2}h\bar{1})$ that corresponds to the blue region marked in A).

7.3 The Crystal Structure of Belite α'_H

One diffraction dataset of the α'_H polymorph was acquired for each clinker sample and satellite reflections were identified in all of them. However, the "clinker_5" data exhibits textured reflections as well as strong background intensity that decrease the quality of the reflection intensities. For this reason, this dataset has been excluded from the following crystallographic analysis.

The *Pmnb* setting was used in previous sections in order to easily visualize the phase transitions between the glaserite-type structures of belite. Here the orientation matrix of the standard *Pnma* setting is chosen, and the modulation wavevector becomes $0.3725\vec{a^*}$ and $0.3795\vec{a^*}$ for "clinker_0" and "clinker_2.5", respectively.

7.3.1 Determination of the Average Structure

First of all, the structure analysis of α'_H-C_2S is carried out by ignoring the satellite reflections. $0kl$, $h0l$ and $hk0$ sections displayed in Figure 7.3.1 show the reflection conditions related to the extinction symbol Pn-a, i.e. the n-glide plane perpendicular to the a-axis that produces the $k + l = 2n$ condition in the $0kl$ section, and the a-glide plane perpendicular to the c-axis related to the $h = 2n$ condition in the $hk0$ section. The resulting extinction symbol points toward the $Pn2_1a$ and *Pnma* space groups as possible candidates for the atomic ordering of the crystal.

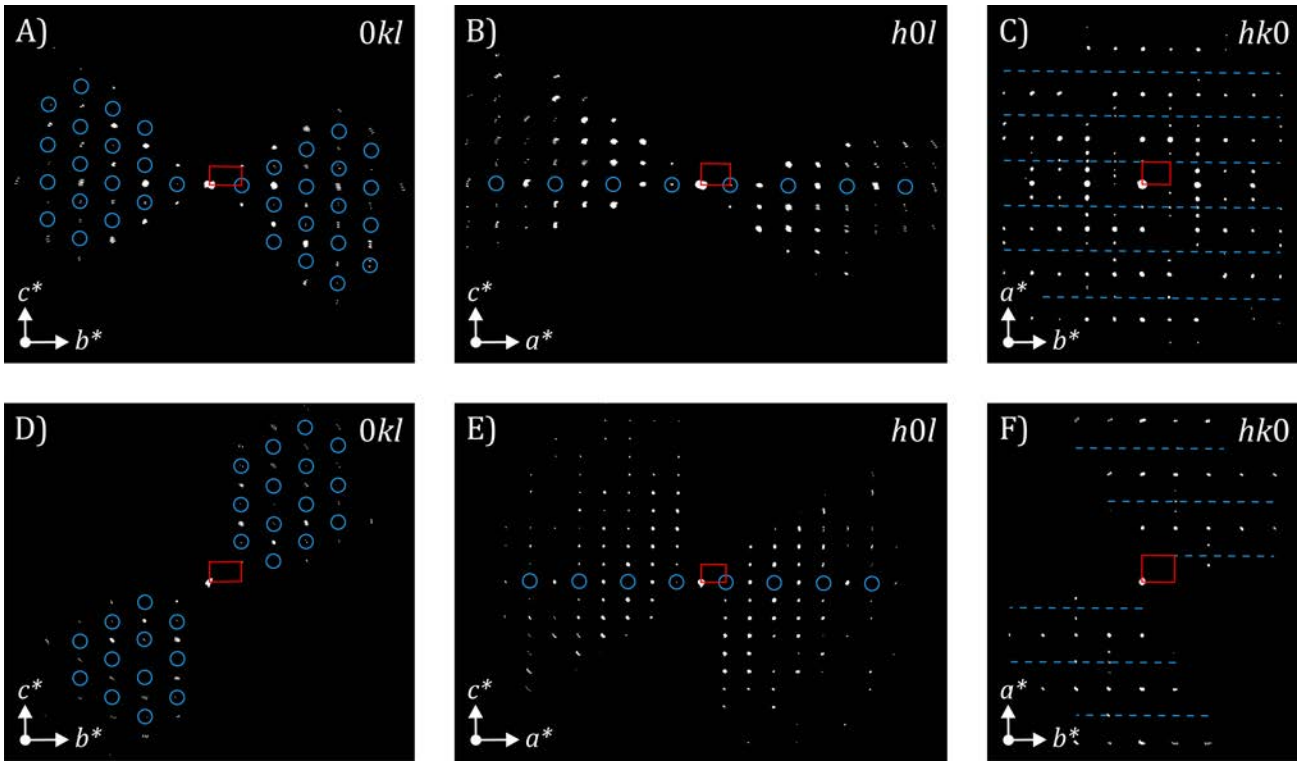

Figure 7.3.1: $0kl$, $h0l$ and $hk0$ sections of the reconstructed ODS from "clinker_0" (upper figures) and "clinker_2.5" (lower figures) obtained from *eADT*. The red rectangles correspond to the projected unit cell along the different directions of the ODS sections. The blue circles and dashed lines mark the positions of the systematic extinctions according to the *Pnma* space group.

The reported crystal structures of α'_H-C_2S are always in the *Pnma* space group [313, 316, 317]. These models place the calcium and two oxygen positions on the mirror plane or slightly shifted from it and half occupied to compensate the creation of the symmetrically-related atom at the other side of the plane. For this reason, a structure solution with the $Pn2_1a$ space group is a reasonable assumption because it allows these atoms to sit at any specific position along the *b*-axis without the limitation of the mirror symmetry. In this way, structure solutions were obtained from DM and the retrieved models were refined by three cycles of the least-squares refinement routine in *Sir2014*.

	"clinker_0"		**"clinker_2.5"**	
	Kinematical	*Dynamical*	*Kinematical*	*Dynamical*
Completeness (%)	72.9		85.3	
R_{int} (%)	13.5		11.6	
Reflections at 0.7 Å (#)	415/436	1710/2440	451/498	1489/1996
Refl./Param. (-)	16.0	12.5	17.3	10.4
GoF (-)	15.1/14.7	2.03/1.77	13.6/12.9	2.37/2.09
R (%)	20.5/20.8	5.57/ 7.87	19.1/20.0	5.50/7.08
R_w (%)	25.1/25.1	5.62/5.85	22.6/22.6	6.07/6.23

Table 7.3.1: Resulting figures of merit from the structure refinements in space group *Pnma* from *Jana2006*. Reflections, *GoF*, *R* and R_w parameters are calculated and reported from observed and all (obs/all) reflections. The criterion for observed (obs) reflections was $I(\vec{g}) > 3\sigma(\vec{g})$. The "Refl./Param." parameter refers to the number of observed reflections over the number of refined parameters. *R* and R_w are based on the square root of reflection intensities. Dynamical refinements were carried out with N_{or} of 128, g_{max} of 1.6 Å^{-1}, S_g^{max} (matrix) of 0.01 Å^{-1} , S_g^{max} (refine) of 0.1 Å^{-1} and RS_g of 0.4.

The resulting models from DM provided less distorted silicon tetrahedra for the *Pnma* solutions than the $Pn2_1a$ ones. While silicon to oxygen distances are ranged between 1.54 Å and 1.61 Å in the *Pnma* structure, the range is increased up to 1.42 Å and 1.87 Å for the $Pn2_1a$ case. Kinematical refinements were carried out in *Jana2006* to check if the distortions observed in the $Pn2_1a$ model are minimized by the least-squares procedure, but the geometrical distortions in the tetrahedra were highly increased and these structure models were disregarded from further crystal refinement. On the other side, the structure models with the *Pnma* space group provided good tetrahedra geometry and Si-O distances ranged between 1.57 and 1.69 Å. The difference Fourier maps in the first refinement executions showed extra potentials around the oxygen positions placed on the mirror plane ($4c$ Wyckoff position), thus they were moved out of the symmetry-limited position and the occupancy factor was set to 0.5. Extra spherical potential was also observed close to the oxygen at the $8d$ Wyckoff site in both datasets that indicated their splitting. In this case, an extra oxygen was added and the occupancy factors were set to 0.5 for each atom of the pair. During the refinement, the DPs were restricted to be the same for both oxygens and their total occupancy was restricted to 1, while the occupancy and DPs of one of them were refined. Table 7.3.1 shows the figures of merit for these

kinematical refinements in which the displacement parameters turn out positive and low, and the least-squares procedure converged.

The structure models obtained from the kinematical refinements were then used for dynamical refinements in order to anisotropically refine the DPs and obtain a more accurate description of the crystal. The obtained R(obs) values of 5.57% and 5.50% for "clinker_0" and "clinker_2.5" datasets, respectively, demonstrate the reliability of the retrieved structure model. Table 7.3.2 shows the refined structural parameters for the atoms in the asymmetric unit from both diffraction datasets.

"clinker_0"

	x/a	*y/b*	*z/c*	*Occup. (-)*	B_{eq} (Å^2)
Ca1	0.16658(12)	0.75	0.42940(20)	0.5	1.98(5)
Ca2	0.50920(11)	0.75	0.70437(19)	0.5	1.27(4)
Si	0.28069(16)	0.25	0.58720(31)	0.5	1.24(6)
O1	0.74790(61)	0.47970(60)	0.80140(74)	0.621(6)	2.0(4)
O1_2	0.67810(88)	0.48970(11)	0.85630(14)	0.379(0)	2.0(0)
O2	0.49270(32)	0.81220(47)	0.45000(66)	0.5	1.9(2)
O3	0.15740(34)	0.32190(45)	0.43780(66)	0.5	2.4(2)

"clinker_2.5"

	x/a	*y/b*	*z/c*	*Occup. (-)*	B_{eq} (Å^2)
Ca1	0.16774(15)	0.75	0.42906(13)	0.5	2.02(4)
Ca2	0.50905(13)	0.75	0.70488(13)	0.5	1.36(3)
Si	0.28113(18)	0.25	0.58717(17)	0.5	1.34(5)
O1	0.74695(66)	0.47940(81)	0.80502(54)	0.647(7)	2.5(1)
O1_2	0.6761(13)	0.4871(16)	0.8553(12)	0.353(0)	2.5(0)
O2	0.49458(48)	0.7701(38)	0.45091(44)	0.5	7.5(2)
O3	0.15785(41)	0.31835(89)	0.43887(39)	0.5	2.5(2)

Table 7.3.2: Structural parameters of α'_H-C_2S after the dynamical refinements from the two diffraction datasets. Unit cell parameters obtained from *eADT* and scaled according to the scale factors of β-C_2S datasets were used for the refinements. The values in parentheses for the different parameters are the estimated standard deviations. B_{eq} is calculated from the anisotropic DPs as $B_{eq} = 1/3 \sum\sum B_{ij} a_i^* a_j^* \vec{a}_i \vec{a}_j$.

The refinement of the α'_H-C_2S model from the "clinker_0" sample results in positive principal components of the anisotropic DP tensors and the equivalent isotropic DPs range between 1.2 and 2.4 Å^2, which indicates a reliable positioning of the atoms. The visualization of atom volumes scaled according to the anisotropic DPs in Figure 7.3.2A shows that split oxygens near the mirror planes (placed at $y = 0.25$ and $y = 0.75$) have a displacement along the b-axis, and the remaining pair of split oxygens tend to move to each other while the oxygen to silicon distance is maintained. Calcium atoms also display a movement parallel to the b-axis, although less severe, and silicon atoms do not exhibit such significant anisotropic displacement. Interestingly, O1 has a higher occupation factor than its split pair O1_2, which points towards a preference movement positioning across the cells.

The dynamical refined "clinker_2.5" model also results in positive principal DPs components, but O3 exhibits a significantly higher component along the b-axis (see Figure 7.3.2B). The small distance between these split oxygens in comparison to the crystal structure of "clinker_0" indicates that the DPs and the pair distance along the y component are correlated, yet the least squares procedure estimates these values to minimize the R value. Furthermore, the dataset does not cover either b and c axes (see Figure 7.3.1) and, as a consequence, the resulting electrostatic potential is spread along these directions. Therefore, the high DP could be explained as an effect of the symmetry-constrained position, missing ODS information and the use of an average structure to describe the modulation. In the case of O2, the pair distance is higher and the resulting DP through the b-axis direction is not that strong. The left oxygen pair as well as the calcium positions show the same behaviour as the "clinker_0" model, but silicon has a slightly higher displacement along the b-axis. The higher occupation factor for O1 in comparison to O1_2 also suggests the preferred positioning of this oxygen seen in the "clinker_0" structure.

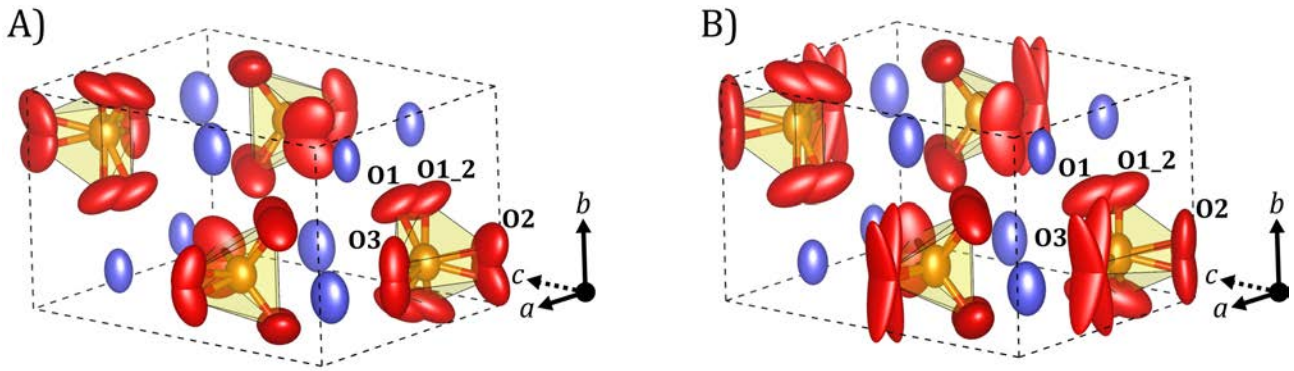

Figure 7.3.2: Projections of the averaged structure model of α'_H-C_2S after the dynamical refinements from A) "clinker_0" and B) "clinker_2.5" datasets. Blue/purple atoms correspond to calcium, orange ones to silicon and red ones to oxygen. Atom volumes are scaled according to the principal components of the anisotropic DPs.

The very similar refined crystal structures determined from these two different diffraction datasets illustrate that the structure model is reliable and it can be used to analyse clinker mixtures manufactured at different conditions (see Appendix for the *Cif* files of the two average structures). Nevertheless, the significant anisotropic behaviour of the found DPs indicates that a strong struc-

tural modulation is present in the crystalline material, which at the same time is observed in the strong satellite reflections. For this reason, the shown models can only be considered as the average structure and the incommensurate characteristic of the diffraction data needs to be taken into account for a proper crystal structure description.

7.3.2 Characterization & Refinement of the Modulated Structure

The $hk0$ sections in Figures 7.3.1C and 7.3.1F as well as the projections of the reconstructed ODS in Figure 7.3.3 show that satellite reflections cannot be ignored because of their strong intensity, thus the superspace formalism has to be used for a correct crystal structure characterization.

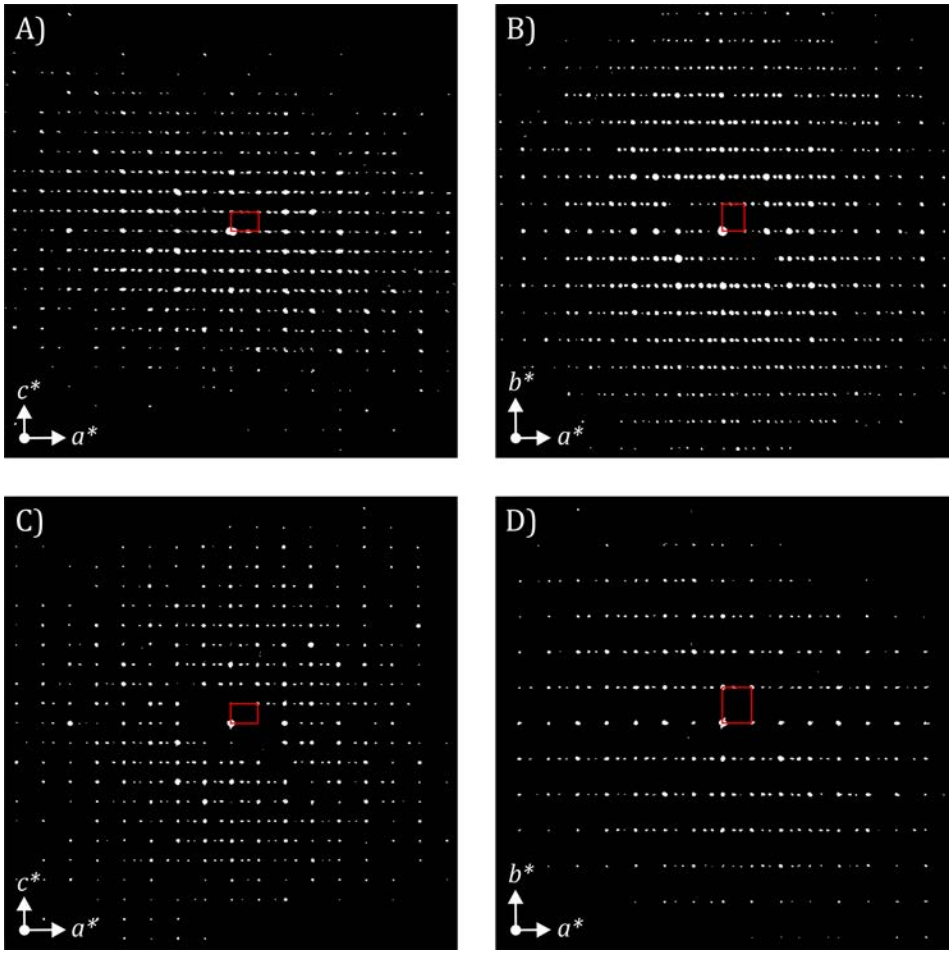

Figure 7.3.3: Projections along b^* and c^* axes of the reconstructed ODS for "clinker_0" (upper figures) and "clinker_2.5" (lower figures), respectively. The red rectangle in all figures represents the projected average unit cell along the corresponding axis.

The indexing of all reflections in the reconstructed ODS requires the expansion of the 3D space to a 3+d superspace. In the presented case, a 4D superspace has to be used since there is only one modulation wavevector along the a^*-axis, $\vec{q} = 0.3725\vec{a^*}$ for "clinker_0" and $\vec{q} = 0.3795\vec{a^*}$ for "clinker_2.5".

First order satellites are clearly seen in both datasets but second order ones do not appear. In this way, m_{max} is restricted to 1, which leads to an almost 100% indexing of all observed reflections.

The *Pnma* space group identified in the average structure is a good starting point because main reflections correctly follow its reflection conditions. The International Tables for Crystallography vol. C [54] shows two possible superspace groups for the space group number 62; 62.1, $Pnma(00\gamma)000$, and 62.2, $Pnma(00\gamma)0s0$. In the first one, the superspace symmetry operations do not have any glide components along the additional dimension, while the second one applies a 1/2 translation along the fourth superspace coordinate for the mirror plane perpendicular to $\vec{b}$. Although not listed, $Pnma(00\gamma)s00$ and $Pnma(00\gamma)ss0$ are also possible and they have to be considered. If these superspace groups are taken into account with the modulation vector along the a^*-axis, the following superspace groups with their related reflection conditions are identified and shown in Table 7.3.3. Such conditions can now be evaluated in the ODS sections shown previously in Figure 7.3.1 but using the four *hklm* indices.

Superspace group	**Reflection conditions**
$Pnma(\alpha00)000$	$hk0m$: $h = 2n$, $0kl0$: $k + l = 2n$
	$h00m$: $h = 2n$, $0k00$: $k = 2n$, $00l0$: $l = 2n$
$Pnma(\alpha00)0s0$	$hk0m$: $h = 2n$, $h0lm$: $m = 2n$, $0kl0$: $k + l = 2n$
	$h00m$: $h + m = 2n$, $0k00$: $k = 2n$, $00l0$: $l = 2n$
$Pnma(\alpha00)00s$	$hk0m$: $h + m = 2n$, $0kl0$: $k + l = 2n$
	$h00m$: $h + m = 2n$, $0k00$: $k = 2n$, $00l0$: $l = 2n$
$Pnma(\alpha00)0ss$	$hk0m$: $h + m = 2n$, $h0lm$: $m = 2n$, $0kl0$: $k + l = 2n$
	$h00m$: $h + m = 2n$, $0k00$: $k = 2n$, $00l0$: $l = 2n$

Table 7.3.3: Superspace groups compatible with the *Pnma* space group and one modulation wavevector along the a^*-axis. Reflection conditions obtained from *Jana2006*.

The $h0lm$ sections of Figure 7.3.1B and Figure 7.3.1D clearly show that no satellite reflections are visible, therefore the $h0lm$: $m = 2n$ is fulfilled because the fourth index m is limited to $\pm$ 1 and should be observable in this plane. The $hk0m$ sections displayed in Figure 7.3.4 show that the $h = 2n$ condition for the main reflections of the sub-plane $hk0$ is fulfilled, i.e. there are no significant reflections along the blue dashed lines. This indicates the presence of the *a*-glide plane perpendicular to the *c*-axis. However, satellite reflections are observed in this case and almost all of them appear around the reflections in the $hk00$ rows with $h = 2n + 1$, which are marked by red dashed arrows in Figure 7.3.4. Some weak reflections violate these conditions but this is most probably a result of dynamical effects. When taking into account these two reflection conditions, the $h + m = 2n$ condition is obtained for the $hk0m$ plane. From the symmetry point of view, a 1/2 translation along the fourth superspace coordinate for the *a*-glide plane perpendicular to $\vec{c}$ has to be added to the 1/2 translation for the mirror plane perpendicular to $\vec{b}$ identified in the $h0lm$ plane. Therefore, the superspace group for the incommensurately modulated structure of α'_H-C_2S is $Pnma(\alpha00)0ss$.

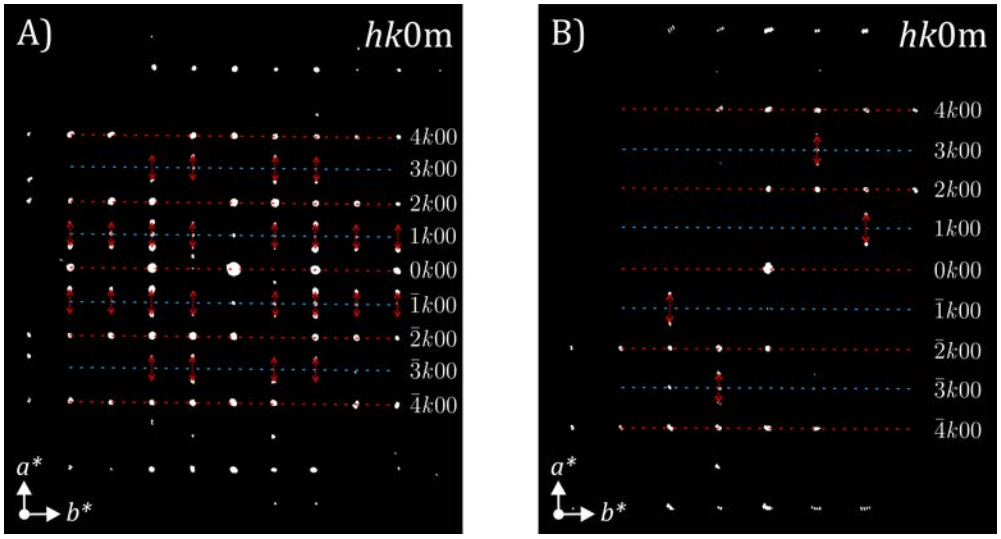

Figure 7.3.4: $hk0m$ sections from the ODS reconstructions of A) "clinker_0" and B) "clinker_2.5" diffraction datasets. Red and blue dashed lines correspond to $hk00$ rows with even and odd h indices, respectively. Red dashed arrows point to the visible satellite reflections from their closest main reflection.

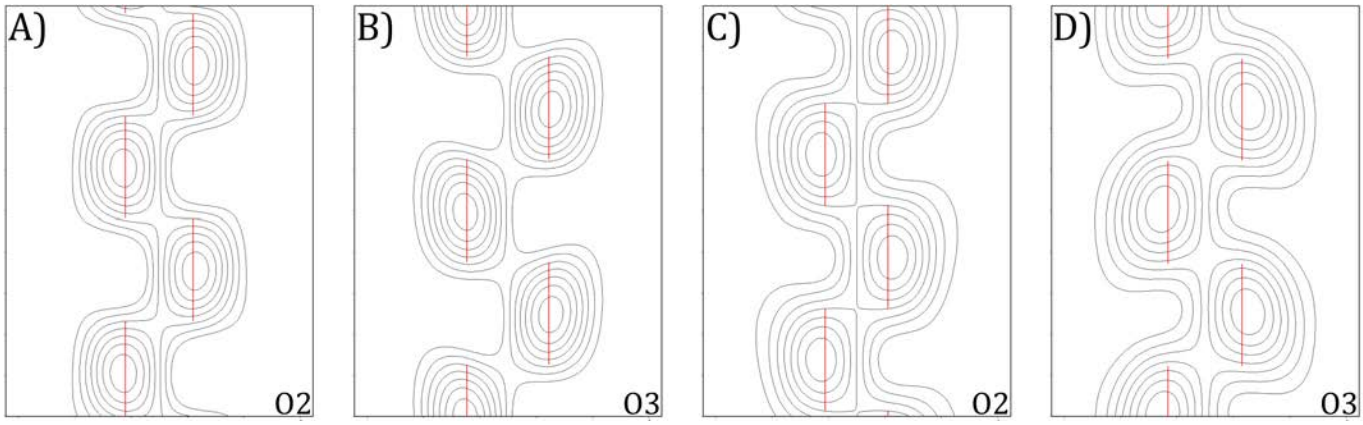

Figure 7.3.5: ($x_{s,2}$,$x_{s,4}$) de Wolff sections of O2 and O3 domains from A)-B) "clinker_0" and C)-D) "clinker_2.5". Vertical axis corresponds to $x_{s,4}$ ($t = [0, 2]$) and horizontal axis to $x_{s,2}$. Red lines correspond to the dynamical refined crenel functions assigned to the atomic domains.

At this point, main and satellite reflection intensities were integrated and extracted from *PETS2*, and the obtained *hklm* files were imported to *Jana2006*. First, the CFA implemented in *SUPERFLIP* [243] was used to obtain structure models that directly contain a first order harmonic function for each atomic domain, as the CFA is able to retrieve electrostatic potentials in a n-dimensional space. One of the oxygens in the $4c$ position was missing in both diffraction datasets but they were found by a Fourier synthesis. It is worth to note that the Fourier synthesis also takes into account the 4D space, thus the suggested domains and their related averaged positions include modulation parameters as well. Both initial structure models were retrieved with two of the oxygens placed in $4c$

positions. After all atomic positions were found, a first kinematical refinement was done with unconstrained modulation parameters but fixed isotropic DPs. The inspection of the ($x_{s,1}$,$x_{s,4}$), ($x_{s,2}$,$x_{s,4}$) and ($x_{s,3}$,$x_{s,4}$) de Wolff sections for all atoms revealed that a harmonic function fits well for calcium, silicon and the oxygen on the $8d$ site, yet the oxygens on the mirror plane exhibit discontinuous trends at the ($x_{s,2}$,$x_{s,4}$) de Wolff section. This suggests that the displacive modulation of O2 and O3 atomic domains could be better described by crenel functions. In this way, the $x_{s,2}$ and $x_{s,4}$ coordinates of the maximum peaks in the ($x_{s,2}$,$x_{s,4}$) de Wolff sections for O2 and O3 were used to place these atomic domains out of the mirror plane (shift along the b-axis and occupancy set to 1), and assign crenel functions with $x^0_{s,4}$ parameters initially set to the found $x_{s,4}$ coordinates for subsequent refinements and $\Delta = 0.5$. The symmetry of the superspace group ensures that there is no discontinuity along $\vec{a}_{s,4}$ for these atomic domains while they follow discontinuous functions. Figure 7.3.5 shows the ($x_{s,2}$,$x_{s,4}$) de Wolff sections of O2 and O3 for both diffraction datasets and Figure 7.3.6 at the end of this subsection shows all the other de Wolff plots.

	"clinker_0"	**"clinker_2.5"**
Main reflections		
Reflections at 0.7 Å (#)	1726/2500	1848/2466
R (%)	7.10/9.54	7.63/9.28
R_w (%)	7.30/7.57	8.25/8.41
Satellite reflections		
Reflections at 0.7 Å (#)	2007/4796	1228/4531
R (%)	19.9/27.9	15.9/31.2
R_w (%)	19.5/20.8	17.8/19.9
All reflections		
Reflections at 0.7 Å (#)	3733/7296	3076/6997
Refl./Param. (-)	29.6	23.8
R (%)	12.3/18.2	9.64/16.9
R_w (%)	11.2/12.0	9.85/10.5

Table 7.3.4: Resulting figures of merit (obs/all) from the dynamical refinements in *Jana2006*. The criterion for observed (obs) reflections was $I(\vec{g}) > 3\sigma(\vec{g})$. The "Refl./Param." parameter refers to the number of observed reflections over the number of refined parameters in the least-squares procedure. R and R_w are based on the square root of reflection intensities. N_{or} of 128, g_{max} of 1.6 Å^{-1}, S_g^{max} (matrix) of 0.01 Å^{-1} , S_g^{max} (refine) of 0.1 Å^{-1} were selected in both datasets, but RS_g was set to 0.4 for "clinker_0" and 0.5 for "clinker_2.5".

Once the modulation functions were clear, further least-squares refinements were performed. First, the modulated model was refined with free modulation parameters (except Δ) and fixed isotropic DPs. After convergence, modulation parameters were fixed and the isotropic DPs were refined, which led to convergence and small and positive DPs. Finally, all structural parameters were refined and the least-squares procedure converged with well fitted functions to the de Wolff sections as well as physically meaningful isotropic DPs. These kinematical refined models were then used as input to dynamical refinements [325]. The same refinement workflow as the kinematical case was followed here, but the optimization of the orientation angles from all patterns according to the calculated dynamical reflection intensities was carried out prior to the last refinement execution with all structural parameters free. Table 7.3.4 shows the resulting figures of merit from the dynamical refinements of the two datasets, and tables 7.3.5 and 7.3.6 show the structural parameters for both refined incommensurately modulated structures (see Appendix for the *Cif* files of the two modulated structures). Low isotropic DPs, well fitted modulation functions as well as good R values considering main, satellite or all reflections demonstrate the reliability of the determined crystal structure.

	Ca1	**Ca2**	**Si**	**O1**	**O2**	**O3**
x/a	0.16654(15)	0.50881(13)	0.28050(20)	0.72280(29)	0.49130(36)	0.15780(39)
y/b	0.75	0.75	0.25	0.48270(32)	0.81010(45)	0.32280(47)
z/c	0.42860(24)	0.70450(24)	0.58812(37)	0.82190(46)	0.45150(62)	0.43520(65)
Occup.	0.5	0.5	0.5	1.0	1.0	1.0
B_{iso} (Å^2)	1.03(3)	0.55(2)	0.79(3)	1.18(4)	1.53(6)	1.69(6)
Harmonic Function Parameters						
A_1(xsin)	0	0	0	-0.02638(50)	-	-
B_1(xcos)	0	0	0	0.03824(48)	-	-
A_2(ysin)	-0.02368(32)	-0.03250(26)	-0.01781(42)	-0.02070(49)	-	-
B_2(ycos)	0.02811(30)	-0.01538(32)	-0.01703(43)	0.000491(48)	-	-
A_3(zsin)	0	0	0	0.00964(76)	-	-
B_3(zcos)	0	0	0	-0.03646(65)	-	-
Crenel Function Parameters						
Δ	-	-	-	-	0.5	0.5
$x^0_{s,4}$	-	-	-	-	0.7150(22)	0.0025(18)

Table 7.3.5: Structural parameters of the incommensurately modulated model from the "clinker_0" diffraction dataset. Unit cell parameters obtained from *eADT* and scaled according to the scale factor of the β-C_2S datasets were used for the refinement. Values in parentheses for the different parameters are the estimated standard deviations. The dynamical refinement was carried out with N_{or} of 128, g_{max} of 1.6 Å^{-1}, S_g^{max} (matrix) of 0.01 Å^{-1} , S_g^{max} (refine) of 0.1 Å^{-1} and RS_g of 0.4.

	Ca1	**Ca2**	**Si**	**O1**	**O2**	**O3**
x/a	0.16766(12)	0.50894(13)	0.28114(16)	0.72400(28)	0.49140(31)	0.15750(34)
y/b	0.75	0.75	0.25	0.48183(43)	0.80560(54)	0.31530(53)
z/c	0.42933(11)	0.70467(11)	0.58733(15)	0.82170(24)	0.45180(30)	0.44020(29)
Occup.	0.5	0.5	0.5	1.0	1.0	1.0
B_{iso} (Å^2)	1.33(2)	0.722(9)	0.80(3)	2.19(4)	2.13(5)	2.06(5)
Harmonic Function Parameters						
A_1(xsin)	0	0	0	0.02570(44)	-	-
B_1(xcos)	0	0	0	-0.03327(40)	-	-
A_2(ysin)	-0.01738(37)	0.02735(30)	0.01406(49)	0.01938(63)	-	-
B_2(ycos)	-0.02311(33)	-0.01049(36)	0.02090(48)	-0.00247(64)	-	-
A_3(zsin)	0	0	0	0.01061(39)	-	-
B_3(zcos)	0	0	0	-0.02919(31)	-	-
Crenel Function Parameters						
Δ	-	-	-	-	0.5	0.5
$x^0_{s,4}$	-	-	-	-	0.7772(24)	0.4957(20)

Table 7.3.6: Structural parameters of the incommensurately modulated model from the "clinker_2.5" diffraction dataset. Unit cell parameters obtained from *eADT* and scaled according to the scale factor of the β-C_2S datasets were used for the refinement. Values in parentheses for the different parameters are the estimated standard deviations. The dynamical refinement was carried out with N_{or} of 128, g_{max} of 1.6 Å^{-1}, S_g^{max} (matrix) of 0.01 Å^{-1} , S_g^{max} (refine) of 0.1 Å^{-1} and RS_g of 0.5.

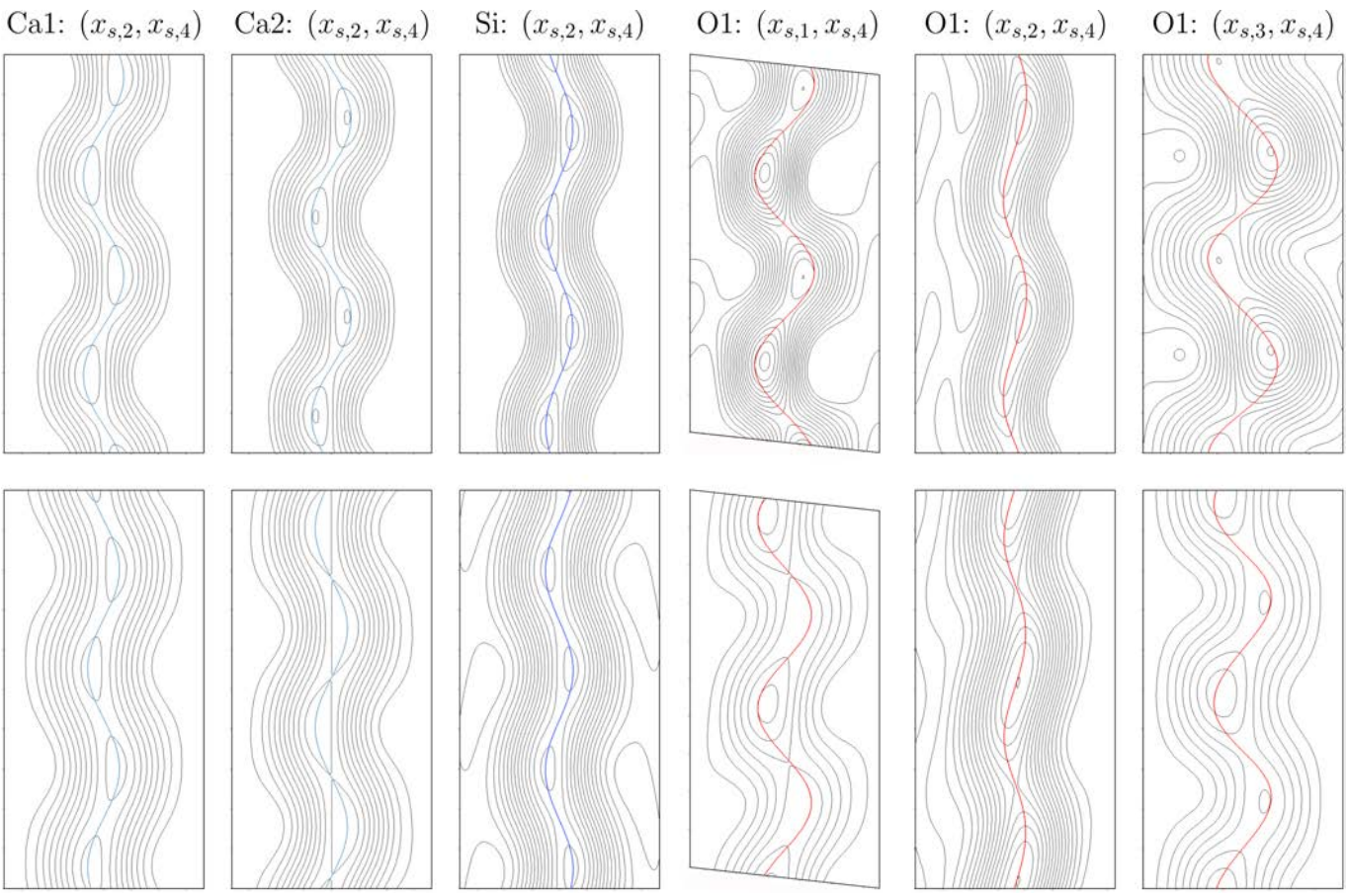

Figure 7.3.6: De Wolff sections for Ca1, Ca2, Si and O1 that show modulation. The coloured lines represent the harmonic functions obtained from the final dynamical refinement. Upper figures correspond to "clinker_0" and lower ones to "clinker_2.5".

7.3.3 Crystal Structure Description

The reference crystal structure of α'_H-C_2S from Mumme et al. [317] shows that all atoms except silicon are split into half-occupied positions. However, no satellite reflections are reported in this publication, most likely because of the high population of reflections in the powder diffraction pattern. The electron diffraction structure analysis carried out here demonstrates that the atomic position splitting observed in powder diffraction comes from the intrinsic incommensurate modulation of the crystal structure. In fact, the average structure retrieved by using the main reflections only coincides with the X-ray model without the splitting of the calcium positions. It is worth to note as well that the obtained unit cell parameters are very similar between the two datasets of electron diffraction, but also to the X-ray structure, which indicates that this crystal structure can be reliably used for phase quantifications in powder patterns of different cement samples (Mumme et al.: 6.7673 Å, 5.5191 Å & 9.3031 Å / "clinker_0": 6.776 Å, 5.496 Å & 9.252 Å / "clinker_2.5": 6.765 Å, 5.514 Å & 9.250 Å).

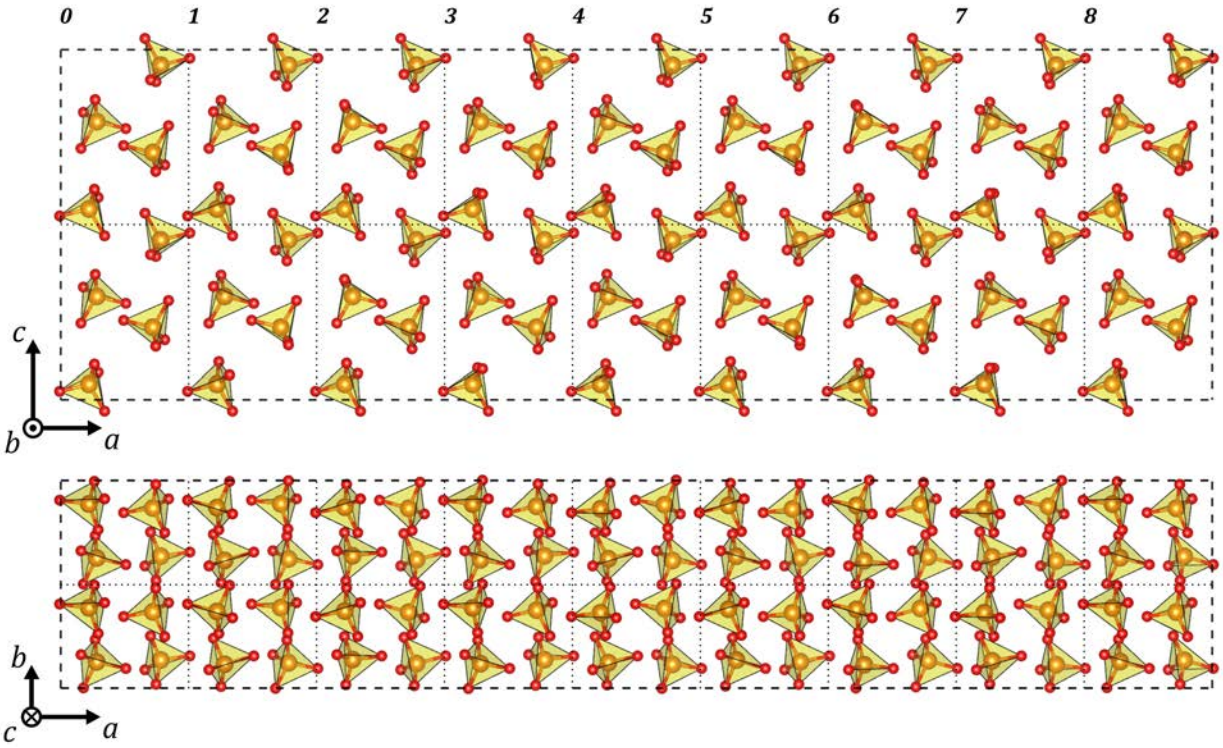

Figure 7.3.7: Approximated superstructure with 9 × $\vec{a}$, 2 × $\vec{b}$ and 2 × $\vec{c}$ the unit cell of the incommensurately modulated structure of "clinker_0". Upper figure is the projection along the b-axis, and the lower one is along $\vec{c}$. Calcium atoms are omitted for the clarity of the modulated distortion and orientation of Si-O tetrahedra. Dotted lines are displayed to show the position of the subcells.

Nevertheless, the strong intensities of the satellite reflections observed in both diffraction datasets, as well as the high anisotropy of the DPs for the average structure, implies that the modulation cannot be ignored for a proper crystal structure determination. The inspection of the reconstructed ODS pointed to the superspace group $Pnma(\alpha 00)0ss$ as the symmetry group that fits to the reflection conditions. The subsequent structure solutions and least-squares refinements in *Jana2006* showed

that such superspace group allows to solve and refine the crystal structure by using harmonic and crenel functions to describe the incommensurate modulation. Furthermore, the high DPs obtained in the averaged models were not retrieved in the refined modulated structures.

The visualization and description of aperiodic crystals is not trivial because such crystals are represented in a (3+d)D space, yet they need to be illustrated back to the physical 3D space [326]. One way is to build a superstructure with the unit cell of the aperiodic crystal as the subcell of the supercell. Figure 7.3.7 shows the superstructure along $\vec{b}$ and $\vec{c}$ for the "clinker_0" refined model ($9 \times \vec{a}$, $2 \times \vec{b}$, $2 \times \vec{c}$). Since the modulation wavevector is along the a^*-axis, the crystal structure preserves the translational symmetry in the $\vec{b}$ - $\vec{c}$ plane, which means that the orientation and geometry of the Si-O tetrahedra as well as the calcium positions can change while going through the x component of the unit cell framework, but the atomic positions translated through the y and z components are preserved. This can be seen in Figure 7.3.7 as the tetrahedron positions and geometries in the subcell limited by the dotted lines is the same when shifted to the subcells along $\vec{b}$ or $\vec{c}$, yet they change along $\vec{a}$. Another interesting characteristic of the approximated superstructure is that the best supercell to fit all reflections can be identified by checking which subcell resembles most the initial one. This coincides with the cell that corresponds to an integer period of the modulation wavevector. In the case of α'_H-C_2S, this is fulfilled after 8 subcells and it is shown in Figure 7.3.7, where the ninth subcell (labelled as 8) is the most comparable to the first one (labelled as 0).

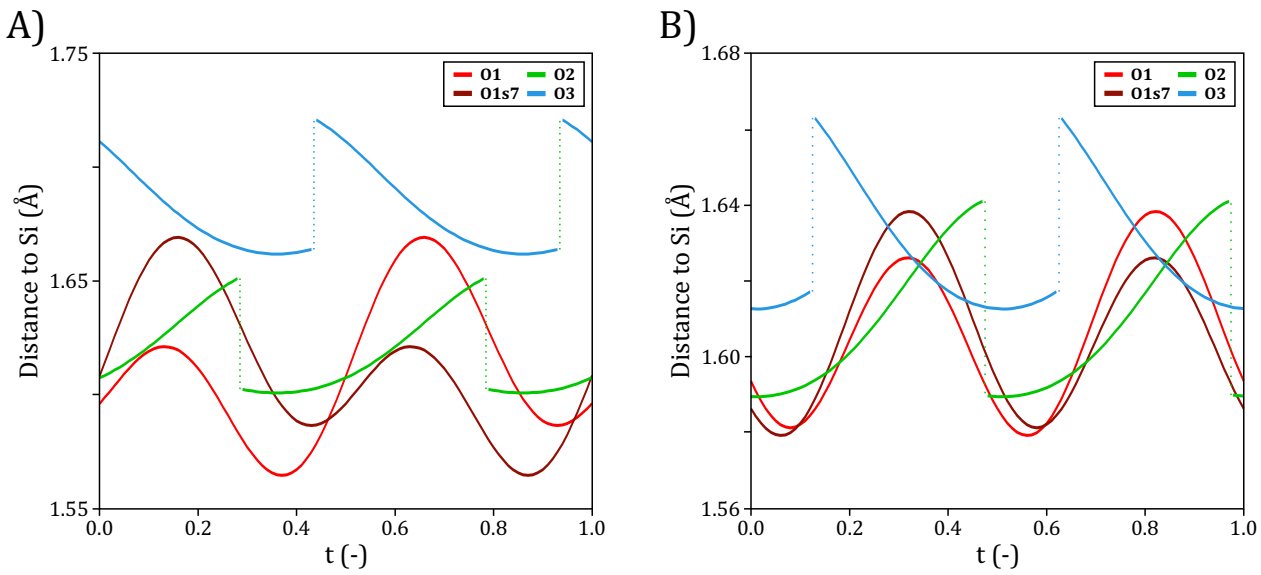

Figure 7.3.8: Distances between silicon and the four tetrahedra oxygens with respect to the modulation phase t. A) corresponds to "clinker_0" and B) to "clinker_2.5".

The projections of the superstructure in Figure 7.3.7 graphically show that the silicon-oxygen tetrahedra geometry and their orientation change through the a-axis as a consequence of the modulation of their atoms. A better way to quantify these modulation characteristics is to plot the inter-atomic distances with respect to the phase t of the modulation wavevector. Figure 7.3.8 shows the silicon to oxygen plots for the "clinker_0" and "clinker_2.5" models. O3 presents the longer distance to

Si, up to 1.721(6) Å and 1.663(3) Å for "clinker_0" and "clinker_2.5", respectively. The harmonic modulation of silicon and the discontinuous positioning of O2 and O3 result in a decrease of the Si-O3 distance and an increase of the Si-O2 distance for every half period of the modulation function, which tend to an average distance of 1.661(4) Å ("clinker_0") and 1.627(3) Å ("clinker_2.5") until the oxygens jump to the mirror-related positions. O1 and its related-symmetry oxygen O1s7 that completes the tetrahedra have silicon-oxygen curves that are almost in phase between them. This indicates that the harmonic modulation of silicon is in phase to one of these oxygens, while the other is out of phase due to the symmetry relation. Such particular displacement points towards a silicon to oxygen distance that changes due to the higher displacement value of the oxygen with respect to the silicon, but the direction of the silicon-oxygen movement is almost the same for one of the oxygens and the other way around for the symmetry-related one.

The calcium coordination is complicated to illustrate through superstructure projections and interatomic distance plots because of the high number of related oxygens. Nevertheless, careful inspection of both refined structures shows that calcium has octahedral and dodecahedral coordination when Ca-O distances between 2.2 Å and 3.2 Å are taken into account. The geometry of these coordination environments changes through the a-axis and that is why the Ca-O distance for some oxygens is increased to $\sim$ 3.2 Å in comparison to the $\sim$ 2.8 Å distance of the averaged structure.

	Mumme et al. [317]	**Average Structure**		**Modulated Structure**	
		"clinker_0"	*"clinker_2.5"*	*"clinker_0"*	*"clinker_2.5"*
Ca1	0.34770	-	-	0.404(1)	0.320(1)
Ca2	0.24394	-	-	0.396(1)	0.324(1)
Si	-	-	-	0.272(1)	0.278(1)
O1	0.58797*	0.696(12)*	0.670(11)*	0.938(1)	0.81(1)
O2	0.63470	0.684(6)	0.22(5)	0.665(1)	0.617(1)
O3	0.76495	0.790(5)	0.754(10)	0.797(1)	0.723(1)

Table 7.3.7: Distances between split positions for the average structures and the total modulated displacements for the modulated structures in Å. * corresponds to the O1-O1_2 distance.

The use of crenel functions for O2 and O3 confirms that the split and half-occupied atoms in the average structure is a good approximation of the real nature of the crystal structure. However, the rest of the atoms require harmonic functions to describe its intrinsic modulation, as shown in the de Wolff sections of Figure 7.3.6. Table 7.3.7 reports the distances between split positions for the structure reported by Mumme et al. [317], the average structures and the total modulated displacements for the modulated structures. These values show that in general the total movement of the atoms in the modulated crystal structure is bigger than the reported one on the average structures, especially for O1. Furthermore, silicon also has a displacive modulation that is not directly detected in the average approximations, although much weaker, but provides a better description of the crystal structure.

Finally, it is worth to note that the values of “clinker_0” are higher than “clinker_2.5”, which demonstrates that the modulation is stronger in the first dataset as observed in the also stronger intensity of satellite reflections.

7.4 Conclusions

During more than half a century the crystalline characterization of cement samples was hampered by the difficulties on acquiring diffraction datasets from individual crystals of actual cement powders. The development of the 3D ED technique as well as systematic acquisition methods in a TEM, like the Fast-ADT routine, have proved in this work to be suitable for the identification and crystallographic analysis of individual particles in clinker powders.

The processing of the acquired diffraction datasets showed that the majority of the acquisitions belonged to β-C_2S, from which some of them contained the typical [100] twinning of monoclinic crystals. The ODS reconstruction of the α'_H polymorph datasets exhibited an incommensurately modulated component along the a-axis that was previously reported but never properly characterized. The inspection of the reconstructed ODS indicated that the structure could be described in the $Pnma(\alpha 00)0ss$ superspace group and $hklm$ files were extracted for structure determinations based on the superspace formalism. The subsequent use of harmonic and crenel functions to describe the modulation of all atoms in dynamical refinements resulted in good figures of merit as well as good fitting of the functions in the de Wolff sections, which confirmed the proper crystal structure determination of the novel incommensurately modulated structure.

The fact that two different diffraction datasets from two different manufactured samples result in such close refined structure models indicates that the crystalline description of α'_H-C_2S in this work is generally valid for different processed cements. The Mumme et al. [317] and refined average structures reported here show that these models do not highly deviate from the real crystalline nature of the material and they can be used as good approximations. Nevertheless, the incommensurately modulated structure provides a better model for this crystalline phase, which can be used in the phase quantifications frequently carried out in XRPD patterns to enhance the reliability of the fitting by the Rietveld method.

Chapter 8

Final Conclusions & Outlook

Scepticism may be painful, and may be barren, but at least it is honest and an outcome of the quest for truth.

The Scientific Outlook
Bertrand Russell

This doctoral thesis has been focused on the analysis, development and operation of the TEM as an electron nano-diffractometer to solve crystallography problems. From a general point of view, it is divided in two different parts: a first, technical, one that involves the alignment of a quasi-parallel and precessed electron beam in STEM mode and the implementation of a novel technique called Fast-ADT to acquire 3D ED datasets, and a second, analytical, one that applies the acquisition method to different crystallographic studies as well as different materials.

After a general introduction in chapter 1 and a summary about the transmission electron microscope, diffraction and crystallography concepts in chapter 2, chapter 3 describes different alignment methods in order to set a quasi-parallel electron beam in STEM mode, with and without precession, according to the condenser system configurations of commercial TEMs. These routines have been introduced in the most general way to establish a universal set of instructions that enables the microscope to acquire "spotty-like" diffraction patterns suitable for 3D ED acquisitions but also 4D-STEM applications. The universality of the described alignments has been proved by the use of different microscope setups; JEOL/FEI microscopes, acceleration voltages of 200/300 kV, LaB_6/FEG electron sources, with/without aberration correctors and HRP/UHRP/S-Twin objective lenses. In this context, the implementation of specific and flexible quasi-parallel default settings in STEM mode by TEM manufacturers would benefit the crystallography community. In fact, the current four lenses condenser system of new TEMs allows this flexible beam configuration. It would only require the storage of specific lens and coil values with the probe corrector, if available, switched off or adjusted not to interfere with the tuning of the small and low-convergent beam, which size is only limited by the diffraction of the condenser aperture instead of the aberrations.

Chapter 4 is dedicated to the development of the Fast-ADT technique, which is introduced as a novel acquisition method based on two consecutive tilt scans of the TEM goniometric stage; one to image the crystal and generate a crystal tracking file, and a second one to acquire the diffraction patterns

while the beam is automatically shifted to follow the crystal at the different tilt angles. The technique has been implemented in the *Digital Micrograph* environment in both operation modes of the microscope (TEM or STEM) following the sequential or continuous tilt of the stage. Such flexibility was aimed to develop an acquisition software that could be adapted to any microscope regardless of the availability of the STEM mode and fit to the tilting capabilities of the stage. In this way, the acquisition of 3D ED datasets can be extended to other, less specialized, labs that usually complain about the lack of automatization of these data collections. The Fast-ADT acquisition method has also been implemented in the *Matlab* environment while working in TEM mode in order to take control of non-Gatan cameras and not restrict the technique to one commercial brand of TEM detectors. The software bundle that includes the Fast-ADT and ADT modules is freely provided to expand the use of 3D ED and tackle crystallography problems in the TEM (for further information see: `https://www.ak-kolb.chemistry.uni-mainz.de/publications/software/`).

By using the developed Fast-ADT modules, chapter 5 provides a comparison of two types of CCD-based detectors and their benefits for the crystal structure characterization of three already-known materials. While the Allied Vision Stingray F-145B camera enables a faster acquisition, the Gatan UltraScan 4000 provides better signal-to-noise ratio and higher sensitivity. The higher frame recording rate of the F-145B detector also allows the feasible test of the continuous tilt approach with the Fast-ADT technique in comparison to the US4000. The collected 3D ED datasets are shown to be suitable to solve and refine crystal structures with similar accuracy as X-ray techniques, characterize disorder features of crystals by the analysis of diffuse scattering, and reliably determine the absolute structure of chiral materials. Therefore, it demonstrates the power of electron diffraction to answer a variety of crystallographic questions.

Any data acquisition system can be used to collect diffraction data; yet, the key point is to previously characterize the detector and process the data accordingly. In this work, it has been shown that the F-145B data need to be treated carefully to obtain meaningful structure models, but requires alternative methods or techniques to validate them. The main advantage of such external detectors in comparison to slow TEM-designed cameras is that the observable diffraction space can be finely sliced in a few minutes, which facilitates the analysis of disorder in crystals like RUB-5.

At this point, since more and more attention is brought to the use of a TEM as a diffractometer, it is worth to list the needed requirements that a diffraction-dedicated microscope should have in the same way as analytical or high-resolution TEMs are provided. The electron nano-diffractometer would have the following specifications:

- A four-lens condenser system (3 condenser lenses and 1 condense minilens) to have the flexibility to independently choose the probe size and convergence angle. The Köhler illumination based on three lenses is not the most suitable situation because the beam size is determined by the condenser aperture, and it mechanically limits the achievement of a diffraction-limited probe for 4D-STEM applications as well as for the most challenging 3D ED acquisitions of nanometre-sized areas.

- A Schottky FEG to produce small probes to obtain good lateral resolutions for 4D-STEM applications.

- An objective lens with a pole piece gap that is large enough to let the sample holder tilt as much as possible but not as large as to produce a magnetic field that is only homogeneous at a very small area, as this limits the scanning area of the beam free from tilt artefacts produced by the lens aberrations.
- An integrated module of precession in the microscope interface in order to centralize all the beam controlling features in one single platform.
- A HAADF detector at the entry-side port of the viewing chamber to generate rapid scanned images of the sample, and a direct detection camera of 1024 × 1024 or 2048 × 2048 pixels, with a small physical pixel size placed at the post-column position, to acquire patterns of high diffraction data resolution without reflection overlapping from all kinds of materials. Here, the couple of a CMOS-based TEM detector with the Fast-ADT technique would be advantageous because of the lower acquisition times, less beam damage to beam sensitive materials and good signal-to-noise ratio for reflection intensities.
- A well aligned and stable goniometric stage for tomographic applications to ensure that the Fast-ADT routine could successfully acquire 3D ED datasets with beam sizes down to the diffraction limit.
- Scripting capabilities for the full control of the microscope and detectors to facilitate the further development of electron diffraction applications.

Such microscope setup is already available in most commercial TEMs (except for the direct detection camera specifics), but the introduction of other electron-optics and mechanical systems in the microscope complicates its use and default options for diffraction-based applications are not immediately available.

After demonstrating the success of the Fast-ADT technique to handle different crystallographic studies from known materials, the last two chapters of this doctoral thesis are focused on two unknown crystal structures; an organic dye and an inorganic industrial mineral.

The crystal structure determination of the DRED1 organic dye in chapter 6 demonstrates that current TEM-designed CCDs can be used to obtain *ab initio* structure solutions of electron beam sensitive materials of very low symmetry. The key step for this result has been the careful analysis and process of the datasets to enhance the outcome of the structure solution algorithms. Furthermore, the dynamical refinement on two DRED1 datasets has led to the visualization of some of the hydrogens forming the H-bond network, which confirmed their positions based on previous geometrical considerations and allowed their further refinement. Such outcome shows that the data processing of electron diffraction is accurate enough to reliably localize even hydrogen atoms.

The investigation of clinker samples of chapter 7 presents the Fast-ADT routine as an efficient tool to measure different crystal structures and identify features from individual crystals of commercially-available phase mixtures of the industry. The successful structure determination and refinement of the incommensurate modulated structure of the α'_H polymorph of belite, one of the major components of commercial cement, demonstrates the current potential of electron diffraction across different

types of materials and crystallography problems. The crystal structures of powder constituents are often so similar that production process monitoring using methods, like X-ray powder diffraction or nuclear magnetic resonance, can only be applied with uncertainties, and the problem gets worse when some of the phases have unclear structures. In this particular case, such electron diffraction approach helps to better understand the crystalline nature of cement towards the CO_2 reduction of its manufacturing process, thus a real application of the Fast-ADT technique to tackle world problems.

As final remarks it is worth mentioning that after $\sim$ 1.3 terabytes of acquired and processed data during the working time of this doctoral thesis, the Fast-ADT and ADT modules were successfully implemented and applied to several materials. Apart from the crystals analysed and detailed in this work, this acquisition software has been used to characterize iron oxide and fluorinated tungsten oxide nanoparticles [276, 327], double perovskites [127, 328], the first oxynitride of tin [284], zeolites and layer silicates, as well as more beam sensitive materials such as calcium carbonate hemihydrate or calcium acetate hemihydrate [277, 329], organic pigments and pharmaceutical compounds, some of which are not published yet. In this context, a novel technique for the collection of 3D ED datasets has been developed to increase the range of reliable available tools for a proper characterization of the atomic structure of new materials.

Acknowledgements

First of all, I would like to acknowledge my thesis supervisors; Dr. Joaquim Portillo (Quim), Dr. Sònia Estradé and Prof. Ute Kolb for their scientific and personal support to help me achieve this doctoral work. Many thanks Quim to transfer me most of the technical knowledge of the TEM that I know and how to approach technical problems with patience and following a step-by-step approach to get the best possible outcome. Thanks Sònia to welcome me in the TEM group of the university of Barcelona and teach me through the scientific academy world. I still remember when I did my bachelor's degree and you told me that I had to improve my English if I want to move forward. This thesis was still plenty of english mistakes, but I hope that I manage to fulfil your request at some degree! Many thanks Ute for accepting me in your Mainz/Darmstadt group, teach me on everything related to the use of electron diffraction to solve crystallography problems, and introduce me to the different personalities of the electron crystallography community to strengthen my network. All together, it was a long journey with some painful and sometimes very painful situations, although, at the end, totally worth it.

I would like to thank Prof. Francesca Peiró for her support and acceptance to the LENS group in the university of Barcelona through these years, as well as her very valuable comments regarding the different scientific works carried out in this thesis. I want to thank as well Prof. Hans-Joachim Kleebe to accept me in his group at the university of Darmstadt and Dr. rer. nat. Stefan Lauterbach to show me how to align and deal with aberration-corrected TEMs. In Mainz, I have to acknowledge Prof. Wolfgang Tremel and Dr. rer. nat. Martin Panthöfer to give me a space in their working group and allow me to discuss, exchange and test ideas with all the nanoparticle-related PhD students.

A special acknowledgement has to be made to Dr. Stavros Nicolopoulos as well as all NanoMegas SRPL crew for their personal support since I started learning everything around a TEM. To Stavros, in particular, for his very grateful references that triggered the initial collaboration with Germany and the realization of this jointly-supervised PhD thesis a reality, and, of course, the sponsorship for the marathon in Frankfurt, very much appreciated! I also want to thank Alejandro Gómez (er Alex) for our scientific and life discussions while being serious persons in the university, but also when drinking several beers. I still remember that night in Barcelona! Well, in fact, I don't ... I take the opportunity here to thank once again Spiros Panaretos for his technical help when dealing with the electronics of the TEM, it was really helpful to push the developments forward.

In Germany, I first have to acknowledge Dr. rer. nat. Yaşar Krysiak. Thanks for teaching me crystallography, show me your ways to deal with the FEI Tecnai F30 and to join efforts to get "nice and beautiful" results; Sixties and Dorett Bar definitely await us! I want to thank as well Dr. rer. nat. Galina Matveeva to be always nice while discussing different stuff in the group, as well as Dr. rer. nat. Haishuang Zhao for his industrial view of science that sometimes is worth to keep it in mind. From Prof. Tremel's research group, I have to acknowledge M. A. Sarif (Abdullah), P. Opitz (Der Philos), M. Maslyk (Betongos), M. A. Lange (Langos), D. H. Pham (The honey badger), J. Hilgert

(Hilgertos), D.-H. Quak (Just DO it!) and all the others for their kindness to ask me to participate in their group activities and drink one (or several) beers whenever was necessary. The combination of my TEM experience at that time and their characterization needs matched a really good situation that at the end translated in several co-authored publications. That was a nice experience that I will never forget and I strongly recommend to any other PhD student.

In Barcelona, I have to thank the people from the place where I start my journey in the electron microscopy world, els Centres Cíentifics i Tecnològics de la Universitat de Barcelona (CCiT-UB): J. Mendoza (Mendozakis), F. Mata (Felix the Cat or the Dog), A. Villuendas (Zazu!), M. Barba (Barbie), Dr. J. M. Bassas (Estancs), F. Menéndez (Pack), S. Mas (Sussie Peligru), J. Pons (Bridges) and others that I am sure forgetting for their support and motivation while I was working there. From the LENS group, I have to acknowledge Dr. Lluís López, Dr. Gemma Martín as well as Dr. Pau Torruella for their help when I start learning TEM and let me sneak in their microscope sessions. I also want to thank Catalina Coll for her undoubtedly help when dealing with university bureaucracy, since she is definitely the right person to ask for this kind of information!, and Javier Blanco (Mr. White) whom I persuaded to continue in the LENS group after the master thesis and it's always good to work with, although drama is one of his primary characteristics!

I want to thank as well all the collaborators through this years from different institutions that made me grow as a scientist. Especially, the collaborations with the group of Prof. Oliver Clemens in Darmstadt, Dr. Josep Roqué in Barcelona, Prof. Leopoldo Molina and his PhD student Alexander Zintler in Darmstadt, and the valuable opinion of Dr. Paul Klar (ja klar!) from Prague. At this point, I would like to encourage my PhD-candidate colleagues from the groups I belong to; Catalina, Mr. White, Daniel (Solenya), Emilia and Philipp to push forward and get the PhD recognition. If I kind of did it, yes, you can do it!

Finally, I would like to acknowledge the financial support given by the Spanish ministry of economy and competitivity via the project MAT2016-79455-P, and the industrial collaboration with Schwenk Zement KG and BASF Construction Solutions GmbH to motivate the application of new scientific knowledge and tools to improve "real life" products.

Last, but not least, I want to thank my parents, to whom this thesis is dedicated, for their continuous support during all my life to everything that I have done, and because without them this would have not been possible at all. Thank you!

Bibliography

[1] G. P. Thomson and A. Reid, "Diffraction of Cathode Rays by a Thin Film," *Nature*, vol. 119, pp. 890–890, June 1927.

[2] C. Davisson and L. H. Germer, "Diffraction of Electrons by a Crystal of Nickel," *Phys. Rev.*, vol. 30, pp. 705–740, Dec. 1927.

[3] U. Kolb, T. Gorelik, C. Kübel, M. T. Otten, and D. Hubert, "Towards automated diffraction tomography: Part I—Data acquisition," *Ultramicroscopy*, vol. 107, pp. 507–513, June 2007.

[4] U. Kolb, T. Gorelik, and M. T. Otten, "Towards automated diffraction tomography. Part II—Cell parameter determination," *Ultramicroscopy*, vol. 108, pp. 763–772, July 2008.

[5] D. Zhang, P. Oleynikov, S. Hovmöller, and X. Zou, "Collecting 3D electron diffraction data by the rotation method," *Zeitschrift für Kristallographie International journal for structural, physical, and chemical aspects of crystalline materials*, vol. 225, no. 2-3, pp. 94–102, 2010.

[6] I. Nederlof, E. van Genderen, Y.-W. Li, and J. P. Abrahams, "A Medipix quantum area detector allows rotation electron diffraction data collection from submicrometre three-dimensional protein crystals," *Acta Crystallographica Section D Biological Crystallography*, vol. 69, pp. 1223–1230, July 2013.

[7] B. L. Nannenga, D. Shi, A. G. W. Leslie, and T. Gonen, "High-resolution structure determination by continuous-rotation data collection in MicroED," *Nature Methods*, vol. 11, pp. 927–930, Sept. 2014.

[8] M. Gemmi, M. G. I. La Placa, A. S. Galanis, E. F. Rauch, and S. Nicolopoulos, "Fast electron diffraction tomography," *J Appl Cryst*, vol. 48, pp. 718–727, June 2015.

[9] M. O. Cichocka, J. Ångström, B. Wang, X. Zou, and S. Smeets, "High-throughput continuous rotation electron diffraction data acquisition via software automation," *J Appl Cryst*, vol. 51, pp. 1652–1661, Dec. 2018.

[10] P. Oleynikov, "EDT Process Software Package." Analitex: Stockholm, Sweden, 2011.

[11] W. Wan, J. Sun, J. Su, S. Hovmöller, and X. Zou, "Three-dimensional rotation electron diffraction: Software *RED* for automated data collection and data processing," *Journal of Applied Crystallography*, vol. 46, pp. 1863–1873, Dec. 2013.

[12] U. Kolb, Y. Krysiak, and S. Plana-Ruiz, "Automated electron diffraction tomography – development and applications," *Acta Cryst B*, vol. 75, pp. 463–474, Aug. 2019.

[13] L. Palatinus, P. Brázda, M. Jelínek, J. Hrdá, G. Steciuk, and M. Klementová, "Specifics of the data processing of precession electron diffraction tomography data and their implementation in the program PETS2.0," *Acta Cryst B*, vol. 75, pp. 512–522, Aug. 2019.

[14] M. Gemmi, E. Mugnaioli, T. E. Gorelik, U. Kolb, L. Palatinus, P. Boullay, S. Hovmöller, and J. P. Abrahams, "3D Electron Diffraction: The Nanocrystallography Revolution," *ACS Cent. Sci.*, vol. 5, pp. 1315–1329, Aug. 2019.

[15] N. Mahasenan, S. Smith, and K. Humphreys, "The Cement Industry and Global Climate ChangeCurrent and Potential Future Cement Industry CO2 Emissions," in *Greenhouse Gas Control Technologies - 6th International Conference*, vol. II, pp. 995–1000, Elsevier, 2003.

[16] H. F. W. Taylor, *Cement Chemistry*. London: T. Telford, 2nd ed ed., 1997.

[17] F. Dunstetter, M.-N. de Noirfontaine, and M. Courtial, "Polymorphism of tricalcium silicate, the major compound of Portland cement clinker," *Cement and Concrete Research*, vol. 36, pp. 39–53, Jan. 2006.

[18] Y. J. Kim, I. Nettleship, and W. M. Kriven, "Phase Transformations in Dicalcium Silicate: II, TEM Studies of Crystallography, Microstructure, and Mechanisms," *Journal of the American Ceramic Society*, vol. 75, no. 9, pp. 2407–2419, 1992.

[19] G. J. Redhammer, G. Tippelt, G. Roth, and G. Amthauer, "Structural variations in the brownmillerite series Ca2(Fe2–xAlx)O5: Single-crystal X-ray diffraction at 25 C and high-temperature X-ray powder diffraction (25 C $\leq$ T $\leq$ 1000 C)," *American Mineralogist*, vol. 89, pp. 405–420, Feb. 2004.

[20] I. G. Richardson, C. Hall, and G. W. Groves, "TEM study of the composition of the interstitial phase in an oil-well cement clinker," *Advances in Cement Research*, vol. 5, pp. 15–21, Jan. 1993.

[21] S. D. Jacobsen, J. R. Smyth, R. J. Swope, and R. T. Downs, "Rigid-body character of the SO 4 groups in celestine, anglesite and barite," *The Canadian Mineralogist*, vol. 36, pp. 1053–1060, Aug. 1998.

[22] Y. Krysiak, B. Marler, B. Barton, S. Plana-Ruiz, H. Gies, R. B. Neder, and U. Kolb, "New zeolite-like RUB-5 and its related hydrous layer silicate RUB-6 structurally characterized by electron microscopy," *IUCrJ*, vol. 7, pp. 522–534, May 2020.

[23] J. Čejka, R. E. Morris, and P. Nachtigall, eds., *Zeolites in Catalysis: Properties and Applications*. London: The Royal Society of Chemistry, June 2017.

[24] W. B. Burdett, "US Patent: Stainless steel alloy," Aug. 1997.

[25] D. Bowden, Y. Krysiak, L. Palatinus, D. Tsivoulas, S. Plana-Ruiz, E. Sarakinou, U. Kolb, D. Stewart, and M. Preuss, "A high-strength silicide phase in a stainless steel alloy designed for wear-resistant applications," *Nature Communications*, vol. 9, p. 1374, Apr. 2018.

[26] Z. Sekkat and M. Dumont, "Photoassisted poling of azo dye doped polymeric films at room temperature," *Applied Physics B Photophysics and Laser Chemistry*, vol. 54, pp. 486–489, May 1992.

[27] G. Schottner, S. Hofacker, and J. Sandrock, "Organic Dye-Doped Hybrid Sol-Gel Coatings and Pigments – Synthesis, Structural Elucidation and Application," *MRS Proceedings*, vol. 519, p. 251, Jan. 1998.

[28] A. Miniewicz, S. Bartkiewicz, J. Sworakowski, J. A. Giacometti, and M. M. Costa, "On optical phase conjugation in polystyrene films containing the azobenzene dye Disperse Red 1," *Pure and Applied Optics: Journal of the European Optical Society Part A*, vol. 7, pp. 709–721, July 1998.

[29] Y. Cui, M. Wang, L. Chen, and G. Qian, "Synthesis and spectroscopic characterization of an alkoxysilane dye containing C. I. Disperse Red 1," *Dyes and Pigments*, vol. 62, pp. 43–47, July 2004.

[30] M. von Laue, "Eine quantitative Prüfung der Theorie für die Interferenz-Erscheinungen bei Röntgenstrahlen," *Verlag der Königlich Bayerischen Akademie der Wissenschaften*, pp. 363–373, 1912.

[31] W. L. Bragg, "The Structure of Some Crystals as Indicated by Their Diffraction of X-rays," *Proceedings of the Royal Society A: Mathematical, Physical and Engineering Sciences*, vol. 89, pp. 248–277, Sept. 1913.

[32] D. P. Mitchell and P. N. Powers, "Bragg Reflection of Slow Neutrons," *Phys. Rev.*, vol. 50, pp. 486–487, Sept. 1936.

[33] H. Von Halban and P. Preiswerk, "Recherches sur les neutrons lents," *J. Phys. Radium*, vol. 8, no. 1, pp. 29–40, 1937.

[34] L. D. Broglie, "Recherches sur la théorie des Quanta," *Ann. Phys.*, vol. 10, no. 3, pp. 22–128, 1925.

[35] C. Huygens, *Traite de la lumiere*. Leiden: Pieer van der Aa, 1690.

[36] I. Newton, "A letter of Mr. Isaac Newton," *Philosophical Transactions of the Royal Society of London*, vol. 6, pp. 3075–3087, Jan. 1671.

[37] A. Fresnel, "Mémoire sur la diffraction de la lumière," *Oeuvres complètes*, vol. 1, pp. 247–363, 1866.

[38] G. Kirchhoff, "Zur Theorie der Lichtstrahlen," *Annalen der Physik*, vol. 254, no. 4, pp. 663–695, 1882.

[39] G. Green, *An Essay on the Application of Mathematical Analysis to the Theories of Electricity and Magnetism*. Nottingham: Published by himself, 1828.

[40] A. Cauchy, "Sur les intégrales qui s'étendent à tous les points d'une courbe fermée," *Comptes rendus*, no. 23, pp. 251–255, 1846.

[41] B. Riemann, *Grundlagen für eine allgemeine Theorie der Functionen einer veränderlichen complexen Grösse*. Göttingen: Verlag von Adalbert Rente, 1867.

[42] W. Heisenberg, "Über den anschaulichen Inhalt der quantentheoretischen Kinematik und Mechanik," *Z. Physik*, vol. 43, pp. 172–198, Mar. 1927.

[43] R. N. Bracewell, *The Fourier Transform and Its Applications*. Singapore: McGraw Hill, 2000.

[44] J.-B. J. Fourier, *Théorie analytique de la chaleur*. Paris: F. Didot, 1822.

[45] U. Shmueli, ed., *International Tables for Crystallography. Vol. B: Reciprocal Space*. Dordrecht: Kluwer Acad. Publ, 2001.

[46] P. Hirsch, A. Howie, R. Nicholson, D. Pashley, and M. Whelan, *Electron Microscopy of Thin Crystals*. Florida: Krieger Pub Co, 1977.

[47] J. C. H. Spence and J. M. Zuo, *Electron Microdiffraction*. New York: Springer Verlag, 1992.

[48] J. C. H. Spence, "On the accurate measurement of structure-factor amplitudes and phases by electron diffraction," *Acta Cryst A*, vol. 49, pp. 231–260, Mar. 1993.

[49] J. M. Cowley, *Diffraction Physics*. Amsterdam ; New York: Elsevier Science B.V, 1995.

[50] A. L. Patterson, "A Fourier Series Method for the Determination of the Components of Interatomic Distances in Crystals," *Phys. Rev.*, vol. 46, pp. 372–376, Sept. 1934.

[51] A. L. Patterson, "A Direct Method for the Determination of the Components of Interatomic Distances in Crystals," *Zeitschrift für Kristallographie - Crystalline Materials*, vol. 90, no. 1-6, pp. 517–542, 1935.

[52] "Report of the Executive Committee for 1991," *Acta Crystallographica Section A*, vol. 48, no. 6, pp. 922–946, 1992.

[53] N. F. Mott and N. H. D. Bohr, "The scattering of fast electrons by atomic nuclei," *Proceedings of the Royal Society of London. Series A, Containing Papers of a Mathematical and Physical Character*, vol. 124, pp. 425–442, June 1929.

[54] E. Prince, ed., *International Tables for Crystallography. Vol. C: Mathematical, Physical and Chemical Tables*. Dordrecht: Kluwer Acad. Publ, 3rd ed., 2004.

[55] P. P. Ewald, "Zur Begründung der Kristalloptik," *Annalen der Physik*, vol. 359, no. 23, pp. 519–556, 1917.

[56] P. P. Ewald, "Zur Begründung der Kristalloptik," *Annalen der Physik*, vol. 359, no. 24, pp. 557–597, 1917.

[57] P. Debye, "Interferenz von Röntgenstrahlen und Wärmebewegung," *Annalen der Physik*, vol. 348, no. 1, pp. 49–92, 1913.

[58] J. Lange, "The Lorentz factor for the Laue technique," *Acta Crystallographica Section A*, vol. 51, no. 4, pp. 559–565, 1995.

[59] E. Abbe, "Beiträge zur Theorie des Mikroskops und der mikroskopischen Wahrnehmung," *Archiv f. mikrosk. Anatomie*, vol. 9, pp. 413–468, Dec. 1873.

[60] H. Helmholtz, "Die theoretische Grenze für die Leistungsfähigkeit der Mikroskope," *Poggendorff's Annalen Jubelband*, pp. 557–584, 1874.

[61] J. W. S. Rayleigh, "On the theory of optical images, with special reference to the microscope," *The London, Edinburgh, and Dublin Philosophical Magazine and Journal of Science*, vol. 42, pp. 167–195, Aug. 1896.

[62] O. Lummer and F. Reiche, *Die Lehre von Der Bildentstehung Im Mikroskop von Ernst Abbe*. Braunschweig: F. Vieweg, 1910.

[63] H. A. Lorentz, *Versuch Eine Theorie Der Electrischen Und Optischen Erscheinungen in Bewegten Körpern*. Leiden: E. J. Brill, 1895.

[64] E. Ruska, "Current efforts to attain the resolution limit of the transmission electron microscope," *Journal of the Royal Microscopical Society*, vol. 84, no. 1, pp. 77–103, 1965.

[65] H. Busch, "Berechnung der Bahn von Kathodenstrahlen im axialsymmetrischen elektromagnetischen Felde," *Annalen der Physik*, vol. 386, no. 25, pp. 974–993, 1926.

[66] H. Busch, "Über die Wirkungsweise der Konzentrierungsspule bei der Braunschen Röhre," *Archiv f. Elektrotechnik*, vol. 18, pp. 583–594, Nov. 1927.

[67] E. Ruska and M. Knoll, "Die magnetische Sammelspule für schnelle Elektronenstrahlen," *Zeitschrift für technische Physik*, no. 12, pp. 389–400 and 448, 1931.

[68] M. Knoll and E. Ruska, "Das Elektronenmikroskop," *Z. Physik*, vol. 78, pp. 318–339, May 1932.

[69] P. W. Hawkes, E. Kasper, and A. Kirkland, *Principle of Electron Optics, Volume 2*. London: Academic Press, second ed., 2017.

[70] N. Shibata, Y. Kohno, A. Nakamura, S. Morishita, T. Seki, A. Kumamoto, H. Sawada, T. Matsumoto, S. D. Findlay, and Y. Ikuhara, "Atomic resolution electron microscopy in a magnetic field free environment," *Nat Commun*, vol. 10, pp. 1–5, May 2019.

[71] J. C. Maxwell, "On physical lines of force," *Philosophical Magazine*, pp. 161–175 (vol. 21), 338–349 (vol. 21), 12–24 (vol. 23), 85–95 (vol. 23), 1861.

[72] W. Glaser, "Strenge Berechnung magnetischer Linsen der Feldform H=H01+(z/a)2," *Z. Physik*, vol. 117, pp. 285–315, Mar. 1941.

[73] W. Glaser, *Grundlagen der Elektronenoptik*. Berlin, Heidelberg: Springer Berlin Heidelberg, 1952.

[74] L. Reimer and H. Kohl, *Transmission Electron Microscopy: Physics of Image Formation*. No. 36 in Springer Series in Optical Sciences, New York, NY: Springer, 5th ed ed., 2008.

[75] J. Orloff, "Survey of electron sources for high-resolution microscopy," *Ultramicroscopy*, vol. 28, pp. 88–97, Apr. 1989.

[76] D. B. Williams and C. B. Carter, *Transmission Electron Microscopy: A Textbook for Materials Science*. New York: Springer, second ed., 2008.

[77] A. J. F. Metherell, "Energy Analyzing and Energy Selecting Electron Microscopes," *Advances in Optical and Electron Microscopy*, vol. 4, pp. 263–360, 1971.

[78] K. Kimoto, "Practical aspects of monochromators developed for transmission electron microscopy," *Microscopy (Oxf)*, vol. 63, pp. 337–344, Oct. 2014.

[79] J. Orloff, ed., *Handbook of Charged Particle Optics*. Boca Raton: CRC Press/Taylor & Francis, second ed., 2009.

[80] O. Scherzer, "Über einige Fehler von Elektronenlinsen," *Z. Physik*, vol. 101, pp. 593–603, Sept. 1936.

[81] O. Scherzer, "The Theoretical Resolution Limit of the Electron Microscope," *Journal of Applied Physics*, vol. 20, pp. 20–29, Jan. 1949.

[82] F. Zemlin, K. Weiss, P. Schiske, W. Kunath, and K. H. Herrmann, "Coma-free alignment of high resolution electron microscopes with the aid of optical diffractograms," *Ultramicroscopy*, vol. 3, pp. 49–60, Jan. 1978.

[83] O. L. Krivanek, N. Dellby, and A. R. Lupini, "Towards sub-Å electron beams," *Ultramicroscopy*, vol. 78, pp. 1–11, June 1999.

[84] S. Uhlemann and M. Haider, "Residual wave aberrations in the first spherical aberration corrected transmission electron microscope," *Ultramicroscopy*, vol. 72, pp. 109–119, May 1998.

[85] H. Sawada, T. Sannomiya, F. Hosokawa, T. Nakamichi, T. Kaneyama, T. Tomita, Y. Kondo, T. Tanaka, Y. Oshima, Y. Tanishiro, and K. Takayanagi, "Measurement method of aberration from Ronchigram by autocorrelation function," *Ultramicroscopy*, vol. 108, pp. 1467–1475, Oct. 2008.

[86] J. Zach and M. Haider, "Aberration correction in a low voltage SEM by a multipole corrector," *Nuclear Instruments and Methods in Physics Research Section A: Accelerators, Spectrometers, Detectors and Associated Equipment*, vol. 363, pp. 316–325, Sept. 1995.

[87] M. Haider, P. Hartel, H. Müller, S. Uhlemann, and J. Zach, "Information Transfer in a TEM Corrected for Spherical and Chromatic Aberration," *Microscopy and Microanalysis*, vol. 16, pp. 393–408, Aug. 2010.

[88] C. Kisielowski, B. Freitag, M. Bischoff, H. van Lin, S. Lazar, G. Knippels, P. Tiemeijer, M. van der Stam, S. von Harrach, M. Stekelenburg, M. Haider, S. Uhlemann, H. Müller, P. Hartel, B. Kabius, D. Miller, I. Petrov, E. A. Olson, T. Donchev, E. A. Kenik, A. R. Lupini, J. Bentley, S. J. Pennycook, I. M. Anderson, A. M. Minor, A. K. Schmid, T. Duden, V. Radmilovic, Q. M. Ramasse, M. Watanabe, R. Erni, E. A. Stach, P. Denes, and U. Dahmen, "Detection of Single Atoms and Buried Defects in Three Dimensions by Aberration-Corrected Electron Microscope with 0.5-Å Information Limit," *Microscopy and Microanalysis*, vol. 14, pp. 469–477, Oct. 2008.

[89] J. Barthel, L. Houben, and K. Tillmann, "FEI Titan G3 50-300 PICO," *Journal of large-scale research facilities JLSRF*, vol. 1, p. 34, Nov. 2015.

[90] E. Ruska, "über Fortschritte im Bau und in der Leistung des magnetischen Elektronenmikroskops," *Z. Physik*, vol. 87, pp. 580–602, Sept. 1934.

[91] E. Ruska, "The development of the electron microscope and of electron microscopy," *Biosci Rep*, vol. 7, pp. 607–629, Aug. 1987.

[92] G. Benner and W. Probst, "Köhler illumination in the TEM: Fundamentals and advantages," *Journal of Microscopy*, vol. 174, no. 3, pp. 133–142, 1994.

[93] A. Köhler, "Ein neues Beleuchtungsverfahren fur mikrophotographische Zwecke," *Z. wiss Mikr.*, no. 10, pp. 433–440, 1893.

[94] P. C. Tiemeijer, M. Bischoff, B. Freitag, and C. Kisielowski, "Using a monochromator to improve the resolution in TEM to below 0.5Å. Part I: Creating highly coherent monochromated illumination," *Ultramicroscopy*, vol. 114, pp. 72–81, Mar. 2012.

[95] K. Yamazaki, "Development of JEM-F200(F2) Multi-Purpose Electron Microscope," *JEOL NEWS*, vol. 51, pp. 49–56, July 2016.

[96] P. W. Hawkes, "The correction of electron lens aberrations," *Ultramicroscopy*, vol. 156, pp. A1–A64, Sept. 2015.

[97] M. von Ardenne, "Das Elektronen-Rastermikroskop," *Z. Physik*, vol. 109, pp. 553–572, Sept. 1938.

[98] A. V. Crewe, "Scanning Electron Microscopes: Is High Resolution Possible?," *Science*, vol. 154, pp. 729–738, Nov. 1966.

[99] A. V. Crewe, M. Isaacson, and D. Johnson, "A Simple Scanning Electron Microscope," *Review of Scientific Instruments*, vol. 40, pp. 241–246, Feb. 1969.

[100] A. V. Crewe, J. Wall, and J. Langmore, "Visibility of Single Atoms," *Science*, vol. 168, pp. 1338–1340, June 1970.

[101] J. N. Chapman, P. E. Batson, E. M. Waddell, and R. P. Ferrier, "The direct determination of magnetic domain wall profiles by differential phase contrast electron microscopy," *Ultramicroscopy*, vol. 3, pp. 203–214, Jan. 1978.

[102] J. Chapman, I. McFadyen, and S. McVitie, "Modified differential phase contrast Lorentz microscopy for improved imaging of magnetic structures," *IEEE Transactions on Magnetics*, vol. 26, pp. 1506–1511, Sept. 1990.

[103] N. Shibata, Y. Kohno, S. D. Findlay, H. Sawada, Y. Kondo, and Y. Ikuhara, "New area detector for atomic-resolution scanning transmission electron microscopy," *J Electron Microsc (Tokyo)*, vol. 59, pp. 473–479, Dec. 2010.

[104] R. F. Egerton, *Electron Energy-Loss Spectroscopy in the Electron Microscope*. The Language of Science, New York: Springer, 3rd ed., 2011.

[105] L. E. Thomas, "High spatial resolution in stem x-ray microanalysis," *Ultramicroscopy*, vol. 9, pp. 311–318, Jan. 1982.

[106] T. Hanai and M. Hibino, "Effect of the Spherical Aberration on Electron Probe Size," *J Electron Microsc (Tokyo)*, vol. 33, pp. 116–122, Jan. 1984.

[107] A. M. Airy, "On the diffraction of an object-glass with circular aperture," *Transaction of the Cambridge Philosophical Society*, vol. 5, pp. 283–291, 1834.

[108] J. R. Michael and D. B. Williams, "A consistent definition of probe size and spatial resolution in the analytical electron microscope," *Journal of Microscopy*, vol. 147, no. 3, pp. 289–303, 1987.

[109] M. Tanaka, "Convergent-beam electron diffraction," *Acta Cryst A*, vol. 50, pp. 261–286, May 1994.

[110] M. J. Buerger, "The Photography of the Reciprocal Lattice," *ASXRED Monograph*, vol. 1, 1944.

[111] R. Vincent and P. A. Midgley, "Double conical beam-rocking system for measurement of integrated electron diffraction intensities," *Ultramicroscopy*, vol. 53, pp. 271–282, Mar. 1994.

[112] J. P. Morniroli, A. Redjaïmia, and S. Nicolopoulos, "Contribution of electron precession to the identification of the space group from microdiffraction patterns," *Ultramicroscopy*, vol. 107, pp. 514–522, June 2007.

[113] J.-P. Morniroli, P. Stadelmann, G. Ji, and S. Nicolopoulos, "The symmetry of precession electron diffraction patterns," *Journal of Microscopy*, vol. 237, no. 3, pp. 511–515, 2010.

[114] P. A. Midgley and A. S. Eggeman, "Precession electron diffraction – a topical review," *IUCrJ*, vol. 2, pp. 126–136, Jan. 2015.

[115] L. Palatinus, V. Petříček, and C. A. Corrêa, "Structure refinement using precession electron diffraction tomography and dynamical diffraction: Theory and implementation," *Acta Crystallographica Section A Foundations and Advances*, vol. 71, pp. 235–244, Mar. 2015.

[116] L. Palatinus, C. A. Corrêa, G. Steciuk, D. Jacob, P. Roussel, P. Boullay, M. Klementová, M. Gemmi, J. Kopeček, M. C. Domeneghetti, F. Cámara, and V. Petříček, "Structure refinement using precession electron diffraction tomography and dynamical diffraction: Tests on experimental data," *Acta Crystallographica Section B Structural Science, Crystal Engineering and Materials*, vol. 71, pp. 740–751, Dec. 2015.

[117] E. Mugnaioli, T. Gorelik, and U. Kolb, ""Ab initio" structure solution from electron diffraction data obtained by a combination of automated diffraction tomography and precession technique," *Ultramicroscopy*, vol. 109, pp. 758–765, May 2009.

[118] J. Portillo, E. F. Rauch, S. Nicolopoulos, M. Gemmi, and D. Bultreys, "Precession Electron Diffraction Assisted Orientation Mapping in the Transmission Electron Microscope," *Materials Science Forum*, vol. 644, pp. 1–7, 2010.

[119] D. Viladot, M. Véron, M. Gemmi, F. Peiró, J. Portillo, S. Estradé, J. Mendoza, N. Llorca-Isern, and S. Nicolopoulos, "Orientation and phase mapping in the transmission electron microscope using precession-assisted diffraction spot recognition: State-of-the-art results," *Journal of Microscopy*, vol. 252, no. 1, pp. 23–34, 2013.

[120] D. Cooper, N. Bernier, and J.-L. Rouvière, "Combining 2 nm Spatial Resolution and 0.02% Precision for Deformation Mapping of Semiconductor Specimens in a Transmission Electron Microscope by Precession Electron Diffraction," *Nano Lett.*, vol. 15, pp. 5289–5294, Aug. 2015.

[121] A. Béché, J. L. Rouvière, J. P. Barnes, and D. Cooper, "Strain measurement at the nanoscale: Comparison between convergent beam electron diffraction, nano-beam electron diffraction, high resolution imaging and dark field electron holography," *Ultramicroscopy*, vol. 131, pp. 10–23, Aug. 2013.

[122] P. Oleynikov, S. Hovmöller, and X. D. Zou, "Precession electron diffraction: Observed and calculated intensities," *Ultramicroscopy*, vol. 107, pp. 523–533, June 2007.

[123] J. M. Rebled, L. Yedra, S. Estradé, J. Portillo, and F. Peiró, "A new approach for 3D reconstruction from bright field TEM imaging: Beam precession assisted electron tomography," *Ultramicroscopy*, vol. 111, pp. 1504–1511, Aug. 2011.

[124] S. Estradé, J. Portillo, L. Yedra, J. M. Rebled, and F. Peiró, "EELS signal enhancement by means of beam precession in the TEM," *Ultramicroscopy*, vol. 116, pp. 135–137, May 2012.

[125] Y. Liao and L. D. Marks, "Reduction of electron channeling in EDS using precession," *Ultramicroscopy*, vol. 126, pp. 19–22, Mar. 2013.

[126] L. Yedra, P. Torruella, A. Eljarrat, A. D. Darbal, J. K. Weiss, F. Peiró, and S. Estradé, "Precessed electron beam electron energy loss spectroscopy of graphene: Beyond channelling effects," *Appl. Phys. Lett.*, vol. 105, p. 053117, Aug. 2014.

[127] K. Wissel, A. M. Malik, S. Vasala, S. Plana-Ruiz, U. Kolb, P. R. Slater, I. da Silva, L. Alff, J. Rohrer, and O. Clemens, "Topochemical Reduction of La2NiO3F2: The First Ni-Based Ruddlesden-Popper n = 1 T'-Type Structure and the Impact of Reduction on Magnetic Ordering," *Chem. Mater.*, vol. 32, pp. 3160–3179, Feb. 2020.

[128] S. J. Leake, G. A. Chahine, H. Djazouli, T. Zhou, C. Richter, J. Hilhorst, L. Petit, M.-I. Richard, C. Morawe, R. Barrett, L. Zhang, R. A. Homs-Regojo, V. Favre-Nicolin, P. Boesecke, and T. U. Schülli, "The Nanodiffraction beamline ID01/ESRF: A microscope for imaging strain and structure," *J Synchrotron Rad*, vol. 26, pp. 571–584, Mar. 2019.

[129] T. R. Welberry and T. Weber, "One hundred years of diffuse scattering," *Crystallography Reviews*, vol. 22, pp. 2–78, Jan. 2016.

[130] E. Mugnaioli and T. E. Gorelik, "Structure analysis of materials at the order–disorder borderline using three-dimensional electron diffraction," *Acta Crystallographica Section B*, vol. 75, no. 4, pp. 550–563, 2019.

[131] T. Willhammar and X. Zou, "Stacking disorders in zeolites and open-frameworks – structure elucidation and analysis by electron crystallography and X-ray diffraction," *Zeitschrift für Kristallographie - Crystalline Materials*, vol. 228, no. 1, pp. 11–27, 2012.

[132] T. Willhammar, J. Sun, W. Wan, P. Oleynikov, D. Zhang, X. Zou, M. Moliner, J. Gonzalez, C. Martínez, F. Rey, and A. Corma, "Structure and catalytic properties of the most complex intergrown zeolite ITQ-39 determined by electron crystallography," *Nature Chemistry*, vol. 4, pp. 188–194, Mar. 2012.

[133] T. Proffen and R. B. Neder, "DISCUS: A program for diffuse scattering and defect-structure simulation," *J Appl Cryst*, vol. 30, pp. 171–175, Apr. 1997.

[134] H. Zhao, Y. Krysiak, K. Hoffmann, B. Barton, L. Molina-Luna, R. B. Neder, H.-J. Kleebe, T. M. Gesing, H. Schneider, R. X. Fischer, and U. Kolb, "Elucidating structural order and disorder phenomena in mullite-type Al4B2O9 by automated electron diffraction tomography," *Journal of Solid State Chemistry*, vol. 249, pp. 114–123, May 2017.

[135] Y. Krysiak, B. Barton, B. Marler, R. B. Neder, and U. Kolb, "Ab initio structure determination and quantitative disorder analysis on nanoparticles by electron diffraction tomography," *Acta Cryst A*, vol. 74, pp. 93–101, Mar. 2018.

[136] P. Opitz, M. P. Asta, A. Fernandez-Martinez, M. Panthöfer, A. Kabelitz, F. Emmerling, M. Mondeshki, and W. Tremel, "Monitoring a Mechanochemical Reaction Reveals the Formation of a New ACC Defect Variant Containing the HCO3- Anion Encapsulated by an Amorphous Matrix," *Crystal Growth & Design*, vol. 20, pp. 6831–6846, Oct. 2020.

[137] J. B. L. de Romé de L'Isle, *Cristallographie, Ou Description Des Formes Propres a Tous Les Corps Du Regne Minéral.* Paris: Imprimerie de Monsieur, 1783. First published in 1772 with title: *Essai de cristallographie.*

[138] R.-J. Haüy, *Traité de Minéralogie.* Paris: Imprimerie de Delance, 1801.

[139] G. P. H. Smith, "Ueber das bemerkenswerthe Problem der Entwickelung der Krystallformen des Calaverit," *Zeitschrift für Kristallographie - Crystalline Materials*, vol. 37, pp. 209–234, Dec. 1903.

[140] U. Dehlinger, "über die Verbreiterung der Debyelinien bei kaltbearbeiteten Metallen," *Zeitschrift für Kristallographie - Crystalline Materials*, vol. 65, pp. 615–631, Dec. 1927.

[141] G. D. Preston, "The diffraction of X-rays by an age-hardening alloy of aluminium and copper. The structure of an intermediate phase," *The London, Edinburgh, and Dublin Philosophical Magazine and Journal of Science*, vol. 26, no. 178, pp. 855–871, 1938.

[142] V. Daniel, H. S. Lipson, and W. L. Bragg, "An X-ray study of the dissociation of an alloy of copper, iron and nickel," *Proceedings of the Royal Society of London. Series A. Mathematical and Physical Sciences*, vol. 181, pp. 368–378, July 1943.

[143] S. Tanisaki, "Microdomain Structure in Paraelectric Phase of $NaNO_2$," *Journal of the Physical Society of Japan*, vol. 16, no. 3, pp. 579–579, 1961.

[144] S. Tanisaki, "X-ray Study on the Ferroelectric Phase Transition of NaNO2," *J. Phys. Soc. Jpn.*, vol. 18, pp. 1181–1191, Aug. 1963.

[145] E. Brouns, J. W. Visser, and P. M. de Wolff, "An anomaly in the crystal structure of Na2CO3," *Acta Cryst*, vol. 17, pp. 614–614, May 1964.

[146] H. Völlenkle, A. Preisinger, H. Nowotny, and A. Wittmann, "Die Kristallstrukturen von Cr11Ge19, Mo13Ge23 und V17Ge31," *Zeitschrift für Kristallographie - Crystalline Materials*, vol. 124, pp. 9–25, Nov. 1967.

[147] P. M. de Wolff, "The Pseudo-Symmetry of Modulated Crystal Structures," *Acta Cryst A*, vol. 30, pp. 777–785, Nov. 1974.

[148] D. Shechtman, I. Blech, D. Gratias, and J. W. Cahn, "Metallic Phase with Long-Range Orientational Order and No Translational Symmetry," *Phys. Rev. Lett.*, vol. 53, pp. 1951–1953, Nov. 1984.

[149] S. van Smaalen, *Incommensurate Crystallography*. No. 21 in International Series of Monographs on Physics, Oxford ; New York: Oxford University Press, 2007.

[150] W. Steurer, "The structure of quasicrystals," *Zeitschrift für Kristallographie - Crystalline Materials*, vol. 190, pp. 179–234, Dec. 1990.

[151] A. Yamamoto, "Crystallography of Quasiperiodic Crystals," *Acta Cryst A*, vol. 52, pp. 509–560, July 1996.

[152] P. M. de Wolff, "Symmetry operations for displacively modulated structures," *Acta Cryst A*, vol. 33, pp. 493–497, May 1977.

[153] S. S. van, "An elementary introduction to superspace crystallography," *Zeitschrift für Kristallographie - Crystalline Materials*, vol. 219, no. 11, pp. 681–691, 2009.

[154] J. C. Marmeggi, G. H. Lander, S. van Smaalen, T. Brückel, and C. M. E. Zeyen, "Neutron-diffraction study of the charge-density wave in α-uranium," *Phys. Rev. B*, vol. 42, pp. 9365–9376, Nov. 1990.

[155] A. Janner and T. Janssen, "Symmetry of periodically distorted crystals," *Phys. Rev. B*, vol. 15, pp. 643–658, Jan. 1977.

[156] W. van Aalst, J. den Holander, W. J. a. M. Peterse, and P. M. de Wolff, "The modulated structure of γ-Na2CO3 in a harmonic approximation," *Acta Cryst B*, vol. 32, pp. 47–58, Jan. 1976.

[157] V. Petříček, V. Eigner, M. Dušek, and A. Čejchan, "Discontinuous modulation functions and their application for analysis of modulated structures with the computing system JANA2006," *Zeitschrift für Kristallographie - Crystalline Materials*, vol. 231, pp. 301–312, May 2016.

[158] S. Van Aert, K. J. Batenburg, M. D. Rossell, R. Erni, and G. Van Tendeloo, "Three-dimensional atomic imaging of crystalline nanoparticles," *Nature*, vol. 470, pp. 374–377, Feb. 2011.

[159] R. Xu, C.-C. Chen, L. Wu, M. C. Scott, W. Theis, C. Ophus, M. Bartels, Y. Yang, H. Ramezani-Dakhel, M. R. Sawaya, H. Heinz, L. D. Marks, P. Ercius, and J. Miao, "Three-dimensional coordinates of individual atoms in materials revealed by electron tomography," *Nature Materials*, vol. 14, pp. 1099–1103, Nov. 2015.

[160] S. J. Pennycook, M. Varela, A. R. Lupini, M. P. Oxley, and M. F. Chisholm, "Atomic-resolution spectroscopic imaging: Past, present and future," *J Electron Microsc (Tokyo)*, vol. 58, pp. 87–97, June 2009.

[161] L. Yedra, A. Eljarrat, R. Arenal, E. Pellicer, M. Cabo, A. López-Ortega, M. Estrader, J. Sort, M. D. Baró, S. Estradé, and F. Peiró, "EEL spectroscopic tomography: Towards a new dimension in nanomaterials analysis," *Ultramicroscopy*, vol. 122, pp. 12–18, Nov. 2012.

[162] P. Torruella, R. Arenal, F. de la Peña, Z. Saghi, L. Yedra, A. Eljarrat, L. López-Conesa, M. Estrader, A. López-Ortega, G. Salazar-Alvarez, J. Nogués, C. Ducati, P. A. Midgley, F. Peiró, and S. Estradé, "3D Visualization of the Iron Oxidation State in FeO/Fe3O4 Core–Shell Nanocubes from Electron Energy Loss Tomography," *Nano Lett.*, vol. 16, pp. 5068–5073, Aug. 2016.

[163] T. E. Weirich, X. D. Zou, R. Ramlau, A. Simon, G. L. Cascarano, C. Giacovazzo, and S. Hovmöller, "Structures of nanometre-size crystals determined from selected-area electron diffraction data," *Acta Cryst A*, vol. 56, pp. 29–35, Jan. 2000.

[164] U. Kolb and G. N. Matveeva, "Electron crystallography on polymorphic organics," *Zeitschrift für Kristallographie - Crystalline Materials*, vol. 218, pp. 259–268, Apr. 2003.

[165] T. E. Weirich, J. Portillo, G. Cox, H. Hibst, and S. Nicolopoulos, "Ab initio determination of the framework structure of the heavy-metal oxide CsxNb2.54W2.46O14 from 100kV precession electron diffraction data," *Ultramicroscopy*, vol. 106, pp. 164–175, Feb. 2006.

[166] P. J. Bereciartua, Á. Cantín, A. Corma, J. L. Jordá, M. Palomino, F. Rey, S. Valencia, E. W. Corcoran, P. Kortunov, P. I. Ravikovitch, A. Burton, C. Yoon, Y. Wang, C. Paur, J. Guzman, A. R. Bishop, and G. L. Casty, "Control of zeolite framework flexibility and pore topology for separation of ethane and ethylene," *Science*, vol. 358, pp. 1068–1071, Nov. 2017.

[167] L. Palatinus, P. Brázda, P. Boullay, O. Perez, M. Klementová, S. Petit, V. Eigner, M. Zaarour, and S. Mintova, "Hydrogen positions in single nanocrystals revealed by electron diffraction," *Science*, vol. 355, pp. 166–169, Jan. 2017.

[168] P. Brázda, L. Palatinus, and M. Babor, "Electron diffraction determines molecular absolute configuration in a pharmaceutical nanocrystal," *Science*, vol. 364, pp. 667–669, May 2019.

[169] J. P. Morniroli, *Large-Angle Convergent-Beam Electron Diffraction (LACBED): Applications to Crystal Defects*. Monograph of the French Society of Microscopies, Paris: Société Française des Microscopies, 2002.

[170] E. F. Rauch and L. Dupuy, "Rapid spot diffraction patterns identification through template matching," *Archives of Metallurgy and Materials*, vol. 50, no. 1, pp. 87–99, 2005.

[171] E. F. Rauch, J. Portillo, S. Nicolopoulos, D. Bultreys, S. Rouvimov, and P. Moeck, "Automated nanocrystal orientation and phase mapping in the transmission electron microscope on the basis of precession electron diffraction," *Zeitschrift für Kristallographie*, vol. 225, pp. 103–109, Mar. 2010.

[172] C. Ophus, "Four-Dimensional Scanning Transmission Electron Microscopy (4D-STEM): From Scanning Nanodiffraction to Ptychography and Beyond," *Microscopy and Microanalysis*, vol. 25, pp. 563–582, June 2019.

[173] J. S. Barnard, D. N. Johnstone, and P. A. Midgley, "High-resolution scanning precession electron diffraction: Alignment and spatial resolution," *Ultramicroscopy*, vol. 174, pp. 79–88, Mar. 2017.

[174] M. Tanaka and M. Terauchi, *Convergent-Beam Electron Diffraction*, vol. I. Tokyo, Japan: JEOL Ltd., 1985.

[175] D. Alloyeau, C. Ricolleau, C. Mottet, T. Oikawa, C. Langlois, Y. Le Bouar, N. Braidy, and A. Loiseau, "Size and shape effects on the order–disorder phase transition in CoPt nanoparticles," *Nature Materials*, vol. 8, pp. 940–946, Dec. 2009.

[176] K. J. Ganesh, M. Kawasaki, J. P. Zhou, and P. J. Ferreira, "D-STEM: A Parallel Electron Diffraction Technique Applied to Nanomaterials," *Microscopy and Microanalysis*, vol. 16, pp. 614–621, Oct. 2010.

[177] P. M. Voyles and D. A. Muller, "Fluctuation microscopy in the STEM," *Ultramicroscopy*, vol. 93, pp. 147–159, Nov. 2002.

[178] F. Yi, P. Tiemeijer, and P. M. Voyles, "Flexible formation of coherent probes on an aberration-corrected STEM with three condensers," *J Electron Microsc (Tokyo)*, vol. 59, pp. S15–S21, Aug. 2010.

[179] O. Panova, X. C. Chen, K. C. Bustillo, C. Ophus, M. P. Bhatt, N. Balsara, and A. M. Minor, "Orientation mapping of semicrystalline polymers using scanning electron nanobeam diffraction," *Micron*, vol. 88, pp. 30–36, Sept. 2016.

[180] C. S. Own, W. Sinkler, and L. D. Marks, "Prospects for aberration corrected electron precession," *Ultramicroscopy*, vol. 107, pp. 534–542, June 2007.

[181] R. Egerton, "Control of radiation damage in the TEM," *Ultramicroscopy*, vol. 127, pp. 100–108, Apr. 2013.

[182] R. Erni, M. D. Rossell, C. Kisielowski, and U. Dahmen, "Atomic-Resolution Imaging with a Sub-50-pm Electron Probe," *Phys. Rev. Lett.*, vol. 102, p. 096101, Mar. 2009.

[183] C. T. Koch, "Aberration-compensated large-angle rocking-beam electron diffraction," *Ultramicroscopy*, vol. 111, pp. 828–840, June 2011.

[184] W. R. Hendee, "Cross sectional medical imaging: A history.," *RadioGraphics*, vol. 9, pp. 1155–1180, Nov. 1989.

[185] T. Gruene, J. T. C. Wennmacher, C. Zaubitzer, J. J. Holstein, J. Heidler, A. Fecteau-Lefebvre, S. De Carlo, E. Müller, K. N. Goldie, I. Regeni, T. Li, G. Santiso-Quinones, G. Steinfeld, S. Handschin, E. van Genderen, J. A. van Bokhoven, G. H. Clever, and R. Pantelic, "Rapid Structure Determination of Microcrystalline Molecular Compounds Using Electron Diffraction," *Angewandte Chemie International Edition*, vol. 57, no. 50, pp. 16313–16317, 2018.

[186] C. G. Jones, M. W. Martynowycz, J. Hattne, T. J. Fulton, B. M. Stoltz, J. A. Rodriguez, H. M. Nelson, and T. Gonen, "The CryoEM Method MicroED as a Powerful Tool for Small Molecule Structure Determination," *ACS Central Science*, vol. 4, pp. 1587–1592, Nov. 2018.

[187] B. L. Nannenga and T. Gonen, "The cryo-EM method microcrystal electron diffraction (MicroED)," *Nature Methods*, vol. 16, pp. 369–379, May 2019.

[188] R. Rigamonti, "La struttura della catena paraffinica studiata mediante i raggi di elettroni," *Gazzeta Chimica Italiana*, no. 66, pp. 174–182, 1936.

[189] B. Vainshtein, A. Lobachev, and M. Stasova, "Electron diffraction determination of the C-H distance in some paraffins," *Soviet Physics, Crystallography*, no. 3, pp. 452–459, 1958.

[190] D. L. Dorset and H. A. Hauptman, "Direct phase determination for quasi-kinematical electron diffraction intensity data from organic microcrystals," *Ultramicroscopy*, vol. 1, pp. 195–201, Jan. 1976.

[191] D. L. Dorset, "The interpretation of quasi-kinematical single-crystal electron diffraction intensity data from paraffins," *Acta Cryst A*, vol. 32, pp. 207–215, Mar. 1976.

[192] D. L. Dorset, "Aliphatic chain packing in three crystalline polymorphs of a saturated racemic phosphatidylethanolamine: A quantitative electron diffraction study," *Biochimica et Biophysica Acta (BBA) - Lipids and Lipid Metabolism*, vol. 424, pp. 396–403, Mar. 1976.

[193] J. M. Cowley, "Structure analysis of single crystals by electron diffraction. II. Disordered boric acid structure," *Acta Cryst*, vol. 6, pp. 522–529, June 1953.

[194] M. Stasova and B. Vainshtein, "Electron-diffraction investigation of cryptohalite," *Trud. Inst. Krist. Akad. Nauk SSSR*, no. 12, p. 18, 1956.

[195] B. B. Zvyagin, *Electron-Diffraction Analysis of Clay Mineral Structures*. Boston, MA: Springer US, 1967.

[196] W. E. Laschkarew and I. D. Usyskin, "Die Bestimmung der Lage der Wasserstoffionen im NH4Cl-Kristallgitter durch Elektronenbeugung," *Z. Physik*, vol. 85, pp. 618–630, Sept. 1933.

[197] S. Kuwabara, "Accurate Determination of Hydrogen Positions in NH4Cl by Electron Diffraction," *J. Phys. Soc. Jpn.*, vol. 14, pp. 1205–1216, Sept. 1959.

[198] B. K. Vainshtein, "Application of electron diffraction to the study of the chemical bond in crystals," *Q. Rev. Chem. Soc.*, vol. 14, pp. 105–132, Jan. 1960.

[199] B. K. Vainshtein, *Structure Analysis by Electron Diffraction*. New York: Pergamon Press Ltd., 1964.

[200] D. L. Dorset, *Structural Electron Crystallography*. Boston, MA: Springer US, 1995.

[201] D. L. Dorset, "Electron crystallography," *Acta Cryst B*, vol. 52, pp. 753–769, Oct. 1996.

[202] J. M. Cowley, "Structure analysis of single crystals by electron diffraction. III. Modification of alumina," *Acta Cryst*, vol. 6, pp. 846–853, Nov. 1953.

[203] J. M. Cowley, "Electron-diffraction study of the structure of basic lead carbonate, 2PbCO3.Pb(OH)2," *Acta Cryst*, vol. 9, pp. 391–396, Apr. 1956.

[204] J. M. Cowley, "Crystal structure determination by electron diffraction," *Progress in Materials Science*, vol. 13, pp. 267–321, Jan. 1968.

[205] S. Hovmöller, A. Sjögren, G. Farrants, M. Sundberg, and B.-O. Marinder, "Accurate atomic positions from electron microscopy," *Nature*, vol. 311, pp. 238–241, Sept. 1984.

[206] S. Hovmöller, "CRISP: Crystallographic image processing on a personal computer," *Ultramicroscopy*, vol. 41, pp. 121–135, Apr. 1992.

[207] D. L. Dorset, "Direct Phasing in Protein Electron Crystallography – Phase Extension and the Prospects for Ab Initio Determinations," *Acta Cryst A*, vol. 52, pp. 480–489, May 1996.

[208] T. E. Weirich, R. Ramlau, A. Simon, S. Hovmöller, and X. Zou, "A crystal structure determined with 0.02 Å accuracy by electron microscopy," *Nature*, vol. 382, pp. 144–146, July 1996.

[209] D. L. Dorset, "The Accurate Electron Crystallographic Refinement of Organic Structures Containing Heavy Atoms," *Acta Cryst A*, vol. 53, pp. 356–365, May 1997.

[210] S. Nicolopoulos, J. M. Gonzalez-Calbet, M. Vallet-Regi, A. Corma, C. Corell, J. M. Guil, and J. Perez-Pariente, "Direct Phasing in Electron Crystallography: Ab Initio Determination of a New MCM-22 Zeolite Structure," *J. Am. Chem. Soc.*, vol. 117, pp. 8947–8956, Sept. 1995.

[211] J. Gjønnes, V. Hansen, B. S. Berg, P. Runde, Y. F. Cheng, K. Gjønnes, D. L. Dorset, and C. J. Gilmore, "Structure Model for the Phase AlmFe Derived from Three-Dimensional Electron Diffraction Intensity Data Collected by a Precession Technique. Comparison with Convergent-Beam Diffraction," *Acta Cryst A*, vol. 54, pp. 306–319, May 1998.

[212] M. Gemmi, X. D. Zou, S. Hovmöller, A. Migliori, M. Vennström, and Y. Andersson, "Structure of Ti2P solved by three-dimensional electron diffraction data collected with the precession technique and high-resolution electron microscopy," *Acta Cryst A*, vol. 59, pp. 117–126, Mar. 2003.

[213] K. Gjønnes, "On the integration of electron diffraction intensities in the Vincent-Midgley precession technique," *Ultramicroscopy*, vol. 69, pp. 1–11, Aug. 1997.

[214] K. Gjønnes, Y. Cheng, B. S. Berg, and V. Hansen, "Corrections for Multiple Scattering in Integrated Electron Diffraction Intensities. Application to Determination of Structure Factors in the [001] Projection of AlmFe," *Acta Cryst A*, vol. 54, pp. 102–119, Jan. 1998.

[215] W. Kabsch, "XDS," *Acta Cryst D*, vol. 66, pp. 125–132, Feb. 2010.

[216] M. T. B. Clabbers, E. van Genderen, W. Wan, E. L. Wiegers, T. Gruene, and J. P. Abrahams, "Protein structure determination by electron diffraction using a single three-dimensional nanocrystal," *Acta Cryst D*, vol. 73, pp. 738–748, Sept. 2017.

[217] M. T. B. Clabbers, T. Gruene, J. M. Parkhurst, J. P. Abrahams, and D. G. Waterman, "Electron diffraction data processing with DIALS," *Acta Crystallographica Section D*, vol. 74, no. 6, pp. 506–518, 2018.

[218] S. R. Sternberg, "Biomedical Image Processing," *Computer*, 1983.

[219] G. Friedel, "Sur les symétries cristallines que peut révéler la diffraction des rayons Röntgen," *Comptes rendus*, vol. 157, pp. 1533–1536, 1913.

[220] G. Wulff, "Untersuchungen im Gebiete der optischen Eigenschaften isomorpher Krystalle," *Zeitschrift für Kristallographie - Crystalline Materials*, vol. 36, pp. 1–28, Dec. 1902.

[221] M. Ester, H.-P. Kriegel, J. Sander, and X. Xu, "A Density-Based Algorithm for Discovering Clusters in Large Spatial Databases with Noise," *AAAI Press*, pp. 226–231, 1996.

[222] S. Schlitt, T. E. Gorelik, A. A. Stewart, E. Schömer, T. Raasch, and U. Kolb, "Application of clustering techniques to electron-diffraction data: Determination of unit-cell parameters," *Acta Cryst A*, vol. 68, pp. 536–546, Sept. 2012.

[223] I. Rozhdestvenskaya, E. Mugnaioli, M. Czank, W. Depmeier, U. Kolb, A. Reinholdt, and T. Weirich, "The structure of charoite, (K,Sr,Ba,Mn)15–16(Ca,Na)32[(Si70(O,OH)180)](OH,F)4.0.nH2O, solved by conventional and automated electron diffraction," *Mineralogical Magazine*, vol. 74, pp. 159–177, Feb. 2010.

[224] J. Rius, E. Mugnaioli, O. Vallcorba, and U. Kolb, "Application of δ recycling to electron automated diffraction tomography data from inorganic crystalline nanovolumes," *Acta Cryst A*, vol. 69, pp. 396–407, July 2013.

[225] E. Mugnaioli and U. Kolb, "Applications of automated diffraction tomography (ADT) on nanocrystalline porous materials," *Microporous and Mesoporous Materials*, vol. 166, pp. 93–101, Jan. 2013.

[226] I. V. Rozhdestvenskaya, E. Mugnaioli, M. Schowalter, M. U. Schmidt, M. Czank, W. Depmeier, and A. Rosenauer, "The structure of denisovite, a fibrous nanocrystalline polytypic disordered 'very complex' silicate, studied by a synergistic multi-disciplinary approach employing methods of electron crystallography and X-ray powder diffraction," *IUCrJ*, vol. 4, pp. 223–242, May 2017.

[227] P. P. Das, E. Mugnaioli, S. Nicolopoulos, C. Tossi, M. Gemmi, A. Galanis, G. Borodi, and M. M. Pop, "Crystal Structures of Two Important Pharmaceuticals Solved by 3D Precession Electron Diffraction Tomography," *Org. Process Res. Dev.*, vol. 22, pp. 1365–1372, Oct. 2018.

[228] D. W. M. Hofmann, "Fast estimation of crystal densities," *Acta Cryst B*, vol. 58, pp. 489–493, June 2002.

[229] J. D. Dunitz, V. Schomaker, and K. N. Trueblood, "Interpretation of atomic displacement parameters from diffraction studies of crystals," *The Journal of Physical Chemistry*, vol. 92, pp. 856–867, Feb. 1988.

[230] A. J. C. Wilson, "Determination of Absolute from Relative X-Ray Intensity Data," *Nature*, vol. 150, p. 152, Aug. 1942.

[231] I. Waller, "Zur Frage der Einwirkung der Wärmebewegung auf die Interferenz von Röntgenstrahlen," *Z. Physik*, vol. 17, pp. 398–408, Dec. 1923.

[232] H. A. Hauptman and J. Karle, *Solution of the Phase Problem: 1. The Centrosymmetric Crystal*. American Crystallographic Association, 1953.

[233] W. Cochran, "Relations between the phases of structure factors," *Acta Cryst*, vol. 8, pp. 473–478, Aug. 1955.

[234] R. von Mises, "über die "Ganzzahligkeit" der Atomgewicthe und verwandte Fragen," *Physikalische Zeitschrift*, vol. 19, pp. 490–500, 1918.

[235] C. Giacovazzo, "A general approach to phase relationships: The method of representations," *Acta Cryst A*, vol. 33, pp. 933–944, Nov. 1977.

[236] C. Giacovazzo, "The method of representations of structure seminvariants. II. New theoretical and practical aspects," *Acta Cryst A*, vol. 36, pp. 362–372, May 1980.

[237] M. C. Burla, R. Caliandro, B. Carrozzini, G. L. Cascarano, C. Cuocci, C. Giacovazzo, M. Mallamo, A. Mazzone, and G. Polidori, "Crystal structure determination and refinement via SIR2014," *J Appl Cryst*, vol. 48, pp. 306–309, Feb. 2015.

[238] G. Cascarano, C. Giacovazzo, M. Camalli, R. Spagna, M. C. Burla, A. Nunzi, and G. Polidori, "The method of representations of structure seminvariants. The strengthening of triplet relationships," *Acta Cryst A*, vol. 40, pp. 278–283, May 1984.

[239] M. C. Burla, B. Carrozzini, G. L. Cascarano, C. Giacovazzo, and G. Polidori, "More power for direct methods: SIR2002," *Zeitschrift für Kristallographie - Crystalline Materials*, vol. 217, pp. 629–635, Dec. 2002.

[240] G. Luca Cascarano, C. Giacovazzo, and B. Carrozzini, "Crystal structure solution via precession electron diffraction data: The BEA algorithm," *Ultramicroscopy*, vol. 111, pp. 56–61, Dec. 2010.

[241] G. Oszlányi and A. Sütő, "Ab initio structure solution by charge flipping," *Acta Cryst A*, vol. 60, pp. 134–141, Mar. 2004.

[242] L. Palatinus, "The charge-flipping algorithm in crystallography," *Acta Cryst B*, vol. 69, pp. 1–16, Feb. 2013.

[243] L. Palatinus and G. Chapuis, "SUPERFLIP – a computer program for the solution of crystal structures by charge flipping in arbitrary dimensions," *J Appl Cryst*, vol. 40, pp. 786–790, Aug. 2007.

[244] L. Palatinus, "Ab initio determination of incommensurately modulated structures by charge flipping in superspace," *Acta Cryst A*, vol. 60, pp. 604–610, Nov. 2004.

[245] S. Katrych, T. Weber, M. Kobas, L. Massüger, L. Palatinus, G. Chapuis, and W. Steurer, "New stable decagonal quasicrystal in the system Al–Ir–Os," *Journal of Alloys and Compounds*, vol. 428, pp. 164–172, Jan. 2007.

[246] V. Petříček, M. Dušek, and L. Palatinus, "Crystallographic Computing System JANA2006: General features," *Zeitschrift für Kristallographie - Crystalline Materials*, vol. 229, no. 5, pp. 345–352, 2014.

[247] N. Metropolis, A. W. Rosenbluth, M. N. Rosenbluth, A. H. Teller, and E. Teller, "Equation of State Calculations by Fast Computing Machines," *J. Chem. Phys.*, vol. 21, pp. 1087–1092, June 1953.

[248] S. Kirkpatrick, C. D. Gelatt, and M. P. Vecchi, "Optimization by Simulated Annealing," *Science*, vol. 220, pp. 671–680, May 1983.

[249] W. A. Hendrickson, "Stereochemically restrained refinement of macromolecular structures," in *Methods in Enzymology*, vol. 115 of *Diffraction Methods for Biological Macromolecules Part B*, pp. 252–270, Academic Press, Jan. 1985.

[250] C. Giacovazzo, ed., *Fundamentals of Crystallography*. No. 2 in International Union of Crystallography Texts on Crystallography, [Chester, England], Oxford, New York: International Union of Crystallography, Oxford University Press, 1992.

[251] G. M. Sheldrick, "Crystal structure refinement with SHELXL," *Acta Cryst C*, vol. 71, pp. 3–8, Jan. 2015.

[252] B. Taylor, *Methodus incrementorum directa et inversa*. London: Impensis Gulielmi Innys, 1715.

[253] H. M. Rietveld, "The Rietveld method," *Phys. Scr.*, vol. 89, p. 098002, Aug. 2014.

[254] L. D. Marks, P. Xu, and D. N. Dunn, "UHV transmission electron microscopy of Ir(001)," *Surface Science*, vol. 294, pp. 322–332, Sept. 1993.

[255] J. Jansen, D. Tang, H. W. Zandbergen, and H. Schenk, "MSLS, a Least-Squares Procedure for Accurate Crystal Structure Refinement from Dynamical Electron Diffraction Patterns," *Acta Cryst A*, vol. 54, pp. 91–101, Jan. 1998.

[256] A. Dudka, "ASTRA – a program package for accurate structure analysis by the intermeasurement minimization method," *J Appl Cryst*, vol. 40, pp. 602–608, June 2007.

[257] L. Palatinus, D. Jacob, P. Cuvillier, M. Klementová, W. Sinkler, and L. D. Marks, "Structure refinement from precession electron diffraction data," *Acta Cryst A*, vol. 69, pp. 171–188, Mar. 2013.

[258] F. Bloch, "Über die Quantenmechanik der Elektronen in Kristallgittern," *Z. Physik*, vol. 52, pp. 555–600, July 1929.

[259] C. G. Darwin, "The theory of X-ray reflexion," *The London, Edinburgh, and Dublin Philosophical Magazine and Journal of Science*, vol. 27, pp. 315–333, Feb. 1914.

[260] C. G. Darwin, "The theory of X-ray reflexion. Part II," *The London, Edinburgh, and Dublin Philosophical Magazine and Journal of Science*, vol. 27, pp. 675–690, Apr. 1914.

[261] A. Howie, M. J. Whelan, and N. F. Mott, "Diffraction contrast of electron microscope images of crystal lattice defects - II. The development of a dynamical theory," *Proceedings of the Royal Society of London. Series A. Mathematical and Physical Sciences*, vol. 263, pp. 217–237, Sept. 1961.

[262] S. Miyake and R. Uyeda, "Friedel's law in the dynamical theory of diffraction," *Acta Cryst*, vol. 8, pp. 335–342, June 1955.

[263] P. Goodman and G. Lehmpfuhl, "Observation of the breakdown of Friedel's law in electron diffraction and symmetry determination from zero-layer interactions," *Acta Crystallographica Section A*, vol. 24, no. 3, pp. 339–347, 1968.

[264] W. Massa, *Crystal Structure Determination*. Berlin, Heidelberg: Springer Berlin Heidelberg, 2004.

[265] H. Bethe, "Theorie der Beugung von Elektronen an Kristallen," *Annalen der Physik*, vol. 392, no. 17, pp. 55–129, 1928.

[266] U. Kolb, E. Mugnaioli, and T. E. Gorelik, "Automated electron diffraction tomography – a new tool for nano crystal structure analysis," *Crystal Research and Technology*, vol. 46, no. 6, pp. 542–554, 2011.

[267] H. Klein and J. David, "The quality of precession electron diffraction data is higher than necessary for structure solution of unknown crystalline phases," *Acta Crystallographica Section A Foundations of Crystallography*, vol. 67, pp. 297–302, May 2011.

[268] A. S. Eggeman and P. A. Midgley, "Refining structures against reflection rank: An alternative metric for electron crystallography," *Acta Crystallographica Section A Foundations of Crystallography*, vol. 68, pp. 352–358, May 2012.

[269] S. Smeets and W. Wan, "Serial electron crystallography: Merging diffraction data through rank aggregation," *Journal of Applied Crystallography*, vol. 50, pp. 885–892, June 2017.

[270] D. Shi, B. L. Nannenga, M. J. de la Cruz, J. Liu, S. Sawtelle, G. Calero, F. E. Reyes, J. Hattne, and T. Gonen, "The collection of MicroED data for macromolecular crystallography," *Nat Protoc*, vol. 11, pp. 895–904, May 2016.

[271] E. van Genderen, M. T. B. Clabbers, P. P. Das, A. Stewart, I. Nederlof, K. C. Barentsen, Q. Portillo, N. S. Pannu, S. Nicolopoulos, T. Gruene, and J. P. Abrahams, "Ab initio structure determination of nanocrystals of organic pharmaceutical compounds by electron diffraction at room temperature using a Timepix quantum area direct electron detector," *Acta Cryst A*, vol. 72, pp. 236–242, Mar. 2016.

[272] U. Kolb, T. E. Gorelik, E. Mugnaioli, and A. Stewart, "Structural Characterization of Organics Using Manual and Automated Electron Diffraction," *Polymer Reviews*, vol. 50, pp. 385–409, July 2010.

[273] T. E. Gorelik, J. van de Streek, A. F. M. Kilbinger, G. Brunklaus, and U. Kolb, "*Ab-Initio* crystal structure analysis and refinement approaches of oligo *p* -benzamides based on electron diffraction data," *Acta Crystallographica Section B Structural Science*, vol. 68, pp. 171–181, Apr. 2012.

[274] T. Rhauderwiek, H. Zhao, P. Hirschle, M. Döblinger, B. Bueken, H. Reinsch, D. D. Vos, S. Wuttke, U. Kolb, and N. Stock, "Highly stable and porous porphyrin-based zirconium and hafnium phosphonates – electron crystallography as an important tool for structure elucidation," *Chemical Science*, vol. 9, no. 24, pp. 5467–5478, 2018.

[275] B. Wang, X. Zou, and S. Smeets, "Automated serial rotation electron diffraction combined with cluster analysis: An efficient multi-crystal workflow for structure determination," *IUCrJ*, vol. 6, pp. 854–867, Sept. 2019.

[276] M. Kluenker, M. N. Tahir, R. Dören, M. Deuker, P. Komforth, S. Plana-Ruiz, B. Barton, S. I. Shylin, V. Ksenofontov, M. Panthöfer, N. Wiesmann, J. Herzberger, A. Möller, H. Frey, J. Brieger, U. Kolb, and W. Tremel, "Iron Oxide Superparticles with Enhanced MRI Performance by Solution Phase Epitaxial Growth," *Chemistry of Materials*, vol. 30, pp. 4277–4288, July 2018.

[277] Z. Zou, W. J. E. M. Habraken, G. Matveeva, A. C. S. Jensen, L. Bertinetti, M. A. Hood, C.-y. Sun, P. U. P. A. Gilbert, I. Polishchuk, B. Pokroy, J. Mahamid, Y. Politi, S. Weiner, P. Werner, S. Bette, R. Dinnebier, U. Kolb, E. Zolotoyabko, and P. Fratzl, "A hydrated crystalline calcium carbonate phase: Calcium carbonate hemihydrate," *Science*, vol. 363, pp. 396–400, Jan. 2019.

[278] U. Ziese, A. H. Janssen, J.-L. Murk, W. J. C. Geerts, T. Van der Krift, A. Verkleij, and A. Koster, "Automated high-throughput electron tomography by pre-calibration of image shifts," *Journal of Microscopy*, vol. 205, pp. 187–200, Feb. 2002.

[279] S. Smeets, B. Wang, M. O. Cichocka, J. Ångström, and W. Wan, "Instamatic." Zenodo, Dec. 2018.

[280] S. Smeets, X. Zou, and W. Wan, "Serial electron crystallography for structure determination and phase analysis of nanocrystalline materials," *J Appl Cryst*, vol. 51, pp. 1262–1273, Oct. 2018.

[281] B. Wang, T. Rhauderwiek, A. K. Inge, H. Xu, T. Yang, Z. Huang, N. Stock, and X. Zou, "A Porous Cobalt Tetraphosphonate Metal–Organic Framework: Accurate Structure and Guest Molecule Location Determined by Continuous-Rotation Electron Diffraction," *Chemistry – A European Journal*, vol. 24, no. 66, pp. 17429–17433, 2018.

[282] C. Zhang, E. Kapaca, J. Li, Y. Liu, X. Yi, A. Zheng, X. Zou, J. Jiang, and J. Yu, "An Extra-Large-Pore Zeolite with 24x8x8-Ring Channels Using a Structure-Directing Agent Derived from Traditional Chinese Medicine," *Angewandte Chemie International Edition*, vol. 57, pp. 6486–6490, May 2018.

[283] S. Petzold, A. Zintler, R. Eilhardt, E. Piros, N. Kaiser, S. U. Sharath, T. Vogel, M. Major, K. P. McKenna, L. Molina-Luna, and L. Alff, "Forming-Free Grain Boundary Engineered Hafnium Oxide Resistive Random Access Memory Devices," *Advanced Electronic Materials*, vol. 5, no. 10, p. 1900484, 2019.

[284] S. Bhat, L. Wiehl, S. Haseen, P. Kroll, K. Glazyrin, P. Gollé-Leidreiter, U. Kolb, R. Farla, J.-C. Tseng, E. Ionescu, T. Katsura, and R. Riedel, "A Novel High-Pressure Tin Oxynitride Sn2N2O," *Chemistry – A European Journal*, vol. 26, pp. 2187–2194, Feb. 2020.

[285] A. A. Colville and K. Staudhammer, "A refinement of the structure of barite," *Mineralogical Notes*, vol. 52, p. 1877, 1967.

[286] R. J. Hill, "A further refinement of the barite structure," *The Canadian Mineralogist*, vol. 15, pp. 522–526, 1977.

[287] D. Waterman and G. Evans, "Estimation of errors in diffraction data measured by CCD area detectors," *J Appl Cryst*, vol. 43, pp. 1356–1371, Dec. 2010.

[288] C. F. Jasso-Gastinel and J. M. Kenny, eds., *Modification of Polymer Properties*. Elsevier, 2017.

[289] P. G. Lacroix, I. Malfant, G. Iftime, A. C. Razus, K. Nakatani, and J. A. Delaire, "Azo-Azulene Derivatives as Second-Order Nonlinear Optical Chromophores," *Chemistry – A European Journal*, vol. 6, no. 14, pp. 2599–2608, 2000.

[290] N. K. Nath, L. Pejov, S. M. Nichols, C. Hu, N. Saleh, B. Kahr, and P. Naumov, "Model for Photoinduced Bending of Slender Molecular Crystals," *Journal of the American Chemical Society*, vol. 136, pp. 2757–2766, Feb. 2014.

[291] M. U. Schmidt, S. Brühne, A. K. Wolf, A. Rech, J. Brüning, E. Alig, L. Fink, C. Buchsbaum, J. Glinnemann, J. van de Streek, F. Gozzo, M. Brunelli, F. Stowasser, T. Gorelik, E. Mugnaioli, and U. Kolb, "Electron diffraction, X-ray powder diffraction and pair-distribution-function analyses to determine the crystal structures of Pigment Yellow 213, C23H21N5O9," *Acta Cryst B*, vol. 65, pp. 189–199, Apr. 2009.

[292] T. Gorelik, M. U. Schmidt, J. Brüning, S. Bekő, and U. Kolb, "Using Electron Diffraction to Solve the Crystal Structure of a Laked Azo Pigment," *Crystal Growth & Design*, vol. 9, pp. 3898–3903, Sept. 2009.

[293] J. L. Teteruk, J. Glinnemann, T. E. Gorelik, A. Linden, and M. U. Schmidt, "Explanation of the stacking disorder in the β-phase of Pigment Red 170," *Acta Cryst B*, vol. 70, pp. 296–305, Apr. 2014.

[294] T. E. Gorelik, M. U. Schmidt, U. Kolb, and S. J. L. Billinge, "Total-Scattering Pair-Distribution Function of Organic Material from Powder Electron Diffraction Data," *Microscopy and Microanalysis*, vol. 21, pp. 459–471, Apr. 2015.

[295] T. E. Gorelik, C. Czech, S. M. Hammer, and M. U. Schmidt, "Crystal structure of disordered nanocrystalline α II -quinacridone determined by electron diffraction," *CrystEngComm*, vol. 18, no. 4, pp. 529–535, 2016.

[296] I. E. S. G. , "Cryoprotection in electron microscopy," *Journal of Microscopy*, vol. 141, pp. 385–391, Mar. 1986.

[297] A. L. Spek, "LEPAGE – an MS-DOS program for the determination of the metrical symmetry of a translation lattice," *J Appl Cryst*, vol. 21, pp. 578–579, Oct. 1988.

[298] D. Louër and A. Boultif, "Some further considerations in powder diffraction pattern indexing with the dichotomy method," *Powder Diffraction*, vol. 29, pp. S7–S12, Dec. 2014.

[299] G. S. Pawley, "Unit-cell refinement from powder diffraction scans," *J Appl Cryst*, vol. 14, pp. 357–361, Dec. 1981.

[300] F. Banihashemi, G. Bu, A. Thaker, D. Williams, J. Y. S. Lin, and B. L. Nannenga, "Beam-sensitive metal-organic framework structure determination by microcrystal electron diffraction," *Ultramicroscopy*, vol. 216, p. 113048, Sept. 2020.

[301] E. Mugnaioli and U. Kolb, "Structure solution of zeolites by automated electron diffraction tomography – Impact and treatment of preferential orientation," *Microporous and Mesoporous Materials*, vol. 189, pp. 107–114, May 2014.

[302] "Materials Studio, version 5." BIOVIA: San Diego, USA, 2009.

[303] A. A. Coelho, "TOPAS and TOPAS-Academic: An optimization program integrating computer algebra and crystallographic objects written in C++," *Journal of Applied Crystallography*, vol. 51, no. 1, pp. 210–218, 2018.

[304] F. H. Allen, S. Bellard, M. D. Brice, B. A. Cartwright, A. Doubleday, H. Higgs, T. Hummelink, B. G. Hummelink-Peters, O. Kennard, W. D. S. Motherwell, J. R. Rodgers, and D. G. Watson, "The Cambridge Crystallographic Data Centre: Computer-based search, retrieval, analysis and display of information," *Acta Cryst B*, vol. 35, pp. 2331–2339, Oct. 1979.

[305] S. Plana-Ruiz, Y. Krysiak, J. Portillo, E. Alig, S. Estradé, F. Peiró, and U. Kolb, "Fast-ADT: A fast and automated electron diffraction tomography setup for structure determination and refinement," *Ultramicroscopy*, vol. 211, p. 112951, Apr. 2020.

[306] C. Jose Chirayil, J. Abraham, R. Kumar Mishra, S. C. George, and S. Thomas, "Chapter 1 - Instrumental Techniques for the Characterization of Nanoparticles," in *Thermal and Rheological Measurement Techniques for Nanomaterials Characterization* (S. Thomas, R. Thomas, A. K. Zachariah, and R. K. Mishra, eds.), Micro and Nano Technologies, pp. 1–36, Elsevier, Jan. 2017.

[307] K. Fukuda and I. Maki, "Transitional Phase of Ca2SiO4 Solid Solution with Incommensurate Superstructure," *Journal of the American Ceramic Society*, vol. 72, no. 11, pp. 2204–2207, 1989.

[308] K. Morsli, Á. G. De La Torre, S. Stöber, A. J. M. Cuberos, M. Zahir, and M. A. G. Aranda, "Quantitative Phase Analysis of Laboratory-Active Belite Clinkers by Synchrotron Powder Diffraction," *Journal of the American Ceramic Society*, vol. 90, pp. 3205–3212, Oct. 2007.

[309] S. Udagawa, K. Urabe, M. Natsume, and T. Yano, "Refinement of the crystal structure of γ-Ca2SiO4," *Cement and Concrete Research*, vol. 10, pp. 139–144, Mar. 1980.

[310] D. K. Smith, A. Majumdar, and F. Ordway, "The crystal structure of γ-dicalcium silicate," *Acta Cryst*, vol. 18, pp. 787–795, Apr. 1965.

[311] C. M. Midgley, "The crystal structure of β dicalcium silicate," *Acta Crystallographica*, vol. 5, no. 3, pp. 307–312, 1952.

[312] K. H. Jost, B. Ziemer, and R. Seydel, "Redetermination of the structure of β-dicalcium silicate," *Acta Cryst B*, vol. 33, pp. 1696–1700, June 1977.

[313] M. Regourd, M. Bigaré, J. Forest, and A. Guinier, "Synthesis and crystallographic investigation of some belites," *Proceedings of the 5th International Symposium on the Chemistry of Cement*, pp. 44–48, 1968.

[314] Y. Kumashiro and E. Sakuma, "Comments on "The chemistry of dicalcium silicate mineral"," *J Mater Sci*, vol. 15, pp. 1324–1325, May 1980.

[315] A. M. Il'inets and M. Y. Bikbau, "Structural mechanism of polymorphic transitions of dicalcium silicate, Ca_2SiO_4. Part II: Refinement of crystal structure of high-temperature A_L' modification of dicalcium silicate Ca_2SiO_4," *Soviet Physics - Crystallography (English Translation)*, vol. 35, no. 1, pp. 54–56, 1990.

[316] H. Saalfeld, "X-ray investigation of single crystals of β-Ca2SiO4 (Larnite) at High Temperatures," *American Mineralogist*, vol. 60, pp. 824–827, Oct. 1975.

[317] W. G. Mumme, R. J. Hill, G. Bushnell-Wye, and E. R. Segnit, "Rietveld crystal-structure refinements, crystal-chemistry and calculated powder diffraction data for the polymorphs of dicalcium silicate and related phases," *Neues Jahrbuch fur Mineralogie - Abhandlungen*, vol. 169, no. 1, pp. 35–68, 1995.

[318] S. Udagawa, K. Urabe, and T. Yano, "Review of the 34th General Meeting," *Cement Association of Japan*, p. 37, 1980.

[319] M. A. Bredig, "Polymorphism of Calcium Orthosilicate," *Journal of the American Ceramic Society*, vol. 33, no. 6, pp. 188–192, 1950.

[320] H. Saalfeld and K. H. Klaska, "The crystal structure of 6 Ca2SiO4 · 1 Ca3(PO4)2," *Zeitschrift für Kristallographie - Crystalline Materials*, vol. 155, pp. 65–74, Oct. 1981.

[321] I. Jelenić and A. Bezjak, "Electron diffraction evidence for superstructures in A'-modification of dicalcium silicate," *Cement and Concrete Research*, vol. 12, pp. 785–788, Nov. 1982.

[322] A. G. De la Torre and M. a. G. Aranda, "Accuracy in Rietveld quantitative phase analysis of Portland cements," *J Appl Cryst*, vol. 36, pp. 1169–1176, Oct. 2003.

[323] C. Remy, F. Guyot, and M. Madon, "High pressure polymorphism of dicalcium silicate Ca2SiO4. A transmission electron microscopy study," *Physics and Chemistry of Minerals*, vol. 22, pp. 419–427, Oct. 1995.

[324] J. G. Thompson, R. L. Withers, and B. G. Hyde, "Further Consideration of Phases in the System Ba2SiO4–Ca2SiO4," *Journal of the American Ceramic Society*, vol. 70, no. 12, pp. C–383–C–386, 1987.

[325] L. Palatinus, "Dynamical refinement of modulated structures against electron diffraction data," *Acta Cryst A*, vol. 73, p. C810, 2017.

[326] T. Wagner and A. Schönleber, "A non-mathematical introduction to the superspace description of modulated structures," *Acta Cryst B*, vol. 65, pp. 249–268, June 2009.

[327] M. A. Lange, Y. Krysiak, J. Hartmann, G. Dewald, G. Cerretti, M. N. Tahir, M. Panthöfer, B. Barton, T. Reich, W. G. Zeier, M. Mondeshki, U. Kolb, and W. Tremel, "Solid State Fluorination on the Minute Scale: Synthesis of WO3-xFx with Photocatalytic Activity," *Advanced Functional Materials*, vol. 30, no. 13, p. 1909051, 2020.

[328] M. A. Nowroozi, K. Wissel, M. Donzelli, N. Hosseinpourkahvaz, S. Plana-Ruiz, U. Kolb, R. Schoch, M. Bauer, A. M. Malik, J. Rohrer, S. Ivlev, F. Kraus, and O. Clemens, "High cycle life all-solid-state fluoride ion battery with La 2 NiO 4+d high voltage cathode," *Communications Materials*, vol. 1, pp. 1–16, May 2020.

[329] S. Bette, J. Stelzner, G. Eggert, T. Schleid, G. Matveeva, U. Kolb, and R. E. Dinnebier, "Corrosion of Heritage Objects: Collagen-Like Triple Helix Found in the Calcium Acetate Hemihydrate Crystal Structure," *Angewandte Chemie International Edition*, vol. 59, no. 24, pp. 9438–9442, 2020.

[330] C. F. Macrae, I. Sovago, S. J. Cottrell, P. T. A. Galek, P. McCabe, E. Pidcock, M. Platings, G. P. Shields, J. S. Stevens, M. Towler, and P. A. Wood, "Mercury 4.0: From visualization to analysis, design and prediction," *J Appl Cryst*, vol. 53, pp. 226–235, Feb. 2020.

Appendix

1. Barite

Anisotropic DPs of the barite structure models obtained from the US4000 datasets

Crystal 1

	U11	U22	U33	U12	U13	U23
Ba1	0.0108(5)	0.0209(4)	0.0154(4)	0	−0.0005(3)	0
S1	0.0067(12)	0.0112(12)	0.0113(9)	0	0.0017(8)	0
O1	0.019(3)	0.039(3)	0.027(2)	0	0.0148(17)	0
O2	0.021(2)	0.023(2)	0.0108(16)	0	−0.0069(15)	0
O3	0.0189(17)	0.0123(13)	0.0194(12)	0.0000(11)	0.0008(11)	−0.0036(10)

Crystal 2

	U11	U22	U33	U12	U13	U23
Ba1	0.0115(8)	0.0167(3)	0.0125(3)	0	0.0013(4)	0
S1	0.006(2)	0.0078(8)	0.0086(8)	0	0.0017(10)	0
O1	0.030(6)	0.027(2)	0.032(2)	0	−0.018(3)	0
O2	0.018(4)	0.0190(15)	0.0134(15)	0	−0.0081(19)	0
O3	0.013(3)	0.0131(10)	0.0148(10)	−0.0034(13)	−0.0003(12)	−0.0020(7)

Crystal 3

	U11	U22	U33	U12	U13	U23
Ba1	0.0150(12)	0.0184(6)	0.0170(5)	0	−0.0003(6)	0
S1	0.012(3)	0.0089(14)	0.0128(12)	0	0.0032(15)	0
O1	0.038(8)	0.025(3)	0.034(3)	0	0.013(4)	0
O2	0.019(6)	0.019(2)	0.012(2)	0	−0.004(3)	0
O3	0.016(4)	0.0150(18)	0.0124(14)	0.0038(17)	0.0019(17)	0.0030(12)

Anisotropic DPs of the barite structure models obtained from the Stingray F-145B and full-background subtracted datasets

Crystal 1

	U11	U22	U33	U12	U13	U23
Ba1	0.0313(7)	0.0517(5)	0.0369(5)	0	−0.0032(4)	0
S1	0.038(2)	0.0246(11)	0.0415(14)	0	0.0087(14)	0
O1	0.056(5)	0.115(4)	0.029(3)	0	0.016(2)	0
O2	0.041(3)	0.0311(16)	0.016(2)	0	−0.0186(15)	0
O3	0.063(3)	0.0351(15)	0.0356(17)	0.0012(14)	−0.0008(16)	0.0097(10)

Crystal 2

	U11	U22	U33	U12	U13	U23
Ba1	0.0334(9)	0.0335(4)	0.0267(4)	0	0.0040(4)	0
S1	0.017(2)	0.0174(8)	0.0249(9)	0	0.0000(10)	0
O1	0.029(5)	0.063(3)	0.033(2)	0	−0.0150(19)	0
O2	0.037(4)	0.0196(14)	0.0243(17)	0	−0.025(2)	0
O3	0.052(3)	0.0231(11)	0.0327(12)	−0.0031(15)	−0.0056(15)	−0.0050(8)

Crystal 3

	U11	U22	U33	U12	U13	U23
Ba1	0.0407(11)	0.0359(4)	0.0335(4)	0	−0.0029(5)	0
S1	0.028(3)	0.0153(9)	0.0256(9)	0	0.0080(11)	0
O1	0.057(7)	0.061(3)	0.047(2)	0	0.002(3)	0
O2	0.034(4)	0.0297(16)	0.0167(15)	0	0.0184(19)	0
O3	0.059(4)	0.0235(12)	0.0364(11)	−0.0017(13)	−0.0015(16)	0.0062(9)

Anisotropic DPs of the barite structure models obtained from the Stingray F-145B and mean-background subtracted datasets

Crystal 1

	U11	U22	U33	U12	U13	U23
Ba1	−0.0015(5)	0.0074(4)	0.0015(3)	0	0.0020(3)	0
O1	0.020(4)	0.036(3)	0.051(4)	0	0.029(3)	0
O2	0.036(4)	0.026(2)	0.016(3)	0	0.001(2)	0
O3	0.004(2)	0.0059(12)	0.0027(15)	−0.0008(11)	−0.0032(11)	−0.0003(10)

Crystal 2

	U11	U22	U33	U12	U13	U23
Ba1	0.0086(7)	0.0044(3)	0.0007(3)	0	−0.0003(4)	0
O1	0.052(7)	0.017(2)	0.037(3)	0	−0.002(3)	0
O2	0.003(4)	0.0170(18)	0.021(2)	0	−0.004(2)	0
O3	0.025(3)	0.0050(11)	0.0026(10)	−0.0002(14)	0.0091(13)	0.0008(7)

Crystal 3

	U11	U22	U33	U12	U13	U23
Ba1	0.0065(8)	0.0016(3)	−0.0011(3)	0	0.0022(4)	0
O1	−0.001(5)	0.037(3)	0.013(2)	0	0.005(2)	0
O2	0.031(6)	0.027(2)	0.0073(19)	0	0.000(2)	0
O3	0.014(3)	−0.0045(11)	−0.0019(10)	−0.0005(12)	−0.0047(12)	0.0017(8)

Comparison of the atomic positions obtained from the dynamical refined structures and the model reported by Jacobsen et al. [21]

		Atomic Position Differences (pm)				
		Ba	*S*	*O1*	*O2*	*O3*
US4000	*Crystal 1*	0.3(1)	0.8(3)	0.6(6)	0.9 (6)	1.3(5)
	Crystal 2	0.2(2)	1.0(4)	**2.9(9)**	1.2(7)	1.6(6)
	Crystal 3	0.6(2)	0.5(5)	2.3(11)	1.2(9)	2.0(7)
F-145B / Full-Bckg	*Crystal 1*	1.9(1)	4.3(4)	3.2(8)	4.3(5)	5.0(6)
	Crystal 2	1.0(2)	1.5(3)	**6.4(8)**	1.9(6)	3.8(5)
	Crystal 3	0.9(2)	3.2(4)	6.2(9)	3.3(6)	6.1(6)
US4000 / Mean-Bckg	*Crystal 1*	1.4(1)	1.7(3)	3.9(8)	6.9(8)	2.9(5)
	Crystal 2	0.2(1)	3.6(3)	**7.5(9)**	5.4(7)	3.8(5)
	Crystal 3	0.5(2)	3.6(4)	6.1(8)	7.4(8)	6.5(5)

2. π-Ferrosilicide

CIF file of the structure model of the correct enantiomorph from the dynamical refinement

```
_chemical_formula_sum                    'Fe16 Si4'
_chemical_formula_weight                 1005.9
_symmetry_cell_setting                   cubic
_symmetry_space_group_name_H-M           'P 21 3'
_symmetry_space_group_name_Hall          'P 2ac;2ab;3'
_symmetry_Int_Tables_number              198

loop_
_space_group_symop_id
_space_group_symop_operation_xyz
1    x,y,z
2    -x+1/2,-y,z+1/2
3    -x,y+1/2,-z+1/2
4    x+1/2,-y+1/2,-z
5    z,x,y
6    z+1/2,-x+1/2,-y
7    -z+1/2,-x,y+1/2
8    -z,x+1/2,-y+1/2
9    y,z,x
10   -y,z+1/2,-x+1/2
11   y+1/2,-z+1/2,-x
12   -y+1/2,-z,x+1/2

_cell_length_a                           6.1669
_cell_length_b                           6.1669
_cell_length_c                           6.1669
_cell_angle_alpha                        90
_cell_angle_beta                         90
_cell_angle_gamma                        90
_cell_volume                             234.5313
_cell_formula_units_Z                    1
_exptl_crystal_density_diffrn            7.122

loop_
_atom_type_symbol
_atom_type_scat_source
Fe   International_Tables_Vol_C
Si   International_Tables_Vol_C

loop_
_atom_site_label
_atom_site_type_symbol
_atom_site_fract_x
_atom_site_fract_y
_atom_site_fract_z
_atom_site_adp_type
_atom_site_U_iso_or_equiv
_atom_site_site_symmetry_multiplicity
_atom_site_occupancy
```

```
Fe1 Fe 0.43705(10) 0.93705(10) 0.56295(10) Uani 0.00523(19) 4 0.891(14)
Fe1_s1 Si 0.43705(10) 0.93705(10) 0.56295(10) Uani 0.00523(19) 4 0.109(14)
Fe2 Fe 0.45305(11) 1.12660(12) 0.20293(11) Uani 0.0178(2) 12 1
Si1 Si 0.68719(17) 0.68719(17) 0.68719(17) Uani 0.0087(4) 4 0.913(15)
Si1_fe1 Fe 0.68719(17) 0.68719(17) 0.68719(17) Uani 0.0087(4) 4 0.087(15)

loop_
_atom_site_aniso_label
_atom_site_aniso_type_symbol
_atom_site_aniso_U_11
_atom_site_aniso_U_22
_atom_site_aniso_U_33
_atom_site_aniso_U_12
_atom_site_aniso_U_13
_atom_site_aniso_U_23
Fe1 Fe 0.0052(3) 0.0052(3) 0.0052(3) 0.0001(2) −0.0001(2) −0.0001(2)
Fe1_s1 Si 0.0052(3) 0.0052(3) 0.0052(3) 0.0001(2) −0.0001(2) −0.0001(2)
Fe2 Fe 0.0111(4) 0.0298(4) 0.0124(4) −0.0061(3) −0.0027(3) 0.0085(3)
Si1 Si 0.0087(7) 0.0087(7) 0.0087(7) 0.0006(4) 0.0006(4) 0.0006(4)
Si1_fe1 Fe 0.0087(7) 0.0087(7) 0.0087(7) 0.0006(4) 0.0006(4) 0.0006(4)
```

3. Disperse Red 1

Acquisition parameters, unit cell parameters from *eADT* and reflections information from *Sir2014* for the six acquired datasets

	Room Temperature			**Liquid N_2 Temperature**		
Ref. Crystal Number:	1	2	3	4	5	6
Tilt Range (°)	-60/60	-60/60	-60/60	-60/60	-60/60	-50/50
Acq. Patterns (#)	121	121	121	121	121	101
CCD Exposure Time (s)	2	4	4	4	4	4
a (Å)	7.93(1)	7.87(1)	7.98(1)	7.79(1)	7.74(1)	7.71(1)
b (Å)	11.26(3)	11.31(3)	11.30(3)	11.13(3)	11.07(3)	11.15(3)
c (Å)	19.67(9)	19.72(9)	19.86(9)	19.97(9)	19.71(9)	19.53(9)
α (°)	73.6(4)	74.6(4)	72.4(4)	74.3(4)	74.5(4)	74.7(4)
β (°)	84.5(5)	83.9(5)	84.6(5)	82.2(5)	82.9(5)	84.4(5)
γ (°)	70.1(4)	69.7(4)	69.7(4)	71.3(4)	71.0(4)	70.8(4)
Ω (Å^3)	1584(20)	1587(20)	1600(20)	1577(20)	1538(20)	1529(20)
Num. of Reflections (#)	10743	10284	5979	10203	9978	6221
Ind. Refl. at 0.8 Å (#)	4195	4150	3508	4180	4139	3090
Completeness (%)	67.4	66.7	56.4	67.1	66.5	49.6
R_{int} (%)	21.6	18.6	17.5	20.0	22.3	12.9

All datasets were acquired with 1 m of camera length except crystal 3 where 1.2 m was used. R_{int} is based on structure factors. The used diffraction data resolution filters the number of reflections that are used for the subsequent parameters of the table. "Ref." stands for reference and "Refl." for reflections. All datasets include the a and b axes but only the data from crystal 3 covers the c-axis as well.

Projections of the ODS reconstructions along the main axes obtained from *eADT*

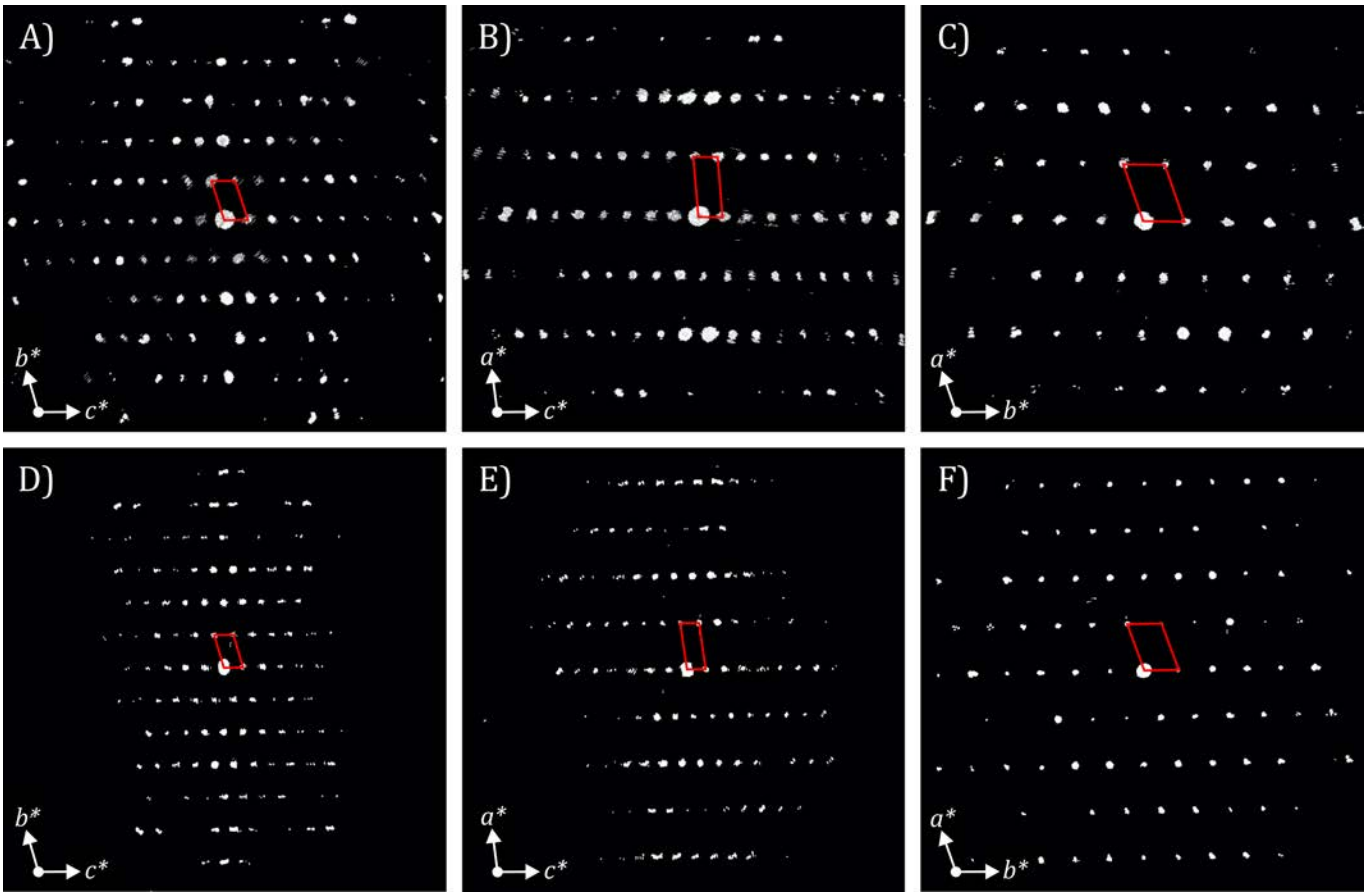

Upper figures correspond to crystal 3 at RT and lower figures to crystal 4 at LT. The red rhomboids are projections of the unit cell.

Comparison of the experimental XRPD pattern with the simulated patterns according to the best structure solutions of simulated annealing and direct methods from *Sir2014*

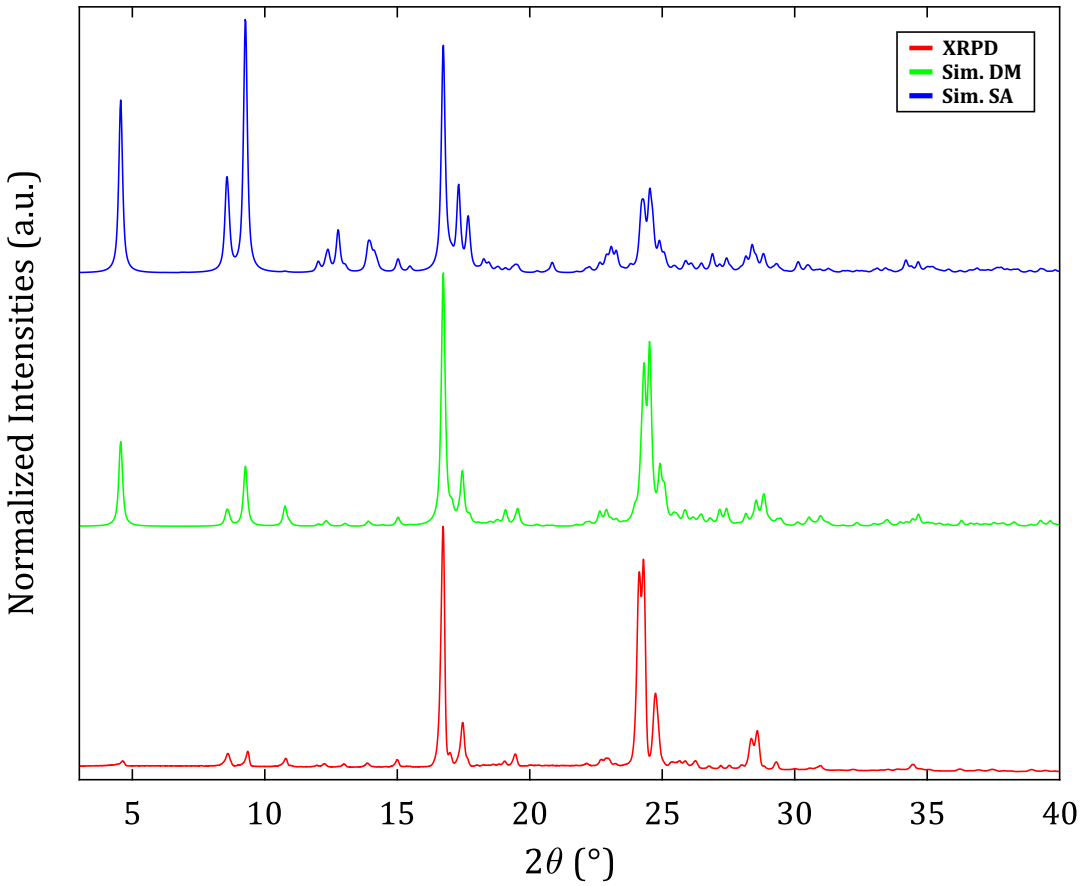

Diffraction patterns simulated with *Mercury* [330].

Averaged rocking-curves of the strongest reflections at different diffraction data resolutions intervals fitted by the precession-dependent double-peaked profile from *PETS2*

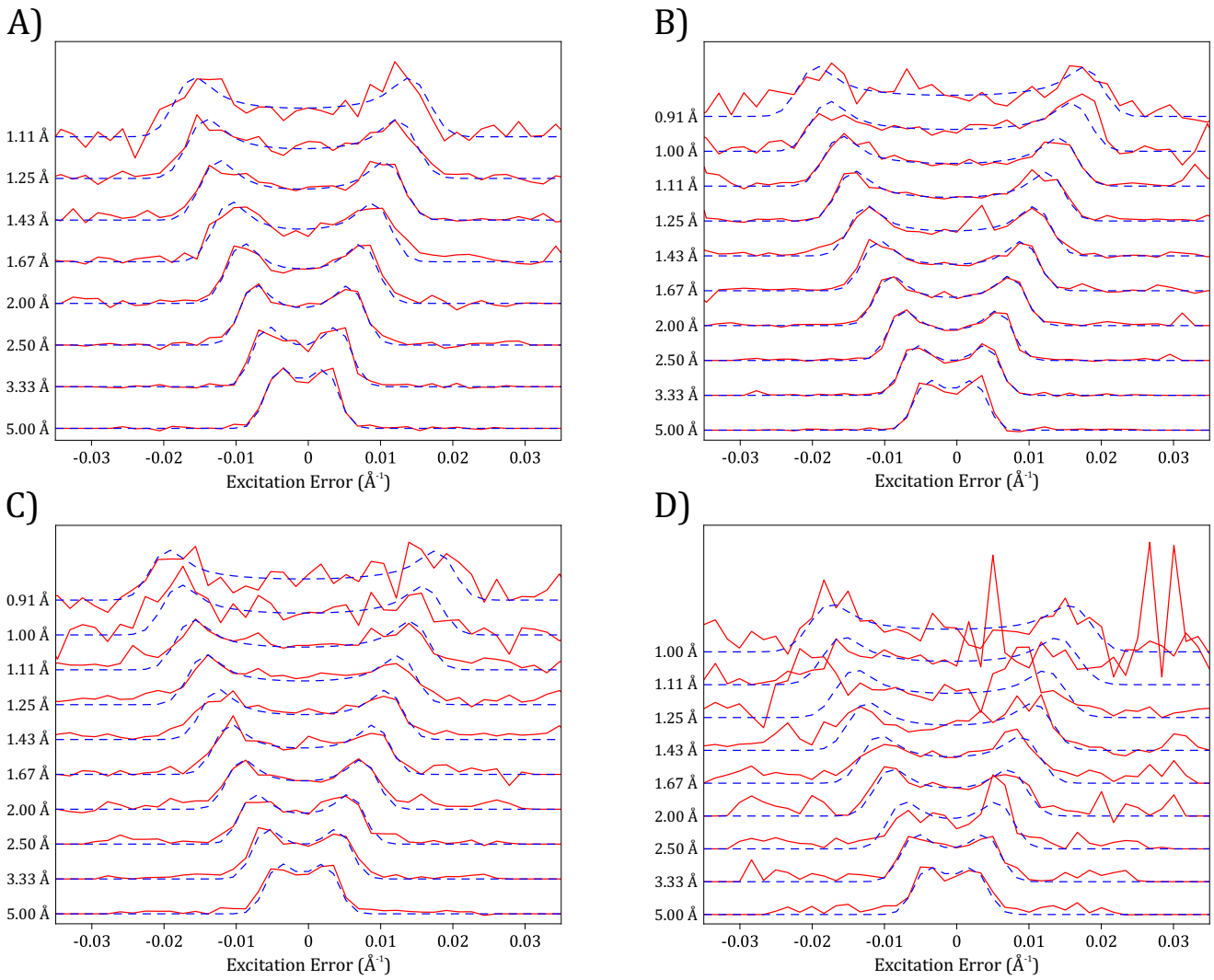

A) corresponds to crystal 3, B) to crystal 4, C) to crystal 5, and D) to crystal 6.

Herringbone-like packing of the structure

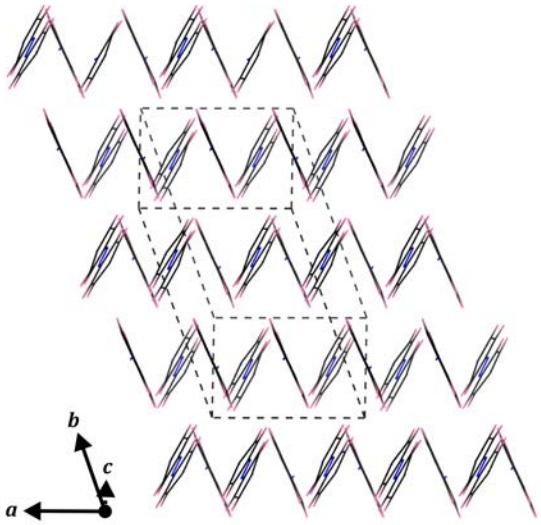

Projection of the azobenzene groups of DRED1 approximately along the *c*-axis. End-groups are removed for better visualization.

Projections of the crystal structure from the dynamical refined model reported in this work and the one reported by Lacroix et al. [289]

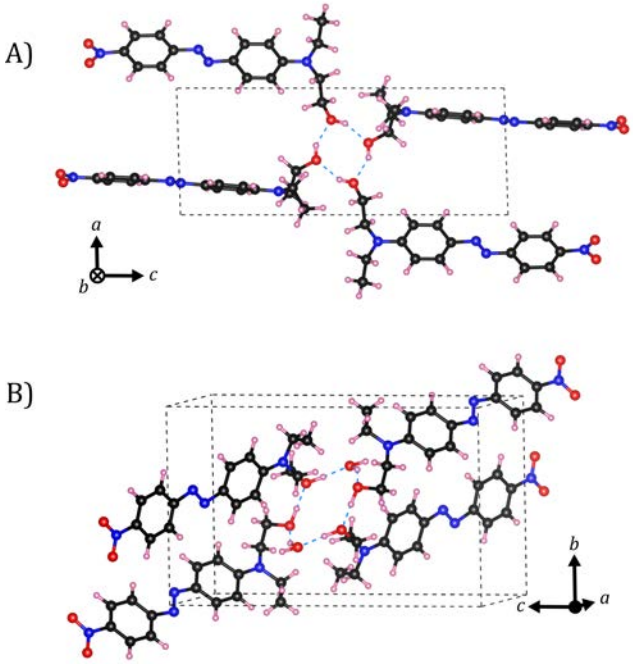

Pink atoms correspond to hydrogen, black ones to carbon, blue ones to nitrogen and red ones to oxygen. The dashed blue lines represent the hydrogen bonds. Only the molecules that are related to the shown network are displayed for better visualization.

CIF file of the structure model from the Rietveld refinement

```
_chemical_formula_sum                    'C64 H72 N16 O12'
_chemical_formula_weight                 1257.4
_symmetry_cell_setting                   triclinic
_symmetry_space_group_name_H-M           'P -1'
_symmetry_space_group_name_Hall          '-P 1'
_symmetry_Int_Tables_number              2

loop_
_space_group_symop_id
_space_group_symop_operation_xyz
1    x,y,z
2    -x,-y,-z

_cell_length_a                           7.7217(2)
_cell_length_b                           11.1397(4)
_cell_length_c                           19.5753(8)
_cell_angle_alpha                        73.800(3)
_cell_angle_beta                         83.040(4)
_cell_angle_gamma                        70.4982(13)
_cell_volume                             1523.47(9)
_cell_formula_units_Z                    1
_exptl_crystal_density_diffrn            1.3705

loop_
_atom_type_symbol
_atom_type_scat_dispersion_real
_atom_type_scat_dispersion_imag
_atom_type_scat_source
C    0.0033   0.0016
'International Tables Vol C tables 4.2.6.8 and 6.1.1.1'
H    0.0000   0.0000
'International Tables Vol C tables 4.2.6.8 and 6.1.1.1'
N    0.0061   0.0033
'International Tables Vol C tables 4.2.6.8 and 6.1.1.1'
O    0.0106   0.0060
'International Tables Vol C tables 4.2.6.8 and 6.1.1.1'

loop_
_atom_site_label
_atom_site_type_symbol
_atom_site_fract_x
_atom_site_fract_y
_atom_site_fract_z
_atom_site_adp_type
_atom_site_U_iso_or_equiv
C1a C 0.2100(15) 1.1090(8) 0.3477(3) Uiso 0.0146
C2a C 0.0849(14) 1.1984(8) 0.3838(3) Uiso 0.0146
C3a C 0.0751(12) 1.1578(8) 0.4607(3) Uiso 0.0146
C4a C 0.1991(11) 1.0440(7) 0.4967(3) Uiso 0.0146
C5a C 0.3251(12) 0.9563(7) 0.4608(3) Uiso 0.0146
C6a C 0.3185(14) 0.9865(8) 0.3858(3) Uiso 0.0146
N1a N 0.1868(7) 1.0189(3) 0.5728(4) Uiso 0.0172
N2a N 0.3048(7) 0.9105(5) 0.6016(4) Uiso 0.0172
C7a C 0.2948(10) 0.8846(7) 0.6780(3) Uiso 0.0146
C8a C 0.1623(12) 0.9718(8) 0.7173(3) Uiso 0.0146
C9a C 0.1550(13) 0.9381(8) 0.7891(3) Uiso 0.0146
C10a C 0.2756(13) 0.8196(9) 0.8270(3) Uiso 0.0146
C11a C 0.4138(12) 0.7408(8) 0.7887(3) Uiso 0.0146
C12a C 0.4175(12) 0.7732(8) 0.7130(3) Uiso 0.0146
N3a N 0.2061(18) 1.1344(8) 0.2722(4) Uiso 0.0172
N4a N 0.2849(10) 0.7960(8) 0.9017(3) Uiso 0.0172
O1a O 0.3052(15) 1.0505(9) 0.2390(5) Uiso 0.024
O2a O 0.1329(16) 1.2512(9) 0.2368(5) Uiso 0.024
C13a C 0.1478(9) 0.8674(6) 0.9419(3) Uiso 0.0146
C14a C -0.0286(9) 0.8408(5) 0.9521(3) Uiso 0.0146
C15a C 0.4234(8) 0.6881(6) 0.9392(3) Uiso 0.0146
C16a C 0.6126(7) 0.7040(5) 0.9343(3) Uiso 0.0146
```

```
O3a O 0.7469(11) 0.5885(7) 0.9621(4) Uiso 0.024
H1a H −0.002(3) 1.276(2) 0.3578(12) Uiso 0.0175
H2a H −0.008(4) 1.211(3) 0.4884(15) Uiso 0.0175
H3a H 0.410(3) 0.879(2) 0.4862(14) Uiso 0.0175
H4a H 0.407(4) 0.932(2) 0.3589(12) Uiso 0.0175
H5a H 0.074(4) 1.051(2) 0.6944(13) Uiso 0.0175
H6a H 0.074(4) 0.998(2) 0.8129(12) Uiso 0.0175
H7a H 0.498(4) 0.663(2) 0.8147(12) Uiso 0.0175
H8a H 0.502(4) 0.717(2) 0.6859(13) Uiso 0.0175
H9a H 0.810(3) 0.582(2) 1.0075(15) Uiso 0.0175
H10a H −0.101(3) 0.877(2) 0.9085(12) Uiso 0.0175
H11a H −0.008(4) 0.743(2) 0.9699(17) Uiso 0.0175
H12a H −0.093(4) 0.884(2) 0.9892(14) Uiso 0.0175
H13a H 0.189(4) 0.847(2) 0.9896(15) Uiso 0.0175
H14a H 0.127(4) 0.960(2) 0.9203(13) Uiso 0.0175
H15a H 0.383(3) 0.6706(19) 0.9889(14) Uiso 0.0175
H16a H 0.434(4) 0.612(2) 0.9213(13) Uiso 0.0175
H17a H 0.645(3) 0.7348(19) 0.8840(11) Uiso 0.0175
H18a H 0.610(3) 0.771(2) 0.9600(16) Uiso 0.0175
C1b C 0.2005(14) 0.6483(7) 0.2513(3) Uiso 0.0146
C2b C 0.2233(14) 0.7454(6) 0.2791(3) Uiso 0.0146
C3b C 0.2344(12) 0.7128(6) 0.3535(3) Uiso 0.0146
C4b C 0.2312(11) 0.5897(6) 0.3947(3) Uiso 0.0146
C5b C 0.2063(12) 0.4951(6) 0.3669(3) Uiso 0.0146
C6b C 0.1924(13) 0.5242(6) 0.2960(3) Uiso 0.0146
N1b N 0.2502(7) 0.5635(7) 0.4693(4) Uiso 0.0172
N2b N 0.2464(5) 0.4506(7) 0.5027(4) Uiso 0.0172
C7b C 0.2682(11) 0.4194(6) 0.5806(3) Uiso 0.0146
C8b C 0.2906(12) 0.5131(6) 0.6117(3) Uiso 0.0146
C9b C 0.3041(13) 0.4837(6) 0.6856(3) Uiso 0.0146
C10b C 0.3025(14) 0.3563(6) 0.7283(3) Uiso 0.0146
C11b C 0.2765(14) 0.2655(6) 0.6962(3) Uiso 0.0146
C12b C 0.2652(13) 0.2984(6) 0.6223(3) Uiso 0.0146
N3b N 0.2031(18) 0.6692(7) 0.1755(3) Uiso 0.0172
N4b N 0.3125(11) 0.3235(6) 0.8022(3) Uiso 0.0172
O1b O 0.2390(15) 0.5839(8) 0.1437(5) Uiso 0.024
O2b O 0.1694(15) 0.7855(8) 0.1367(5) Uiso 0.024
C13b C 0.2916(8) 0.2027(6) 0.8418(3) Uiso 0.0146
C14b C 0.4544(7) 0.0992(5) 0.8838(3) Uiso 0.0146
C15b C 0.3365(7) 0.4119(6) 0.8364(3) Uiso 0.0146
C16b C 0.1668(7) 0.5117(5) 0.8525(3) Uiso 0.0146
O3b O 0.0630(10) 0.4507(7) 0.9080(4) Uiso 0.024
H1b H 0.212(3) 0.834(3) 0.2504(14) Uiso 0.0175
H2b H 0.245(4) 0.774(2) 0.3762(12) Uiso 0.0175
H3b H 0.208(4) 0.411(2) 0.3951(12) Uiso 0.0175
H4b H 0.182(4) 0.457(2) 0.2757(13) Uiso 0.0175
H5b H 0.286(4) 0.599(2) 0.5837(13) Uiso 0.0175
H6b H 0.310(4) 0.553(2) 0.7065(13) Uiso 0.0175
H7b H 0.279(4) 0.180(2) 0.7240(13) Uiso 0.0175
H8b H 0.253(3) 0.239(2) 0.5991(11) Uiso 0.0175
H9b H −0.057(4) 0.510(3) 0.9254(13) Uiso 0.0175
H10b H 0.419(4) 0.027(3) 0.9135(13) Uiso 0.0175
H11b H 0.555(3) 0.065(2) 0.8522(11) Uiso 0.0175
H12b H 0.495(4) 0.140(2) 0.9140(12) Uiso 0.0175
H13b H 0.262(4) 0.166(2) 0.8061(13) Uiso 0.0175
H14b H 0.188(3) 0.2203(19) 0.8752(12) Uiso 0.0175
H15b H 0.416(4) 0.456(2) 0.8067(12) Uiso 0.0175
H16b H 0.396(4) 0.362(2) 0.8808(12) Uiso 0.0175
H17b H 0.194(4) 0.582(2) 0.8668(12) Uiso 0.0175
H18b H 0.096(3) 0.553(2) 0.8091(12) Uiso 0.0175
```

CIF file of the structure model from the dynamical refinement

```
_chemical_formula_sum                    'C64 H72 N16 O12'
_chemical_formula_weight                 1257.4
_symmetry_cell_setting                   triclinic
_symmetry_space_group_name_H-M           'P -1'
_symmetry_space_group_name_Hall          '-P 1'
_symmetry_Int_Tables_number              2

loop_
_space_group_symop_id
_space_group_symop_operation_xyz
1    x,y,z
2    -x,-y,-z

_cell_length_a                           7.7217
_cell_length_b                           11.1397
_cell_length_c                           19.5753
_cell_angle_alpha                        73.8
_cell_angle_beta                         83.04
_cell_angle_gamma                        70.498
_cell_volume                             1523.462
_cell_formula_units_Z                    1
_exptl_crystal_density_diffrn            1.3705

loop_
_atom_type_symbol
_atom_type_scat_source
C    International_Tables_Vol_C
H    International_Tables_Vol_C
N    International_Tables_Vol_C
O    International_Tables_Vol_C

loop_
_atom_site_label
_atom_site_type_symbol
_atom_site_fract_x
_atom_site_fract_y
_atom_site_fract_z
_atom_site_adp_type
_atom_site_U_iso_or_equiv
_atom_site_site_symmetry_multiplicity
_atom_site_occupancy
C1a C 0.2097(6) 0.1066(4) 0.3439(3) Uiso 0.0093(3) 2 1
C2a C 0.0883(6) 0.1938(5) 0.3778(4) Uiso 0.0093(3) 2 1
C3a C 0.0820(6) 0.1652(5) 0.4541(4) Uiso 0.0093(3) 2 1
C4a C 0.1999(6) 0.0488(5) 0.4939(4) Uiso 0.0093(3) 2 1
C5a C 0.3282(8) 0.9566(5) 0.4553(4) Uiso 0.0093(3) 2 1
C6a C 0.3293(8) 0.9886(5) 0.3841(4) Uiso 0.0093(3) 2 1
N1a N 0.1958(6) 0.0176(5) 0.5703(4) Uiso 0.0094(9) 2 1
N2a N 0.2932(6) 0.9134(5) 0.6001(4) Uiso 0.0094(9) 2 1
C7a C 0.2820(5) 0.8906(4) 0.6768(3) Uiso 0.0093(3) 2 1
C8a C 0.1516(6) 0.9703(4) 0.7121(4) Uiso 0.0093(3) 2 1
C9a C 0.1526(6) 0.9393(5) 0.7870(4) Uiso 0.0093(3) 2 1
C10a C 0.2891(5) 0.8249(4) 0.8265(3) Uiso 0.0093(3) 2 1
C11a C 0.4208(6) 0.7447(4) 0.7900(4) Uiso 0.0093(3) 2 1
C12a C 0.4180(6) 0.7765(5) 0.7161(4) Uiso 0.0093(3) 2 1
N3a N 0.2250(7) 0.1262(5) 0.2706(4) Uiso 0.0093(3) 2 1
N4a N 0.2898(5) 0.7948(4) 0.8998(4) Uiso 0.0093 2 1
O1a O 0.3015(8) 0.0485(6) 0.2366(5) Uiso 0.0209(9) 2 1
O2a O 0.1486(8) 0.2407(6) 0.2353(5) Uiso 0.0209(9) 2 1
C13a C 0.1471(7) 0.8707(5) 0.9367(4) Uiso 0.0219(7) 2 1
C14a C 0.9710(7) 0.8370(6) 0.9500(5) Uiso 0.0219(7) 2 1
C15a C 0.4254(7) 0.6830(5) 0.9378(4) Uiso 0.0219(7) 2 1
C16a C 0.6120(7) 0.6996(5) 0.9426(5) Uiso 0.0219(7) 2 1
O3a O 0.7507(7) 0.5807(6) 0.9689(6) Uiso 0.0170(17) 2 1
H1a H -0.004116 0.28526 0.346963 Uiso 0.0186 2 1
H2a H -0.015395 0.234939 0.480993 Uiso 0.0186 2 1
H3a H 0.421207 0.863575 0.484466 Uiso 0.0186 2 1
```

```
H4a H 0.426289 0.920635 0.356066 Uiso 0.0186 2 1
H5a H 0.047905 1.056997 0.682779 Uiso 0.0186 2 1
H6a H 0.048695 1.002673 0.815504 Uiso 0.0186 2 1
H7a H 0.525232 0.657858 0.818811 Uiso 0.0186 2 1
H8a H 0.521432 0.713374 0.687319 Uiso 0.0186 2 1
H9a H 0.778(4) 0.577(2) 1.0111(11) Uiso 0.0255 2 1
H10a H 0.937986 0.81671 0.902057 Uiso 0.0439 2 1
H11a H 0.986976 0.749343 0.99492 Uiso 0.0439 2 1
H12a H 0.859143 0.92034 0.962591 Uiso 0.0439 2 1
H13a H 0.197336 0.867995 0.987508 Uiso 0.0439 2 1
H14a H 0.117855 0.975641 0.909204 Uiso 0.0439 2 1
H15a H 0.371414 0.648143 0.991692 Uiso 0.0439 2 1
H16a H 0.444805 0.599289 0.915112 Uiso 0.0439 2 1
H17a H 0.655098 0.749945 0.889859 Uiso 0.0439 2 1
H18a H 0.597447 0.766975 0.976253 Uiso 0.0439 2 1
C1b C 0.2106(3) 0.6437(4) 0.2487(3) Uiso 0.0093(3) 2 1
C2b C 0.2273(4) 0.7358(4) 0.2810(4) Uiso 0.0093(3) 2 1
C3b C 0.2346(4) 0.7072(5) 0.3526(4) Uiso 0.0093(3) 2 1
C4b C 0.2257(3) 0.5855(4) 0.3953(3) Uiso 0.0093(3) 2 1
C5b C 0.2087(4) 0.4899(5) 0.3638(4) Uiso 0.0093(3) 2 1
C6b C 0.2010(4) 0.5211(5) 0.2889(4) Uiso 0.0093(3) 2 1
N1b N 0.2346(5) 0.5618(5) 0.4718(4) Uiso 0.0094(9) 2 1
N2b N 0.2490(5) 0.4515(5) 0.5038(4) Uiso 0.0094(9) 2 1
C7b C 0.2660(3) 0.4218(4) 0.5797(3) Uiso 0.0093(3) 2 1
C8b C 0.2879(4) 0.5135(5) 0.6145(4) Uiso 0.0093(3) 2 1
C9b C 0.3036(4) 0.4802(5) 0.6876(4) Uiso 0.0093(3) 2 1
C10b C 0.2987(3) 0.3552(4) 0.7295(3) Uiso 0.0093(3) 2 1
C11b C 0.2766(4) 0.2625(5) 0.6944(4) Uiso 0.0093(3) 2 1
C12b C 0.2610(4) 0.2986(5) 0.6204(4) Uiso 0.0093(3) 2 1
N3b N 0.2032(5) 0.6737(5) 0.1758(4) Uiso 0.0093 2 1
N4b N 0.3143(5) 0.3230(4) 0.8016(3) Uiso 0.0093 2 1
O1b O 0.2441(8) 0.5857(6) 0.1448(5) Uiso 0.0209(9) 2 1
O2b O 0.1767(8) 0.7854(6) 0.1378(5) Uiso 0.0209(9) 2 1
C13b C 0.2873(7) 0.2057(5) 0.8447(4) Uiso 0.0219(7) 2 1
C14b C 0.4534(7) 0.1015(5) 0.8783(5) Uiso 0.0219(7) 2 1
C15b C 0.3286(7) 0.4171(5) 0.8352(4) Uiso 0.0219(7) 2 1
C16b C 0.1531(8) 0.5091(5) 0.8568(5) Uiso 0.0219(7) 2 1
O3b O 0.0680(8) 0.4477(6) 0.9196(5) Uiso 0.0196(18) 2 1
H1b H 0.234497 0.831012 0.248493 Uiso 0.0186 2 1
H2b H 0.247514 0.779948 0.377408 Uiso 0.0186 2 1
H3b H 0.20171 0.394746 0.396586 Uiso 0.0186 2 1
H4b H 0.187733 0.450076 0.262803 Uiso 0.0186 2 1
H5b H 0.292065 0.610081 0.582981 Uiso 0.0186 2 1
H6b H 0.319806 0.550996 0.713159 Uiso 0.0186 2 1
H7b H 0.272094 0.165626 0.725333 Uiso 0.0186 2 1
H8b H 0.244598 0.228938 0.59416 Uiso 0.0186 2 1
H9b H −0.0474(19) 0.487(2) 0.9201(15) Uiso 0.0294 2 1
H10b H 0.46095 0.006987 0.868977 Uiso 0.0439 2 1
H11b H 0.576868 0.127817 0.854917 Uiso 0.0439 2 1
H12b H 0.445379 0.092714 0.935914 Uiso 0.0439 2 1
H13b H 0.221304 0.165138 0.813833 Uiso 0.0439 2 1
H14b H 0.181134 0.228947 0.886128 Uiso 0.0439 2 1
H15b H 0.413135 0.474268 0.801255 Uiso 0.0439 2 1
H16b H 0.416341 0.366183 0.88156 Uiso 0.0439 2 1
H17b H 0.180137 0.594555 0.86546 Uiso 0.0439 2 1
H18b H 0.056933 0.548559 0.812828 Uiso 0.0439 2 1
```

Geometrical restraints applied in *Jana2006* for the dynamical refinement

```
restric C1a 12 C2a C3a C4a C5a C6a C7a C8a C9a C10a C11a C12a C1b C2b C3b C4b C5b C6b C7b C8b C9b
C10b C11b C12b
restric N1a 12 N2a N1b N2b
restric O1a 12 O2a O1b O2b
restric C13a 12 C14a C15a C16a C13b C14b C15b C16b
restric N3a 12 N4a N3b N4b
restric C1a 12 N3a

distfix 1.392 0.010 C1a c2a; c2a C3a; C3a c4a; c4a C5a#t0,-1,0; c5a c6a; c6a C1a#t0,1,0;
distfix 1.392 0.010 c7a c8a; c8a c9a; c9a c10a; c10a c11a; c11a c12a; c12a c7a;
distfix 1.230 0.010 n3a o1a; n3a o2a;
distfix 1.442 0.010 C1a n3a; c4a n1a;
distfix 1.402 0.010 n4a c13a; n4a c15a;
distfix 1.500 0.010 c13a C14a#t-1,0,0; c15a c16a;
distfix 1.253 0.010 n1a N2a#t0,-1,0;
distfix 1.420 0.010 n2a c7a;
distfix 1.368 0.010 c10a n4a;
distfix 1.424 0.010 c16a O3a;
distfix 1.392 0.010 c1b c2b; c2b c3b; c3b c4b; c4b c5b; c5b c6b; c6b c1b;
distfix 1.392 0.010 c7b c8b; c8b c9b; c9b c10b; c10b c11b; c11b c12b; c12b c7b;
distfix 1.230 0.010 n3b o1b; n3b o2b;
distfix 1.442 0.010 c1b n3b; c4b n1b;
distfix 1.402 0.010 n4b c13b; n4b c15b;
distfix 1.500 0.010 c13b c14b; c15b c16b;
distfix 1.253 0.010 n1b n2b;
distfix 1.420 0.010 n2b c7b;
distfix 1.368 0.010 c10b n4b;
distfix 1.424 0.010 c16b o3b;
distfix 0.856 0.010 H9b O3b;
distfix 0.856 0.010 H9a O3a;

anglefix 120 0.5 c2a C1a n3a; c6a C1a n3a; C6a#t0,-1,0 C1a c2a; C1a c2a C3a;
anglefix 120 0.5 c2a C3a c4a; C3a c4a C5a#t0,-1,0; c4a c5a c6a; c5a c6a C1a;
anglefix 120 0.5 C3a c4a n1a; c5a c4a n1a; c8a c7a n2a; c12a c7a n2a;
anglefix 120 0.5 c12a c7a c8a; c7a c8a c9a; c8a c9a c10a; c9a c10a c11a;
anglefix 120 0.5 c10a c11a c12a; c11a c12a c7a; c9a c10a n4a; c11a c10a n4a;
anglefix 120 0.5 c10a n4a c13a; c10a n4a c15a; c13a n4a c15a; n4a c13a C14a#t-1,0,0;
anglefix 120 0.5 n4a c15a c16a; c15a c16a O3a;
anglefix 113 0.5 o1a n3a o2a;
anglefix 112 0.5 c4a n1a N2a#t0,-1,0;
anglefix 114 0.5 n1a n2a c7a;
anglefix 110 0.5 c15a c16a O3a;
anglefix 120 0.5 c2b c1b n3b; c6b c1b n3b; c6b c1b c2b; c1b c2b c3b;
anglefix 120 0.5 c2b c3b c4b; c3b c4b c5b; c4b c5b c6b; c5b c6b c1b;
anglefix 120 0.5 c3b c4b n1b; c5b c4b n1b; c8b c7b n2b; c12b c7b n2b;
anglefix 120 0.5 c12b c7b c8b; c7b c8b c9b; c8b c9b c10b; c9b c10b c11b;
anglefix 120 0.5 c10b c11b c12b; c11b c12b c7b; c9b c10b n4b; c11b c10b n4b;
anglefix 120 0.5 c10b n4b c13b; c10b n4b c15b; c13b n4b c15b; n4b c13b c14b;
anglefix 120 0.5 n4b c15b c16b; c15b c16b o3b;
anglefix 113 0.5 o1b n3b o2b;
anglefix 112 0.5 c4b n1b n2b;
anglefix 114 0.5 n1b n2b c7b;
anglefix 110 0.5 c15b c16b o3b;
anglefix 108.6 1.0 H9b O3b C16b;
anglefix 108.6 1.0 H9a O3a C16a;

keep geom plane n3a C1a c2a C3a c4a C5a#t0,-1,0 C6a#t0,-1,0 n1a
keep geom plane n2a c7a c8a c9a c10a c11a c12a n4a
keep geom plane n3b c1b c2b c3b c4b c5b c6b n1b
keep geom plane n2b c7b c8b c9b c10b c11b c12b n4b
keep hydro triang C2a 2 1 C1a C3a 1.09 H1a
keep ADP riding C2a 2 H1a
keep hydro triang C3a 2 1 C2a C4a 1.09 H2a
keep ADP riding C3a 2 H2a
keep hydro triang C5a 2 1 C6a C4a#t0,1,0 1.09 H3a
keep ADP riding C5a 2 H3a
keep hydro triang C6a 2 1 C5a C1a#t0,1,0 1.09 H4a
```

```
keep ADP riding C6a 2 H4a
keep hydro triang C8a 2 1 C9a C7a 1.09 H5a
keep ADP riding C8a 2 H5a
keep hydro triang C9a 2 1 C8a C10a 1.09 H6a
keep ADP riding C9a 2 H6a
keep hydro triang C11a 2 1 C12a C10a 1.09 H7a
keep ADP riding C11a 2 H7a
keep hydro triang C12a 2 1 C11a C7a 1.09 H8a
keep ADP riding C12a 2 H8a
keep hydro triang C2b 2 1 C3b C1b 1.09 H1b
keep ADP riding C2b 2 H1b
keep hydro triang C3b 2 1 C2b C4b 1.09 H2b
keep ADP riding C3b 2 H2b
keep hydro triang C5b 2 1 C6b C4b 1.09 H3b
keep ADP riding C5b 2 H3b
keep hydro triang C6b 2 1 C5b C1b 1.09 H4b
keep ADP riding C6b 2 H4b
keep hydro triang C8b 2 1 C9b C7b 1.09 H5b
keep ADP riding C8b 2 H5b
keep hydro triang C9b 2 1 C8b C10b 1.09 H6b
keep ADP riding C9b 2 H6b
keep hydro triang C11b 2 1 C12b C10b 1.09 H7b
keep ADP riding C11b 2 H7b
keep hydro triang C12b 2 1 C11b C7b 1.09 H8b
keep ADP riding C12b 2 H8b
keep hydro tetrahed C13a 2 2 N4a C14a#t-1,0,0 1.1 H14a H13a
keep ADP riding C13a 2 H14a H13a
keep hydro tetrahed C14a 1 3 C13a#t1,0,0 1.1 H12a H10a H11a
keep ADP riding C14a 2 H12a H10a H11a
keep hydro tetrahed C15a 2 2 N4a C16a 1.1 H16a H15a
keep ADP riding C15a 2 H16a H15a
keep hydro tetrahed C16a 2 2 O3a C15a 1.1 H17a H18a
keep ADP riding C16a 2 H17a H18a
keep hydro tetrahed C13b 2 2 N4b C14b 1.1 H13b H14b
keep ADP riding C13b 2 H13b H14b
keep hydro tetrahed C14b 1 3 C13b 1.1 H10b H11b H12b
keep ADP riding C14b 2 H10b H11b H12b
keep hydro tetrahed C15b 2 2 N4b C16b 1.1 H15b H16b
keep ADP riding C15b 2 H15b H16b
keep hydro tetrahed C16b 2 2 O3b C15b 1.1 H17b H18b
keep ADP riding C16b 2 H17b H18b
keep ADP riding O3a 1.5 H9a
keep ADP riding O3b 1.5 H9b
```

4. Belite Polymorphs

Acquisition and output parameters from the successful structure solutions of DM in *Sir2014* for the analysed datasets

	"clinker_0"				**"clinker_2.5"**		**"clinker_5"**		
Ref. Crystal Number:	1 (β)	2 (β)	3 (β*)	4 (α'_H)	1 (β*)	2 (α'_H)	1 (β*)	2 (β)	3 (α'_H)
Tilt Range (°)	-45/45	-45/45	-45/45	-45/45	-35/45	-60/60	-45/45	-45/45	-45/45
Acq. Patterns (#)	91	91	91	91	81	121	91	91	91
CCD Exposure Time (s)	2	1	1	1	0.2	0.5	1	1	1
Num. of Reflections (#)	3671	3681	3632	3575	1376	1643	1559	1529	1536
Ind. Refl. at 0.7 Å (#)	696	825	865	444	550	512	616	601	424
Completeness (%)	65.9	78.1	81.9	72.9	52.1	85.3	58.6	57.0	70.8
Refl./Param. Ratio (-)	16.4	19.5	21.2	11.8	12.5	13.5	13.7	13.8	11.7
Overall B (Å^2)	1.01	0.95	0.90	1.84	1.04	1.97	0.64	0.73	2.01
R_{int} (%)	11.5	8.1	8.1	13.5	15.4	11.6	8.13	10.9	12.7
R (%)	17.0	20.0	23.3	14.8	23.6	16.0	26.5	17.7	20.8

"clinker_0" datasets were acquired at 750 mm of camera length, while "clinker_2.5" and "clinker_5" datasets at 1 m. R_{int} is based on structure factors and R is based on structure factors and the BEA algorithm. "Ref." stands for reference, "Refl." for reflections and "Param." for structure parameters.
* Twinned crystal from which one of the twins structure solutions is reported.

CIF file of the average structure of α'-C_2S from the dynamical refinement of "clinker_0"

```
_chemical_formula_sum                    'Ca8 O16 Si4'
_chemical_formula_weight                 689
_symmetry_cell_setting                   orthorhombic
_symmetry_space_group_name_H-M           'P n m a'
_symmetry_space_group_name_Hall          '-P -2xabc;-2yb;-2zac'
_symmetry_Int_Tables_number              62

loop_
_space_group_symop_id
_space_group_symop_operation_xyz
1    x,y,z
2    -x+1/2,-y,z+1/2
3    -x,y+1/2,-z
4    x+1/2,-y+1/2,-z+1/2
5    -x,-y,-z
6    x+1/2,y,-z+1/2
7    x,-y+1/2,z
8    -x+1/2,y+1/2,z+1/2

_cell_length_a                           6.776
_cell_length_b                           5.496
_cell_length_c                           9.252
_cell_angle_alpha                        90
_cell_angle_beta                         90
_cell_angle_gamma                        90
_cell_volume                             344.5528
_cell_formula_units_Z                    1
_exptl_crystal_density_diffrn            3.3204

loop_
_atom_type_symbol
_atom_type_scat_source
Ca   International_Tables_Vol_C
O    International_Tables_Vol_C
Si   International_Tables_Vol_C

loop_
_atom_site_label
_atom_site_type_symbol
_atom_site_fract_x
_atom_site_fract_y
_atom_site_fract_z
_atom_site_adp_type
_atom_site_U_iso_or_equiv
_atom_site_site_symmetry_multiplicity
_atom_site_occupancy
Ca1 Ca 0.66658(12) 0.75 0.5706(2) Uani 0.0251(6) 4 1
Ca2 Ca 0.49080(11) 0.25 0.79563(19) Uani 0.0161(5) 4 1
Si1 Si 0.78069(16) 0.25 0.4128(3) Uani 0.0157(8) 4 1
O1 O 0.7521(6) 0.5203(6) 0.8014(7) Uani 0.0258(18) 8 0.621(6)
O2 O 0.6574(3) 0.3219(4) 0.5622(7) Uani 0.030(2) 8 0.5
O3 O 1.0073(3) 0.3122(5) 0.4500(7) Uani 0.024(2) 8 0.5
```

```
O1_2 O 0.8219(9) 0.5103(11) 0.8563(14) Uani 0.0258(18) 8 0.379(6)

loop_
_atom_site_aniso_label
_atom_site_aniso_type_symbol
_atom_site_aniso_U_11
_atom_site_aniso_U_22
_atom_site_aniso_U_33
_atom_site_aniso_U_12
_atom_site_aniso_U_13
_atom_site_aniso_U_23
Ca1 Ca 0.0123(4) 0.0387(6) 0.0244(17) 0 −0.0005(6) 0
Ca2 Ca 0.0090(4) 0.0275(5) 0.0118(14) 0 −0.0004(5) 0
Si1 Si 0.0114(5) 0.0201(7) 0.016(2) 0 0.0002(7) 0
O1 O 0.026(2) 0.0194(9) 0.032(5) −0.0089(13) 0.0070(18) −0.0099(17)
O2 O 0.0141(11) 0.037(2) 0.039(6) −0.0012(8) 0.0088(17) 0.0096(17)
O3 O 0.0159(11) 0.042(3) 0.014(5) −0.0063(8) 0.0023(15) −0.0050(14)
O1_2 O 0.026(2) 0.0194(9) 0.032(5) −0.0089(13) 0.0070(18) −0.0099(17)
```

CIF file of the average structure of α'-C_2S from the dynamical refinement of "clinker_2.5"

```
_chemical_formula_sum                    'Ca8 O16 Si4'
_chemical_formula_weight                 689
_symmetry_cell_setting                   orthorhombic
_symmetry_space_group_name_H-M           'P n m a'
_symmetry_space_group_name_Hall          '-P -2xabc;-2yb;-2zac'
_symmetry_Int_Tables_number              62

loop_
_space_group_symop_id
_space_group_symop_operation_xyz
1    x,y,z
2    -x+1/2,-y,z+1/2
3    -x,y+1/2,-z
4    x+1/2,-y+1/2,-z+1/2
5    -x,-y,-z
6    x+1/2,y,-z+1/2
7    x,-y+1/2,z
8    -x+1/2,y+1/2,z+1/2

_cell_length_a                           6.765
_cell_length_b                           5.514
_cell_length_c                           9.25
_cell_angle_alpha                        90
_cell_angle_beta                         90
_cell_angle_gamma                        90
_cell_volume                             345.0454
_cell_formula_units_Z                    1
_exptl_crystal_density_diffrn            3.3157

loop_
_atom_type_symbol
_atom_type_scat_source
Ca   International_Tables_Vol_C
O    International_Tables_Vol_C
Si   International_Tables_Vol_C

loop_
_atom_site_label
_atom_site_type_symbol
_atom_site_fract_x
_atom_site_fract_y
_atom_site_fract_z
_atom_site_adp_type
_atom_site_U_iso_or_equiv
_atom_site_site_symmetry_multiplicity
_atom_site_occupancy
Ca1 Ca 0.16773(15) 0.75 0.42906(13) Uani 0.0256(5) 4 1
Ca2 Ca 0.50905(13) 0.75 0.70488(13) Uani 0.0172(4) 4 1
Si1 Si 0.28113(18) 0.25 0.58717(17) Uani 0.0170(6) 4 1
O1 O 0.7470(7) 0.4794(8) 0.8050(5) Uani 0.0312(15) 8 0.647(7)
O2 O 0.4946(5) 0.770(4) 0.4509(4) Uani 0.095(3) 8 0.5
O3 O 0.1579(4) 0.3184(9) 0.4389(4) Uani 0.032(2) 8 0.5
```

```
O1_2 O 0.6761(12) 0.4871(16) 0.8553(12) Uani 0.0312(15) 8 0.353(7)

loop_
_atom_site_aniso_label
_atom_site_aniso_type_symbol
_atom_site_aniso_U_11
_atom_site_aniso_U_22
_atom_site_aniso_U_33
_atom_site_aniso_U_12
_atom_site_aniso_U_13
_atom_site_aniso_U_23
Ca1 Ca 0.0156(5) 0.0412(11) 0.0200(8) 0 0.0016(5) 0
Ca2 Ca 0.0114(5) 0.0286(8) 0.0117(6) 0 −0.0009(4) 0
Si1 Si 0.0146(7) 0.0258(13) 0.0106(10) 0 −0.0008(6) 0
O1 O 0.030(2) 0.0249(19) 0.039(3) −0.0082(18) −0.0135(17) 0.0129(19)
O2 O 0.0247(17) 0.239(10) 0.020(2) 0.067(6) 0.0038(14) 0.007(7)
O3 O 0.0181(13) 0.060(6) 0.018(2) 0.0032(17) −0.0090(12) −0.0079(17)
O1_2 O 0.030(2) 0.0249(19) 0.039(3) −0.0082(18) −0.0135(17) 0.0129(19)
```

CIF file of the modulated structure of α'-C_2S from the dynamical refinement of "clinker_0"

```
_chemical_formula_sum                          'Ca8 O16 Si4'
_chemical_formula_weight                       689
_symmetry_cell_setting                         orthorhombic
_space_group_ssg_name                          'Pnma(\a00)0ss'

loop_
_space_group_symop_ssg_id
_space_group_symop_ssg_operation_algebraic
1    x1,x2,x3,x4
2    -x1+1/2,-x2,x3+1/2,-x4+1/2
3    -x1,x2+1/2,-x3,-x4+1/2
4    x1+1/2,-x2+1/2,-x3+1/2,x4
5    -x1,-x2,-x3,-x4
6    x1+1/2,x2,-x3+1/2,x4+1/2
7    x1,-x2+1/2,x3,x4+1/2
8    -x1+1/2,x2+1/2,x3+1/2,-x4

_cell_length_a                                 6.776
_cell_length_b                                 5.496
_cell_length_c                                 9.252
_cell_angle_alpha                              90
_cell_angle_beta                               90
_cell_angle_gamma                              90
_cell_volume                                   344.5528
_cell_modulation_dimension                     1
loop_
_cell_wave_vector_seq_id
_cell_wave_vector_x
_cell_wave_vector_y
_cell_wave_vector_z
1  0.372500  0.000000  0.000000
_cell_formula_units_Z                          1
_exptl_crystal_density_diffrn                  3.3204

loop_
_atom_type_symbol
_atom_type_scat_source
Ca  International_Tables_Vol_C
O   International_Tables_Vol_C
Si  International_Tables_Vol_C

loop_
_atom_site_label
_atom_site_type_symbol
_atom_site_fract_x
_atom_site_fract_y
_atom_site_fract_z
_atom_site_adp_type
_atom_site_U_iso_or_equiv
_atom_site_site_symmetry_multiplicity
_atom_site_occupancy
Ca1 Ca 1.16654(15) 0.75 0.5714(2) Uiso 0.0130(3) 4 1
```

```
Ca2 Ca 1.00881(13) 0.75 0.2045(2) Uiso 0.0069(3) 4 1
Si1 Si 0.7195(2) 0.75 0.5881(4) Uiso 0.0100(4) 4 1
O1 O 0.7772(3) 0.9827(3) 0.6781(5) Uiso 0.0150(5) 8 1
O2 O 0.8422(4) 0.6772(5) 0.4352(7) Uiso 0.0215(7) 8 0.5
O3 O 0.4913(4) 0.8101(4) 0.5485(6) Uiso 0.0194(7) 8 0.5

loop_
_atom_site_Fourier_wave_vector_seq_id
_jana_atom_site_Fourier_wave_vector_q1_coeff
1     1

loop_
_atom_site_occ_special_func_atom_site_label
_atom_site_occ_special_func_crenel_c
_atom_site_occ_special_func_crenel_w
O2   0.0025(18)   0.5
O3   0.715(2)   0.5

loop_
_atom_site_displace_Fourier_atom_site_label
_atom_site_displace_Fourier_axis
_atom_site_displace_Fourier_wave_vector_seq_id
_atom_site_displace_Fourier_param_cos
_atom_site_displace_Fourier_param_sin
Ca1   x   1      0                  0
Ca1   y   1      0.0281(3)         -0.0237(3)
Ca1   z   1      0                  0
Ca2   x   1      0                  0
Ca2   y   1     -0.0154(3)         -0.0325(3)
Ca2   z   1      0                  0
Si1   x   1      0                  0
Si1   y   1     -0.0170(4)         -0.0178(4)
Si1   z   1      0                  0
O1    x   1      0.0382(5)         -0.0264(5)
O1    y   1      0.0049(5)         -0.0207(5)
O1    z   1     -0.0365(7)          0.0096(8)

loop_
_geom_bond_atom_site_label_1
_geom_bond_atom_site_label_2
_geom_bond_distance_av
_geom_bond_distance_min
_geom_bond_distance_max
Si1 O1 1.611(6) 1.564(6) 1.669(6)
Si1 O1 1.611(6) 1.564(6) 1.669(6)
Si1 O2 1.682(6) 1.662(6) 1.721(6)
Si1 O2 1.683(6) 1.662(6) 1.721(6)
Si1 O3 1.618(3) 1.601(3) 1.651(3)
Si1 O3 1.617(3) 1.601(3) 1.651(3)
```

CIF file of the modulated structure of α'-C_2S from the dynamical refinement of "clinker_2.5"

```
_chemical_formula_sum                          'Ca8 O16 Si4'
_chemical_formula_weight                       689
_symmetry_cell_setting                         orthorhombic
_space_group_ssg_name                          'Pnma(\a00)0ss'

loop_
_space_group_symop_ssg_id
_space_group_symop_ssg_operation_algebraic
1    x1,x2,x3,x4
2    -x1+1/2,-x2,x3+1/2,-x4+1/2
3    -x1,x2+1/2,-x3,-x4+1/2
4    x1+1/2,-x2+1/2,-x3+1/2,x4
5    -x1,-x2,-x3,-x4
6    x1+1/2,x2,-x3+1/2,x4+1/2
7    x1,-x2+1/2,x3,x4+1/2
8    -x1+1/2,x2+1/2,x3+1/2,-x4

_cell_length_a                                 6.765
_cell_length_b                                 5.514
_cell_length_c                                 9.25
_cell_angle_alpha                              90
_cell_angle_beta                               90
_cell_angle_gamma                              90
_cell_volume                                   345.0454
_cell_modulation_dimension                     1
loop_
_cell_wave_vector_seq_id
_cell_wave_vector_x
_cell_wave_vector_y
_cell_wave_vector_z
1  0.379500  0.000000  0.000000
_cell_formula_units_Z                          1
_exptl_crystal_density_diffrn                  3.3157

loop_
_atom_type_symbol
_atom_type_scat_source
Ca  International_Tables_Vol_C
O   International_Tables_Vol_C
Si  International_Tables_Vol_C

loop_
_atom_site_label
_atom_site_type_symbol
_atom_site_fract_x
_atom_site_fract_y
_atom_site_fract_z
_atom_site_adp_type
_atom_site_U_iso_or_equiv
_atom_site_site_symmetry_multiplicity
_atom_site_occupancy
Ca1 Ca 0.49106(12) 0.75 0.20467(11) Uiso 0.0091(2) 4 1
```

```
Ca2 Ca 0.83234(13) 0.75 −0.07067(11) Uiso 0.0169(3) 4 1
Si1 Si 0.21886(16) 0.25 0.41267(15) Uiso 0.0101(3) 4 1
O1 O 0.2760(3) 0.4818(4) 0.3217(2) Uiso 0.0278(5) 8 1
O2 O 0.6575(3) 0.8153(5) 0.4402(3) Uiso 0.0261(6) 8 0.5
O3 O 0.5086(3) 0.8056(5) −0.0482(3) Uiso 0.0270(7) 8 0.5

loop_
_atom_site_Fourier_wave_vector_seq_id
_jana_atom_site_Fourier_wave_vector_q1_coeff
1     1

loop_
_atom_site_occ_special_func_atom_site_label
_atom_site_occ_special_func_crenel_c
_atom_site_occ_special_func_crenel_w
O2   0.496(2)   0.5
O3   0.777(2)   0.5

loop_
_atom_site_displace_Fourier_atom_site_label
_atom_site_displace_Fourier_axis
_atom_site_displace_Fourier_wave_vector_seq_id
_atom_site_displace_Fourier_param_cos
_atom_site_displace_Fourier_param_sin
Ca1   x   1      0                  0
Ca1   y   1     −0.0105(4)          0.0274(3)
Ca1   z   1      0                  0
Ca2   x   1      0                  0
Ca2   y   1     −0.0231(3)         −0.0174(4)
Ca2   z   1      0                  0
Si1   x   1      0                  0
Si1   y   1      0.0209(5)          0.0141(5)
Si1   z   1      0                  0
O1    x   1     −0.0333(4)          0.0257(4)
O1    y   1     −0.0025(6)          0.0194(6)
O1    z   1     −0.0292(3)          0.0106(4)

loop_
_geom_bond_atom_site_label_1
_geom_bond_atom_site_label_2
_geom_bond_distance_av
_geom_bond_distance_min
_geom_bond_distance_max
Si1 O1 1.606(5) 1.579(5) 1.638(5)
Si1 O1 1.606(5) 1.579(5) 1.638(5)
Si1 O2 1.627(3) 1.613(3) 1.663(3)
Si1 O2 1.628(3) 1.613(3) 1.663(3)
Si1 O3 1.609(2) 1.590(3) 1.641(3)
Si1 O3 1.609(2) 1.590(3) 1.641(3)
```

List of Figures

List of Tables

Scientific Curriculum

Workshops & Schools

- Electron Crystallography School 2015 (ECS2015). 28^{th} to 31^{st} of August 2015. Poreč, Croatia.
- Electron Diffraction - X-ray Powder Diffraction Workshop. 6^{th} to 10^{th} of June 2016. Stockholm, Sweden.
- International School of Crystallography. 51st Course: Electron Crystallography (ISC-EC2018). 1^{st} to 10^{th} of June 2018. Erice, Italy.

Congress Attendances

- 20th International Congress on Magnetism (ICM2015). 5^{th} to 10^{th} of July 2015. Barcelona, Catalonia.
- 10ème édition des Journées de l'EELS (JEELS2016). 28^{th} to 30^{th} of June 2016. Tarragona, Catalonia.
- 16th European Microscopy Congress (EMC2016). 28^{th} of August to 2^{nd} of September 2016. Lyon, France.
- Microscopy at the Frontiers of Science 2017 (MFS2017). 5^{th} to 8^{th} of September 2017. Zaragoza, Spain.
- 26th Annual Meeting of the German Crystallographic Society (DGK2018). 5^{th} to 8^{th} of March 2018. Essen, Germany.
- Microscopy Conference 2019 (MC2019). 1^{st} to 5^{th} of September 2019. Berlin, Germany.
- Microscopy at the Frontiers of Science 2019 (MFS2019). 11^{th} to 13^{th} September 2019. Granada, Spain.

Congress Contributions

- Poster: *"Interpretation of HRTEM images of $Sr_{0.67}Ba_{0.33}NbO$ by simulations through the multislice approach"*. ECS2015.
- Oral: *"Enhancement of EELS quantification by means of precession electron diffraction"*. JEELS2016.

- Poster: *"Precession-assisted Quasi-Parallel Illumination STEM on three Condenser Lens TEMs"*. EMC2016.
- Oral: *"Quasi-Parallel PED-STEM made easy: a new reliable method to aling it"*. MFS2017.
- Poster: *"Universal Alignment Method for Quasi-Parallel Diffraction on Scanning Transmission Electron Microscopes"*. ISC-EC2018.
- Oral: *"Structural Characterization of an Ultra-High Strength Fe-Cr-Ni Silicide Phase"*. DGK2018.
- Poster: *"Fast and Automated Diffraction Tomography: Universal Acquisition Module"*. MC2019.
- Oral: *"Fast-ADT: how to acquire 3D Electron Diffraction in a systematic and accurate way"*. MFS2019.

Journal Articles

1. *"A high-strength silicide phase in a stainless steel alloy designed for wear-resistant applications"*, D. Bowden, Y. Krysiak, L. Palatinus, D. Tsivoulas, **S. Plana-Ruiz**, E. Sarakinou, U. Kolb, D. Stewart & M. Preuss. *Nature Communications* 9 (2018) 1374.

2. *"Au crystal growth on natural occurring Au-Ag aggregate elucidated by means of precession electron diffraction (PED)"*, J. R. Rosell, J. P. Serra, T. Aiglsperger, **S. Plana-Ruiz**, T. Trifonov & J. A. Proenza. *Journal of Crystal Growth* 483 (2018) 228-235.

3. *"Quasi-parallel precession diffraction: Alignment method for scanning transmission electron microscopes"*, **S. Plana-Ruiz**, J. Portillo, S. Estradé, F. Peiró, U. Kolb & S. Nicolopoulos. *Ultramicroscopy* 193 (2018) 39-51.

4. *"Calcium Sulfate Nanoparticles with Unusual Dispersibility in Organic Solvents for Transparent Film Processing*, S. Leukel, M. Panthöfer, M. Mondeshki, W. Schärtl, **S. Plana-Ruiz** & W. Tremel. *Langmuir* 34 (2018) 7096-7105.

5. *"Iron Oxide Superparticles with Enhanced MRI Performance by Solution Phase Epitaxial Growth"*, M. Kluenker, M. N. Tahir, R. Dören, M. Deuker, P. Komforth, **S. Plana-Ruiz**, B. Barton, S. I. Shylin. V. Ksenofontov, M. Panthöfer, N. Wiesmann, J. Herzberger, A. Möller, H. Frey, J. Brieger, U. Kolb & W. Tremel. *Chemistry of Materials* 30 (2018) 4277-4288.

6. *"Controlling the Morphology of Au-Pd Heterodimer Nanoparticles by Surface Ligands"*, M. Kluenker, B. M. Connolly, D. M. Marolf, M. N. Tahir, K. Korschelt, P. Simon, U. Köhler, **S. Plana-Ruiz**, B. Barton, M. Panthöfer, U. Kolb & W. Tremel. *Inorganic Chemistry* 57 (2018) 13640-13652.

7. *"Structural characterization and ab-initio resolution of natural occurring zaccariniite (RhNiAs) by means of Precession Electron Diffraction"*, J. R. Rosell, J. Portillo, T. H. Aiglsperger, **S. Plana-Ruiz**, P. P. Das, J. M. Gonzalvez, T. Trifonov & J. A. Proenza. *Microchemical Journal* 148 (2019) 130-140.

8. *"Crystallographic information data of natural occurring zaccariniite (RhNiAs) obtained by means of precession electron diffraction"*, J. R. Rosell, J. Portillo, T. Aiglsperger, **S. Plana-Ruiz**, P. P. Das, J. M. Gonzalvez, T. Trifonov & J. A. Proenza. *Data in brief* 25 (2019) 104346.

9. *"Automated electron diffraction tomography - development and applications"*, U. Kolb, Y. Krysiak & **S. Plana-Ruiz**. *Acta Cryst.* B75 (2019) 463-474.

10. *"Fast-ADT: A fast and automated electron diffraction tomography setup for structure determination and refinement"*, **S. Plana-Ruiz**, Y. Krysiak, J. Portillo, E. Alig, S. Estradé, F. Peiró & U. Kolb. *Ultramicroscopy* 211 (2020) 112951.

11. *"Topochemical Reduction of $La_2NiO_3F_2$: The First Ni-Based Ruddlesden-Popper n = 1 T'-Type Structure and the Impact of Reduction on Magnetic Ordering"*, K. Wissel, A. M. Malik, S. Vasala, **S. Plana-Ruiz**, U. Kolb, P. R. Slater, I. da Silva, L. Alf, J. Rohrer & O. Clemens. *Chemistry of Materials* 32 (2020) 3160-3179.

12. *"New zeolite-like RUB-5 and its related hydrous layer silicate RUB-6 structurally characterized by electron microscopy"*, Y. Krysiak, B. Marler, B. Barton, **S. Plana-Ruiz**, H. Gies, R. B. Neder & U. Kolb. *IUCrJ* 7 (2020) 522-534.

13. *"High cycle life all-solid-state fluoride ion battery with La_2NiO_{4+d} high voltage cathode"*, M.A. Nowroozi, K. Wissel, M. Donzelli, N. Hosseinpourkahvaz, **S. Plana-Ruiz**, U. Kolb, R. Schoch, M. Bauer, A. M. Malik, J. Rohrer, S. Ivlev, F. Kraus & O. Clemens. *Communication Materials* 1 (2020) 27.

Declaration of the Author

I hereby declare that I have completed the dissertation only using the sources and tools specified without the help of third parties. All resources taken from other entities are referenced as such. This work has not been submitted before to an examination authority in the same or similar form.

Barcelona,

Sergi Plana Ruiz